QBlade: A Modern Tool for the Aeroelastic Simulation of Wind Turbines

vorgelegt von
Dipl.-Ing.
David Marten
ORCID: 0000-0002-7749-1026

an der Fakultät V – Verkehrs- und Maschinensysteme
der Technischen Universität Berlin
zur Erlangung des akademischen Grades

Doktor der Ingenieurwissenschaften
- Dr.-Ing. -

genehmigte Dissertation

Promotionsausschuss:

Vorsitzender:	Prof. Dr.-Ing. Clemens Biet
Gutachter:	Prof. Dr.-Ing. Christian Oliver Paschereit
Gutachter:	Prof. Dr.-Ing. Jens Fortmann
Gutachter:	Dr. Athanasios Barlas

Tag der wissenschaftlichen Aussprache : 19.09.2019

Berlin 2020

Abstract

Wind turbines are large and complex machines which operate in a highly unsteady environment. Due to the spatially and temporally stochastic nature of the wind resource, a large amount of simulation data is needed when one wants to assess the lifetime of such a machine. Both extreme events, such as storms, strong gusts or significant wind direction changes and normal operation, representative of the stochastic characteristics of the wind site, must be present in the evaluated data set to obtain meaningful results.

This necessitates the evaluation of many simulations, until the statistics of the synthesized wind input fields converge to those of field data, measured over long periods of time. The required time steps to resolve the key loading characteristics of the turbine are typically small, scaled to around $3°$ to $10°$ of rotor advancement. This leads to an overall number of time steps in the order of 10^6 to 10^7 that need to be evaluated for a lifetime assessment according to the IEC 61400-1 standard. This large number of time steps is a serious constraint when it comes to the selection of suitable methods for the aeroelastic simulation of wind turbines. An aeroelastic simulation tool requires two models, one for the simulation of the wind turbine aerodynamics and one for the simulation of the structural dynamics of the system. Both models are then coupled to simulate and resolve all machine relevant aeroelastic effects.

As a part of this work the wind turbine simulation and design software QBlade has been developed. The main goal during this development process was to facilitate the usage of modern simulation models within the wind turbine design and certification process. Generally, higher order methods lead to more accurate simulation results, which enables wind turbine designers and manufacturers to lower the levelized cost of energy by applying smaller structural safety margins and more efficient aeroelastic designs. However, this improved accuracy comes with the penalty of higher computational costs.

The application of these methods in the aforementioned certification and design process, where a large number of computations is required, is made possible through the steady increase of processing power of widely available consumer hardware and the application of massive parallelization, leveraging the enormous computational potential of modern graphics processing units (GPUs). This work presents the methods applied in the QBlade simulation code and gives reasoning for their selection and their classification within the range of different simulation methods that can be applied to model wind turbine aero-elastics. Finally, a range of examples for the applications of the aero-elastic simulation framework in QBlade are given.

Zusammenfassung

Windenergieanlagen sind große und komplexe Maschinen, die über ihre gesamte Lebensdauer unter hochgradig instationären Randbedingungen betrieben werden. Um die Lebensdauer einer solchen Anlage vorherzusagen müssen eine große Anzahl von Simulationen durchgeführt werden, welche die stochastischen Eigenschaften des am Standort vorherrschenden Windes abbilden. Sowohl extreme Lasten, hervorgerufen durch Unwetter, Stürme oder Erdbeben, als auch Dauerlasten, welche sich aus dem normalen Betrieb unter Einfluss einer turbulenten Wind Anströmung ergeben, müssen in den Berechnungen zum Lebensdauernachweis enthalten sein.

Aus diesen Anforderungen ergibt sich, dass eine große Anzahl an Simulationen benötigt wird um statisch aussagekräftige Daten zu erhalten. In der Regel werden Lastsimulationen mit Zeitschrittweiten durchgeführt die einem Rotorfortschritt zwischen 3° und 10° entsprechen. Dies führt dazu, dass bei einer vollständigen Lebensdauerberechnung nach dem IEC 61400-1 Standard insgesamt zwischen 10^6 bis 10^7 konvergierte aero-elastische Zeitschritte berechnet werden. Daraus lässt sich eine der zentralen Anforderungen an aero-elastische Simulationsmethoden für den Windenergiebereich ableiten: Die verwendeten Simulationsverfahren müssen zwangsläufig sehr effizient sein. Aeroelastische Simulationsmethoden setzen sich im Wesentlichen aus einem aerodynamischen- und einem strukturellen Simulationsverfahren zusammen. Diese Verfahren werden gekoppelt um die Auswirkungen des Zusammenspiels von aerodynamischen-, trägheits-, gravitations- und elastischen Kräften und Momenten zu berechnen.

Als ein Teil der hier vorgestellten Arbeit wurde in den letzten 8 Jahren das aero-elastische Simulationstool QBlade entwickelt. Als Hauptziel hierbei galt es die Verwendung von neuen Aerodynamik- und Strukturmodellierungsmethoden zu ermöglichen, welche genauere und verlässlichere Ergebnisse liefern als die bisher in der Industrie verwendeten Verfahren. Generell lassen sich durch genauere Simulationsverfahren die Stromgestehungskosten senken da Sicherheitsfaktoren reduziert werden können, Material eingespart wird und damit effizientere Designs ermöglicht werden. Im Vergleich mit den bisher eingesetzten Verfahren führen diese neuen Methoden allerdings zu einem gesteigerten Rechenbedarf.

Die Verwendung dieser neuen Methoden im Auslegungs- und Zertifizierungskontext wird erst durch die konstante Steigerung der für den Endnutzer verfügbaren Rechenleistung in die letzten Jahre ermöglicht. Mithilfe von massiver Parallelisierung durch high-end Garfikprozessoren (GPUs), sowie die Optimierung der neuen Berechnungsmethoden selbst, können diese nun im großen Umfang eingesetzt werden. In dieser Arbeit werden die in QBlade verwendeten aerodynamischen und strukturellen Modelle vorgestellt, ihre Verwendung im Vergleich mit anderen Methoden begründet sowie ihre Optimierung erläutert. Anhand einiger Beispiele wird weiterhin die Flexibilität sowie das Anwendungsspektrum der hier entwickelten Simulationssoftware demonstriert.

Contents

List of Figures

List of Tables

Listings

Chapter 1 | Introduction

It is commonly accepted that global warming is one of the largest challenges that humanity is facing today. The greenhouse effect, caused by the accumulation of carbon dioxide emissions (see Figure 1.1) and other pollutants in the atmosphere, leads to a global increase in average temperature at an accelerating rate. The severe effects resulting from this temperature increase that are already starting to manifest are heat waves, droughts, local heavy rainfalls, violent storms and floods. It is predicted that once one of the so-called tipping points is reached (related to the condition of the cryosphere, the biosphere and global circulation patterns) the process of global warming becomes a self-reinforcing process that is not easily reversible and endangers the lives of millions of people.

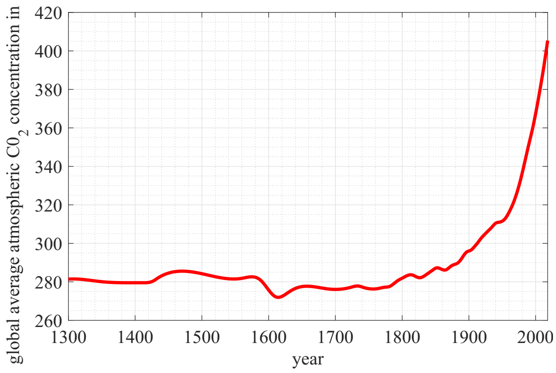

Figure 1.1.: Annual global carbon dioxide concentration, merged from historical ice core data [1] and atmospheric concentrations measured at Mauna Loa measuring station [2]

In 2015, the Paris-Agreement, signed by 195 UNFCCC members, was passed with the goal to limit the average global temperature rise to well below 2°C, compared to pre-industrial levels. In 2018, the special report on global warming (SR15) (see [3] for a summary) suggests that the more ambitious target of limiting the temperature rise to a maximum of 1.5°C is realistically obtainable, and would limit the overall risks that humanity faces from global warming dramatically.

A recent study in 2019 [4], that was published in Nature, estimates the carbon dioxide 'budget' that humanity has left to achieve the 1.5°C target. The main statement is that humanity can only continue to cause CO_2 emissions at the current rate of 41 gigatons per year for another 12 years. After that the budget is up and the odds to stay below the recommended limit of 1.5°C fall below 50%. This implies the necessity to start acting now - as the time left is very short.

The largest single contributor to the energy-related global CO_2 emissions is coal-fired electricity generation with a share of 30% [5]. Due to economic growth and increased energy demand, the total energy related CO_2 emissions would have grown by 1.25 Gt from 2017-2018. At the same time the simultaneous growth of renewable forms of energy production avoided 215 Mt of emissions, which is the largest contributor to emission savings other than the general efforts to increase energy efficiency.

The Sustainable Development Scenario (SDS), devised by the IEA, shows a pathway to achieve an overall reduction of energy related CO_2 emissions to abide the goals of the Paris Agreement, while still providing universal energy access to humanity. As a metric for this pathway the IEA tracks if the progress and dissemination of 45 critical energy technologies is in line with the SDS.

From these 45 technologies only Solar PV and Bioenergy are deemed as 'on track', whereas the growth of both onshore[1] and offshore[2] wind power generation needs to increase much faster to reach the projected targets of 3750 TWh for onshore and 606 TWh for offshore power generation by 2030 (see Figures 1.2).

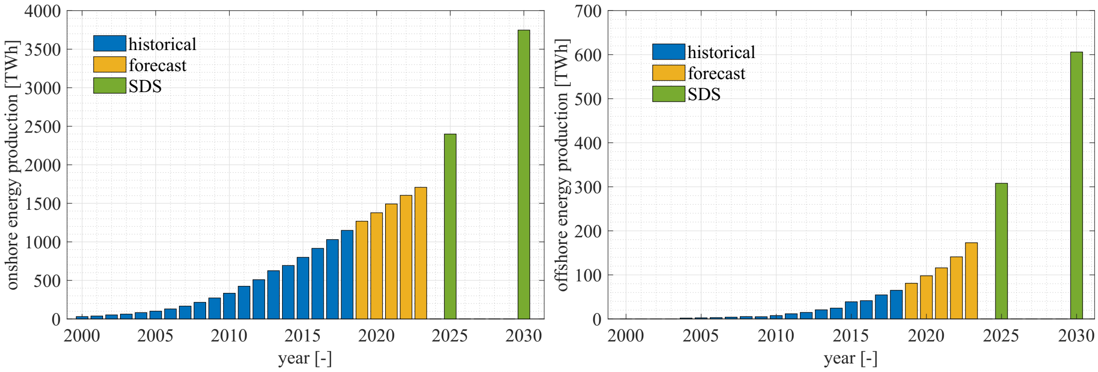

Figure 1.2.: Global on- and offshore wind power generation, historical data and predictions compared to SDS, data from [6]

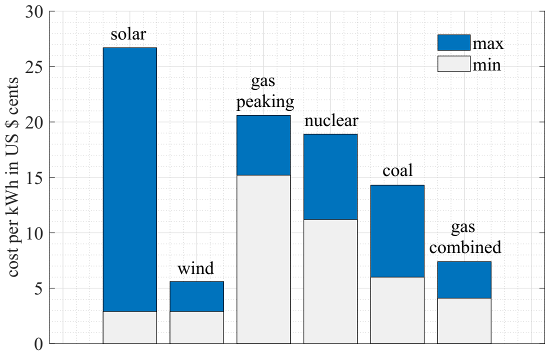

Figure 1.3.: Comparison of LCoE of different energy sources, data from [7]

Besides the need to develop cost efficient storage technologies and to improve the grid integration of renewables one of the innovation gaps in wind power generation that needs to be resolved is named *"Next generation turbine, power-train and system management technology"* [8]. The IEA has identified the up-scaling of current turbine sizes as a key requirement to achieve the projected aims for 2030 through a continuous reduction of the Levelized Cost of Electricity (LCoE) (see Figure 1.3). However, up-scaling is associated with longer, more flexible blades that require a better understanding of their operational behavior and might necessitate the development of load reduction techniques. To obtain a better understanding, and to be able to further progress the technology, work on advanced computational models is needed - especially with respect to the fluid dynamics that play an important role for the overall loads and the lifetime of wind turbines.

Furthermore, focusing on the growth of onshore wind power, where the computational side also requires advancements[3], an alternative type of turbine, the vertical axis wind turbine (VAWT), might have *"...a second chance at sea"* [9], as its comparatively lower center of gravity is beneficial for the design of floating offshore support structures.

1 Onshore wind energy production growth in 2018 was 12%, with 1149 TWh
2 Offshore wind energy production growth in 2018 was 20%, with 65.8 TWh
3 In the modeling of floating platforms and wave induced oscillations of wind turbines

1.1. The Structure of this Work

The work presented in this thesis deals with the development and application of a tool, using modern methods for the aeroelastic design and simulation of the new generation of wind turbines.

- In **Chapter 1** an overview of the different methods, that can be used to model the structural and aerodynamic behavior of wind turbines, is given.
- **Chapter 2** deals with the development of the aeroelastic simulation framework that has been integrated with QBlade.
- In **Chapter 3** examples for the application for the developed simulation framework are given in the form of previously published and unpublished work.
- **Chapter 4** focuses on highlighting the shortcomings of the current status of the aeroelastic formulation, discusses areas for improvements and gives recommendations for future work.
- The thesis is concluded in **Chapter 4.5** where the work is summed up and its overall impact is discussed.

1.2. Aeroelastic Modeling of Wind Turbines

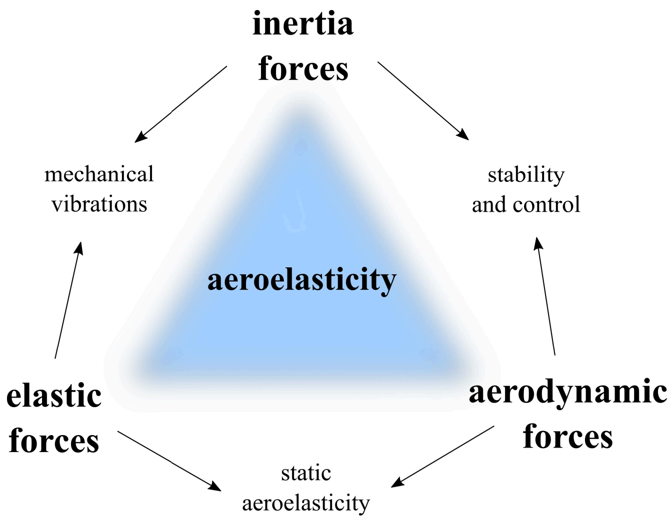

Figure 1.4.: Collar's triangle of forces, reproduced from [10]

Aeroelastic modeling plays a crucial role throughout the complete design and certification process of a wind turbine. Due to the inevitable underlying assumptions that are involved when modeling a complex physical system by means of simulation, simulations cannot fully replace experimental investigations, but generally yield results much faster and cheaper. Furthermore, they can imitate arbitrary environmental conditions and model properties.

While the aerodynamic performance of a wind turbine rotor and its optimization do not necessarily require the consideration of its structural properties, the aeroelastic characteristics of a wind turbine have huge implications for its final design. Rotor blades cannot be optimized solely based on aerodynamics but a compromise between aerodynamic and structural properties has to be made already when selecting suitable airfoils in the early stages of the design. However, only looking at their static structural integrity is not sufficient, but one also has to consider the complex nonlinear interplay of aerodynamic, elastic and inertial forces (see Figure 1.4) that arises from the complete assembly of the wind turbine. In addition to the forces depicted in Collar's triangle the *control* forces, originating from blade pitch, generator or active flow control, have a significant influence on the turbines aeroelastic characteristics [11].

As wind turbine blades are highly flexible, lightweight structures, the interplay of aero-servo-elastic forces is already strong and is further increasing with the prevalent trend towards larger rotor diameters. As the softness of the blade increases aeroelastic stability gets more and more into the focus of wind turbine designers, as larger and softer blades are more susceptible to edge or flapwise instabilities [11]. The correct identification of such instabilities during the turbine design process does require aerodynamic and structural models that are capable of resolving all relevant features, while at the same time offering a computational cost that is not prohibitive for an early design process where a large number of design evaluations (10^6 to 10^7 [12]) is required.

The following sections (1.3 and 1.4) give an overview over the different methods that we have at our disposal when choosing the components for an aeroelastic simulation framework.

1.3. Aerodynamic modeling of wind turbines

Wind turbine aerodynamic models must be able to represent the rotor blade aerodynamics and the wake aerodynamics in an accurate manner. In contrast to aircraft aerodynamics, where the wake mainly affects the assessment of suitable separation distances between landing or starting aircraft [13], but does not have a large impact[4] on the performance of an isolated aircraft, a modeling of the wake is absolutely crucial when predicting the performance of a wind turbine.

The helical rolled up vortex structure behind a wind turbine, consisting mainly of the dominant vortices shed at the root and tip of the blades, is densely packed and is inducing a velocity field in the vicinity of the rotor which is affecting the inflow conditions that the rotor is exposed to. Thus, the simulation method has to be able to represent both: blade aerodynamics and wake aerodynamics. A large range of different methods is available to model wind turbine aerodynamics over which a brief overview is given in this chapter.

In this context, it is also important to note that blade and wake aerodynamics do not necessarily have to be modeled by the same method. Due to the different challenges, originating from the large difference in time- and length scales that need to be resolved (see Table 1.1), different methods are often used to model the blade and wake aerodynamics and are then combined into a single simulation environment. In the following, an overview over the different methods that are available is given and some of the most commonly used techniques and their area of application are highlighted.

Table 1.1.: Comparison of length and time scales in wind turbine aerodynamics, reproduced after [14]

Aerodynamic subject	Length scale [m]	Time scale [s]
Airfoil boundary layer	0.001	0.00001
Airfoil	1	0.001
Rotor	100	10
Rotor with wake	1000	100
Wind park	10000	1000

1.3.1. Methods to Model Rotor Blade Aerodynamics

Blade aerodynamics are mostly associated with the generation of lift through a curvature of flow, or bound circulation, over the blade surface [16]. Small-scale aerodynamic phenomena, occurring in the viscous flow at the scale of the airfoil boundary layer, can have a large effect on flow separation or boundary layer transition and thereby on the overall lift and drag that is generated by an airfoil

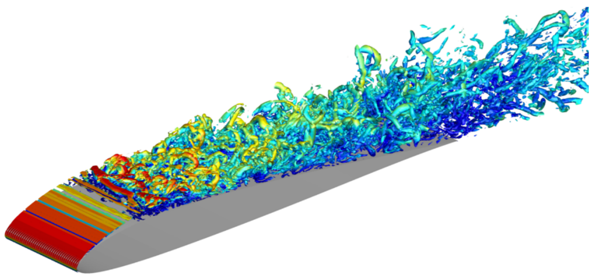

Figure 1.5.: DNS Simulation of turbulent flow over an airfoil, reproduced after [15]

4 The wake does cause tip-losses at the wings, thereby slightly reducing lift

[17, 18, 19]. To accurately capture these effects, a highly resolved simulation method also needs to take into account the exact shape of the rotor blade, including its roughness. Quantifying the exact surface geometry and local surface roughness of an airfoil in operation is challenging, especially for rotor blades that have experienced surface degradation due to rain or sand, or surface contamination due to an accretion of insects or other particles [20, 21].

Boundary layer separation, or stall is an effect most often observed in the inboard region of wind turbine blades [22, 23] where, due to their their structural integrity, the thickest airfoils are located [24]. As the blade twist in the root region is often not optimal, as it is challenging to manufacture the large required twist angles [25], these airfoil sections are often operating at high angles of attack where stall is a common phenomenon. Stall can either occur as mainly static in steady operating conditions, when the blades angles of attack are constant in time, or as dynamic, when the wind turbine is in unsteady operating conditions, influenced by non-uniform, sheared or gusty inflow [26, 27, 28, 29]. Dynamic stall leads to a lift hysteresis loop (see [30] for experimental results) with a lift overshoot, caused by the convection of the separated leading-edge vortex over the airfoils surface and a lift deficit that is observed when this leading-edge vortex is leaving the airfoil's surface. The occurrence of dynamic stall and the amplitude of the hysteresis loop are nonlinearly dependent of airfoil geometry, dimensionless frequency and amplitude of angle of attack variations.

Blade tip losses [31, 32] due to the finite aspect ratio of the blade are the result of vortices that are shed at the tip of the blade caused by an equalizing flow in spanwise direction from the blades pressure side to the blades suction side. Similar effects are also observed in the root regions of wind turbine blades where airfoil geometries are transitioning into non-lifting cylindrical shapes.

Spanwise flow on the blade surface [33, 34, 35], at the level of the boundary layer, caused by centrifugal forces may affect the separation of the boundary layer at the inner parts of the blade.

Blade Element Method

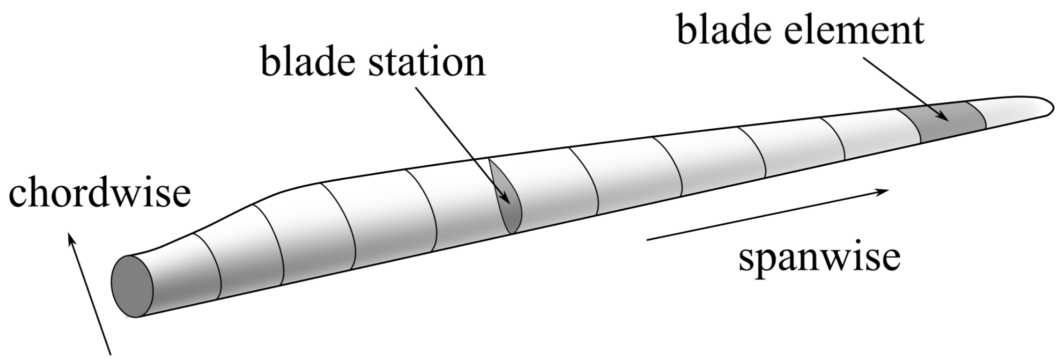

Figure 1.6.: Terms and definitions of the blade element method

The blade element method [36, 37], developed by Froude in 1878 is, despite its simplicity, still the basis of almost all engineering level wind turbine simulation codes that are used in the industry today (see Table 2.1 in Section 2.2). While being simple to setup and evaluate and only possessing a marginal computational cost, it is remarkably accurate in its estimation of rotor performance.

When the blade element method is applied, the blade is discretized into two-dimensional airfoil sections (see Figure 1.6). At each of these sections a data table is representing the airfoils non-dimensionalized aerodynamic force vector, usually split up into a lift, drag and torque component that is measured at the airfoils quarter-chord position for a range of angles of attack. Depending on the current angle of attack, that the airfoil is exposed to, the force vector is read from the data table and then integrated over the width of the discretized blade element[5]. Summing up the contribution from all blade elements of all blades then results in the overall aerodynamic force and moment that is acting on the rotor.

In the simplest case the $\frac{2\pi}{rad}$ lift slope can be used to model the airfoil performance. More sophisticated data, including friction drag, can be extracted from wind tunnel experiments or two- or three-dimensional CFD simulations. The main limitation of this method is that the flow over the airfoils surface is assumed to be two-dimensional, oriented along the chordwise direction of the blade. Cross-flow effects, originating from small aspect ratios, blade tip flow or centrifugal forces cannot be modeled by this method. However, a large number of empirical corrections have been developed (see [12, 38] for an overview) and added to the blade element method to include these effects. Furthermore, the airfoil data that is used by this method is of static nature (a single data point per angle of attack) and thus does not include the effect of dynamic stall. This can be overcome by coupling the blade element method with a dynamic stall model, which synthesizes the dynamic stall hysteresis loop from the static airfoil data. Nevertheless, most of the dynamic stall models that are used today need to be fine tuned to match the measured dynamic stall characteristics of an airfoil geometry. Furthermore, they only perform well over a limited range of angles of attack. This severely restricts their applicability when employed for the simulation of vertical axis wind turbines, which may experience drastic angle of attack changes of more than 180° during their startup phase [39, 40, 41].

Panel Methods

Panel methods [43, 44] can be used to model the two- or three-dimensional flow on the surface and within the domain around an object. Only the surface of the object under investigation needs to be discretized with panels (see Figure 1.7). Different singular aerodynamic elements, elementary solutions to the Laplace equation, may be used to represent a panel, such as sources, sinks, vortex points or doublets [44]. To satisfy the incompressible, inviscid flow around the object either a Dirichlet or Neumann boundary condition is imposed on the velocity potential to satisfy the *no flow through the surface* boundary condition. Additionally, the Kutta condition at the trailing edge of the object provides equations for the additional unknown if lifting objects are modeled with doublet elements. A resulting

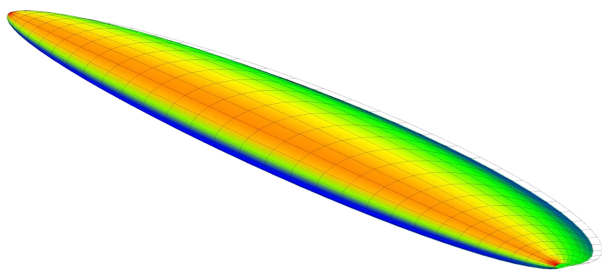

Figure 1.7.: Simulation of the inviscid flow around an elliptical wing using a panel method in QBlade, from [42]

5 Depending on the implementation polar data may or may not be interpolated between different stations

matrix composed of the panel influence coefficients can then be solved to arrive at the solution. The resulting velocity vectors on the surface can then be converted into a surface pressure distribution, which yields the aerodynamic performance. The evaluation of panel method calculations may be accelerated by using tree-codes [45] or multi level grid approaches [46].

The main limitation of the panel method is that it cannot account for low separation as inviscid flow is assumed. Furthermore, the thin viscous boundary layer on the blade surface is neglected – and so is the drag resulting from surface friction. This can be overcome by coupling a panel method with a boundary layer method to create a so-called viscous-inviscid coupling. While such a coupling is quite straightforward to setup in two dimensions, which led to the development of Drela's popular XFoil code [47], or derivatives of XFoil such as JavaFoil [48] or RFoil [49], such a coupling is somewhat more complicated to carry out in three dimensions. However, due to the potentially low computational cost[6] and high accuracy of viscous-inviscid coupled panel methods in three dimensions, many different approaches are currently being investigated [50, 51, 52, 53]. The main challenges of such a coupling are the coupling of parabolic (boundary layer) and elliptic (Laplace's) equations and the identification of the separation line in three-dimensions.

Eulerian Finite-Volume CFD Methods

Computational Fluid Dynamics (CFD) is the encompassing term for a range of different approximations to numerically solve a fluid dynamics problem within a certain domain [54]. The fluid dynamics problem might be described by the Navier-Stokes equations, the Euler equations or the Laplace equations. Eulerian, in this context, indicates that the whole domain under investigation is discretized with a space-fixed grid. The Finite Volume Method (FVM) is a numerical technique that is often used to discretize partial differential equations that are based on a conservation principle [55]. Because the conservation characteristics of the equations are retained by FVM, it is a conservative method of discretization. The primary variables that the system of equations is solving for are velocity and pressure. Eulerian FVM, approximating the Navier-Stokes equations, can be broadly classified by how they model the small scale turbulence within viscous flows:

Direct Numerical Simulations (DNS) [56], models the turbulence directly. This requires a very fine simulation grid and time step size; the computational cost grows proportional to $Re^{2.25}$. The significant computational cost makes DNS simulation only applicable to low Reynolds number flow problems. For wind turbine rotor blade aerodynamics, where the Reynolds number usually is in a range between $Re = 10^5$ to $Re = 10^7$, the large computational cost is prohibitive. Simulations of the three dimensional flow around a complete blade or rotor geometry are not feasible in a reasonable time frame, even if excessive computational resources are at hand.

Large Eddy Simulations (LES) model the turbulence up to a scale that can be resolved by the grid and time step size and uses turbulence models for the sub-grid scale turbulence [57]. To obtain accurate results in the vicinity of the blade surface, for the relevant Reynolds numbers of $Re = 10^5$ to $Re = 10^7$, a very fine mesh is needed which causes very large computational costs

Reynolds Averaged Navier-Stokes Simulations (RANS) [59], are not resolving, but only modeling

6 When compared with standard finite volume methods such as RANS or LES

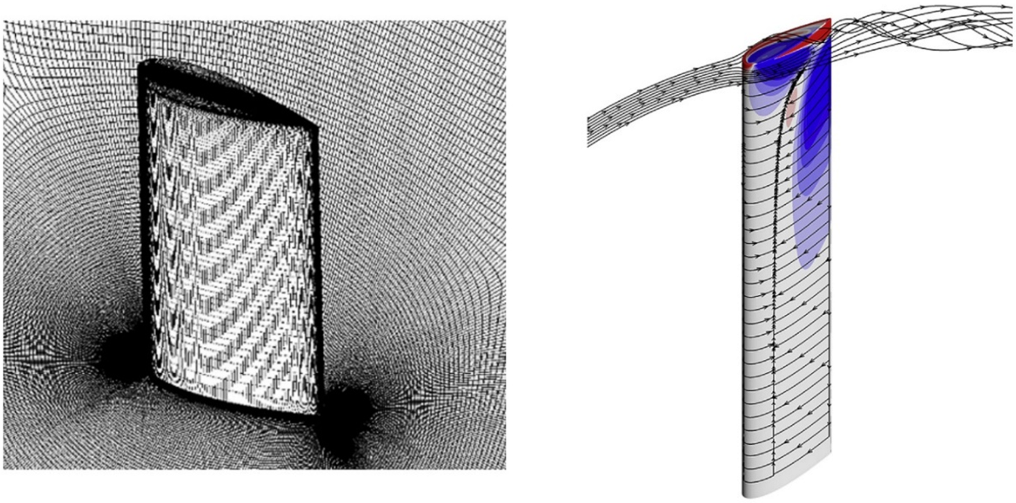

Figure 1.8.: Example of a blade resolved CFD simulation, showing mesh (left) and frictions lines on the surface (right) with streamlines in the tip region and spanwise velocity contours; reproduced from [58]

the turbulence. A Reynolds-decomposition is performed on the flow quantities[7], leading to a time-averaged, or ensemble averaged[8], mean part and a fluctuating part. This leads to an additional term in the Navier-Stokes equations, the Reynolds stress term. To close the RANS equations, which now include the Reynolds stress term, a range of turbulence models [60] may be used – such as the commonly used Spalart-Allmaras, $k - \epsilon$, $k - \omega$ or SST models. The modeling of turbulence allows one to perform RANS simulations with relatively coarse meshes and time steps[9], and several simulations of full wind turbine rotors have been performed with RANS [61, 62, 63].

A combination between RANS and LES, the Detached Eddy Simulation (DES), is often used for airfoil or rotor blade simulations [64, 65, 66, 67]. In this case RANS is used near the blade surface, to circumvent the prohibitively fine mesh that LES requires near a wall, and LES is used in the unbounded regions.

CFD methods offer the highest level of fidelity of all simulation methods. They allow to gain insight into the viscous blade boundary layer flow, flow separation lines on the blade surface and vortex shedding at the blades trailing edge. Because of the necessity to discretize a large flow domain, that is needed to ensure consistent boundary conditions, with a resolution that is able to properly resolve the highly viscous flow within the boundary layer, the number of volume cells needed quickly grows very large[10]. Furthermore, suitable boundary conditions need to be specified, which itself often affect the simulation results. Finally, if simulating with RANS, turbulence models are significantly affecting the simulation results [68, 69, 70], especially within

7 Pressure and velocity
8 Unsteady RANS
9 Compared to DNS and LES
10 In the order of 10^7 cells for a RANS simulation

the viscous boundary layer, which introduces another level of uncertainty.

While a large number of researchers use CFD as their primary tool for wind turbine aerodynamic simulations, the computational cost associated with their evaluation is too large to apply these simulation methods in a design and certification setting, where millions of aerodynamics time steps have to be evaluated. The meshing process, that is required during the pre-processing of FVM simulations, is crucial for the accuracy of the simulation and can be very time consuming. During the post processing, handling very large amounts of data is necessary, which also adds to the time-cost of CFD simulations.

1.3.2. Methods to model wake aerodynamics

The helical wakes [71] shed from wind turbines are observed to be highly stable structures, which can still be traced up to 15 rotor diameters [72] behind the turbine from which they originate.

The most important effect of wind turbine wakes on the performance of the wind turbine is the velocity that is induced in the rotor plane. The wake causes a velocity deficit in the rotor plane via an induction of velocity fields, caused by the rotation of the helical vortices in a continuum. If the velocity deficit is not accurately estimated the predicted inflow at the rotor plane and the resulting performance prediction becomes erroneous.

The magnitude of the velocity that is induced by a vortex filament becomes smaller with growing distance and can be expressed by the Biot-Savart law:

$$V_{ind} = \frac{\Gamma}{2\pi r}, \tag{1.1}$$

where V_{ind} is the induced velocity, r the radial distance from the vortex core and Γ the circulation of the vortex. The tangential velocity of the blade tip divided by the velocity of the incoming wind, the tip speed ratio (TSR), is a factor that describes how densely the vortex rings are packed behind the turbine. Depending on this ratio, vorticity that was shed up to ten revolutions prior may still significantly contribute to the current total induced velocity inside the rotor plane. Thus, it is important to properly model the time history and evolution of the wake behind the turbine over a large spatial and temporal domain.

Most wind turbines are operating in clusters or wind parks [73, 74, 75, 76]. In these conditions the wake shed by upstream turbines might, fully or partially, impinge on downstream turbines and affect their performance and structural loading. The wake deficit behind a wind turbine is eventually recovered through viscous diffusion and the entrainment of high momentum fluid into the center of the wake. This recovery process depends on a multitude of influencing environmental factors such as temperature, humidity and turbulence levels [77, 78, 79]. Due to vertical wind veer, caused by the earth Coriolis forces, a dynamic meandering of wakes can be observed [80, 81, 82]. If wind turbines are operating in yaw, their wakes are deflected by the non-uniform loading of the blades during a rotation of the rotor. Furthermore, the stable structure of helical wakes contains unstable modes which can cause an accelerated wake breakdown and recovery process if the wake structure is excited at certain frequencies[11] [83, 84, 85, 86, 87].

11 See also Publication IV in Section 3.3

Overall, wake dynamics develop over time- and length scales that are orders of magnitude larger (see Table 1.1) than those that are necessary to resolve when modeling blade aerodynamics.

Momentum Balance Methods

In almost all engineering-level design and certification codes wake aerodynamics are approximated by balancing the extraction of energy from the flow by the rotor with the reduction of velocity within the rotor plane.

Depending on the type of turbine that is being modeled, a system of equations needs to be set up, considering the kinematics of the rotor blades and the general shape of the wake. For horizontal axis wind turbine wakes such a balance is performed for several annular rings, usually coinciding with the discretization that is chosen for the blade element method, resulting in the commonly used Blade Element Momentum Method (BEM) [36, 37]. If a vertical axis wind turbine wake is modeled the problem needs to be formulated differently, either by performing two successive momentum balances[12] when using the Double-Multiple-Streamtube Method (DMST) [88] or by performing the momentum balance over a cylindrical shape that follows the trajectory of the rotor blades (Actuator Cylinder Method, [89]).

The main assumption of the momentum balance is that the flow conditions are idealized and static. After the momentum balance is carried out the wake velocities and rotor performance are representative of the static equilibrium conditions. In reality transient inflow conditions or changed in rotor operation, such as blade pitch, change of rotational speed or relative blade or rotor disc movement, cause a lagged response due to the wake memory effect. The wake memory effect describes the influence of the wake induction onto the velocity field within the vicinity of the rotor. The total induction that the wake exerts on the rotor results from the summed up influence of the whole wake structure, which is a combination of all vortices that have been shed from the blades and have been convected downstream over time. In momentum balance based codes this lagged response is usually modeled by introducing semi empirical dynamic inflow models, such as the Oye or ECN models (see [90, 91] for an overview and validation of the models).

Another assumption is that the rotor blades are always assumed to be located inside the rotor plane over which the momentum balance is evaluated. This assumption is especially violated for large wind turbines where, due to the softer blade structure, large blade tip deflections are observed. Furthermore, wind turbine rotors are often designed with a cone angle to prevent blade-tower strike or have a tilted main shaft. The larger the violation of the rotor plane assumption, the larger the loss in accuracy.

Furthermore, the rotor plane is assumed to be oriented normal to the incoming flow, which is often violated. This assumption can be corrected through a skewed wake correction [92], that accounts for non-axisymmetric inflow. Other corrections to the momentum balance include the Glauert correction [93], to account for the heavy loading states (turbulent wake state) of the rotor. An assumption that is especially violated with respect to floating wind turbines is that the location rotor plane is assumed to be stationary. Floating offshore wind turbines might undergo

12 One for the upstream half of the blade rotation, one for the downstream half

large oscillations, due to wave loads. As a result of these oscillations the wake itself might interact with the rotor blades, which is not considered in momentum balance based methods.

It is also important to note that the momentum balance only results in three velocities[13] for the axial and the tangential directions. Thus, this method is not suitable to calculate velocity fields within the wake or the wake shape, its deflection and recovery. To evaluate first order wake shapes and velocity contours several engineering methods exist, such as the Jensen model or the Frandsen model (an overview is given in [94]). Such models are only used as a quick first estimate and some are also heavily reliant on empirical tuning factors.

Lagrangian Vortex Methods

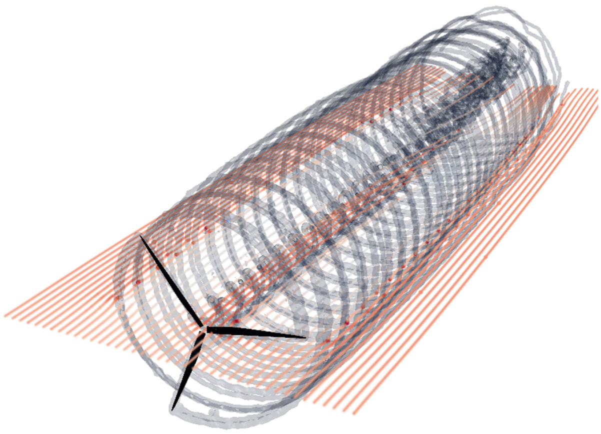

Figure 1.9.: Free vortex wake simulation of a HAWT wake using QBlade

Opposed to Eulerian CFD methods, the term vortex methods is associated with a Lagrangian approach to the discretization of the flow problem. Instead of discretizing the domain with a space fixed volumetric mesh, only the regions within the flow that are containing vorticity are discretized and potential flow is assumed within the whole domain. Furthermore, instead of solving for the pressure and velocity, the primary variable is the vorticity. The evolution of these regions of vorticity is solved for and its convection is tracked in a Lagrangian fashion. Many different element types can be used to mesh the regions of vorticity. Among them are vortex panels, vortex filaments and vortex particles[14].

Using the Biot-Savart Law the velocity distribution, induced by the vortex elements, can be evaluated. The Biot-Savart-Kernel (Equation 1.1) inherits a singularity at the core, where the induced velocity approaches infinity. To ensure numerical stability of the simulation that is carried out, the kernel needs to be desingularized. Different models, that describe the velocity distribution within the vicinity of the core exist, such as the Rankine, Lamb-Oseen or Ramasay and Leishman models [95], or simple cut-off radius implementations, as used by van Garrel [96]. After the evaluation of the velocity field a numerical scheme of choice is used to advance the simulation in time. Commonly used schemes are the simple first order Euler-forward integration, second order schemes, like the predictor-corrector scheme or higher order schemes such as the Runge-Kutta schemes.

The evolution of the vorticity field, convection, strain and diffusion, is handled depending on the element type. The strain of vortex panels and vortex filaments is satisfied through the convection of the panel's or filament's end points up to a first order approximation. If vortex particles are

13 One velocity in front, one within and one behind the rotor plane
14 Also referred to as vortex blobs

used to represent the vorticity field different schemes can be applied to satisfy the strain equation, such as the direct, transpose and mixed schemes [97]. Diffusion can be modeled through a vortex core growth model [38], or several other approaches, such as the random walk method or particle strength exchange[15].

In contrast to momentum balanced based methods, vortex methods explicitly resolve the wake shape and its evolution. Velocity, vorticity and pressure fields can be reconstructed from the distribution of vortex elements. Also, effects such as the wake memory or tip losses do not need to be empirically modeled but are resolved by the simulation. The great advantage of Lagrangian vortex methods, when compared to Eulerian CFD, is the fact that the number of mesh elements that is required to sufficiently discretize a domain, containing a coherent vortex structure[16], is significantly smaller than the number of volumetric cells that an Eulerian FVM requires to model the same problem. This leads to computational times that are orders of magnitude lower than those of similar FVM CFD simulations (more than 6 orders of magnitude in [99])[17]. Furthermore, artificial numerical diffusion, a problem in Eulerian CFD, is avoided through the Lagrangian tracking of the vorticity.

The major downside of vortex methods is that the computational cost scales with $O(N^2)$, where N is the number of vortex elements within the domain. The $O(N^2)$ cost results from the convection step, where at the position of each single vortex element the influence of all other vortex elements needs to be evaluated[18]. This usually limits the number of vortex elements that a simulation can handle in a reasonable time frame[19]. This problem can be somewhat mitigated by employing massive parallelization for the evaluation of the N^2 Biot-Savart equations. Moreover, a tree-code [100, 101] or multi-level [46, 102][20] approach can be used to reduce the computational cost for large problems, through the implementation of a hierarchic mesh. Tree-codes or multi-level codes, depending on their implementation, can reduce the computational cost from $O(N^2)$ to $O(Nlog(N))$ or even $O(N)$. However, this comes with the disadvantage of additional computational overhead to setup and evaluate the hierarchic mesh structure and only pays off for comparatively large problems. Another issue relates to the divergence of the flow field. Even if the flow field, after the initial setup, approximates the divergence-free condition during the first simulation steps, the stretching term causes the flow field to eventually loose this characteristic [103]. To prevent divergence re-meshing of vortex particles, on a regular grid, can be applied.

15 A good explanation of these methods is found in [98]
16 Such as a wind turbine wake
17 Publication II (Section 3.1)
18 Regardless of their relative distance
19 For simulations that solve in real time in the range of 10^5 elements
20 One of the associated publications

Eulerian Finite-Volume CFD Methods

Nowadays, it has become quite common to apply Eulerian CFD for wind turbine wake investigations [104, 72, 105, 106] by using mostly RANS and LES or combinations such as the DES[21]. Since the flow physics are accounted for by solving the Navier-Stokes-equations, great care has to be taken with respect to the simulation setup, domain discretization and the selection of boundary conditions in order to obtain accurate results.

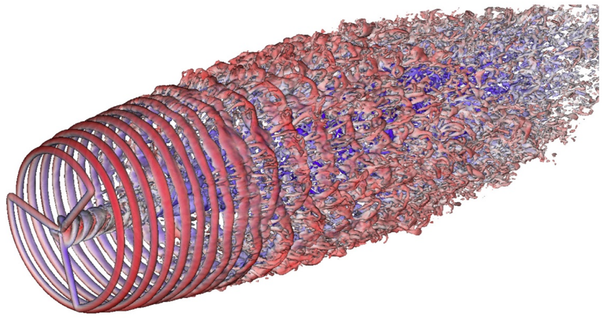

Figure 1.10.: LES simulation of a wind turbine wake, reproduced from [104]

RANS simulations [107, 108, 61] yield the lowest computational cost for large Reynolds number flows. However, especially in the shear layer of the wake, or for highly three-dimensional flows the usage of turbulence closure models, that do not consider the anisotropy of the turbulence, can lead to inaccuracies [72].

An increasing number of researchers lean towards LES simulations for wake aerodynamics [109, 110, 111, 112]. This is mainly due to the fact that the anisotropic turbulence and the resulting turbulent mixing of the turbulent scales that are resolved by the mesh, are solved with a much higher accuracy than in RANS simulations. At smaller scales, when the sub-grid turbulence is modeled, similar problems than with RANS arise.

Another challenge associated with CFD is the introduction of realistic inflow conditions into the domain. While for RANS simulations velocity profiles can be prescribed, LES simulations often need precursor simulations to generate the inflow conditions. If the ground is included in the simulations a direct geometrical implementation of the surface roughness into the mesh would require prohibitively fine grids which is commonly avoided by using wall functions which prescribe the friction at the surface [72].

The wake simulations need to include a rotor model of some sort, from which the wake originates. This can be realized with a direct modeling approach by explicitly including the blade surfaces into the computational domain. In this case DES is often used [113, 114, 115] to reduce the computational cost. The cost can be further reduced by integrating the presence of the rotor via the actuator disc [116], actuator line [117], or actuator surface [118] methods. When using an actuator method the rotor performance is usually obtained via a lower-order method, such as the blade element method, and is then introduced into the CFD simulation through a distribution of body forces on the respective surface or line.

Since the vorticity in CFD simulations is obtained through the evaluation of velocity field gradients on the mesh, numerical dissipation is a problem that is often encountered in CFD simulations. The level of numerical dissipation is a function of mesh resolution and time step size. Furthermore, the exact quantification of the uncertainty, which is introduced by the choice of turbulence model and discretization scheme is still under investigation [119, 120, 121].

21 Using RANS near walls and LES elsewhere

While yielding very detailed and complete results from the wake simulation, the large amount of data generated, the uncertainty, and also the computational cost[22] render the use of CFD for design and certification purposes impractical using today's computational hardware. The interpretation of the results is highly complex and a large part of the information that is generated by the simulations is unessential for the assessment of the lifetime of a wind turbine. Nowadays, high fidelity CFD is most commonly used to validate or tune lower order wake models and to gain basic understanding and insight into the processes that lead to the evolution and recovery of wind turbine wakes. On the other hand simplified CFD tools are commonly used to assess the complete flow through a wind farm while sacrificing most of the details from the rotor aerodynamics through the application of actuator methods.

Generalized Dynamic Wake

The Generalized Dynamic Wake (GDW) method, developed by Peters and He [122, 123, 124], can be derived from Laplace's equation, valid for potential flow. The induced velocities within the rotor plane are calculated with an infinite series of Legendre and Euler equations for the axial and tangential flow directions within the rotor plane. By using series of equations the wake memory effect is explicitly modeled within this method. Furthermore, non-axisymmetric inflow is taken into account. However, the GDW method is only valid for lightly loaded rotors [125] and is usually replaced by the momentum balance, which includes the Glauert correction for the turbulent wake state, when the rotor is heavily loaded[23].

Vortex Particle Mesh Methods

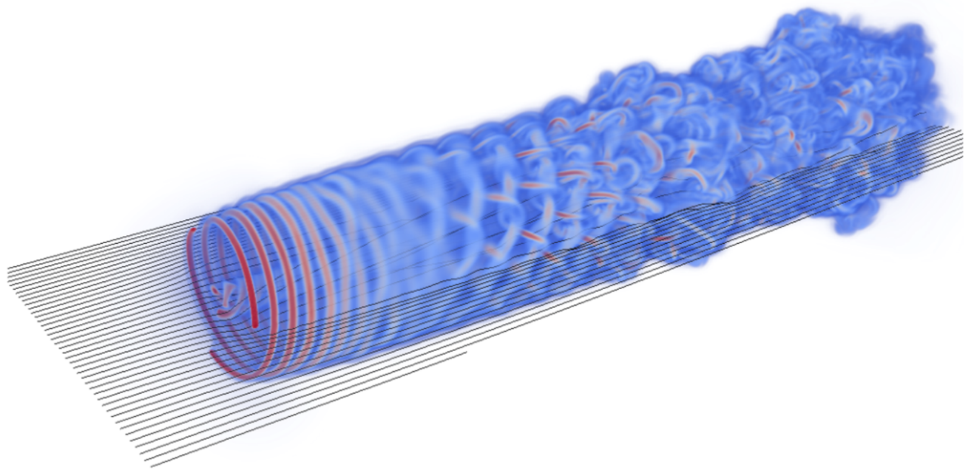

Figure 1.11.: VPM Simulation HAWT, reproduced from [126]

A vortex particle-mesh method is a crossover between Lagrangian vortex- and Eulerian finite volume methods. Generally, such a treatment can combine the advantages of both approaches

22 In the order of days and weeks on high performance computer clusters
23 Heavy loading often occurs when operating at low winds peeds

[127, 128, 126]. The Lagrangian description of the vorticity eliminates the artificial numerical diffusion that CFD methods are facing. The volumetric mesh allows to explicitly evaluate the evolution of the vorticity, while avoiding the divergence of the flow field, which is introducing errors when using purely Lagrangian methods. Using a VPM approach, the convection of the vorticity is handled in a Lagrangian fashion where the vortices are treated as particles. The influence of the vortices on the velocity field is then interpolated back onto a regular grid. Divergence or distortion of the particles is prevented through a periodic re-meshing of the particles onto the underlying grid.

Lattice Boltzmann Methods

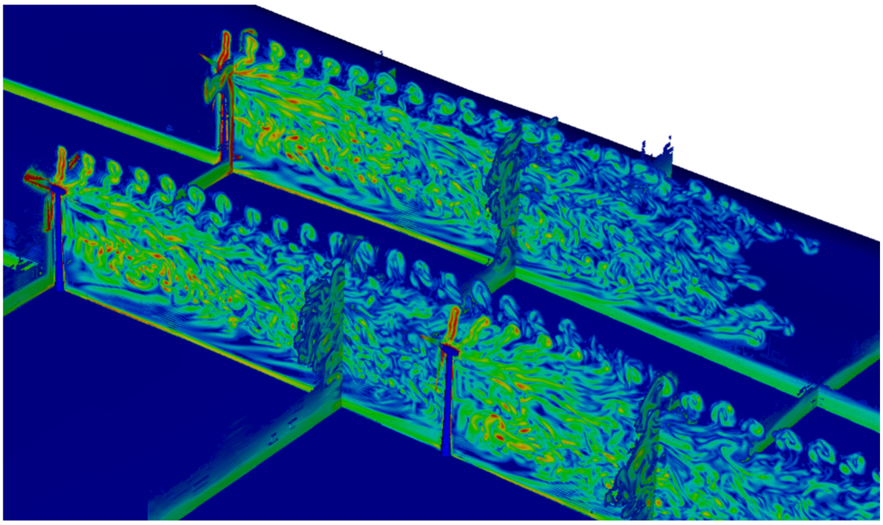

Figure 1.12.: LBM wind turbine wake simulation, reproduced from [129]

The Lattice Boltzmann method (LBM) is a unique approach to simulate the dynamics of a flow[130, 129, 131]. For the LBM the flow domain is discretized with an equidistant mesh. Instead of solving the NS-equations on the mesh, the discrete Boltzmann equation, describing the interaction of fluid particles, is solved. Based on the mesh type, and the possible directions along which a particle can travel from cell to cell, dimensional quantities are converted into mesh units. Properties of the flow are then represented by particles that are traversing the mesh based on a set of streaming and collision rules. LBM methods are relatively new and one of the biggest advantages is their inherent potential for parallelization. Compared with similarly sized finite volume methods, the savings in computational cost are up to two orders of magnitude [132]. While offering promising advantages in computational cost, compared to classical CFD methods, and a high level of fidelity, LBM methods are still subject of research and have not yet reached the maturity to be widely adopted by the wind turbine industry.

1.4. Structural Modeling of Wind Turbines

Similar to the different fidelity of aerodynamic models, there is a large variation of approaches when selecting a suitable structural model for time-domain load simulations of wind turbines. The following overview only considers finite element analysis (FEA) time-domain methods for the calculation of structural loads. While frequency-domain methods are quite common for aeroelastic stability investigations, time domain analysis is the preferred method for wind turbine load evaluations, since system non-linearities, which are not accounted for in linearized models, can be resolved. Furthermore, due to today's computational resources that enable the efficient usage of FEA methods, analytical closed form solutions are not commonly used anymore, due to the difficult process of their derivation for complex systems.

Generally, a structural dynamics simulation method for wind turbines should be capable of resolving the complete wind turbine system loads caused by aerodynamic, gravitational, and inertial forces. The ability to model aeroelastic stability, resulting from the coupling between the aerodynamic and structural dynamics simulation methods (see Figure 1.4), is of high importance and requires an accurate prediction of body deformation and translation. Furthermore, the wind turbine control system has to be integrated with the structural model, thus the formulation of the structural model must be capable of integrating a range of actuators and links, to represent the blade pitch motors the yaw motor and the generator.

The two main variables that result from the coupled aeroelastic load simulations are a time history of the wind turbine's loads (forces and torques) and its positions (translation, rotation, deflection). After a time domain load analysis has been completed the resulting ultimate and fatigue loads are converted into stresses, using higher order structural models that fully discretize the internal structure of the critical components in detail [133].

A Campbell diagram [134] allows one to assess the interaction of the system eigenmodes and frequencies with the main excitation frequencies, expressed as multiples of the rotors rotational frequencies. Taking into account the rotational augmentation of the eigenfrequencies, caused by centrifugal stiffening and gyroscopic effects, is a key requirement for this task. eigenfrequencies and modes can be obtained from the linearized mass, stiffness and damping matrices of an assembled wind turbine system. The influence of centrifugal stiffening and gyroscopic effects can either be accounted by inclusion into the formulation of the structural elements, which are used to discretize the wind turbine components, or by external evaluation and application.

1.4.1. Multi-Body Formulation

Generally, wind turbine structural load analysis models are assembled using a multi-body formulation [135, 136] (see also Table 2.1). Individual components, such as blades, tower, or the nacelle can be represented by suitable structural elements, or be treated as rigid. The components are then assembled using force elements, such as springs or dampers, kinematic links, or a combination of both. The links constrain certain degrees of freedom between the individual components of the multi-body system, while leaving other degrees of freedom unconstrained. As an example; the nacelle is constrained to the tower top by fixing all rotational and translational degrees of freedom except for the rotational degree of freedom along the wind turbine's yaw axis. The tower bottom is constrained to a spring and a damper that are fixed at the ground and representative of the soil stiffness and damping properties [137]. A multi-body formulation allows a large flexibility, when setting up the wind turbines structural model. Components where large deformations are expected, such as the rotor blades, can be modeled with great detail by using a fine discretization, while other bodies, such as the nacelle, can be modeled as rigid to reduce the degrees of freedom of the system and, thereby, the resulting computational cost.

1.4.2. Reduced Order Beam Models

The complexity of a one-dimensional beam model can be significantly decreased by reducing the order, or the number of degrees of freedom (DoF) of the system. Each node, describing an end point of a structural element, has six DoF, three rotational and three translational. Reducing the DoF of the system, by allowing the structure only to deform into linear combinations of pre-calculated mode shapes, reduces the size of the matrix that needs to be solved [138, 139, 140]. Such pre-calculated mode shapes are typically evaluated individually for the main components of the wind turbine. As an example, a rotor blade can be represented by a linear combination of the first and second flapwise, the first edgewise, and the first torsional modes, which are pre-calculated for an isolated clamped blade. While such a treatment reduces the system complexity and computational cost significantly, the main drawback is that nonlinearities are not considered which result from the interaction of the different main components of the turbine system during operation. Furthermore, all modes shapes that are not explicitly included within the reduced order formulation are simply neglected. Moreover, to setup a reduced order model a priori knowledge of the mode shapes and frequencies is needed which have to be obtained by using a different method.

1.4.3. One Dimensional Beam Models

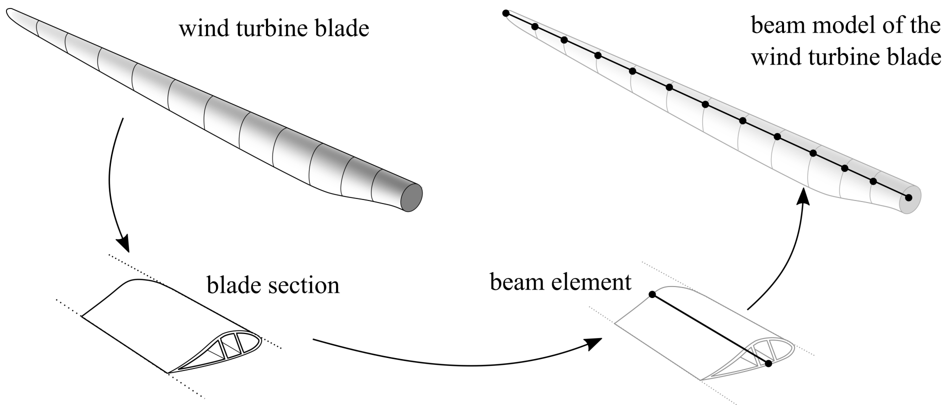

Figure 1.13.: Beam model of a wind turbine blade, reproduced after [141]

The main components of a wind turbine, the blades and the tower, are slender structures. Slender structures can efficiently be approximated using beam elements [142]. The discretization of the structure is carried out by distributing a number of elements along the principal axis of the structure (see Figure 1.13). Compared to a fully three-dimensional discretization the number of degrees of freedom, resulting from a discretization using beams, is significantly reduced. The most commonly used beam elements in wind turbine structural analysis are the Euler-Bernoulli [143] and the Timoshenko beams [144]. Euler-Bernoulli beams account for longitudinal, torsional and bending deflections and loads, while neglecting shear. Timoshenko beams extend these capabilities by also taking into account shear loads and deformations (see [145, 146] for a comparison between the Euler-Benoulli and the Timoshenko beam formulation).

If large levels of rotation and deformation, and the resulting geometrical nonlinearities, shall be taken into account the system formulation has to be laid out accordingly. Suitable formulations are: the co-rotational formulation [147]; the Total Lagrangian Formulation including nonlinear-strain [148], the Floating Frame of Reference Formulation [149], and Flexible Multi Body Formulations [150].

1.4.4. Three Dimensional FEA

Three dimensional FEA can be used to obtain a complete picture of the load and stress distribution (see Figure 1.14) of a wind turbine. Shell elements can be used to discretize the internal structure of a blade, usually consisting of various composite layers. The detailed resolution of the internal component structure allows one to evaluate internal stresses, opposed to one dimensional beam models, where only the loads are evaluated. The meshing of the turbine structure is a time consuming process and the large number of elements that is required to represent a complete three dimensional turbine structure leads to expensive computations. Due to the high computational demand three dimensional FEA cannot be used during the time domain design load simulations. However, three dimensional FEA still plays an important role within the certification process. Commonly, three dimensional FEA is used to generate the cross sectional properties [152, 153] of a component (blades, tower), which are needed to define the properties of the beam elements. In the post-processing of design load calculations, which were performed based on a lower-order method, three dimensional FEA is used to calculate the internal stresses, using the ultimate- and the equivalent fatigue loads that have been extracted from the time series [133].

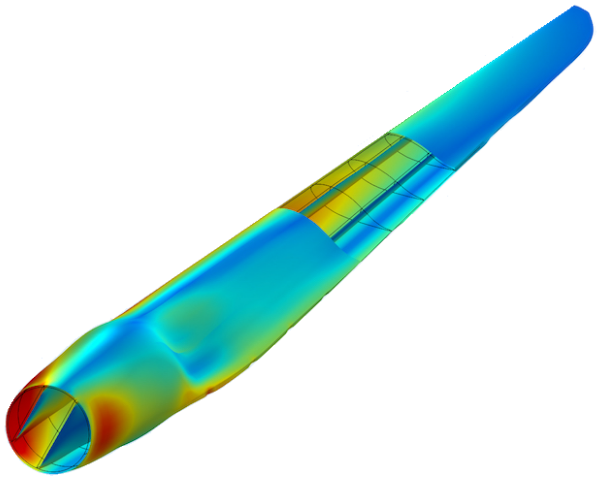

Figure 1.14.: Von Mises stress distribution in a wind turbine blade, reproduced after [151]

1.5. Coupling Methods

An important aspect of any co-simulation (in this case the aeroelastic simulation) is the means by which the different simulation methods are coupled and how the information is exchanged during the different models of the co-simulation. This is a critical aspect as the numerical stability, the efficiency and also the accuracy of the co-simulation [154] is affected by the coupling scheme. Generally, two coupling schemes exist: the loose coupling and the tight coupling [155].

1.5.1. Tight Coupling

Within a tight coupling scheme, the time integration is carried out over the complete system [156] (see Figure 1.15), involving all the different simulation models. Effectively this means that the sub-simulations exchange their information during the setup of the system of equations or the iteration procedure. This requires all sub-simulations to advance at an equal time step. While the tight coupling has advantages concerning the accuracy, and especially the stability of the simulation when increasing the global time step size, a tight coupling requires a highly integrated coupling of the sub-simulations. Besides making the data available between the sub-simulations either their iteration steps need to be directly coupled or a global solution step needs to be carried out for which the system has to be setup by collecting all information of each sub-simulation. The necessity for such an integrated coupling poses a severe constraint for the modularization of a simulation framework where individual sub-simulations (aerodynamic, hydrodynamic, structural, control) can be enabled or disabled based on the required features.

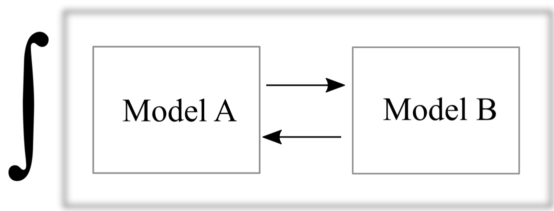

Figure 1.15.: The tight coupling scheme (combined integration), reproduced after [154]

1.5.2. Loose Coupling

In contrast, when using a *loose* coupling scheme all sub-simulations are integrated independently (see Figure 1.16). Three different loose coupling integration processes exist. The direct integration process exchanges the information between the sub-simulations once and then integrates them independently until the next global time step is reached. In the alternated integration process one sub-simulation is integrated once and the simulation results serve as the starting condition for the integration of the other sub-simulations. The iterated integration process starts similar to the direct integration process with an additional iteration step that ensures that an extrapolation based on the starting conditions matches the result of the integration of all sub-simulations. See [154] for illustrations and an overview of the different loose coupling schemes. A loose coupling scheme enables a much more straightforward modularization. Besides the data that needs to be exchanged between the different sub-simulations no other details need to be communicated [157]. Each sub-simulation is solved individually and information between sub-simulations is exchanged at global, or macro, time steps. This also allows each sub-simulation to advance with an individual time step, which can be beneficial to increase the computational efficiency of the simulation.

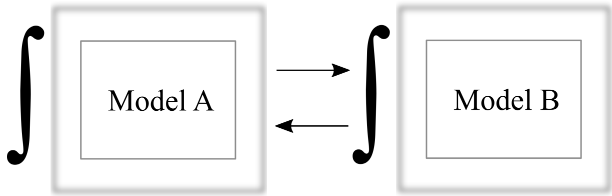

Figure 1.16.: The loose coupling scheme (independent integration), reproduced after [154]

Chapter 2 | Implementation

2.1. Selection of Methods for QBlade's Simulation Framework

From the overview, given in the previous chapter, suitable simulation methods for blade aerodynamics, wake aerodynamics and structural dynamics are selected. The main requirements for the presented choice of methods are:

- **Computational efficiency**: The simulation tool shall be applicable in the context of design and certification where a large number of simulations needs to be evaluated
- **Accuracy**: The simulation tool shall provide an improvement in simulation accuracy over the established and commonly used tools
- **Robustness and usability**: The simulation tool shall be able to generate reproducible and consistent results for all relevant turbine geometries and operating conditions; the sensitivity of the results towards simulation setup parameters shall be minimal

2.1.1. Blade Aerodynamics

The blade element method (Section 1.3.1), despite its age and simplicity, is chosen for modeling the rotor blade aerodynamics. The large advantage, compared to three-dimensional panel methods is its capability to include the friction drag into the blade performance estimation. Although three-dimensional panel methods were also considered due to their manageable computational costs, these models can only take the induced drag into account, neglecting friction drag. Coupling a three-dimensional boundary layer model with a panel method can potentially remedy this limitation, but such a coupling is still the topic of current research as outlined in (Section 1.3.1) and would not have been feasible as part of the development of this simulation framework. Another advantage of the blade element method is the ability to use two dimensional airfoil data, which allows to easily include lift and drag polars from wind tunnel experiments or from two dimensional CFD simulations into the blade model. Moreover, the blade element method has proven its accuracy over many years of application within the context of design and certification, its computational cost is small and it is highly robust. Ideally, CFD would be the method of choice for blade aerodynamics, as it removes the dependency on dynamic stall models and airfoil polar data altogether, however the high computational cost and the intricate pre- and post-processing that it requires prohibits its application within a certification framework.

2.1.2. Wake Aerodynamics

The wake in the presented simulation framework will be modeled using a Lagrangian vortex method. This is a large improvement over commonly used momentum balance based methods, which necessitate the introduction of a large number of empirical corrections into the simulated system. Modeling the wake dynamics explicitly with vortex methods avoids the dependency on such correction models and ensures more physically sound results. Compared to momentum balance based methods, results are improved especially in cases that deviate from the momentum balances assumptions, such as unsteady operation, large blade deformations and high tip speed ratios where the turbulent wake state is approached. Such conditions become more and more prevalent with the ongoing trend towards larger rotor sizes [14, 158] and offshore floating wind turbines. Several researchers already pointed out the the improvements in simulation accuracy, when upgrading from BEM to free vortex models [159, 160, 161]. Furthermore, vortex methods are much more general in their application compared to momentum balance based methods. Vortex methods can be used to model wakes of HAWT and VAWT alike and also work well for pre-bend or helical rotor blade shapes. In addition, vortex methods can be used to assess the wake shape itself and its influence on downstream wind turbines within multi-turbine simulations[24]. Due to the evolution in computational resources that are available to wind turbine designers, the increase in computational cost compared to blade element methods is manageable for certification applications, when parallelization techniques and wake reduction techniques are applied. Ideally LES CFD simulations would be the optimal choice for a wake model, as they allow to gain the most insight into the wake and its evolution and interaction with downstream rotors. However, computational cost disallows for the usage of such methods in the context of design and certification.

2.1.3. Structural Dynamics

The structural model in the QBlade simulation framework should be able to deal with large deflections and geometrical nonlinearities. Thus, a modal reduction technique will not be applied. Furthermore, the structural wind turbine definition within QBlade should also be capable to evaluate the eigen frequencies of the system. The choice was made to use a co-rotational multi-body formulation, employing Euler Bernoulli beam elements to represent the wind turbines elastic components. The co-rotational formulation allows for large solid body rotations and nonlinear displacements. Turbine components are be assembled using constraints and actuators. Extracting linearized mass- and stiffness matrices from time domain simulations allows the calculation of eigen frequencies and mode shapes, influenced by geometrical nonlinearities. Such a formulation is at present slightly above the industry standard, where modal reduction techniques are still employed. Three-dimensional FEA, while preferred from the perspective of accuracy and its ability to evaluate stresses, is not taken into account due to its inherently large computational cost and complexity to setup.

2.1.4. Coupling

The aerodynamic and structural models will be coupled with a loose coupling approach. This approach allows for the independent development of all involved sub-models and the simplifies their coupling. Furthermore, the loose coupling allows for the layout of a modular software, where individual models can easily be replaced, extended or exchanged with other models.

24 See Section 3.4

2.2. Overview of Currently Available Aero-Elastic Wind Turbine Simulation Codes

Table 2.1 gives an overview of the currently available aeroelastic simulation codes for wind turbines. A number of codes have been developed by the industry and public research institutions. Most of these codes were specifically designed for HAWT with some exceptions. In the following, a short description of each of these codes is given.

Bladed

Bladed [162] is a commercial HAWT design code, developed and maintained by DNV-GL, which is commonly used within the industry. Bladed comes with a graphical user interface (GUI) and provides functionality for pre- and post-processing of IEC 61400 design load calculations. Furthermore, functionality for supervisory controller integration and generator models is included. Bladed's aerodynamic formulation is based on BEM, the structural dynamics formulation is based on a multi body formulation with multiple beam elements employing the modal reduction technique. For offshore application Bladed also includes a hydrodynamics module. Bladed is distributed as a commercial proprietary software with yearly license fees.

CP-Lambda

The code CP-Lambda [163], originally developed at the POLI-Wind institute of the Polytechnic University of Milano, is an aero-servo-elastic simulation tool for HAWT. Its aerodynamic model is based on BEM; the structural model is based on a multi-body formulation employing fully populated 6x6 beam elements employing the geometrically exact beam formulation (GEBT) to account for nonlinearities. The code is IEC 61400 compliant for DLC assessments. CP-Lambda is an in-house research code, a license can be obtained from the POLI-Wind Institute.

HAWC2

The aeroelastic code HAWC2 [164] is developed at the DTU Wind Energy Department. For HAWT it uses a BEM aerodynamic model, which is slightly adapted to better account for local variations of induced velocities. For VAWT an Actuator Cylinder model is employed (AC), which is still in the process of being further developed. HAWC2's structural model is based on a multi body formulation employing the *floating frame of reference* approach to include nonlinearities and uses Timoshenko beam elements. Additional modules allow the integration of supervisory controllers and hydrodynamic models for offshore applications. HAWC2 is distributed via commercial and research licensing schemes. Its source code is proprietary.

Phatas / FOCUS6

Phatas has been developed at the Wind Turbine Material Center (WMC), part of LM Wind Power since 2018. The GUI based aeroelastic simulation tool Phatas is part of the FOCUS6 design suite [165]. The aerodynamic formulation in Phatas is based on either BEM or a free vortex wake method. Its structural model is a multi-body formulation using the Craig-Bampton beam model, a modal reduction technique. Several optional modules are available within FOCUS6, such as modules to estimate noise emissions, calculate eigenfrequencies or model hydrodynamics of floating wind turbines. FOCUS6 is distributed by the WMC via various resellers under a commercial license. The source code of Phatas is proprietary.

FAST / FAST-ADAMS

FAST [166] is an open source aero-servo-hydro-elastic simulation code for HAWT, developed, maintained and distributed by the National Renewable Energy Laboratory (NREL). Its aerodynamic module, called AeroDyn, is BEM based. The structural model is a multi-body formulation employing either beams with a modal reduction method, using the ElastoDyn module, or based on geometrically exact beam theory (GEBT), using the BeamDyn module. Furthermore, an optional coupling of FAST to the commercial multi-body software ADAMS (MSC Software) exists. Furthermore, FAST is capable of integrating supervisory controllers and evaluating the hydrodynamics of floating platforms. FAST is distributed under the open-source Apache license.

ADCoS

ADCoS [167] is a GUI based aeroelastic wind turbine simulation tool developed by Aero Dynamik Consult (ADC), which is in development since 1995. ADCoS models HAWT using the BEM method and VAWT using the Double Multiple Streamtube Theory (DMST). Structural dynamics are evaluated using a FEM formulation that is employing either Bernoulli or Timoshenko Beams. Through a collaboration with Frauenhofer IWES the version ADCoS-Offshore can consider the effect of complex wave loads on fixed offshore foundations. Additionally, supervisory controllers can be integrated into the simulations. ADCoS is distributed a proprietary software under a commercial licensing scheme by ADC.

FLEX5

The software FLEX5 [168] was developed at the Fluids Mechanics Section of DTU. FLEX5's aerodynamics are BEM based and its structural model is a reduced order multi-body formulation. Furthermore, FLEX 5 can incorporate generator and/or pitch control models into the simulations. Several adaptations and modifications of the original FLEX5 exist today. A license for the software and the source-code can be obtained from DTU.

GAST / GENUVP

GAST [169] is an aeroelastic simulation code for HAWT, developed at the NTUA. The aerodynamic formulation in GAST is BEM based, but can be replaced with the free vortex particle formulation within GENUVP, a free vortex particle flow solver, also developed at NTUA. The structural dynamics in GAST are evaluated with a multi-body FE formulation in a floating frame of reference that employs Timoshenko beams as elements. GAST and GENUVP are in-house research code.

OneWind Modelica / MoWiT

The OneWind Modelica Library [170], now renamed MoWiT, is an aeroelastic simulation tool for HAWT, developed at Frauenhofer IWES. MoWiT is a library for the open source modeling language Modelica [171]. The aerodynamic method in MoWiT is BEM based, the structural

Table 2.1.: Overview of the most common aeroelastic WT simulation codes

Code	Aero Model	Structural Model	VAWT	GUI	Open Source	Distribution	Publisher	Since
Bladed	BEM	MB Multi Blade Part with Modal Reduction	no	yes	no	commercial	DNV GL	1993
CP Lambda	BEM	MB Geometrically Exact Beam Formulation	no	no	no	commercial	POLIMI, TUM	2006
HAWC2	BEM, AC	MB Floating Frame of Reference withTimoshenko Beams	yes	partial	no	commercial or academic license	DTU	1986
Phatas, Focus6	BEM, Free Wake	MB Craig-Bampton Beam model	no	partial	no	commercial	WMC, ECN	1990
Fast, Adams	BEM, GDW	MB Modal Reduction, Geometrically Exact Beam Formulation, ADAMS	no	no	yes	free online	NREL	1996
ADCoS	BEM, DMST	FE Bernoulli or Timoshenko Beams	yes	partial	no	commercial	ADC	1995
Flex5	BEM	MB Modal Reduction	no	no	yes	inhouse, on request	DTU	1996
GAST, GENUVP	BEM, Free Wake	MB Floating Frame of Reference with Timoshenko Beams	yes	no	no	inhouse, on request	NTUA	1997
OneWind Modelica	BEM, GDW	MB Bernoulli or Timoshenko Beams with Modal Reduction	no	partial	yes	commercial or academic license	IWES	2009
Ashes	BEM	MB Corotational Formulation with Benoulli Beams	no	yes	no	commercial	SIMIS AS	2012
QBlade	BEM, Free Wake	MB Corotational Formulation with Benoulli Beams	yes	yes	yes	free	TUB	2009

model consists of a multi-body formulation employing Euler or Timoshenko beam elements with modal reduction. Additionally, MoWiT is capable of calculating the hydrodynamics of floating platforms, supervisory controllers can be integrated with time-domain simulations. On request MoWit is available free of charge for research institutions.

Ashes

Ashes [172] is a GUI based aeroelastic HAWT design code, developed by Simis, a spin-off company of the Norwegian University of Science and Technology (NTNU). Ashes aerodynamic model is BEM based, its structural model setup in a co-rotational multi-body formulation employing Bernoulli beam elements. Additionally, Ashes can calculate hydrodynamic loads on fixed or floating offshore structures and comes with integrated PID controllers for generator and pitch control. Furthermore, supervisory controller libraries can be integrated with the simulations. Ashes is distributed under a commercial license; its source code is proprietary.

QBlade

The QBlade software [173, 174][25], presented in this work, is an open-source GUI based design and simulation tool for HAWT and VAWT, developed at the TU Berlin. The rotor aerodynamic calculations in QBlade are based on BEM, DMST and free wake vortex methods and a co-rotational multi-body formulation with Bernoulli beam elements is used to calculate the structural dynamics. Turbine supervisory controllers can be integrated into simulations via several library interfaces. Hydrodynamic modules for floating and fixed offshore platform are currently under development. The public version of QBlade is distributed under an open-source GPL license.

25 Associated publications

2.3. Distribution and Licensing of QBlade

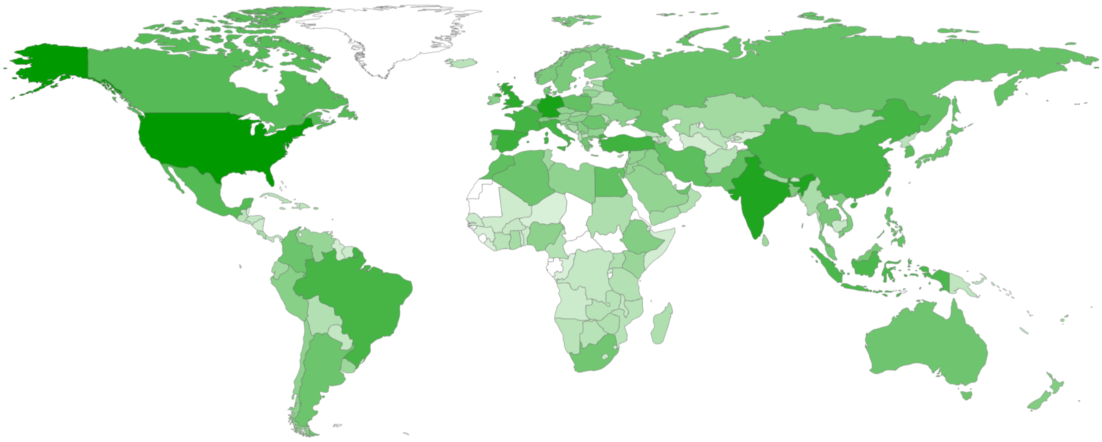

Figure 2.1.: Heatmap of QBlade downloads

Table 2.2.: Total QBlade downloads, showing the top 15 countries, data from sourceforge, taken on 01.10.20

Country		Downloads
1	United States	14385
2	Germany	8836
3	India	7495
4	United Kingdom	6352
5	Spain	4013
6	Turkey	3630
7	France	3365
8	China	3229
9	Italy	3177
10	Brazil	3138
11	Indonesia	2767
12	Mexico	2252
13	Canada	1887
14	Korea	1577
15	Morocco	1549

The QBlade software is distributed under the open source GNU GPL v2 license [175]. At the time of writing QBlade is hosted and distributed on source forge. The source code and pre-compiled binaries can be found at the following web address:

http://sourceforge.com/projects/qblade.

Comparing the available engineering level design and simulation codes for wind turbines, NREL's FAST code is the only other aeroelastic simulation code for wind turbines that is distributed freely under an open source license.

The software QBlade employs a highly optimized free wake vortex method as the aerodynamic model. Free wake methods are known to produce more physically sound predictions and increase the accuracy of the aerodynamic simulation, especially in transient or extreme operating conditions [159, 160, 161]. As the size of wind turbines is constantly increased and a number of large floating offshore wind parks is currently being planned, it is suggested for the industry to switch from BEM to vortex methods for aeroelastic design load calculations of wind turbines. However, so far only the in-house code GAST/GENUVP and the commercial code PHATAS/FOCUS6 offer this feature.

The structural formulation within QBlade's aeroelastic model is current state-of-the-art for wind turbine certification codes. Nonlinearities and large deflections are accurately taken into account due to the co-rotational formulation. Most of the listed codes have adopted a structural simulation method that accounts for nonlinearities, however modal reduction techniques are still widely spread due to their low computational cost.

Most comparable codes are either exclusively used in-house or distributed under commercial licenses. Furthermore, only few codes come with a user friendly GUI. In addition to its time-domain simulation capabilities, QBlade also integrates the XFOIL [47] simulation code and various GUI supported methods for polar extrapolation, blade design and the estimation of performance characteristics.

Such a combination is especially attractive for entry level educational purposes. Hence, QBlade is widely used in wind energy classes at many universities, such as the TU Berlin, HTW Berlin, HS Flensburg, DMU Leicester, Texas Tech University Lubbock, DTU and others. At the time of writing the QBlade code has been downloaded more than 100.000 times, increasing by approximately 1500 downloads per month [26]. Figure 2.1 shows the origin of downloads on Sourceforge, where a darker green indicates a larger number. As can be seen, QBlade is being used worldwide with a large number of users in Europe, USA, Brazil and India (see Table 2.2). One advantage of such widespread usage is the constant independent validation that the code undergoes as well as the discovery of software bugs and issues by the community.

26 Taken from the official repository on Sourceforge, QBlade can also be obtained from many other sources such as Softpedia, Linux repositories, etc...

2.4. Aerodynamic Model Implementation in QBlade

This Section gives a brief overview about the Lifting Line Free Vortex Wake method (LLFVW) implementation in QBlade. Furthermore, additionally implemented models that account for dynamic stall, tower influence, blade crossflow effects and ground effects are detailed. The last parts (2.4.10) of this Section deal with optimizations of the free wake formulation to achieve a high computational efficiency.

2.4.1. Lifting Line Free Vortex Wake Algorithm

The LLFVW algorithm implemented in QBlade generally follows the work carried out by van Garrel [96] during the development of ECN's AWSM code. In QBlade this algorithm is implemented in the object oriented C++ language using the cross platform framework Qt [176].

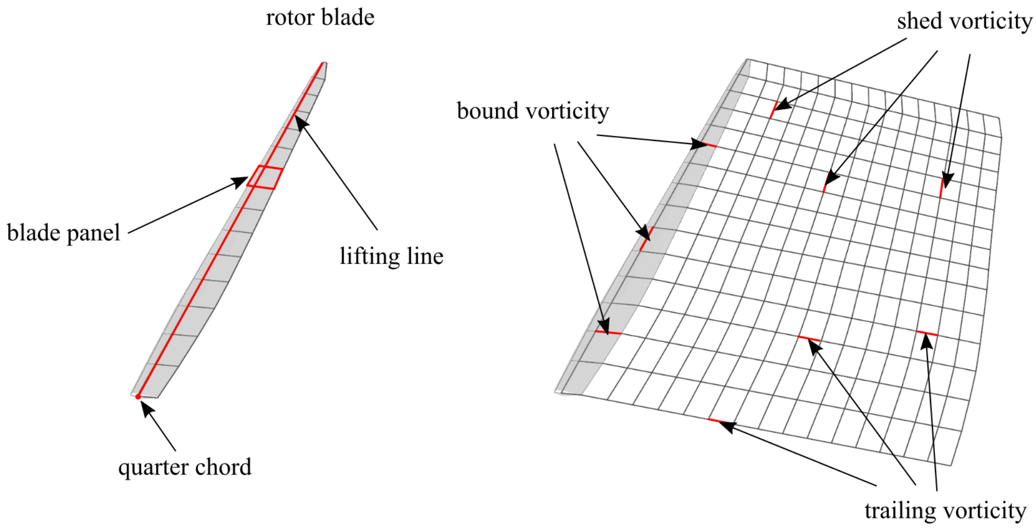

Figure 2.2.: Basic elements of the blade and wake model inside the LLFVW algorithm

The rotor is represented by a lifting line, located at the quarter chord points on the mid chord of the 2D airfoil sections (see Figure 2.2). Each blade panel is represented by a ring vortex that consists of four straight vortex filaments. The circulation of the bound vortex lines, forming the lifting line, is calculated from the relative inflow velocity and the lift and drag coefficients that are obtained from tabulated airfoil data. The circulation is calculated according to the Kutta-Joukowski theorem:

$$\partial C_L(\alpha) = \rho V_{rel} \times \partial \Gamma. \tag{2.1}$$

The relative velocity V_{rel} is obtained from a simple vector addition of the free stream velocity V_∞, the blade motion V_{mot} and the induced velocity V_{ind}, which is calculated from the contribution of all vortex elements inside the domain through the Biot-Savart equation:

$$V_{ind} = -\frac{1}{4\pi} \int \Gamma \frac{\vec{r} \times d\vec{l}}{r^3}. \tag{2.2}$$

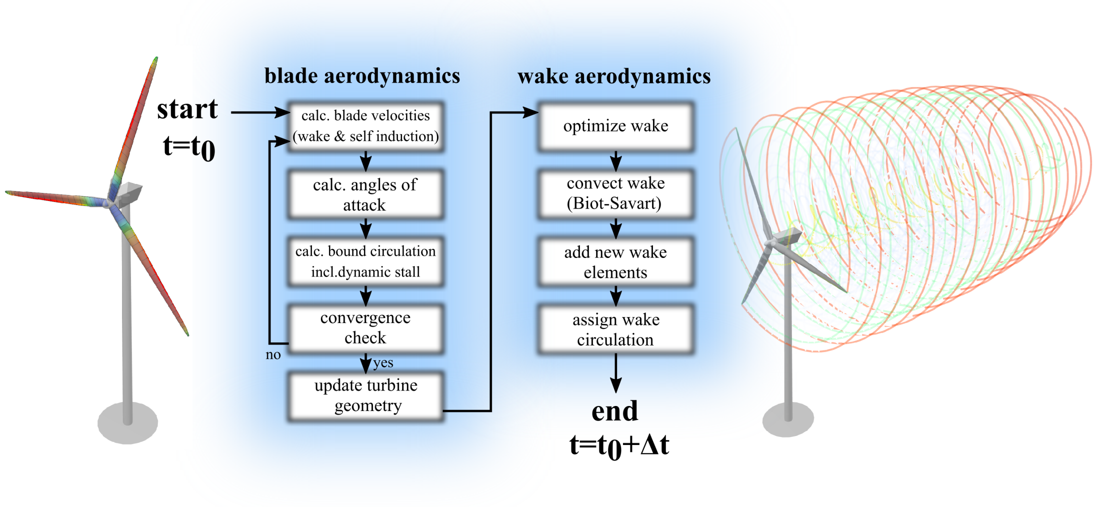

Figure 2.3.: Flowchart for a single time step of the aerodynamic calculations in QBlade

At the beginning of each time step the algorithm iterates to find a circulation distribution for the bound vortices on the lifting line, that matches the lift and drag coefficients obtained via the self-induced angle of attack. During the iteration only the bound vorticity distribution is updated, while the induction of the wake elements onto the blade is only evaluated once. After convergence is obtained the rotor rotation is advanced for a single time step. All free wake vortex elements are convected with the local inflow and local induced velocity. After the wake convection step, new vortex elements are created between the trailing edge of each blade panel and the last row of wake vortices that were convected away from the trailing edge. As a last step the circulation is computed and assigned to the new released vortex lines through the Kutta condition:

$$\Gamma_{trail} = \frac{\partial \Gamma_{bound}}{\partial x} \Delta x. \tag{2.3}$$

$$\Gamma_{shed} = \frac{\partial \Gamma_{bound}}{\partial t} \Delta t. \tag{2.4}$$

Three different integration schemes for the wake convection step are implemented. The first order Euler forward (EF) integration scheme:

$$\vec{x}_{t+1,EF} = \vec{x}_t + (V_\infty + V_{ind}(\vec{x}_t))\Delta t. \tag{2.5}$$

A predictor corrector (PC) method that reevaluates the induced velocity, based on the predicted position (Equation 2.5) is implemented as a second order integration method:

$$\vec{t}_{x+1,PC} = \vec{x}_t + (2V_\infty + V_{ind}(\vec{x}_t) + V_{ind}(\vec{x}_{t+1,EF}))\frac{\Delta t}{2}. \tag{2.6}$$

Additionally, a 2^{nd} order predictor corrector method, as proposed by Bhagwat and Leishman in

[177] is implemented:

$$\vec{t}_{x+1,PC2B} = \vec{x}_t + (3\vec{x}_{t+1,PC} - \vec{x}_t - 3\vec{x}_{t-1} + \vec{x}_{t-2})\frac{1}{4}. \tag{2.7}$$

The downside of the second order methods is that the costly evaluations for the velocity field have to be carried out twice for each time step, effectively doubling the computational time that is needed for the wake convection step. On the other hand, the obtained accuracy is higher, which allows one to choose a larger time step size as compared to the first order method while still maintaining acceptable accuracy. Figure 2.3 shows the order in which the aerodynamic calculations are carried out during a single time step.

2.4.2. Wake Lattice and Connectivity

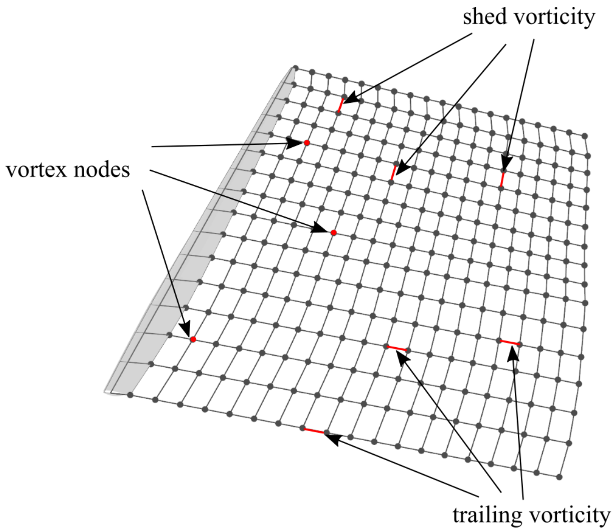

Figure 2.4.: Visualization of the wake lattice structure with wake nodes and filaments

Figure 2.4 shows the wake lattice structure. Shed- and trailing vortices are interconnected via common vortex nodes. During the free wake convection step the evolution of the wake is evaluated by advancing the positions of the vortex nodes in time. One vortex filament always has 2 vortex nodes attached to its two end points. If the vortex lattice would extend to infinity each vortex node would be connected to four vortex elements, thus the total number of vortex nodes is approximately half the number of vortex filaments. Consequently, the Biot-Savart equation has to be evaluated around:

$$N_{nodes} * N_{vortices} \approx \frac{N_{vortices}^2}{2} \tag{2.8}$$

times for a fully populated[27] infinite wake lattice. Compared to a vortex particle discretization, where no inter-connectivity exists, this means a reduction in computational cost by a factor of 2

27 Assuming that no vortex elements have been removed

($f_{opt} \approx 2$), due to the inter-connectivity of the wake lattice. To facilitate strategies that reduce the number of free vortices within the wake a method to remove individual vortices from the wake mesh, by detaching the vortex filament from its nodes, has been implemented. A check is performed during every step of the simulation that removes isolated vortex nodes, which are not attached to any vortex filament. The more vortices have been removed from the wake lattice, the lower the aforementioned leverage of the interconnections.

2.4.3. Vortex Core Desingularization

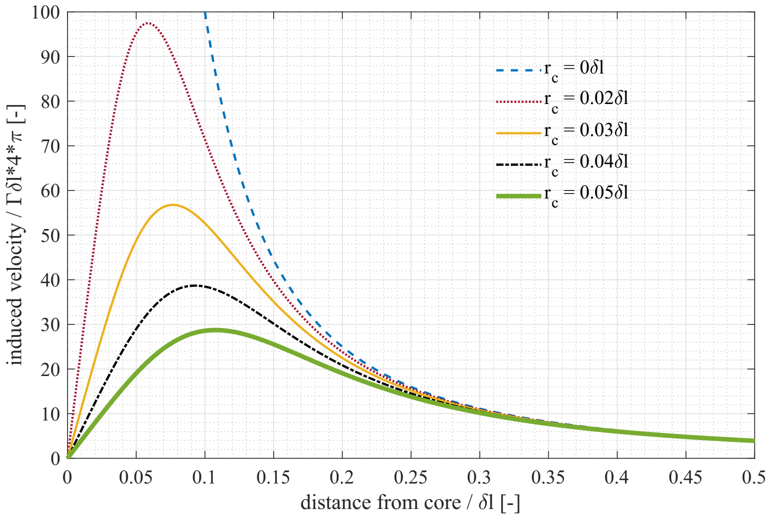

Figure 2.5.: Velocity distribution around the vortex core

The Biot-Savart equation (Equation 2.2) exhibits a singularity at the core where $\vec{r} = 0$ (see Figure 2.5). To prevent this singularity from affecting the stability of the simulation, and also to model the viscous core of the bound and free vortices more accurately, a model for a viscous vortex core needs to be implemented. Many different models that describe the tangential velocity distribution around the core exist, such as the Rankine, Lamb-Oseen or Ramasay and Leishman models (see [95]). In QBlade a simple cut-off radius is used, which is added to the denominator of Equation 2.2 in the form of r_c^2, and ensures that the induced velocity smoothly approaches zero in the vicinity of the core. This is a computationally efficient implementation, because the viscous core modeling is directly implemented in the calculation of the induced velocity. For other vortex models a viscous parameter needs to be evaluated from the relative vortex positions in addition to the Biot-Savart equation. This has a severe effect on the simulation performance, as the evaluation of the viscous parameter is carried $N^2_{vortices}/2$ times per time step. When shed from the blades trailing edge, a vortex is release with an initial core-size r_c[28]. The core-size is updated every time step according to:

$$r_c = r_0 + \sqrt{\frac{4a\delta_v \nu \Delta t}{1+\epsilon}} \tag{2.9}$$

28 a value of around 10% of local chord is proposed from experience

where $a = 1.25643$ is a constant, δ_v is the turbulent viscosity coefficient (a value depending on rotor size, see [38]), ν is the kinematic viscosity and Δt the time step size. The strain rate of the vortex filament is computed as:

$$\epsilon = \frac{\Delta l}{l}. \tag{2.10}$$

The desingularized Biot-Savart equation then becomes:

$$V_{ind} = -\frac{1}{4\pi} \int \Gamma \frac{\vec{r} \times \partial \vec{l}}{r^3 + r_c^2}. \tag{2.11}$$

2.4.4. Unsteady Aerodynamics and Dynamic Stall

To account for dynamic stall the ATEFLap [178] unsteady aerodynamics model for 2D airfoil behavior has been integrated [179][29] in the LLFVW method . The unsteady aerodynamics model consists of mainly two parts; an attached or potential flow model, as proposed by Bergami and Gaunaa in [178], and the classical Beddoes-Leishman dynamic stall model with a custom formulation for vortex lift, as presented by Hansen and Gaunaa in [180]. The implemented ATEFlap model also accounts for unsteady lift contribution of trailing edge flaps.

Polar Decomposition

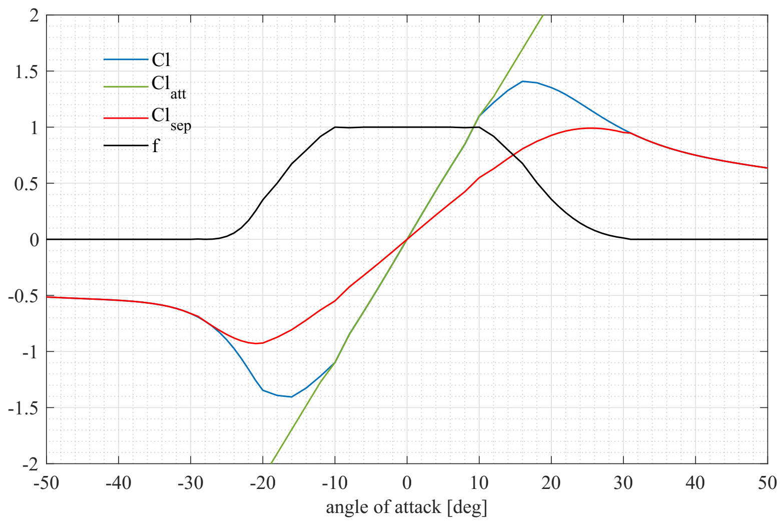

Figure 2.6.: Decomposition of static polar data

The unsteady aerodynamics model is based on a decomposition of the static, two dimensional lift Cl_{st} into a fully attached Cl_{att} and a fully separated Cl_{sep} contribution. The contributions of

29 One of the associated publications

the attached and the separated lift to the static lift are described by the separation function f:

$$Cl_{st} = f * Cl_{att} + (1 - f) * Cl_{sep}. \tag{2.12}$$

A module to perform the decomposition of polar data has been integrated with QBlades airfoil data pre-processor. To generate the decomposed data, the angle of attack for the positive and the negative stall point, as well as the attached lift slope of the static polar, have to be provided as a user input.

Attached Flow Contribution

The potential flow model accounts for non-circulatory (added mass) effects, and circulatory lift which includes wake memory effects that play a role long before the onset of stall. The added mass term models the forces due to the reaction of the fluid to the airfoil motion and the motion of its trailing edge flap:

$$Cl^{nc} = \pi \frac{b_{hc}}{V_\infty} \dot{\alpha}^{str} + \frac{F_{dydxLE}}{\pi} \frac{b_{hc}}{V_\infty} \dot{\beta}. \tag{2.13}$$

b_{hc} denotes the half chord length of the airfoil, V_∞ the free stream velocity and $\dot{\alpha}_{str}$ the pitch rate due to torsional deformation, F_{dxdyLE} is the deflection shape integral, a geometrical property depending on the airfoils shape[30] and $\dot{\beta}$ the flap deflection rate. The quasi steady lift component is the steady lift that is generated by the airfoil at the current angle of attack α_{qs} and the current flap deflection β_{qs} obtained from the relative airfoil motion and free-stream velocity, but without the influence of shed wake vorticity:

$$Cl^{qs} = Cl^{att}(\alpha_{qs}, \beta_{qs}). \tag{2.14}$$

Wake memory effects account for the influence of span wise or shed vorticity in the wake on the quasi-steady angle of attack. As the ATEFlap model has been formulated for BEM codes, the downwash of the wake[31] is modeled with an effective angle of attack that is computed via step responses that are described by exponential indicial response functions. In QBlade's implementation, the effective angle of attack is directly obtained as the induction from the free vortex wake formulation is already considered in the evaluation of the on-blade velocities.

$$Cl^{circ} = Cl^{att}(\alpha eff). \tag{2.15}$$

However, the quasi steady angle of attack, which does not include the effect of wake vorticity, is not known in the free vortex wake formulation of QBlade. As the quasi steady angle α_{qs} is needed for a later evaluation of the induced drag contribution it is computed by calculating the isolated contribution of the wake vorticity on the angle of attack, denoted as α_{shed}, separately. α_{shed} is computed via the induction of the total shed vorticity in the vicinity of the blade, up to 8 chord lengths away from the trailing edge. As the dynamic stall model is formulated for an isolated two-dimensional airfoil, it is necessary to limit the vortices that are involved in the

30 See Gaunaa's work in [181]
31 Which is the wake memory effect

evaluation of α_{shed} to those in the vicinity of the blade to exclude the significant influence of the total shed vorticity from all previous time steps on the global flow field[32]. α_{shed} is then used to calculate the quasi steady angle of attack from the effective angle of attack.

$$\alpha_{qs} = \alpha_{eff} - \alpha_{shed}. \tag{2.16}$$

This extra treatment is necessary because the common unsteady aerodynamics models are formulated for BEM codes and are using indicial functions which are replaced by the free vortex wake model in this adaptation.

Separated Flow Contribution

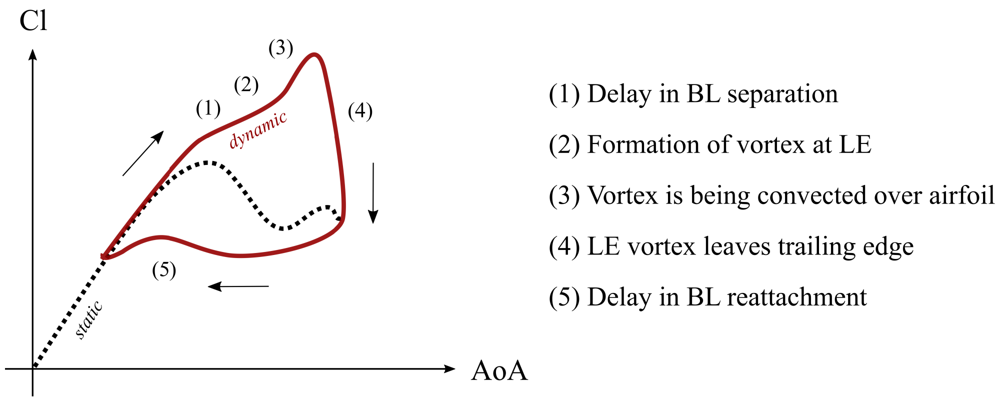

Figure 2.7.: The dynamic stall hysteresis loop

The implementation of the Beddoes-Leishman dynamic stall model follows along the procedure explained in [178]. The dynamic stall effect is modeled from three contributions. The first contribution is the lagged potential lift (leading edge pressure time lag), obtained via a low pass filter with the *pressure time lag constant* τ_p:

$$\dot{Cl}^{lag} = -\frac{V_\infty}{b_{hc}}\frac{1}{\tau_p}Cl^{lag} + \frac{V_\infty}{b_{hc}}\frac{1}{\tau_p}Cl^{pot}. \tag{2.17}$$

Using the lagged potential lift Cl^{lag}, the dynamic separation function f^{dyn} is calculated, by passing the separation function f (obtained from the polar decomposition) through a low pass fiter with the *boundary layer lag constant* τ_f:

$$f^{dyn} = -\frac{V_\infty}{b_{hc}}\frac{1}{\tau_f}f^{dyn} + \frac{V_\infty}{b_{hc}}\frac{1}{\tau_f}f(\alpha^*). \tag{2.18}$$

$$\alpha^* = \frac{Cl^{lag}}{\frac{\partial Cl}{\partial \alpha}} + \alpha_0. \tag{2.19}$$

32 This is especially important for VAWT simulations where the shed vorticity has a major contribution to the total induction field around the rotor

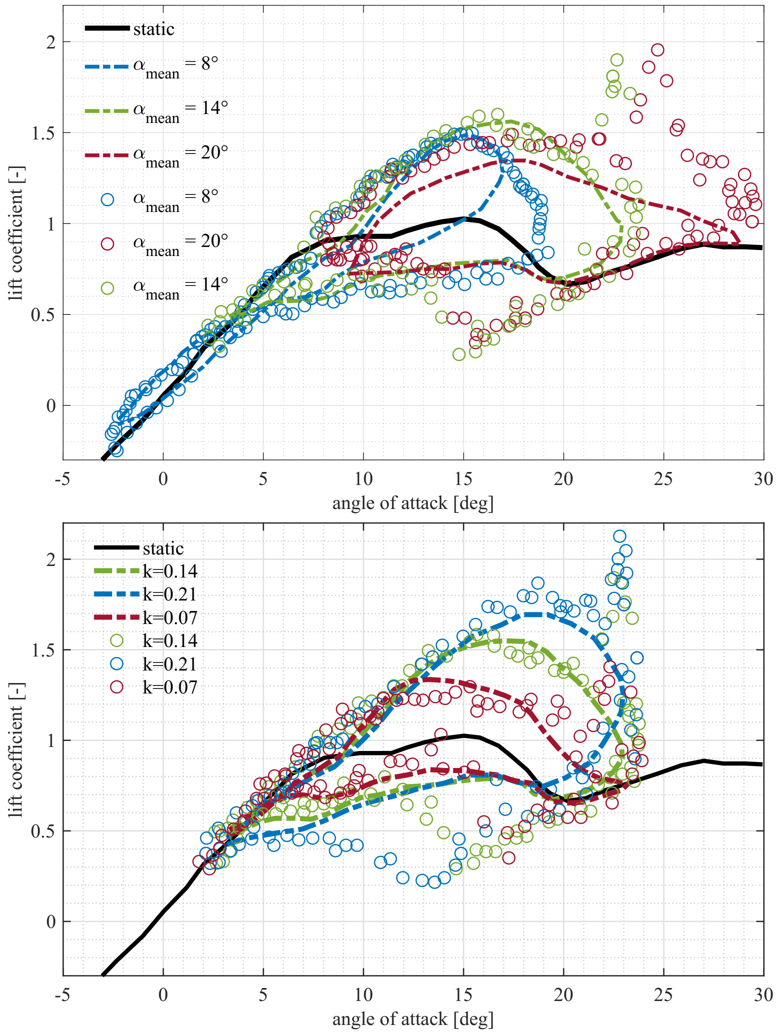

Figure 2.8.: Validation of the unsteady aerodynamics model with OSU test data (in circles) of the S809 airfoil [182]; top: varying mean AoA; bottom: varying dimensionless frequency

The dynamic circulatory lift $Cl^{circ,dyn}$ is then obtained by multiplying the dynamic separation function f^{dyn} with the fully attached Cl^{att} and the fully separated Cl^{sep} lift contributions that were obtained from the polar decomposition:

$$Cl^{circ,dyn} = Cl^{att}(\alpha_{eff}, \beta_{eff})f^{dyn} + Cl^{sep}(\alpha_{eff}, \beta_{eff})(1 - f^{dyn}). \tag{2.20}$$

Within the ATEFlap formulation for separated flow a term for modeling the vortex lift is included:

$$C_v = Cl^{circ,dyn}(1 - \frac{(1 + \sqrt{f^{dyn}})^2}{4}). \tag{2.21}$$

However, it was found, especially when simulating VAWT with large fluctuations in angle of attack, that this term is prone to large fluctuations, often causing unrealistically large values for the total dynamic lift coefficient. Thus, in favor of robustness, it was decided to exclude this term from the calculation of total lift. The total lift, including the attached and separated flow contribution, but excluding the vortex lift, then equals:

$$Cl^{dyn} = Cl^{circ,dyn} + Cl^{nc}. \tag{2.22}$$

The dynamic drag is evaluated from three contributions. The steady drag at the effective angle of attack:

$$Cd^{eff} = Cd(\alpha_{eff}, \beta_{eff}), \tag{2.23}$$

the drag induced from shed wake vorticity, using the quasi steady angle of attack that was evaluated in Equation 4:

$$Cd_{ind} = Cl^{circ,dyn}(\alpha_{qs} - \alpha_{eff}). \tag{2.24}$$

The induced drag contribution from the flap deflection is calculated according to:

$$Cd^{\beta}_{ind} = Cl^{circ,dyn} \frac{\frac{\partial Cl}{\partial \beta}}{\frac{\partial Cl}{\partial \alpha}} (\beta^{st} - \beta^{eff}) f^{dyn}. \tag{2.25}$$

The last contribution is the drag change caused through the separation delay:

$$Cd^{f}_{ind} = (Cd^{eff} - Cd(\alpha_0)) \left[\frac{(1 - \sqrt{f^{dyn}})^2}{4} - \frac{(1 + \sqrt{f^{st}})^2}{4} \right]. \tag{2.26}$$

The total drag is then computed as the sum of these contributions:

$$Cd = Cd^{eff} + Cd_{ind} + Cd^{\beta}_{ind} + Cd^{f}_{ind}. \tag{2.27}$$

More details about the implementation and validation of the unsteady aerodynamics model can be found in [179][33]. Two exemplary validation graphs from this publication are shown in Figure 2.8, where the general sensitivity of the dynamic stall hysteresis loop to the reduced frequency and amplitude is well reproduced.

2.4.5. Tower Influence

A tower shadow model, based on the work of Bak [125] is implemented in QBlade. This model is based on a superposition of the analytical solution for potential flow around a cylinder and a model for the downwind wake behind a cylinder, based on a tower drag coefficient. The tower shadow model only affects velocity components that are normal to the tower centerline; the z-component of the velocity, parallel to the tower centerline, remains unaffected. The tower shadow model is only used when the z-component of the evaluation point is smaller or equal to the tower height. An application of the tower model, including a comparison to CFD simulations and experimental data is found in [63][34].

33 One of the associated publications
34 One of the associated publications

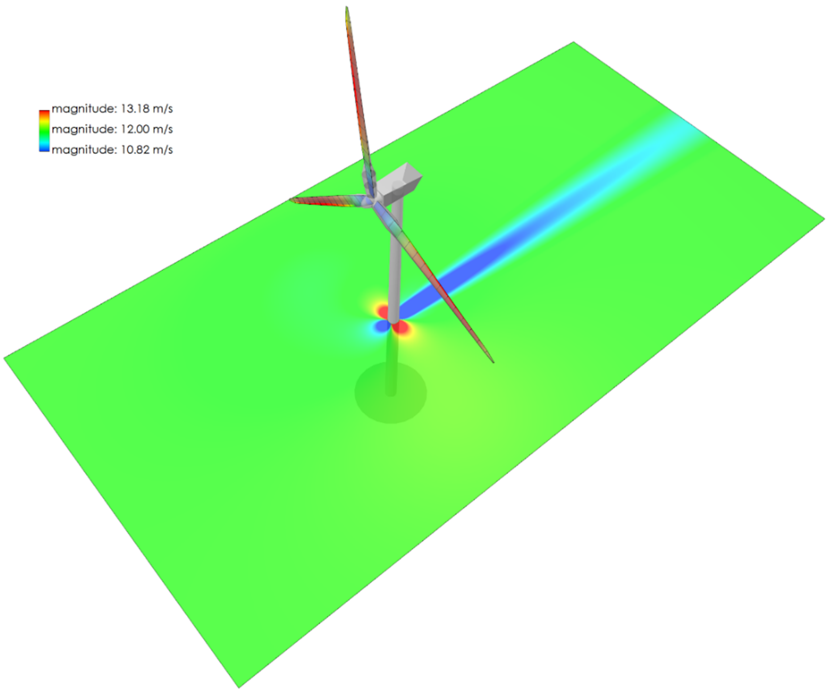

Figure 2.9.: Visualization of the tower shadow model; showing velocity magnitude

2.4.6. Active Flow Control Elements

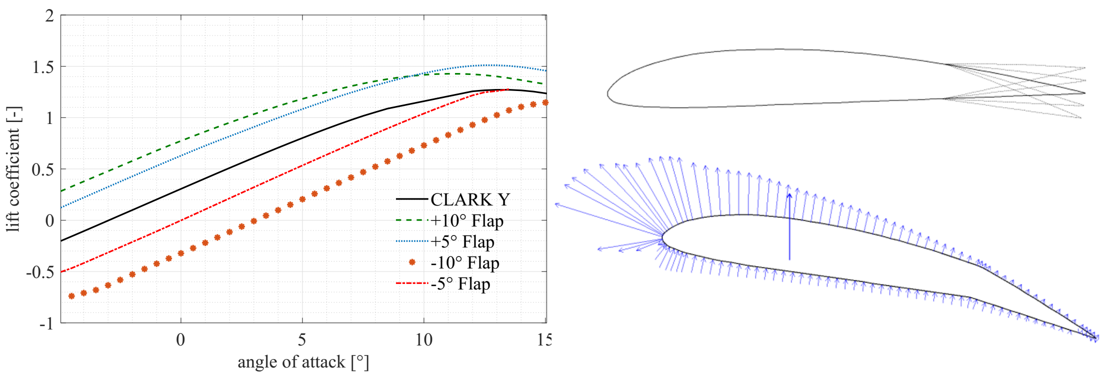

Figure 2.10.: Set of lift polars (left) belonging to a dynamic polar set of a trailing edge flap (right)

Active flow control (AFC) elements are defined by dynamic polar sets (see Figure 2.10), which are assigned to the inner and outer spanwise position of an AFC. A dynamic polar set groups polars, which each represent a discrete state of an AFC element, such as the flap deflection angle of a trailing edge flap. For each state of the AFC device, polars over a range of Reynolds numbers are stored in the dynamic polar set. During the simulation the polar data of the sets is then interpolated between the current AFC state and the Reynolds number. If a trailing edge flap is modeled as an AFC element the unsteady aerodynamics model (see 2.4.4) takes the unsteady flap aerodynamics into account, based on the flap deflection angle β. Figure 2.11 shows an excerpt from a validation study of QBlade's AFC model that was performed in [183][35]. It can be seen that only the other vortex based codes and the CFD codes are able to properly predict the radial distribution of the tangential force components due to a flap deflection accurately. This is mainly due to the shedding of trailing vorticity at the edges of the flap (see Figure 2.12), which is similar to vortex shedding at the blade tips, which cannot be predicted by BEM codes without including dedicated empirical correction models.

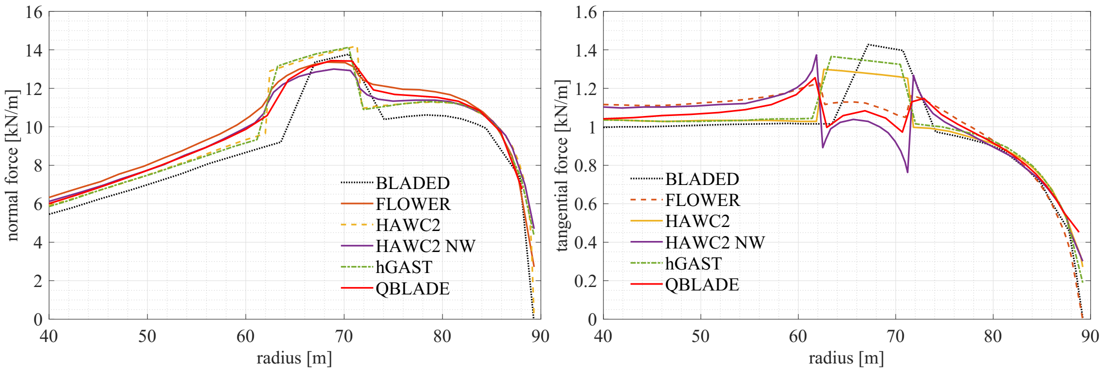

Figure 2.11.: Benchmark of flap model performance across several codes, taken from [183]

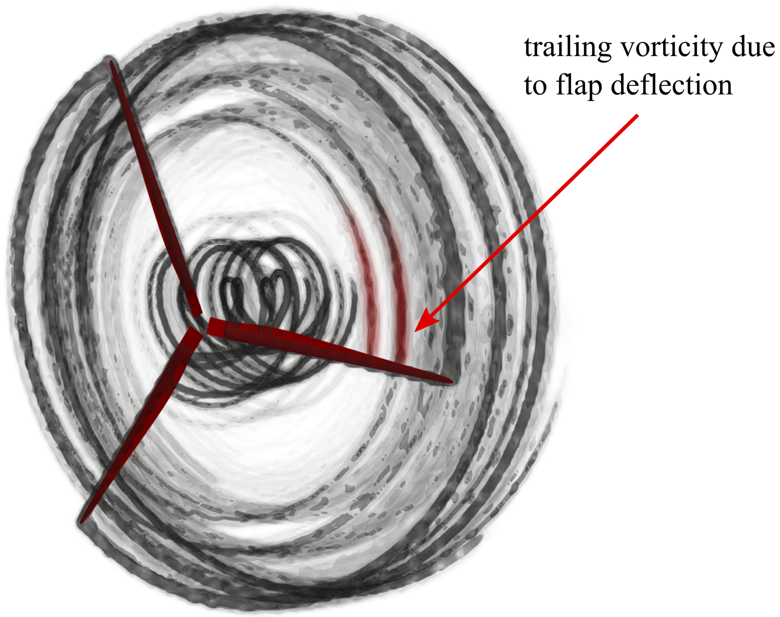

Figure 2.12.: Visualization of the trailing vorticity that is being shed at 70% span of the rotor blade due to the deflection of a flap, simulated using QBlade

35 One of the associated publications

2.4.7. Stall Delay (Himmelskamp) Effect

The maximum lift coefficient of profiles on a rotating rotor blade is significantly higher than the maximum lift coefficient of the same profile measured on a stationary rotor. The centrifugal force accelerates the boundary layer radially. this results in a thinner boundary layer in which stall is delayed. At the same time, air flowing radially, in a rotating reference system, generates a Coriolis force opposite to the rotational direction of the rotor. This force is opposing the rise in pressure of the profile's suction side and delays the stall. This effect, called stall delay or Himmelskamp effect, can be taken into account by modifying the two dimensional polar data. For the affected profiles the stalled region will shift to higher angles of attack. With a viscous-inviscid interaction method, Snel investigated the flow around a rotating rotor blade and developed a semi-empirical formula to correct 2D polar data [184]. According to Snel, only the lift but not the drag coefficient, needs to be modified. The Himmelskamp effect, can be modeled in QBlade using Snel's correction:

$$Cl_{3D} = Cl_{2D} + \frac{3.1\lambda^2}{1+\lambda^2} g \left(\frac{c}{r}\right)^2 \left(\frac{\partial Cl}{\partial \alpha}(\alpha - \alpha_0) - Cl_{2D}\right). \tag{2.28}$$

Where g is a blending factor: $g = 1$ for $0 < \alpha < 30$; $g = 0.5(1 + \cos(6\alpha - 180))$ for $30 < \alpha < 60$ and $g = 0$ for $60 < \alpha < 360$.

More details on this empirical correction can be found in [184]. If this correction is activated for a simulation it is applied on the unmodified, tabulated 2D airfoil data at every timestep.

2.4.8. Turbulent wind input

Design load case calculations require turbulent wind fields as boundary conditions to the aerodynamic simulations. The statistical properties of these wind-fields, or the spatial and temporal correlation of their velocity fluctuations, need to match the properties of the inflow conditions that the wind turbine will experience at its designated site of operation. The external site conditions are classified into different wind turbine classes [185] according to Table 2.3. V_{ref} designates site specific mean reference wind speeds (class I,II,III) and $I_{ref,15}$ different levels of turbulence intensities (A,B,C). For the inclusion of turbulent wind fields (see Figure

Table 2.3.: Parameters for different wind turbine classes

Wind turbine class	I	II	III
V_{ref}	50m/s	42.5m/s	37.5m/s
A	$I_{ref,15} = 0.16$		
B	$I_{ref,15} = 0.14$		
C	$I_{ref,15} = 0.12$		

2.13) into the simulation the wind fields are pre-calculated in the form of so called turbulent wind boxes. Wind boxes are three dimensional boxes, containing a spatially correlated distribution of velocities. Assuming Taylors frozen turbulence hypothesis [186], a wind box is pushed through the simulation domain with the mean inflow velocity. The local turbulent velocities are then simply superimposed with the induced velocity of the wake. Correlated, turbulent wind boxed can be generated inside QBlade, employing an integrated wind field generator based on the

Veers model [187] or an interface to the TurbSim [188] wind field generator. Furthermore, wind boxes can be can be imported in the binary .bts format.

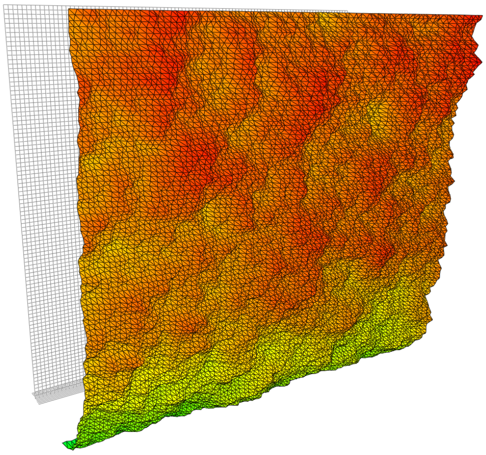

Figure 2.13.: Snapshot of a highly resolved turbulent windfield in QBlade, showing the spatially correlated turbulent structures

2.4.9. Ground Effect

Ground effects are modeled by mirroring all vortex elements, bound and free, at the ground plane [189]. A mirror image (see Figure 2.14) of all bound and free vortices is created at every time step using the ground as a symmetry plane. Such a treatment doubles the number of times that the Biot-Savart equation is calculated and thereby doubles the computational time needed for the evaluation of the convection step.

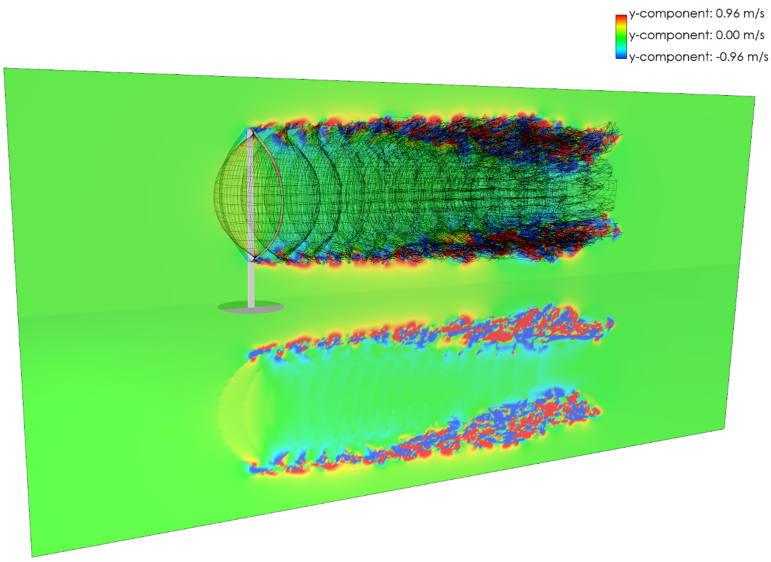

Figure 2.14.: Modeling of ground effect through mirroring of the wake, showing velocity magnitude of the y-component (normal to plane)

2.4.10. Impact of Spatial and Temporal Discretization on N

The computational efficiency of the LLFVW aerodynamic simulation is a key factor for its applicability in a design and certification context. As already mentioned, the computational cost of the LLFVW is significantly larger than that of a comparable BEM based simulation. The largest contributor to the computational cost is the free wake convection step. In this step the induction of all vortex elements within the simulation domain has to be evaluated at all vortex node positions to perform the time integration and advance the wake evolution, leading to roughly N^2 evaluations of the Biot-Savart equation, where N is the number of free vortex elements. N is constantly growing within a simulation as new vortex elements are being shed at the rotor blades trailing edge during every time step. To keep the computational cost reasonable, the N has to be kept as small as possible, without impacting the accuracy of the simulation. The number of free vortex elements that is created during a single revolution of the rotor can be calculated as follows:

$$N_{elems,rev} = \frac{2\pi}{\omega \Delta t}(2N_{B,disc} - 1)N_B, \tag{2.29}$$

where

$$\Delta\Phi = \omega \Delta t, \tag{2.30}$$

is the azimuthal discretization ($\Delta\Phi$) of the rotor revolution. From Equation 2.29 it can be seen that $N_{elems,rev}$ is linearly proportional to the spanwise discretization of the blade ($N_{B,disc}$) and the number of blades (N_B) while $N_{elems,rev}$ is inversely proportional to the time step size (Δt). Choosing appropriate values for the spanwise blade discretization and for the time step size has a large impact on the computational cost[36]. Appropriate values for the blade discretization and the time step size depend largely on the rotor geometry and the simulated operating conditions and need to be evaluated by means of a sensitivity analysis.

2.4.11. Wake Truncation

To prevent the number N from growing indefinitely, it is required to truncate (see Figure 2.15) the wake at some downstream position. This is realized by removing all vortex elements after they have reached a certain age. In this implementation, the vortex age is non-dimensionalized by the number of rotor revolutions that have passed since the vortex element has been shed from the rotor. Depending on the tip speed ratio (TSR), or the wake state of the wind turbine, the minimum age that is required to obtain an accurate induction of the wake inside the rotor disc varies. Figures 2.16 and 2.17 show the effects of wake truncation on the power and thrust coefficients for a generic 3-bladed wind turbine. The simulations were carried out over 30 rotor revolutions. It can be seen that the error that can be expected from truncating the wake grows larger with growing TSR[37]. Furthermore, it can be seen that wake truncation has a larger effect on the power coefficient than on the thrust coefficient. Depending on the TSR, at which the simulated turbine operates, a suitable value for wake truncation needs to be selected. At the design TSR a wake length of 12 revolutions causes an error of under 1% for the power coefficient.

36 Doubling the discretization increases the cost by a factor of four, the same holds for a halving of the time step
37 For larger TSR's the truncated vortices are in closer vicinity to the rotor

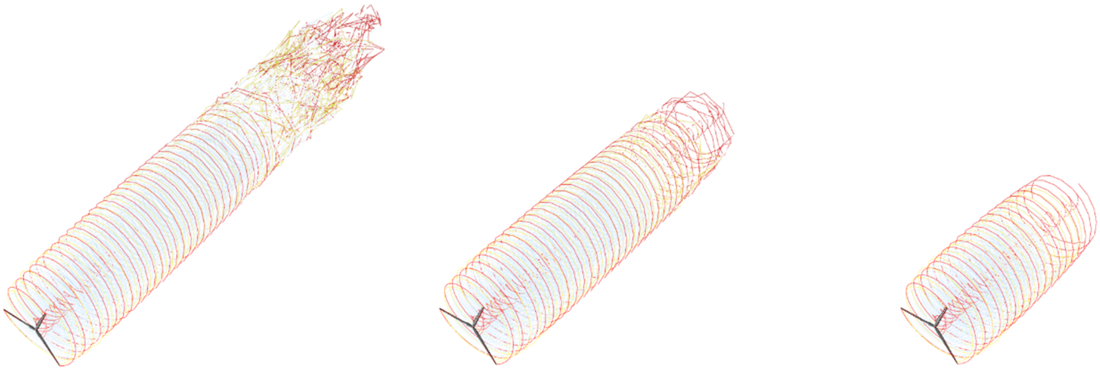

Figure 2.15.: Visualization of three different wake truncation lengths, from left to right: 18 revolutions, 12 revolutions, 6 revolutions

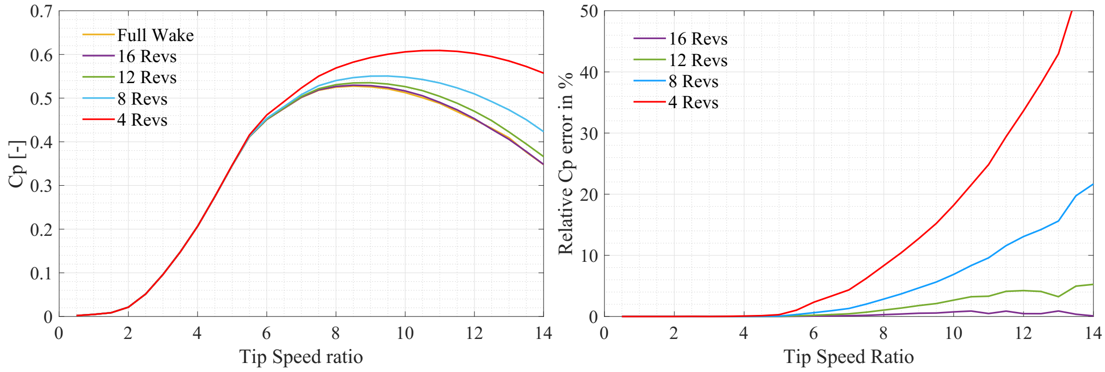

Figure 2.16.: Effect of wake truncation on the estimated power coefficient over a range of tip speed ratios

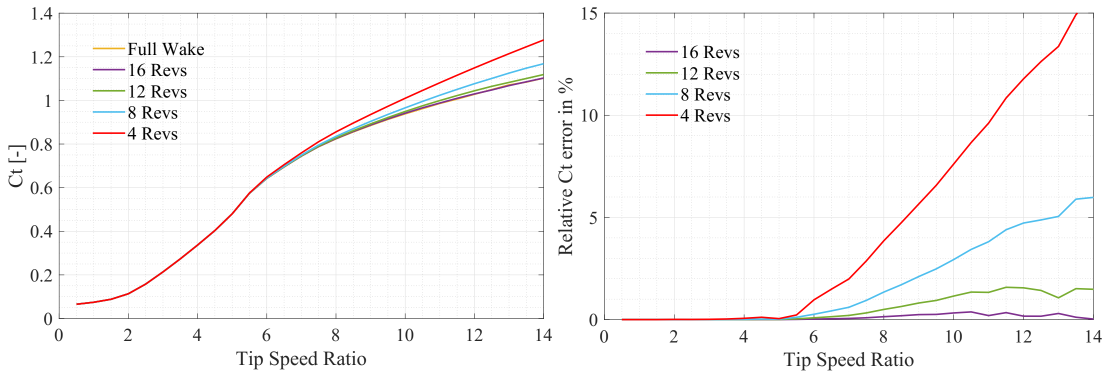

Figure 2.17.: Effect of wake truncation on the estimated thrust coefficient over a range of tip speed ratios

2.4.12. Wake Coarsening

In addition to the wake truncation and reduction techniques a wake coarsening method is implemented. The wake coarsening reduces the number of free wake elements by successively decreasing the spatial resolution of the wake lattice in streamwise direction over four zones. The decrease in resolution is specified by four lengths (defined as vortex ages)[38] (l_1, l_2, l_3 and l_4) and three integer coarsening factors (f_1, f_2 and f_3). After the vortex age has reached l_1, the chordwise resolution of the wake lattice is reduced by the factor f_1. This is carried out by merging f_1 attached trailing vortices into a new single trailing vortex. During the combination of trailing vortices, the vorticity of all combined vortices is averaged between the contributing vortex filaments (weighted by the original vortex length). For the shed vorticity all vortices but the f_1^{th} shed vortices are removed from the lattice. To conserve the total shed vorticity in the wake, the vorticity of the removed shed vortices is divided up over the two neighboring shed vortex elements, weighted by distance. This process is repeated, for the already coarsened wake, with the factor f_2 after the age of a vortex reaches l_2 and the factor f_3 after the age of a vortex reaches l_3. After the vortex age reaches l_4 the wake is truncated. The total factor f_{opt} by which computational cost can be reduced is calculated as follows:

$$f_{opt} = \left(\frac{l_1 + l_2 + l_3 + l_4}{l_1 + \frac{l_2}{f_1} + \frac{l_3}{f_1+f_2} + \frac{l_4}{f_1+f_2+f_3}} \right)^2 . \tag{2.31}$$

Figure 2.18 visualizes how the coarsening method is progressively reducing the wake resolution over the four wake zones (near wake, zone1, zone2, and zone3). A practical example for the wake coarsening method applied to a rotor operating at a TSR of 5, with a timestep size equivalent to 5°of rotor advancement, is shown in Figure 2.19. In this example the total wake length is 10 revolutions, with a near wake length of 1 revolution and a length of three revolutions for each of the three following wake zones. The reduction factor between each of the wake zones is 2. These parameters result in a reduction factor $f_{opt} = 7.6$

38 The age of a vortex element is either defined as a normalized (by the time for a rotor revolution) time span or defined as a number of time steps or defined as an absolute time span

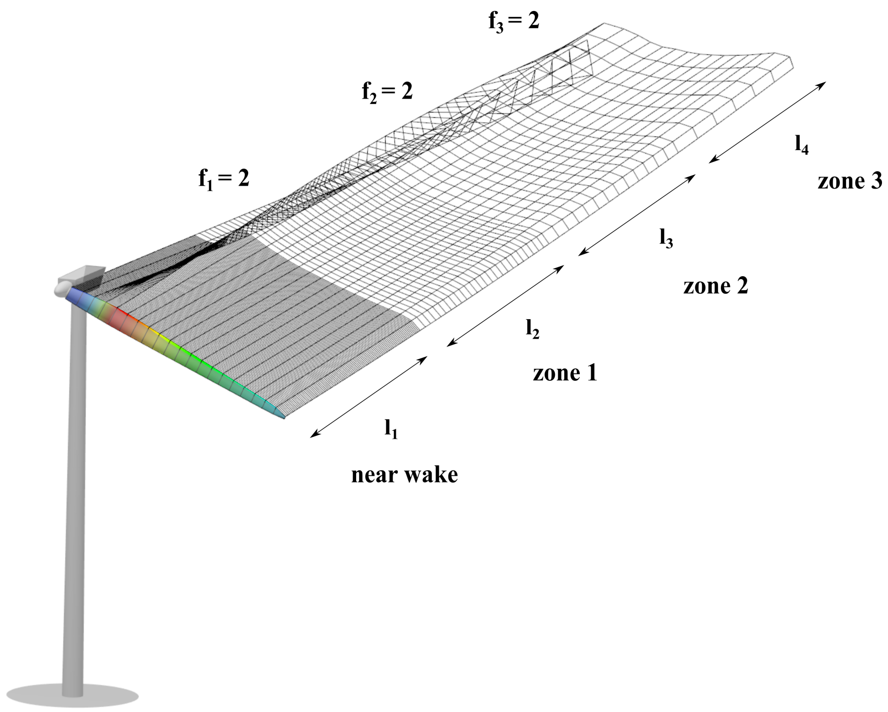

Figure 2.18.: Visualization of the wake coarsening method

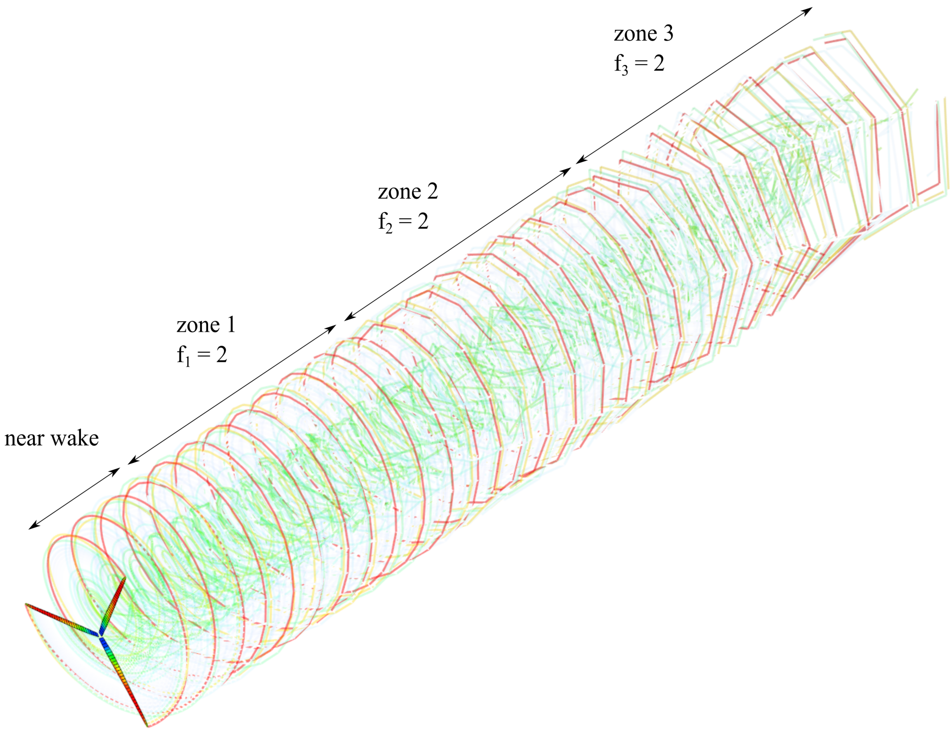

Figure 2.19.: Visualization of the wake coarsening method for a turbine at TSR 5, near wake = 1rev, zone1 = 3rev, zone2 = 3rev; zone3 = 3rev; $f_1 = 2$; $f_2 = 2$; $f_3 = 3$; $f_{opt} = 7.6$

2.4.13. Adaptive Wake Reduction

Another strategy to reduce the number N is to selectively remove vortices with low circulation, as these only have a negligible effect on the total induced velocity field of the wake. In QBlade, this strategy is implemented by specifying the factor F_Γ. The largest circulation of a vortex filament, Γ_{max}, is evaluated at each timestep of a simulation. Each vortex filament with the circulation Γ is removed from the simulation if the following condition holds true:

$$\Gamma < F_\Gamma \Gamma_{max}. \tag{2.32}$$

For HAWT turbines the shed vorticity (see Equation 2.4) has a significantly smaller circulation than the trailing vorticity (see Equation 2.3). In a steady state simulation, when the inflow is uniform and the rotational speed is fixed, the shed circulation is zero, as the bound circulation on the blade is constant over time. In such a case all shed vortex elements will be removed if $F_\Gamma > 0$. In an unsteady simulation of a HAWT the parameter F_Γ mostly affects the shed circulation[39]. Figure 2.20 shows an exemplary case of wake reduction for a generic turbine operating in 15° yawed inflow using the F_Γ parameter. Only the shed vorticity is shown, regions of large circulation are shown in red, regions of low circulation are shown in blue. Using a factor $F_\Gamma = 0.004$ the number of wake elements is reduced from $50,000$ to $25,000$, and the number of wake nodes from $25,000$ to $23,000$, without any notable impact on the simulation accuracy[40]. As a result of this reduction, the computational cost in this example is reduced by a factor of 2.2 ($f_{opt} \approx 2$).

Figure 2.21 shows the results of the adaptive reduction technique on the wake of a VAWT. Here, both shed-, and trailing vortex elements are removed. Using an F_Γ parameter of 0.02, the number of wake elements could be reduced from $35,000$ to $15,000$ while the number of nodes was reduced from $18,000$ to $14,000$ leading to a reduction factor for the computational cost of 3 ($f_{opt} \approx 3$).[41]

2.4.14. Parallelization

A crucial step to make a free wake vortex method applicable for design load calculations is to leverage parallelization techniques for the evaluation of the Biot-Savart equation. Modern Graphics Processing Units (GPUs) are optimized to perform simple vector operations that are required for three dimensional computer graphics. GPUs are equipped with several thousand cores on which vector operations can be carried out in parallel. As all evaluations of the Biot-Savart equation are independent, their evaluation can be easily parallelized. The parallelization in QBlade is implemented within the OpenCL framework [191]. To enable the parallelization, the complete wake data has to be converted into OpenCL vector primitives. A single vortex element is represented by two cl_float4 variables (Table 2.4):
Successively, arrays containing the wake data and the evaluation positions are passed from the RAM to the GPU memory to be accessed by the OpenCL kernel. Within the kernel the

39 If a VAWT is simulated both shed and trailing vortices are affected by the wake reduction. The main reason for the implementation of this technique was its applicability to HAWT and VAWT wakes alike (opposed to the previously implemented wake lumping procedure, see [190])

40 Difference in converged power coefficient due to the adaptive wake reduction in this case is below 0.2%

41 The difference in converged power coefficient, due to the adaptive wake reduction in this case is below 0.1%

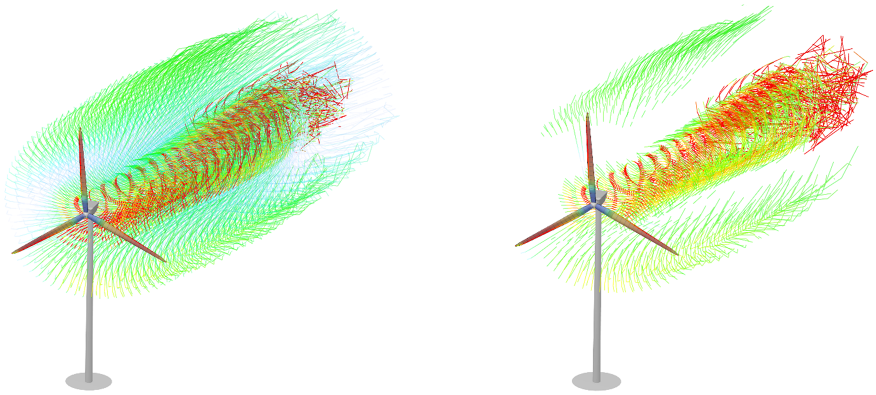

Figure 2.20.: Visualization of the wake reduction method for a HAWT; left: full wake - 50000 elements, right: reduced wake 25000 elements, only shed vorticity is shown

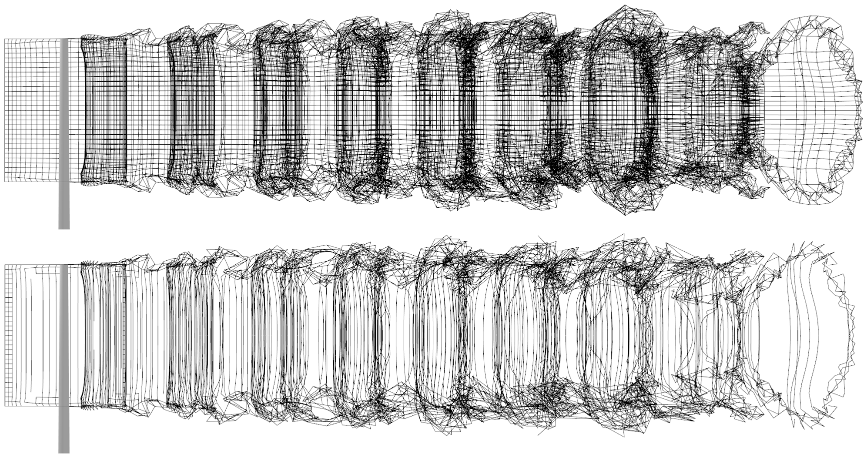

Figure 2.21.: Visualization of the wake reduction method; top: full wake - 35000 elements, bottom: reduced wake - 15000 elements

Table 2.4.: Conversion of the vortex filament data into two cl_float4 primitives

cl_float4 primitive	**vortex data**
cl_floatA.x	nodeA.position.x
cl_floatA.y	nodeA.position.y
cl_floatA.z	nodeA.position.z
cl_floatA.w	r_c^2
cl_floatB.x	nodeB.position.x
cl_floatB.y	nodeB.position.y
cl_floatB.z	nodeB.position.z
cl_floatB.w	Γ

wake arrays are distributed over a set of tiles[42], which then evaluate the Biot-Savart equation in

42 The optimum size of the tiles is GPU specific

parallel. Memory fences ensure that data is not accesses simultaneously by different tiles. After the evaluation of all parallelized equations the induced velocities have been obtained and the time integration takes place. The code of the OpenCL kernel used within QBlade is shown in Appendix A.1 .

The implemented OpenCL parallelization is highly effective in reducing the computational cost. Figure 2.22 shows a comparison between single and multi-core CPU and GPU evaluation. The calculations were performed on an Intel i9-9900k CPU (16 cores, with 3.6GHz) with a NVIDIA Quadro P6000 GPU (3840 CUDA Cores). The multi core calculations are approximately one order of magnitude faster than single core evaluation, the OpenCL evaluation is around two orders of magnitude faster ($f_{opt} \approx 1000$) than the single core evaluation. The OpenCL parallelization is able to handle 13.5×10^9 Biot-Savart evaluations for a wake size of 150000 vortex elements in approximately $0.2s$[43].

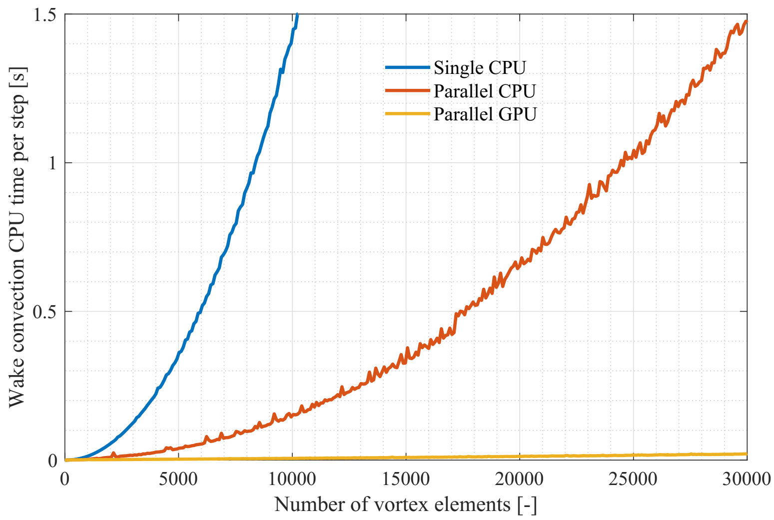

Figure 2.22.: Reduction of computational cost through parallelization

43 150000 free vortex elements are enough to discretize a wake from 35 full rotor revolutions (without truncation or coarsening) with 10° azimuthal discretization and 20 panels per blade

2.5. Structural Dynamics Model Implementation in QBlade

This section deals with the structural model that has been integrated with the QBlade code. To facilitate the generation of structural turbine models a pre-processor has been developed to facilitate the automatic setup of structural turbine definitions for aeroelastic calculations. To integrate full supervisory wind turbine controllers into the aeroelastic simulations standard controller library definitions, based on dynamic link libraries (DLLs), are integrated into the simulations and coupled to actuator links within the structural model. Additionally, an automated eigenvalue solver was implemented, which calculates mode shapes and eigenfrequencies of the fully coupled aeroelastic system.

2.5.1. The Chrono Library

The structural model in QBlade is based on the FEA module of the open source multi-physics engine Project Chrono [192]. Project Chrono is based on a platform independent design [193], which is developed in the C++ language as an object-oriented library, consisting of various components, such as Chrono::Vehicle: a module for vehicle modeling and simulation, Chrono::MKL: an interface for sparse direct solvers or Chrono::FSI: a module for fluid-solid interaction problems.

For the integration into QBlade the Chrono::Engine module is employed. Chrono::Engine is the core module of Project::Chrono, it contains functionality for setting up and solving physical systems containing Newtonian dynamics and finite elements. The SparseLU solver of the EIGEN C++ template library [194] is used as a solver for the finite element problem. A dynamic link library, containing the Chrono module, has been compiled from Project Chrono's GIT repository. The relevant header files of Project Chrono and the EIGEN library are included, and the Chrono DLL is linked to QBlade's source code. This enables the definition of the physical system and the finite elements and grants access to the solver to perform time domain simulation of structural dynamics inside QBlade.

2.5.2. Element Formulation and Multi-Body Formulation

The structural turbine model in the QBlade-Chrono coupling consists of Euler Bernoulli beams in a co-rotational formulation [195]. In the co-rotational formulation (see Figure 2.23), a floating coordinate system is attached to each deformable beam element. The overall motion of a beam element is then the addition of the rigid body motion[44] undergone by the floating coordinate system and a smaller strain deformation, expressed in the floating frame of reference. The global tangent stiffness matrix in Project Chrono's implementation is formulated in a way to include terms for geometric stiffness. In QBlade's implementation of the structural model the complete turbine structure is divided up into body objects. A body object contains an array for its structural nodes, an array for its structural beam elements, a unique identifier and several functions to access forces, torques, positions, velocities, accelerations and deflections. For a common HAWT one body is created for each blade and one body for the tower.

44 Translation and rotation

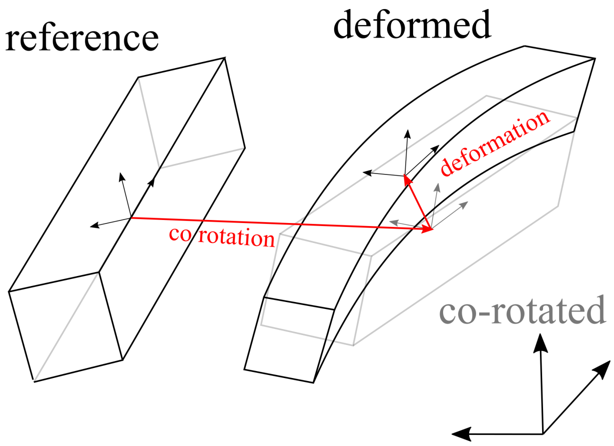

Figure 2.23.: Visualization of the co-rotational beam approach, reproduced after [195]

After the bodies have been created they are assembled using joints or constraints (see Figure 2.24). The tower is fixed to the ground by constraining all six DoF of the bottom tower node. A spring and damper may be defined at the ground to include foundation and soil dynamics. Using a revolute constraint, a free yaw node is connected to the tower top. Another revolute constraint then connects the hub node to the yaw node. Lastly, the blades are fixed around the hub node with revolute constraints, allowing them to rotate around the pitch axis. After the assembly of the bodies is completed, actuators are added to the revolute constraints. These actuators are used to yaw or pitch the turbine, based on controller signals and to model the generator. Actuators are implemented as engine type constraints. At these engine type constraints either a rotational angle, a rotational speed or a torque can be applied. This functionality is used to prescribe pitch angles at the pitch constraints, yaw angles at the yaw constraint and the generator torque at the shaft constraint. Furthermore, if no controller is used within a simulation, a constant rotational speed is prescribed to the main shaft to operate the turbine at a constant rotational speed.

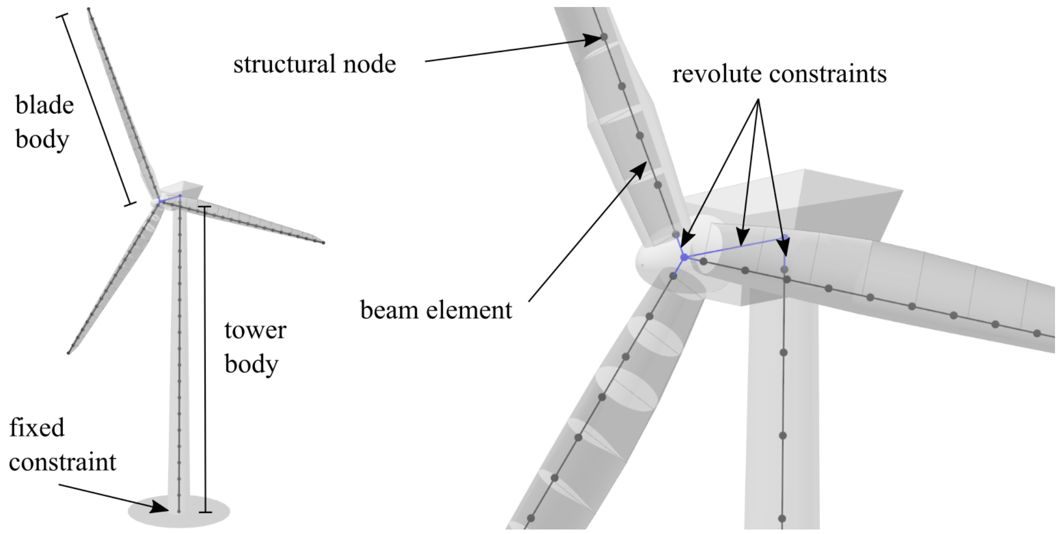

Figure 2.24.: Composition of the structural model in the QBlade-Project::Chrono coupling

2.5.3. Structural Pre-Processor

To facilitate the structural definition of a wind turbine and the setup of aeroelastic simulations a structural pre-processor based on text file templates has been developed. A distinction is made between horizontal axis- and vertical axis wind turbines, as their highly different topologies cannot be easily generalized into a single template.

The basis for a structural definition is the aerodynamic and geometric definition of a rotor inside QBlade's blade design module. From this definition the geometry data is automatically extracted to create the structural discretization of the rotor blades that is parametrized in the structural input file. In addition to the geometric rotor definition the sectional mass and stiffness properties of the turbine structure need to be provided. Lastly, key parameters, such as tower height or rotor tilt angle are used to construct the overall turbine geometry. Based on the structural and geometrical properties the structural bodies are then constructed and assembled via constraints to generate the complete structural model.

The structural and geometric data is provided in plain ASCII files. The data is identified in the form of keywords that need to appear in the same line as the input data. During the data import the file interpreter searches for lines of ASCII characters containing the required keywords and reads in the numeric data, appearing at the first position inside the line of ASCII characters. The order in which the keywords are provided within the file is irrelevant for the data import. If a certain keyword is not found, or the numeric value cannot be interpreted, a warning is issued, and the user is informed of the missing data type. The required data, and the form in which it needs to be provided, is presented in exemplary input files for the NREL 5MW HAWT (see Appendix A.2) and the Sandia 34m VAWT (see Appendix A.3).

HAWT Geometry Parameterization

In the following the most important parameters for the definition of a HAWT turbine geometry (see Figure 2.25) are briefly explained.

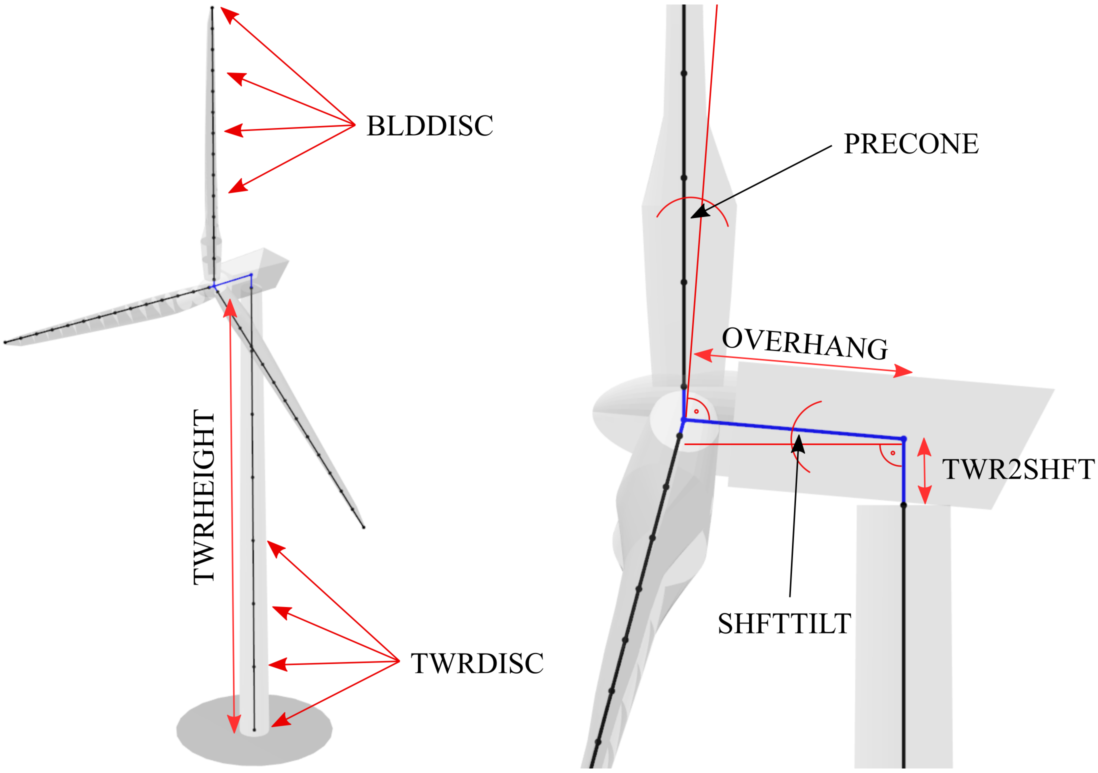

Figure 2.25.: Parameterization of a HAWT geometry

- **PRECONE**: Rotor blade pre-cone angle
- **SHFTTILT**: Tilt angle of the main shaft
- **OVERHANG**: Distance between the tower axis and the rotor plane, along the shaft axis
- **TWR2SHFT**: Distance between the tower top and the shaft, along the tower axis
- **TWRHEIGHT**: Tower height
- **TWRDISC**: Number of structural nodes for the equidistant discretization of the tower
- **BLDDISC**: Number of structural nodes for the equidistant discretization of a blade

VAWT Geometry Parametrization

In the following, the most prominent parameters for the definition of a VAWT turbine geometry (see Figure 2.26) are briefly explained.

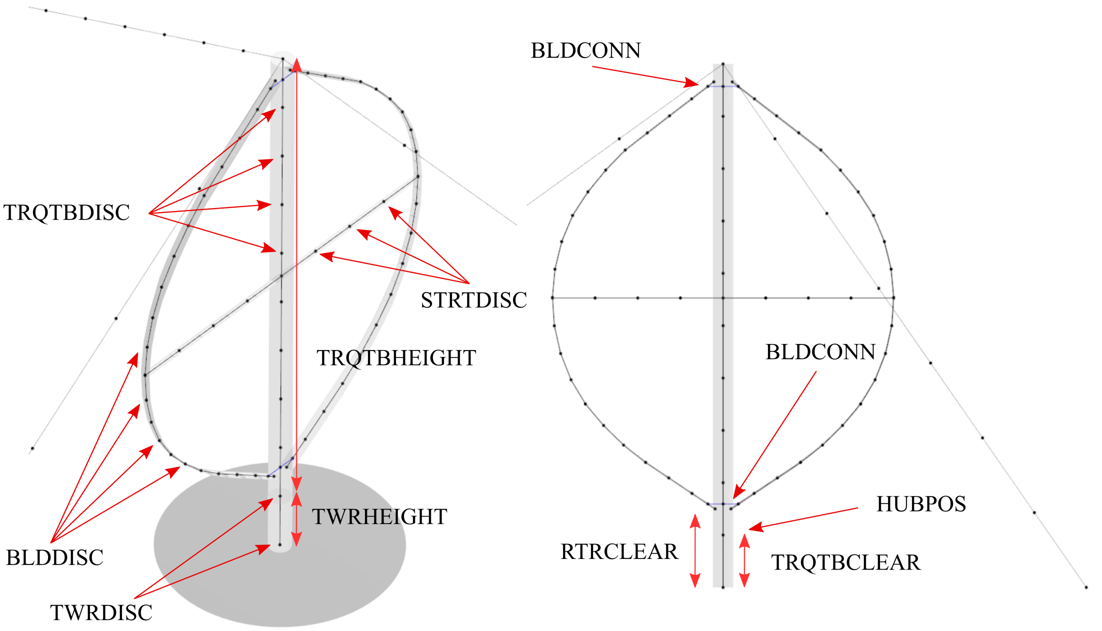

Figure 2.26.: Parameterization of a VAWT geometry

- **HUBPOS**: Height position of the generator hub constraint, connecting torque tube and tower
- **TWRHEIGHT**: Height (or length) of the tower body
- **TRQTBHEIGHT**: Height (or length) of the torque tube body (the rotating part of the tower)
- **TRQTBCLEAR**: Torque tube clearance, measured from the ground
- **RTRCLEAR**: Rotor clearance, measured from the ground
- **BLDCONN**: Local rotor height position of a rigid rotor to tower constraint
- **TRQTBCONN**: Local torque tube height position of a bearing constraint to the tower[45]
- **TWRDISC**: Number of nodes for the equidistant discretization of the tower
- **TRQTBDISC**: Number of nodes for the equidistant discretization of the torque tube
- **BLDDISC**: Number of nodes for the equidistant discretization of a blade
- **STRTDISC**: Number of nodes for the equidistant discretization of a strut

45 This is only needed in some cases, for example for a hollow torque tube that is put over the fixed tower. In the case of Figure 2.26 no such constraint is needed.

Drivetrain Model

The drivetrain model in QBlade is inspired by the drivetrain model of NREL's FAST code. The drivetrain is included in the simulation as a one degree of freedom two mass linear spring and damper system. It is described by the following parameters:

- **GBOXEFF**: The gearbox efficiency, must be between 0 and 1
- **GBRATIO**: The gearbox ratio, between the low (LSS) and the high speed shaft (HSS)
- **HUBINER**: The low speed side (LSS) inertia (excluding the rotor inertia)
- **GENINER**: The high speed side (HSS) inertia (generator, high speed shaft and gearbox
- **DTTORSPR**: The torsional stiffness of the low speed shaft in $\frac{Nm}{rad}$
- **DTTORDMP**: The torsional damping of the low speed shaft in $\frac{Nms}{rad}$

Figure 2.27 illustrates the single DoF model of the drivetrain. The total inertia on the low speed side consists of the rotor inertia [46] and the user defined hub and low speed shaft inertia (J_{LSS}) while the total inertia on the high speed side combines the user defined inertia of the generator, gearbox and high speed shaft (J_{HSS}).

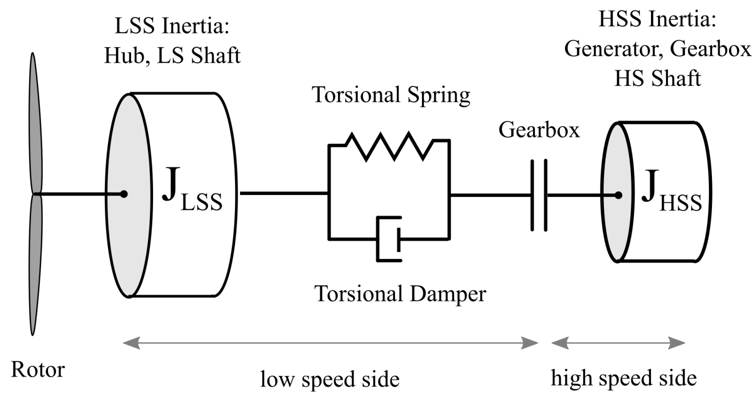

Figure 2.27.: Schematics of the single DoF drivetrain model in QBlade

For a drivetrain without losses the torque balance between the LSS and HSS can be expressed as:

$$T_{LSS} = T_{Aero} - J_{LSS} * \dot{\omega} = T_{HSS} N_{Gear} = T_{Gen} N_{Gear} + J_{HSS} \dot{\omega} N_{Gear}^2, \tag{2.33}$$

where N_{Gear} is the gearbox ratio and ω the rotational speed of the LSS. The resulting restoring torque T_{Res} of the spring and damper system is:

$$T_{Res} = K(\Phi_{Rot} - \Phi_{Gear}) + C(\omega_{Rot} - \omega_{Gear}), \tag{2.34}$$

where Φ_{Rot} is the angular position of the rotor and Φ_{Gear} the angular position of the gearbox, K the torsional stiffness and C the torsional damping of the low speed shaft.

46 The rotor inertia is automatically included via the structural beam definition of the rotor

Definition of Cables

Cable elements can be defined between the individual bodies of the turbine or between a body and the ground. If a cable is attached to a body the body position it is attached to is defined at a normalized curved body length. If a cable is attached to the ground the attachment position is defined as a global x,y and z coordinate. The following table 2.5 gives an example for a guy cable definition.

Table 2.5.: Exemplary definition of a guy cable via a cable input file

Body1	Body2	Density	Area	Iyy / Ixx	EMod	Pretension	Damping	Diameter	Drag	Nodes	Name Tag
"string"	"string"	$[\frac{kg}{m^3}]$	$[m^2]$	$[m^4]$	$[\frac{N}{m^2}]$	$[N]$	[-]	[m]	[-]	[-]	"string"
STR_1_1_1.0	TRQ_0.9631	8000	1.13E-04	1.01E-09	1.93E+11	15000	0.0019	0.012	0.99	4	B1TieRod3

In this example a cable is created between the top of the torque tube (as indicated by the body tag TRQ_1.0) and the ground at an x,y,z position of x=71.4, y=0 and z=0 (as indicated by the body tag GRND_71.4_0_0). For all cable elements the drag force component, normal to the cable direction, is included in the aeroelastic simulation by using the Diameter parameter to calculate the cables projected area and the Drag parameter as the cables drag coefficient. Thus, to disable the cable drag the Drag parameter can be set to zero. Cables can be attached to all bodies by using the following body tags:

- **BLD**_*X*_*Y*: Connection to **blade** ***X*** at the normalized curved length position ***Y***
- **STR**_*X*_*Y*_*Z*: Connection to **strut** ***X*** of **blade** ***Y*** at the normalized curved length position ***Z***
- **TWR**_*X*: Connection to the **tower** at the normalized curved length position ***X***
- **TRQ**_*X*: Connection to the **torque tube** at the normalized curved length position ***X***
- **GRD**_*X*_*Y*_*Z*: Connection to the **ground** at the global ***X*, *Y*, *Z*** coordinates

Definition of the Cross Sectional Properties of a Body

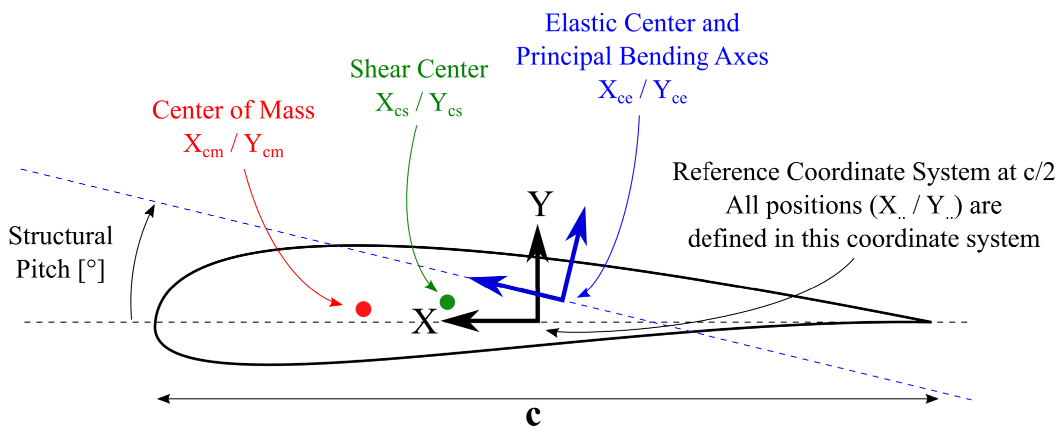

Figure 2.28.: The cross-sectional coordinate system, inspired by [164]

The cross sectional properties of the individual bodies are assigned in the coordinate system depicted in Figure 2.28. The reference coordinate system is located at the $\frac{c}{2}$ position on the airfoil chord-line (the center-line in case of a circular tower section). The distributed structural properties are defined for an arbitrary number of cross sections, distributed between the start and end points of the body. Table 2.6 gives an example for the cross sectional properties of a rotor blade. When the cross sectional properties of a tower are defined an additional column is appended to the table in which the section radius is defined. During the creation of the beam-elements the structural properties are linearly interpolated from the tabulated data based on the relative curved length position of the beam mid-point. An explanation of the structural parameters in the different columns is given in Table 2.7.

Further examples for structural input files can be found in the Appendix: NREL 5MW HAWT (see Appendix A.2) and the Sandia 34m VAWT (see Appendix A.3).

Table 2.6.: Exemplary table definition of cross-sectional properties

LENGTH	BMASSD	FLAP	EDGE	GJ	EA	RGX	RGY	RGZ	XCM	YCM	StrPitch	XCE	YCE	XCS	YCS	KX	KY
norm. by r	kg/m	Nm^2	Nm^2	Nm^2	N	norm. by c	norm. by c	norm. by c	norm. by c	norm. by c	degree	norm. by c	norm. by c	norm. by c	norm. by c	norm. by c	norm. by c
0.000	2332.393	1.183E+11	1.199E+11	3.655E+10	4.671E+10	0.346	0.348	0.510	-0.003	0.000	-0.004	-0.003	0.000	-0.003	0.000	0.540	0.542
0.010	2288.812	1.129E+11	1.144E+11	3.481E+10	4.587E+10	0.342	0.344	0.509	-0.003	0.000	-0.468	-0.004	0.000	-0.003	0.000	0.540	0.542
0.030	1322.691	4.017E+10	7.143E+10	1.834E+10	2.317E+10	0.289	0.371	0.479	-0.024	-0.001	-82.677	-0.030	-0.001	-0.035	0.001	0.545	0.508
0.050	1323.756	4.100E+10	6.739E+10	1.829E+10	2.230E+10	0.290	0.362	0.456	-0.014	0.000	-82.424	-0.021	0.000	-0.019	0.003	0.536	0.556
0.099	1021.587	2.592E+10	3.191E+10	7.536E+09	1.756E+10	0.237	0.270	0.332	0.034	0.008	-21.160	0.028	0.008	0.093	0.015	0.604	0.354
0.149	895.948	1.483E+10	3.098E+10	3.624E+09	1.543E+10	0.168	0.259	0.214	0.057	0.009	-4.733	0.058	0.008	0.155	0.019	0.547	0.270
0.199	776.138	9.643E+09	3.003E+10	2.165E+09	1.300E+10	0.135	0.256	0.167	0.073	0.008	-1.587	0.079	0.007	0.179	0.014	0.451	0.250
0.249	648.257	6.872E+09	2.369E+10	1.229E+09	1.068E+10	0.125	0.250	0.143	0.087	0.005	-0.778	0.096	0.004	0.196	0.012	0.324	0.267
0.323	539.802	4.957E+09	1.589E+10	6.973E+08	8.832E+09	0.126	0.243	0.129	0.099	0.004	-0.078	0.110	0.003	0.204	0.012	0.216	0.310
0.398	475.266	3.429E+09	1.053E+10	5.004E+08	7.992E+09	0.125	0.235	0.131	0.100	0.004	0.296	0.110	0.003	0.193	0.011	0.231	0.312
0.473	409.983	2.025E+09	6.383E+09	3.168E+08	7.153E+09	0.119	0.226	0.129	0.098	0.003	0.438	0.107	0.002	0.178	0.009	0.272	0.283
0.547	347.767	1.052E+09	3.682E+09	1.868E+08	6.294E+09	0.109	0.217	0.124	0.096	0.003	0.550	0.103	0.002	0.160	0.008	0.341	0.245
0.622	291.129	5.091E+08	2.068E+09	1.029E+08	5.450E+09	0.098	0.210	0.117	0.098	0.005	0.697	0.103	0.005	0.147	0.009	0.427	0.206
0.696	235.999	2.418E+08	1.115E+09	5.474E+07	4.520E+09	0.090	0.204	0.114	0.101	0.008	0.831	0.105	0.007	0.139	0.011	0.513	0.178
0.771	180.676	1.131E+08	5.866E+08	3.029E+07	3.489E+09	0.084	0.204	0.111	0.105	0.010	0.843	0.108	0.010	0.141	0.013	0.591	0.170
0.846	127.940	5.504E+07	2.893E+08	1.789E+07	2.454E+09	0.084	0.206	0.118	0.107	0.010	0.596	0.110	0.010	0.141	0.012	0.670	0.186
0.922	75.583	2.239E+07	1.161E+08	8.881E+06	1.398E+09	0.087	0.219	0.123	0.101	0.009	-0.093	0.105	0.008	0.146	0.011	0.734	0.220
0.978	29.664	2.726E+06	2.553E+07	1.359E+06	5.246E+08	0.075	0.265	0.122	0.062	0.012	-0.813	0.072	0.011	0.180	0.012	0.704	0.149
1.000	9.393	2.730E+05	5.083E+06	1.165E+05	1.734E+08	0.065	0.303	0.086	-0.003	0.014	-0.383	0.015	0.014	0.327	0.019	0.707	0.044

Table 2.7.: Definition of the structural cross-sectional data

Column	Variable	Explanation	Unit
1	**Length**	The curved length distance from the first body node normalized by the total body length	-
2	**Mass per unit length**	The mass per unit length (along the curved length)	$\frac{kg}{m}$
3	**Flapwise Stiffness**	The flap wise stiffness (torsion around X)	Nm^2
4	**Edgewise Stiffness**	The edge wise stiffness (torsion around Y)	Nm^2
5	**Torsional Stiffness**	The torsional stiffness GJ (torsion around Z)	Nm^2
6	**Longitudinal Stiffness**	The longitudinal stiffness EA (tension or compression along Z)	N
7	**Radius of Gyration X**	The radius of inertia corresponding to rotation around the elastic x-axis $I_{xx} = rg_x^2 * m$; normalized by chordlength (or diameter); **not used with Euler beams**	-
8	**Radius of Gyration Y**	The radius of inertia corresponding to rotation around the elastic y-axis $I_{yy} = rg_y^2 * m$; normalized by chordlength (or diameter); **not used with Euler beams**	-
9	**Radius of Gyration Z**	The radius of inertia corresponding to rotation around the principal beam (body z) axis) $I_{zz} = rg_z^2 * m$; normalized by chordlength (or diameter)	-
10	**Center of Mass X**	The center of mass X coordinate, defined in the reference coordinate system, normalized by chordlength (or diameter)	-
11	**Center of Mass Y**	The center of mass Y coordinate, defined in the reference coordinate system, normalized by chordlength (or diameter)	-
12	**Structural Pitch**	The structural pitch, angle between the reference X axis and the elastic X axis	$^\circ$
13	**Center of Elasticity X**	The center of elasticity X coordinate, defined in the reference coordinate system, normalized by chordlength (or diameter)	-
14	**Center of Elasticity Y**	The center of elasticity Y coordinate, defined in the reference coordinate system, normalized by chordlength (or diameter)	-
15	**Center of Shear X**	The center of shear X coordinate, defined in the reference coordinate system, normalized by chordlength (or diameter)	-
16	**Center of Shear Y**	The center of shear Y coordinate, defined in the reference coordinate system, normalized by chordlength (or diameter)	-
17	**Shear Factor X**	The shear factor for the force in principal bending axis X direction; **not used with Euler beams**	-
18	**Shear Factor Y**	The shear factor for the force in principal bending axis Y direction; **not used with Euler beams**	-
19	**Section Diameter**	The cross section diameter, needed in the tower and torquetube definition to calculate the tower drag and to scale the normalized properties	m
20	**Drag Coefficient**	**Optional:** Defines the drag coefficient to calculate aerodynamic drag on the tower or torquetube; set to 0 as default if not defined	m

The Global Coordinate System

All shown coordinate systems in QBlade are color coded. The x-axis is always shown in red, the y-axis in green and the z-axis in blue. The global coordinate system is shown in figure 2.29. The x-axis is pointing towards the downwind direction (in case of straight inflow), the z-axis points upwards into the vertical direction and the y-axis is constructed to form a right hand rule coordinate system. Some variables, such as positions or velocities are given in the global coordinate system. If a variable is given in the global coordinate system it is marked in the variable name by the letter *g* appearing after the variable type, such as 'X Pos. g'.

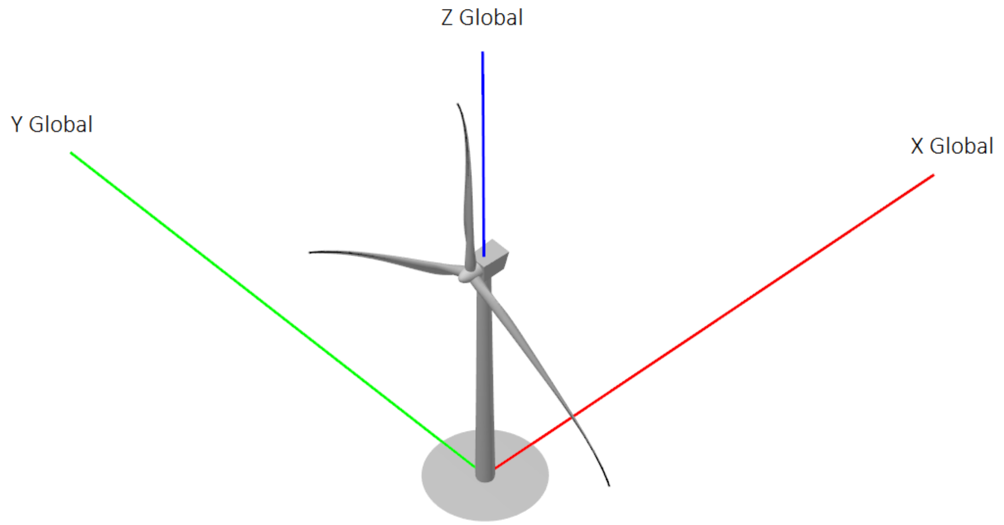

Figure 2.29.: The global coordinate system

Local Reference Coordinate Systems

The local coordinate systems in QBlade, such as the hub-, yaw- or shaft- or blade coordinate system are constructed according to the 'DNVGL Guildeline for the Certification of Wind Turbines' [196].

Local Body Coordinate Systems

Most forces and moments are given in the local body coordinate systems, which is indicated by the letter *l* appearing in the variable type, such as 'X Mom. l'. The local coordinate systems are fixed to their bodies, thus they translate (deflect) and rotate (rotor rotation or pitch) with their bodies. In the following the construction of the local body coordinate systems is briefly explained. Generally, the local coordinate systems are constructed according to the DNVGL Guideline [196]. In addition, Figure 2.30 gives an example of the local coordinate systems of a HAWT and a VAWT.

For all structural bodies (blades, struts, tower, cables) the z-axis is oriented along the principal direction of the beam element.

For the rotor blades and struts the x-axis is oriented in the chord wise direction, pointing towards the trailing edge and the y-axis is oriented normal to the chord, poiting towards the suction side. If the rotor is constructed to rotate in the reverse direction the y-axis is pointing towards the trailing edge instead.

For the tower the local x-axis is oriented along the global x-axis, the local y-axis is pointing towards the global y-axis and the tower z-axis points along the principal beam direction.

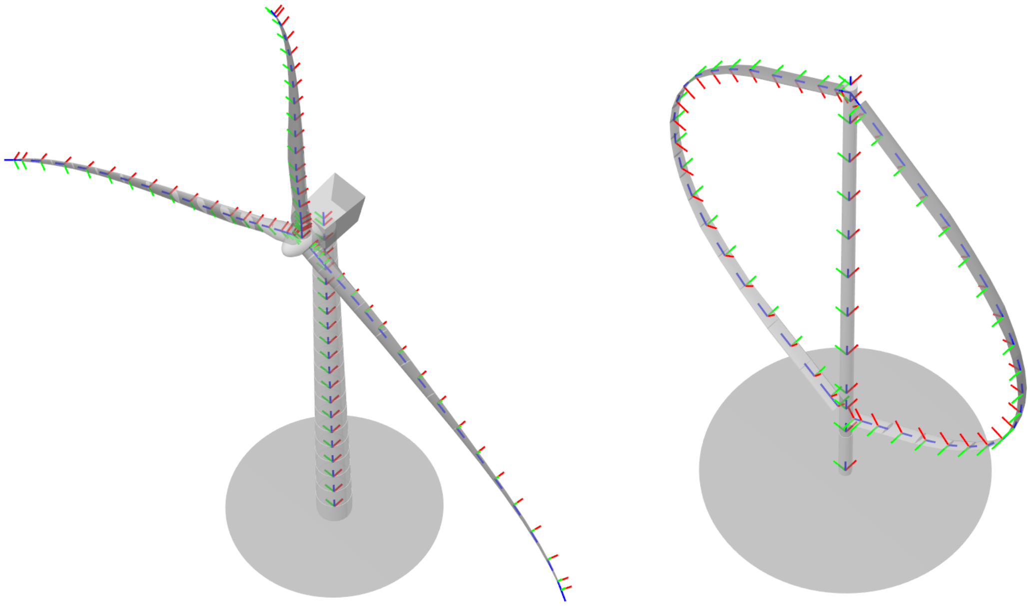

Figure 2.30.: The local body coordinate systems of a HAWT and a VAWT, X-Axis in RED, Y-Axis in GREEN and Z-Axis in BLUE

Loading Data and Loading Sensor Locations

An important feature for any structural simulation tool is the definition of locations at which the generated loading data is stored for a later evaluation. Depending on the type and design of the structure that is being simulated, the exact locations at which the critical loads are to be expected differ. Furthermore, it is not practical to store the loading data at every possible position due to the large amount of data that would be generated and the resulting requirements for storage. Thus, a simple methodology has been implemented into QBlade's input files, based on the concept of keywords to specify the position and type of data that will be stored during the simulation. The locations at which the data will be stored are defined through the following keywords that can be placed anywhere in the structural model input file:

- **BLD_**_X_Y_: Stores data for **blade *X*** at the normalized curved length position ***Y***
- **STR_**_X_Y_Z_: Stores data for **strut *Y*** of **blade *X*** at the normalized curved length position **Z**
- **TWR_**_X_: Stores data for the **tower** at the normalized curved length position ***X***
- **TRQ_**_X_: Stores data for the **torque tube** at the normalized curved length position ***X***
- **CAB_**_X_Y_: Stores data for **guy cable *X*** at the normalized curved length position ***Y***

Furthermore data is automatically stored at each inter body connection of the model. Each inter body connection is identified by a combination of two body name tags and a z value that gives the height position at which the connection was created during the model definition. In the following two exemplary auto-generated variable names are shown and explained:

Y l Mom. TRQ - BLD_3 z=29.7m
The moment around the local Y axis at the connection between the torque tube and blade 3, which was defined at a height of 29.7m. This result is given in the local coordinates of the torque tube since the TRQ tag is the first tag in the variable name.

X l For. STR_2_2 - BLD_2 z=27.5m
This example defines the local reaction force at the connection between the top strut of blade 2 and blade 2, given for the local X axis of the strut.

Nine different data types can be specified to be stored (*true*) or not (*false*) at **all** locations that are specified or automatically generated. These are:

- *true / false* **FOR_OUT**: Store the **local forces** for all locations
- *true / false* **MOM_OUT**: Store the **local moments** for all locations
- *true / false* **DEF_OUT**: Store the **local deflections** for all locations
- *true / false* **ROT_OUT**: Store the **local accumulated rotations** at all chosen locations
- *true / false* **POS_OUT**: Store the **global positions** for all locations
- *true / false* **VEL_OUT**: Store the **global velocities** for all locations
- *true / false* **ACC_OUT**: Store the **global accelerations** for all locations
- *true / false* **LVE_OUT**: Store the **local velocities** for all locations
- *true / false* **LAC_OUT**: Store the **local accelerations** for all locations

The forces and moments that obtained from a structural body are the **internal shear forces and bending moments**. However, the forces and moments given at an inter body connection can be interpreted as the **reaction forces and moments** acting on the constraint. As an example for the definition of output types and locations in an input file see Appendix A.2 and A.3.

2.5.4. Turbine Control

Full Supervisory Controllers

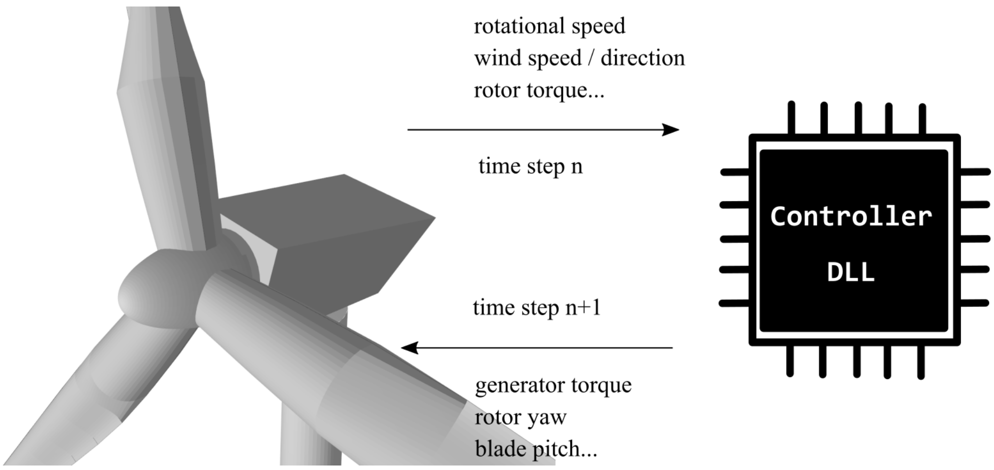

Figure 2.31.: Working principle of the controller integration

Turbine supervisory controllers can be integrated in two standard dynamic link library formats into the aeroelastic simulations. The DLLs can either be provided in the DTU format [197] or in the commonly used Bladed format [162]. Both controller formats perform a two-way exchange of data with a running simulation instance through pre-defined arrays. While the data that is required by the supervisory controller might vary, depending on the control strategy, the controller generally returns values for the blade pitch angle, the yaw angle and the generator torque which are then passed to the engine constraints of the structural model. If no controller library is added to a simulation the turbine operates at a pre-defined constant rotational speed.

Simulation Input Files

Often, to replicate an experiment or to perform parametric studies, the simulated turbine is required to execute a prescribed task, such as ramping up the rotational speed or performing prescribed pitch maneuvers. Such simulations can be setup using the 'Simulation Input File Format' (.sim). Using this format any of the following variables can be freely prescribed over time using ASCII based input files. The following list shows the variables that can be prescribed, starting with the first column, an exemplary input file can be found in the Appendix A.4:

- **TIME**: The time stamps [s] at which the variables are defined.
- **ROT SPEED**: The rotational speed of the rotor [rpm].
- **YAW ANGLE**: The rotor yaw angle [°].

- **BLA X PITCH**: The pitch angle [°] of blade X. One column is appended for each blade.
- **BLA X AFC Y**: The current state variable for the AFC element X of blade Y. One column is appended for each AFC element of each blade.

Prescribed Motion Files

A certain motion can be prescribed to the simulated wind turbine via the prescribed motion file format. The following list shows the variables that are included in the table of a motion file, an exemplary motion file can be found in the Appendix A.5:

- **TIME**: The time stamps [s] at which the variables are defined.
- **PLAT ROLL**: Roll rotation of the tower base (around global x)
- **PLAT PITCH**: Pitch rotation of the tower base (around global y)
- **PLAT YAW**: Yaw rotation of the tower base (around global z)
- **PLAT SURGE**: Surge translation of the tower base (along global x)
- **PLAT SWAY**: Sway translation of the tower base (along global y)
- **PLAT HEAVE**: Heave translation of the tower base (along global z)

The prescribed motion file format allows for a large flexibility in the type of simulations that can be performed. An example for its application was the investigation of the stability of a floating wind turbine by prescribing the platform motions [198][47]. Another example is the simulation of earthquake induced loads by prescribing the motion at the tower bottom (see Section 3.8).

2.5.5. Modal Analysis

A modal analysis can be performed on the assembled wind turbine structure by exporting the linearized tangent mass m, stiffness k, damping d and constraint Cq matrices of the assembled turbine structure from the Chrono system. The matrix export can be performed after the system has been setup or at any point during a time domain simulation. If the matrices are exported from a time domain simulation the geometric stiffness effects, caused by the rotation of the rotor, will be included in the tangent stiffness matrix. Furthermore, in an aeroelastic coupled simulation the stiffening effects of aerodynamic forces are included.

As the constraint matrix has to be included in the formulation of the eigenvalue problem an augmented stiffness, mass and damping matrix has to be created. These matrices take the form:

$$K = \begin{pmatrix} k & Cq' \\ Cq & 0 \end{pmatrix}; D = \begin{pmatrix} d & 0 \\ 0 & 0 \end{pmatrix}; M = \begin{pmatrix} m & 0 \\ 0 & 0 \end{pmatrix} \tag{2.35}$$

Once the augmented matrices have been assembled, a Generalized eigenvalue Problem (GEP) of the form:

$$Ax = \lambda Bx \tag{2.36}$$

47 One of the associated publications

is formulated. The matrices A and B are then assembled using K, D, M and the identity matrix I:

$$A = \begin{pmatrix} K & 0 \\ 0 & I \end{pmatrix}; B = \begin{pmatrix} D & M \\ I & 0 \end{pmatrix} \tag{2.37}$$

The GEP is then solved using the DGGEV [199] function of the LAPACK [200] library. After the GEP has been solved the resulting mode shapes are ordered by frequency and can be visualized. Performing the modal analysis at different rotational speeds of the turbine allows the generation of a Campbell diagram. A thorough validation of the modal analysis feature has been carried out and was published in [201][48] and Publication III, see Section 3.2.

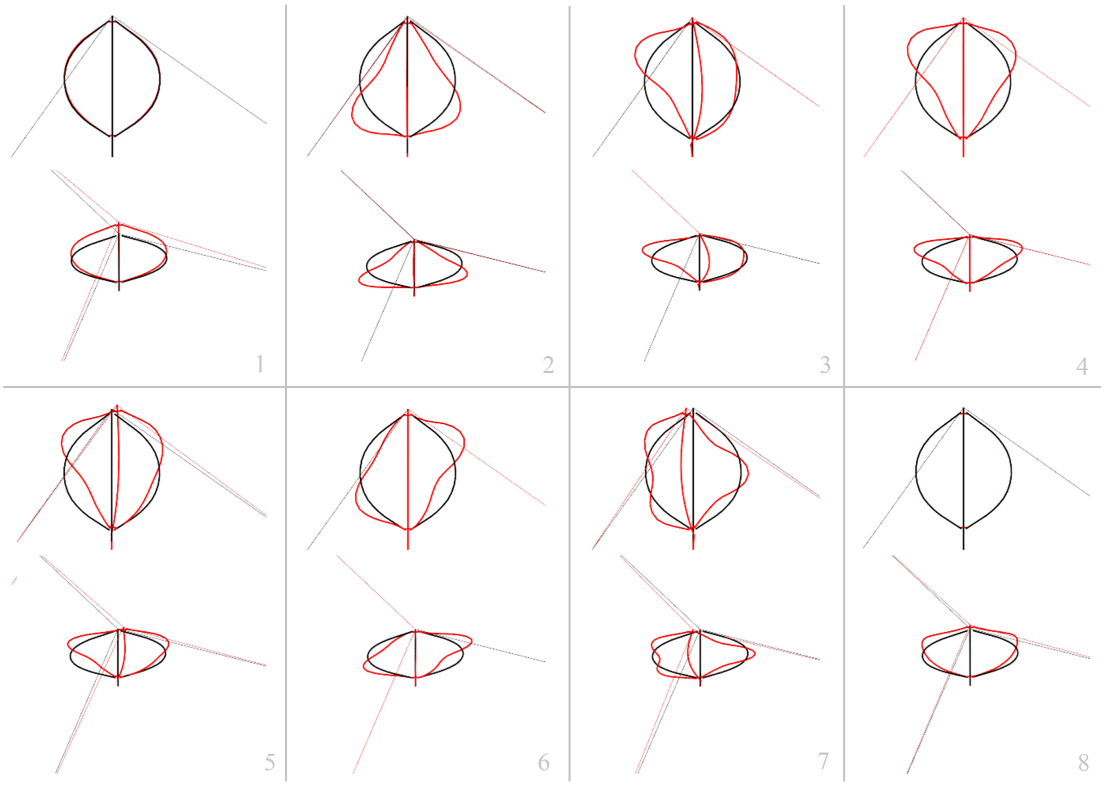

Figure 2.32.: The first 8 mode shapes of the non-rotating SANDIA 34m turbine, showing reference geometry in black and mode shape in red

48 One of the associated publications

2.5.6. Time Integrators and Solver for the Structural Dynamics Simulation

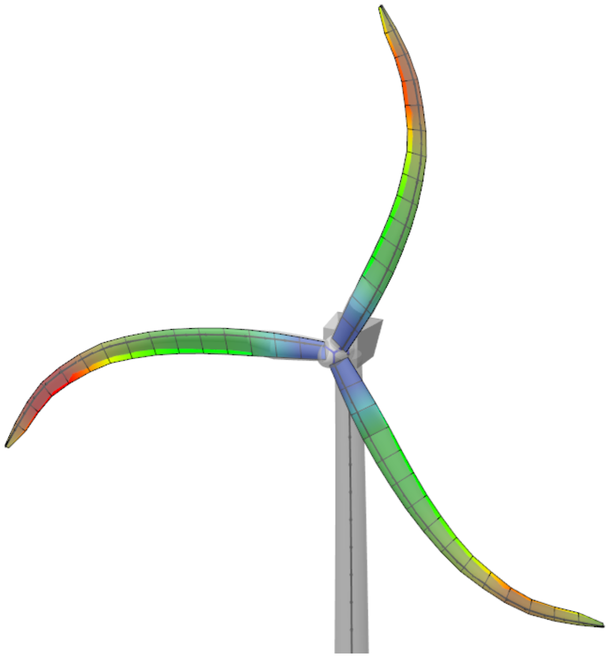

Figure 2.33.: Strong blade deformations caused by inertial forces from the impulsive startup of the rotor

Various factors influence the overall contribution of the structural model to the total computational cost of an aeroelastic simulation. The size of the problem matrix is proportional to the number of degrees of freedom that the system contains. Each main component (blades, struts, tower) of the assembled turbine can be discretized with an arbitrary number of structural nodes, where each node adds 6 degrees of freedom to the system matrix. A sensitivity analysis of the influence of structural discretization of the turbine components on the estimated modal frequencies was carried out in Publication III (see Section 3.2) of this thesis. Clearly, the total contribution of the structural model evaluations to the overall computational cost scales with the time step size of the structural evaluations. Due to the loose coupling method that is being employed the time step size can be set independently of that of the aerodynamic calculations. Depending on the structural model that is being simulated, the size of the aerodynamic time step and the type of time integrator used for the structural simulation, sub time steps might be necessary for the structural simulation before advancing with the aerodynamic simulation step.

In the Chrono library the multi-body FEA problem is formulated as a *Differential Variational Inequality* (DVI) problem. At each time step of the structural simulation the DVI problem is solved using the EIGEN SparseLU solver[49], which is included in the EIGEN C++ template library [194]. The structural simulation is then advanced using a time integrator of choice. Several different time integrators [202] are available in Chrono, however only the iterative HHT (Hilber-Hughes-Taylor formulation) has proven its usability within the current integration of Chrono in QBlade. While other, non-iterative, integrators suffer from constraint drifts or require very small timesteps to yield reasonable results the HHT integrator shows good performance for structural time steps in the range of 3°azimuthal rotor increments.

49 In former versions of QBlade the MKL PARDISO solver was used instead of the SparseLU solver, however the MKL libraries have been removed from the repository to facilitate the cross-compatibility of QBlade

2.6. Aero-Elastic Coupling

As mentioned in Section 2.1.4, a loose coupling approach is employed for the co-simulation using the aforementioned aerodynamic and structural dynamics models. Generally the LLFVW aerodynamics model runs at a time step size that is equivalent to 5° to 10° rotor advancement. While the structural model itself is highly robust for larger time step sizes, the integration of the supervisory controller and the associated actuators and their actuation ranges and frequencies require slightly smaller time steps for the structural model[50]. Figure 2.34 shows the flowchart for one complete aeroelastic time step:

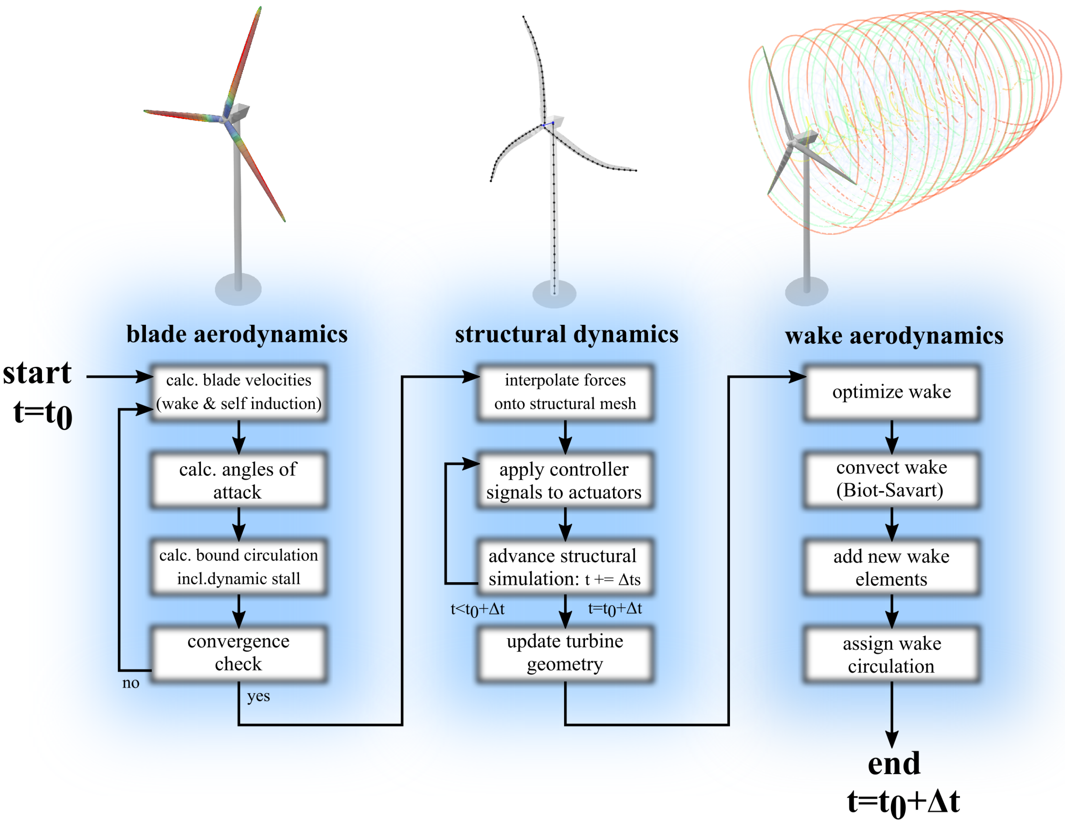

Figure 2.34.: Flowchart for one time step of the aeroelastic model in QBlade

- The simulation starts at the time $t = t_0$. At first, the iteration to find a converged circulation distribution for the bound vorticity of the rotor blade is carried out. In this evaluation, the expensive step of calculating the wake induced velocities for the rotor panels is only carried out once at the beginning of the iteration, as the wake shape remains fixed during the iteration. During this iteration, in the calculation of the blade panels lift and drag characteristics, the unsteady aerodynamics model (Section 2.4.4) and other corrections, such as Snel's correction (Section 2.4.7) are applied. Once a converged solution for the bound circulation is obtained, the blade aerodynamics calculations are finished.

50 In the range of 2° to 5° of rotor advancement

- The blade panel forces and moments, resulting from the associated airfoils lift-, drag- and moment characteristics, are interpolated from the aerodynamic discretization (panels) onto the structural dynamics discretization (beam elements). Furthermore, the controller signals are applied onto the actuators. The simulation is now advanced with the structural time step Δt_s. If the current simulation time has reached $t = t_0 + \Delta t$, the structural dynamics simulation is finished. If $t < t_0 + \Delta t$ the structural simulation is incremented again with Δt_s, applying new controller signals and rotating the aerodynamic forces and moments[51] with the incremental rotor advancement. This is repeated until the simulation time has reached $t = t_0 + \Delta t$. Now, the current positions of all beam elements and rigid bodies are interpolated back onto the aerodynamic mesh and the aerodynamic model is advanced onto its final position for this time step.

- In the last step the wake is updated. The wake discretization is optimized by removing or lumping wake elements, using the various methods that are outlined in Section 2.4. Now, the wake is updated by evaluating the self-induced wake velocities at the wake nodes, updating the vortex core sizes (see Section 2.4.3) and advancing the wake element positions with Δt using one of the implemented time integrators (see Section 2.4.1). The gap that now exists between the new wake positions and the advanced rotor blade positions is 'filled' with new shed and trailing wake elements. Finally, the circulation of the newly created wake elements is assigned using the Kutta condition.

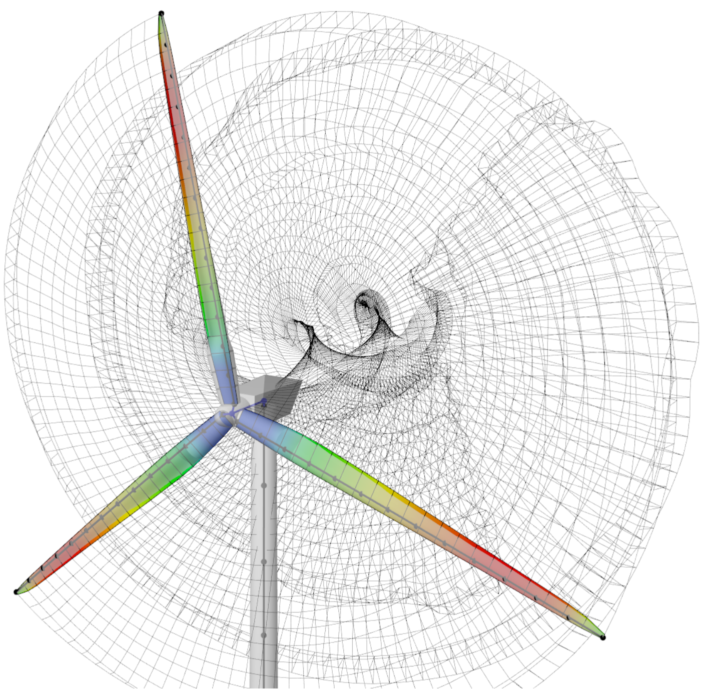

Figure 2.35.: Visualization of the coupled, aero-elastic model, showing vortex filaments, structural elements and nodes

51 These forces remain constant during the structural sub time steps

2.6.1. Performance Metrics

One of the main goals of this work was to optimize the computational efficiency of the aeroelastic model to facilitate its applicability in the context of wind turbine design and certification. Combining the leverage of wake lattice connectivity ($f_{opt} \approx 2$), wake reduction ($f_{opt} \approx 2$), wake coarsening ($f_{opt} \approx 10$) and massive GPU parallelization ($f_{opt} \approx 1000$), the overall reduction in computational cost of the aerodynamic model, compared to a baseline sequential evaluation without any wake optimization is in between four to five orders of magnitude ($f_{opt,combined} \approx 40000$). The coupling with the highly efficient state of the art structural dynamics model of the Chrono library allows the resulting aero-servo-elastics model of QBlade to be applied within the context of design and certification without a need for high performance simulation clusters. Table 2.8 shows the hardware on which the following performance metrics were calculated.

Table 2.9 shows the performance relevant parameters of the aeroelastic simulation that was carried out (see Figure 2.36:left). In total 630s of real time were simulated, which is the typical length for a design load case (DLC) evaluation. This leads to an overall evaluation of 9000 aerodynamic and structural time steps. The maximum number of wake elements, that is reached after 9 rotor revolutions, is 13400 with 7000 wake nodes, leading to $\approx 10^8$ evaluations of the Biot-Savart equation per wake convection step.

Table 2.8.: Hardware specification of the workstation used to obtain the performance metrics

OS	MS Windows 10 Pro, 64-Bit
CPU	Intel Core i9-9900K, 3.6GHz
GPU	NVIDIA Quadro P6000, 4840 CUDA Cores, 24GB RAM
RAM	64GB

Table 2.9.: Relevant simulation parameters for the calculation of the performance metrics

Parameter	**Value**
Wind turbine	NREL 5MW [203]
Inflow	V mean = 13m/s, 16% turbulence, shear exponent 0.2
Simulated time	630s
Aerodynamic time step size	0.07s (5°azimuth)
Structural dynamics time step size	0.07s
Total aeroelastic time steps	9000
Blade discretization	20 panels, sinusoidal spacing
Average number of wake elements	17000
Near-, mid-, far wake length	$l_1 = 0.5$, $l_2 = 2.5$, $l_3 = 3$, $l_4 = 3$,$f_2 = 2$, $f_3 = 2$, $f_4 = 2$
Wake reduction factor	0.01
Number of structural blade nodes	15
Number of structural tower nodes	10
Structural DoF	441

Figure 2.36:right shows the computational time needed per time step for the individual simulation parts: blade aerodynamics, wake aerodynamics and structural dynamics, with time steps according to Table 2.9. The computational cost for the wake calculations is initially growing

quickly (Figure 2.36:right) until the wake truncation starts after 9 revolutions of the rotor (see Figure 2.36:left) and the number of wake elements and nodes remains constant. Overall the individual computational costs are within the same order of magnitude. Looking at Figure 2.37 it can be seen that, due to the wake optimization techniques applied, the wake calculations require roughly the same computational time as the structural calculations.

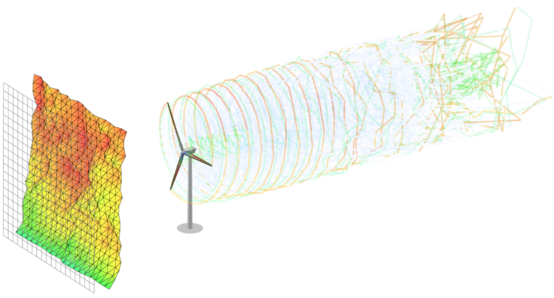

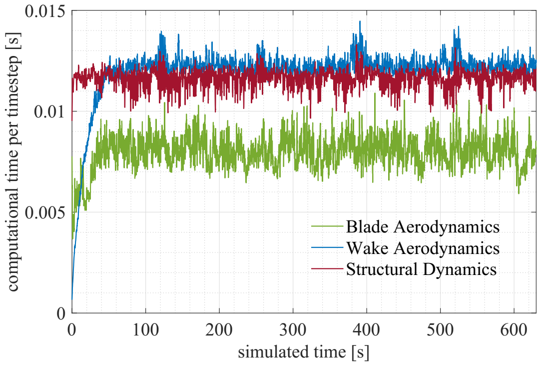

Figure 2.36.: Left: snapshot of the simulation; right: computational cost per time step for the aerodynamic and structural evaluations

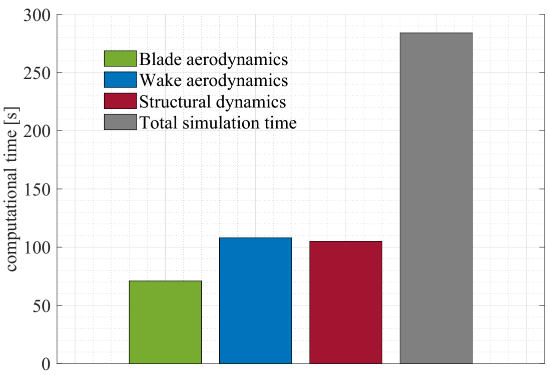

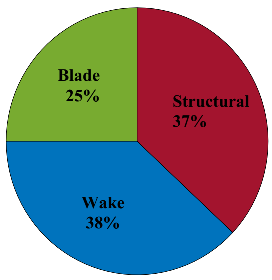

Figure 2.37.: Total simulation time and contributions of the blade aerodynamics, wake aerodynamics and structural dynamics evaluations

The total elapsed CPU time (see Figure 2.37) for the 630s simulation was 283s, resulting in a ratio of $T_{real}/T_{cpu} \approx 2$, which means that the simulation is around 2 times faster than real time. The demonstrated computational efficiency permits the use of the aero-servo-elastic co-simulation in QBlade for design and certification of horizontal- and vertical axis wind turbines. In addition, the time needed for the evaluation of a complete DLC set can be further reduced by distributing the individual DLC evaluations onto a cluster of workstations. It is also important to note that, due to the aerodynamic time discretization being fixed between 5° to 10° increments of rotor advancement, the ratio $T_{real}/T_{cpu} \approx 2$ even increases for larger turbines with lower rotational speeds[52].

52 Compared to the NREL 5MW [203] turbine from this example

2.7. Publication I: Implementation, Optimization, and Validation of a Nonlinear Lifting Line-Free Vortex Wake Module Within the Wind Turbine Simulation Code QBlade

Marten, D., Lennie, M., Pechlivanoglou, G., Nayeri, C. N., & Paschereit, C. O. (2015). Implementation, Optimization, and Validation of a Nonlinear Lifting Line-Free Vortex Wake Module Within the Wind Turbine Simulation Code QBlade. Journal of Engineering for Gas Turbines and Power, 138(7), 072601. https://doi.org/10.1115/1.4031872

This publication concerns the first integration of the Lifting Line Free Vortex Wake (LLFVW) algorithm into the QBlade code. Some of its content has already been discussed in Section 2.4.

It was decided to include the up-to-date description of the LLFVW implementation in Section 2.4 in this thesis as some of the methods presented in this publication were abandoned or revised. As an example: the wake lumping procedure, presented in this publication, works well with HAWT, however it is not applicable for VAWT, due to the large influence of shed induction which would get lost in the lumping process. Thus, it was decided to discontinue the lumping procedure and replace it with the wake coarsening method, presented in Section 2.4.12, that works for both HAWT and VAWT. Additionally, the vortex core growth parameters, that are discussed in this publication, have been reformulated into more tangible variables (see Section 2.4.3).

This publication gives a detailed overview of the iteration process for the bound circulation and furthermore includes some validation results against experimental data from the PhaseVI [204] and MEXICO [205] experiments.

David Marten[1]
Chair of Fluid Dynamics,
Hermann-Föttinger-Institut,
Technische Universität Berlin,
Müller-Breslau-Str. 8,
Berlin D-10623, Germany
e-mail: david.marten@tu-berlin.de

Matthew Lennie
Chair of Fluid Dynamics,
Hermann-Föttinger-Institut,
Technische Universität Berlin,
Müller-Breslau-Str. 8,
Berlin D-10623, Germany

Georgios Pechlivanoglou
Chair of Fluid Dynamics,
Hermann-Föttinger-Institut,
Technische Universität Berlin,
Müller-Breslau-Str. 8,
Berlin D-10623, Germany

Christian Navid Nayeri
Chair of Fluid Dynamics,
Hermann-Föttinger-Institut,
Technische Universität Berlin,
Müller-Breslau-Str. 8,
Berlin D-10623, Germany

Christian Oliver Paschereit
Chair of Fluid Dynamics,
Hermann-Föttinger-Institut,
Technische Universität Berlin,
Müller-Breslau-Str. 8,
Berlin D-10623, Germany

Implementation, Optimization, and Validation of a Nonlinear Lifting Line-Free Vortex Wake Module Within the Wind Turbine Simulation Code QBLADE

The development of the next generation of large multimegawatt wind turbines presents exceptional challenges to the applied aerodynamic design tools. Because their operation is often outside the validated range of current state-of-the-art momentum balance models, there is a demand for more sophisticated, but still computationally efficient simulation methods. In contrast to the blade element momentum method (BEM), the lifting line theory (LLT) models the wake explicitly by a shedding of vortex rings. The wake model of freely convecting vortex rings induces a time-accurate velocity field, as opposed to the annular-averaged induction that is computed from the momentum balance, with computational costs being magnitudes smaller than those of a full computational fluid dynamics (CFD) simulation. The open source code QBLADE, developed at the Berlin Institute of Technology, was recently extended with a lifting line-free vortex wake algorithm. The main motivation for the implementation of an LLT algorithm into QBLADE is to replace the unsteady BEM code AERODYN in the coupling to FAST to achieve a more accurate representation of the unsteady aerodynamics and to gain more information on the evolving rotor wake and flow-field structure. Therefore, optimization for computational efficiency was a priority during the integration and the provisions that were taken will be presented in short. The implemented LLT algorithm is thoroughly validated against other benchmark BEM, LLT, and panel method codes and experimental data from the MEXICO and National Renewable Energy Laboratory (NREL) Phase VI tests campaigns. By integration of a validated LLT code within QBLADE and its database, the setup and simulation of LLT simulations are greatly facilitated. Simulations can be run from already existing rotor models without any additional input. Example use cases envisaged for the LLT code include: providing an estimate of the error margin of lower fidelity codes, i.e., unsteady BEM, or providing a baseline solution to check the soundness of higher fidelity CFD simulations or experimental results. [DOI: 10.1115/1.4031872]

Introduction

The BEM method, developed by Froude in 1878, is still the main tool for rotor blade design that is used by the industry. While it is a robust, well proven, and computationally highly efficient method, it is built upon many assumptions and, therefore, has its limitations. The momentum balance, that is used to model the wake by equating rotor forces with flow momentum, to compute the induction on the rotor, is only formulated in 1D at each annular ring on the rotor disk. The rotor disk itself is assumed to experience a steady, uniform inflow and has to be oriented perpendicular to the flow direction.

To overcome these and other limitations, many empirical corrections have been introduced to the original BEM theory, which expand its application to unsteady or yawed inflow, account for tip and hub losses, or introduce a time lag to the momentum equations which otherwise can only model the stationary equilibrium of a fully developed rotor wake. These corrections are usually derived from experimental investigations, more sophisticated simulations, or theoretical considerations. However, these empirical corrections introduced to the BEM theory do not model the unaccounted flow phenomena directly, but are rather a pre-, post-, or on-the-fly correction that is performed on the simulation results of this method. This also implies that there are cases in the operational range of the wind turbine rotor where these corrections have no validity or break down.

As an example, in a turbulent inflow the averaging of velocities over annular rings to calculate the rotor induction with momentum theory does strictly violate the conservation of momentum in the flow and consequently introduces errors.

However, due to the fact that the BEM has a high computationally efficiency, because of its simplicity, it is still the industry's favored tool to calculate the aerodynamic forces during wind turbine load calculations. Examples for the application of the unsteady BEM are the widely used tools FAST (AERODYN) [1], HAWC [2], PHATAS [3], or BLADED [4].

As an alternative to the BEM, vortex methods can model the wake with far less assumptions and a much higher physical soundness. Computational costs are still magnitudes lower compared to CFD simulations, which is essential for the load calculations that are needed for a wind turbine certification.

These vortex methods model the blade forces either with a lifting line (lift and drag polar data to compute forces at the quarter chord line), vortex lattice method (infinitely thin discrete vortex sheets represent blade geometry), or boundary element method (discretization of 3D blade surface with a no penetration boundary condition). Independent of the blade representation, the wake is modeled with discrete vortex elements (line or point vortices) that are shed at the trailing edge (TE) during every time-step. These vortex elements either move on a prescribed path or are convected freely with the flow and induced velocities.

[1]Corresponding author.
Contributed by the Turbomachinery Committee of ASME for publication in the JOURNAL OF ENGINEERING FOR GAS TURBINES AND POWER. Manuscript received August 26, 2015; final manuscript received September 30, 2015; published online December 4, 2015. Editor: David Wisler.

The advantage of this wake treatment, compared to the BEM, is that the calculation of the induction from the wake is not limited to an annular-averaged rotor disk, but can be accurately calculated at any point in the computational domain during every time-step. In addition to that, the wake always contains the history of the flow (vortex elements from previous time-steps), which gives the ability to simulate transient events with a much higher accuracy than the BEM.

Exemplary for these effects of the different rotor wake treatments, a comparison between experimental results from the MEXICO rotor [5], an unsteady BEM simulation (using AERODYN), and a lifting line-free vortex wake simulation (using both the same lift and drag polar data) is shown in Fig. 1. The outcome of the lifting line simulation is, both in phase and amplitude, in much better agreement with the experimental data. The yaw correction inside the BEM simulation reproduces the normal force variation with a much larger error.

QBLADE: A Wind Turbine Aerodynamics Tool

This significant difference in accuracy between the BEM and the LLT is the driving motivation to integrate an LLT algorithm within the open source wind turbine design and simulation tool QBLADE [6,7]. The software, in its current state of development, already covers a broad spectrum of lower order analysis techniques that are specific for wind turbine blade design and aerodynamic or aeroelastic analysis. The modules currently implemented are

- 2D airfoil design
- 2D airfoil analysis with viscous/inviscid XFOIL code [8]
- 360 deg polar extrapolation after Montgomerie [9] or Viterna and Janetzke [10]
- rotor design and simulation with steady-state BEM
- structural blade design with Euler Bernoulli Beam [11]
- turbulent wind field generator using the Veers method [12]
- integration of FAST [13] and AERODYN [1] for aeroelastic simulations

Through the combination of 2D airfoil design and analysis, 360 deg polar extrapolation, and a graphical user interface, rotor blades can be designed by distributing airfoils and polars or imported from a wide number of formats and stored in a runtime database. The blade definition, as it is implemented for the BEM analysis in QBLADE, already carries all the data that are necessary for LLT simulations. This greatly facilitates the setup of LLT simulations. An LLT algorithm will be implemented into QBLADES' database and user interface to take full advantage of this existing infrastructure, which also includes dynamic graphs and an OpenGL viewer, which will be used for the postprocessing of simulation results.

Nonlinear Lifting Line-Free Vortex Wake Algorithm

The LLT algorithm implemented in QBLADE generally follows the work carried out by van Garrel during the development of ECN's AWSM code [14]. During the integration with QBLADE, this algorithm was implemented in the cross platform C++ framework Qt.

The rotor is represented by a lifting line, located at the quarter chord points on the midchord of the 2D airfoil sections (see Fig. 2). Each blade panel is represented by a ring vortex that consists of four vortex line elements.

The circulation of the bound vortex lines on the lifting line is calculated from the relative inflow velocity and the lift and drag coefficients that are obtained from the tabulated airfoil data. According to the Kutta–Joukowski theorem, the circulation is given by

$$\partial C_L(\alpha) = \rho \ V_{\text{rel}} \times \partial \Gamma \qquad (1)$$

The relative velocity, V_{rel}, is a simple vector addition of the free stream velocity V_∞, the blade motion V_{mot}, and the induced velocity V_{ind}, which is calculated from the contribution of all vortex elements through the Biot–Savart equation

$$V_{\text{ind}}(x) = -\frac{1}{4\pi}\int \Gamma \frac{\mathbf{r} \times \partial \mathbf{l}}{r^3} \qquad (2)$$

At the beginning of each time-step the algorithm iterates to find a converged circulation distribution for the bound vortices on the lifting line that matches the lift and drag coefficients obtained

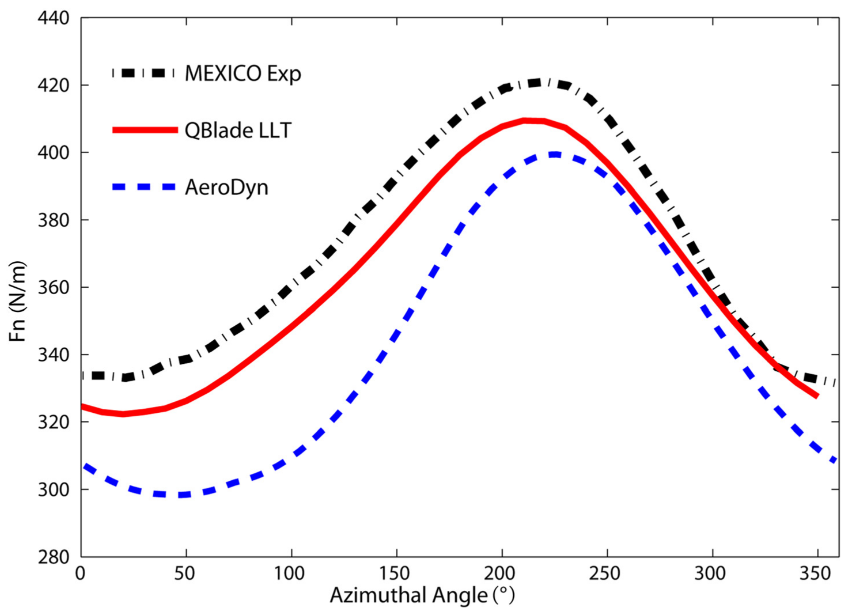

Fig. 1 Azimuthal variation of normal force at 82% radius of the MEXICO rotor operating in 30 deg yaw, 3 deg pitch, and 424.5 rpm

with the induced angle of attack (AoA). After convergence is obtained, the rotor is rotated and all free vortex elements are convected with the local inflow and local induced velocity. Two different schemes for the wake convection step are implemented from which one has to be selected before starting a simulation. As a first-order method, the simple Euler forward integration scheme is implemented

$$\mathbf{x}_{t+1} = \mathbf{x}_t + (V_\infty + V_{\text{ind}}(\mathbf{x}_t))\Delta t \tag{3}$$

A predictor corrector method that re-evaluates the induced velocity, based on the predicted position (Eq. (3)), is implemented as a second-order integration method

$$\mathbf{x}_{t+1,\text{cor}} = \mathbf{x}_t + \left(2V_\infty + V_{\text{ind}}(\mathbf{x}_t) + V_{\text{ind}}(\mathbf{x}_{t+1})\right)\frac{\Delta t}{2} \tag{4}$$

The downside of the second-order method is that two velocity field evaluations have to be performed during each time-step, effectively doubling the simulation time. However, in contrast the obtained accuracy is higher, especially in the far wake region where vortex nodes have been convected over several time-steps. The second-order accuracy of the predictor–corrector method also allows selecting a larger time-step size as compared to the first-order method while still maintaining acceptable accuracy.

After the convection step, new vortex elements are released between the TE of each blade panel and the last row of wake vortices which were convected from the TE. As a last step, the circulation is computed and assigned to the new released vortex lines through the Kutta condition

$$\Gamma_{\text{trail}} = \frac{\partial \Gamma_{\text{bound}}}{\partial x}\Delta x \tag{5}$$

$$\Gamma_{\text{shed}} = \frac{\partial \Gamma_{\text{bound}}}{\partial t}\Delta t \tag{6}$$

Equation (5) implies that for stationary simulations, such as the computation of power output for single operational points with constant inflow, the circulation of the shed vortices approaches zero when the wake is fully developed. To speed up the simulation for these cases, it is optional to include shed vortex line elements in a simulation. Figure 3 shows the different steps that are carried out during one time-step in a flowchart.

In this paragraph, the implemented LLT algorithm was only presented in very brief to give a general overview. A far more detailed description of the integration of an LLT algorithm can be found in Ref. [15] or [16].

Details of the LLT Implementation

One focus during the implementation of the LLT algorithm was versatility and flexibility. Therefore, all simulation parameters are free and may be defined from the user within an input mask. In the following subsections, Vortex Modeling, Tower Shadow Effect, and Turbulent Wind Fields, some light will be shed on important details of this implementation and the various parameters that have to be set.

Vortex Modeling. The Biot–Savart equation (Eq. (2)) exhibits a singularity at the core where $\mathbf{r} = 0$ (see Fig. 4). To prevent this singularity from affecting the simulation and also to model the viscous core of the bound and free vortices more accurately, a model for a viscous vortex core needs to be implemented. Many different models, to describe the tangential velocity distribution around the core exist, such as the Rankine, Lamb–Oseen, or Ramsey and Leishman models [17]. Van Garrel suggests in his report [15] to use a cut-off radius δl_0 that is simply added to the denominator of Eq. (2) in the form of $(\delta l_0)^2$ and ensures that the induced velocity smoothly approaches zero in the vicinity of the core. l_0 is

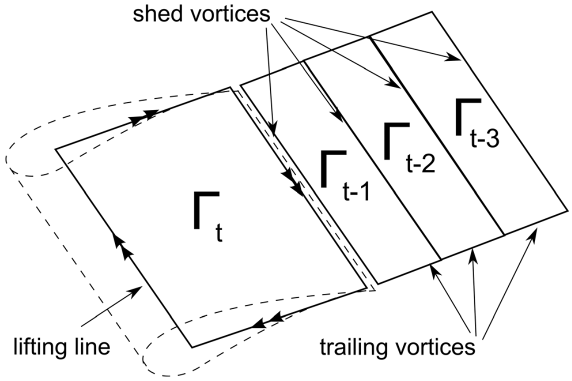

Fig. 2 Geometry of a blade panel, position of the lifting line, and shed and trailing vortex line elements

the length of the vortex element for which the induced velocity is computed and δ the fraction of this length that makes up the radius of the viscous vortex core. This is a very elegant and computationally efficient implementation, because the viscous core modeling is directly implemented in the calculation of the induced velocity. For all other vortex models, a viscous parameter needs to be evaluated whenever the Biot–Savart equation (Eq. (2)) is computed (the driver for computational cost of the LLT), which is considerably slowing down the performance. For this reason, van Garrel's cut of radius approach is implemented. However, instead of using a cut of radius in the form of δl_0, which depends on the length of each vortex element, a method to compute the core radius independent of the vortex length is implemented. The reasoning here is that a core size, depending on the elements length, can lead to very high induced velocities in the vicinity of the singularity when the vortex elements length (and so its core radius) is very small—which is a problem for cases of very fine azimuthal or spanwise discretization. In Eq. (7) (from Ref. [16]), the core size is computed independent of the vortex elements length, also it captures the change of vortex core size due to vortex stretching and viscosity. Once during every time-step the core size is computed for every vortex element

$$r_c = \left[\frac{4a \cdot \delta_v \cdot \nu \cdot (t_v + S_c)}{1+\varepsilon}\right]^{\frac{1}{2}} \tag{7}$$

where a is a constant ($a = 1.25643$), δ_v is the turbulent viscosity coefficient which depends on turbine size and has values ranging from 10 to 1000, ν is the kinematic viscosity, S_c is a time offset parameter, (the influence of δ_v and S_c on r_c is shown in Fig. 5) to prevent initial core sizes of zero, t_v is the vortex age, and ε is the strain rate of the vortex element and computed as

$$\varepsilon = \frac{\Delta l}{l} \tag{8}$$

Tower Shadow Effect. To model the effect of the tower on the upstream or downstream rotor, a model, based on the analytical solution of the potential flow around a cylinder with an added model for the downwind wake, is integrated in the LLT. Whenever the tower influence has to be evaluated at a point in the computational domain, the analytical solution for this potential base flow (in Cartesian coordinates) is made dimensionless with the total velocity (inflow velocity and induced velocity) at the evaluation point and is rotated to face into the inflow direction. The tower influence then is calculated in the rotated coordinate system and after evaluation rotated back into the global coordinate system and superimposed on the flow. An example plot showing the velocity magnitude around the tower that is computed using this

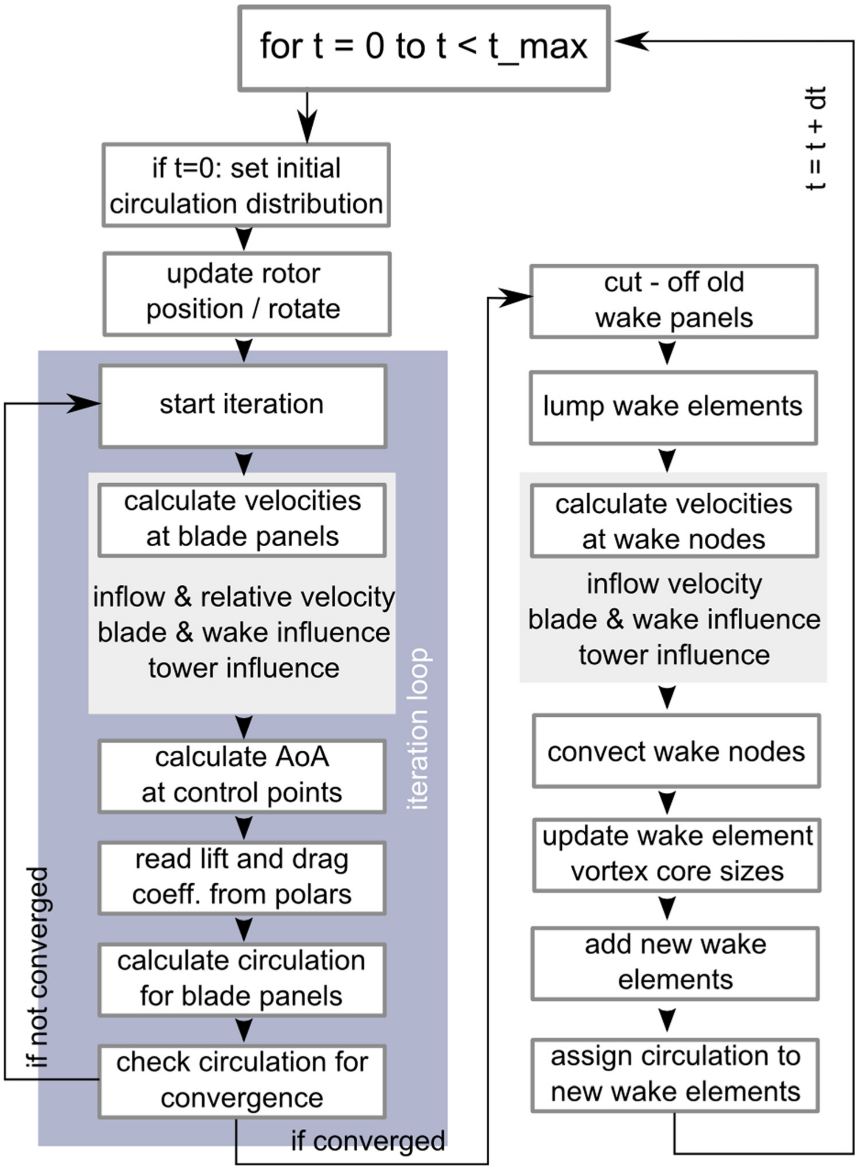

Fig. 3 Flowchart of implemented LLT algorithm for one time-step

method is shown in Fig. 6. More information on the formulas that were used for the tower model and their derivation is described in detail in Ref. [1]. Figure 7 exemplarily shows the effect of the tower model on the simulation results, in this case the power coefficient of a rotor that is undergoing a step change in inflow velocity. The free parameters to set for this tower model are the highest z-coordinate of the tower (the rotor hub is at $z = 0$), the tower radius, the x- and y-position of the tower center, and the tower drag coefficient.

Turbulent Wind Fields. QBLADE includes a generator for correlated, three-dimensional, turbulent wind fields using the Veers method [12]. These wind fields can be included in an LLT simulation. The wind fields can be thought of as a stack of planes with a velocity distribution on each. Each plane represents the wind field at one point in time. In between its spatial grid and temporal points, the wind field is interpolated. During every time-step of the simulation, the wind field is marched through the domain (see Fig. 8) by the mean inflow velocity at hub height. Frozen turbulence is assumed for this treatment. Initially, before the simulation starts, the wind field is already shifted by half of its width behind the rotor plane. This is done, so that even in cases of yaw, the rotor is fully submerged in the wind field during the first time step. During the setup of a simulation, the user can choose if the turbulence in the wind field should only affect the velocities that are computed on the rotor while the wake elements are convected with the mean flow speed. The other option is to use turbulent wind field also for convection of the wake vortices, which, especially for higher levels of turbulence, leads to a relative quick distortion of the wake structure.

Optimization for Computational Efficiency

The driving factor for the computational cost of the LLT method is the number of free line vortex elements in the wake.

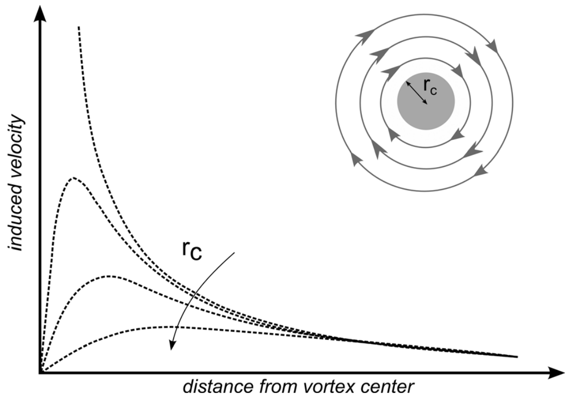

Fig. 4 The qualitative effect of vortex core size on the induced velocity

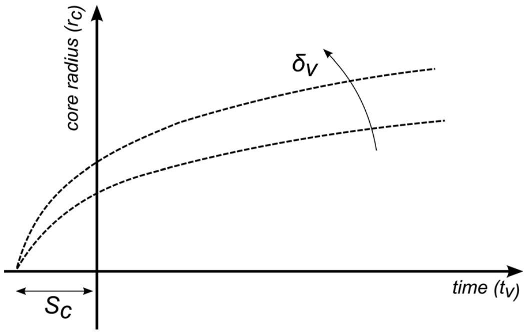

Fig. 5 The qualitative effect of turbulent viscosity and time offset on the vortex core size

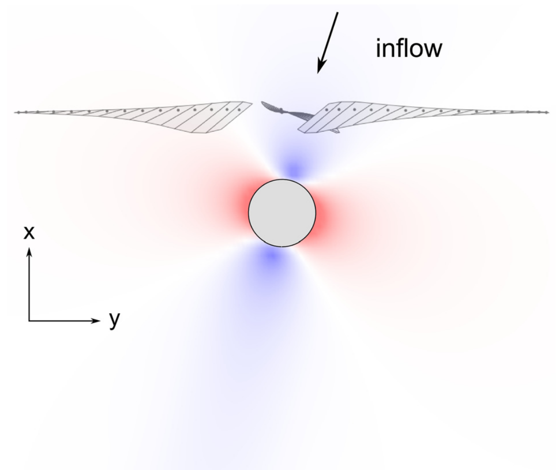

Fig. 6 Qualitative sketch of tower influence on velocity field at 15 deg skewed inflow showing areas of flow stagnation and speedup

The free wake consists of line vortex elements and vortex nodes, which mark the end points of the vortex elements. During every time-step each vortex node is convected by evaluating the induced velocities of all line vortex elements at the nodes position with Eq. (2). Because this number is growing over time, as more and more vortex elements are shed from the TE, the cost of evaluating the Biot–Savart equation eventually outperforms the cost of iterating for a converged solution of circulation of the bound vortices and the rest of the overhead calculations during runtime. Therefore, after a couple of rotor revolutions—when the wake starts to develop, the computational cost is approximately proportional to the number of vortex elements multiplied by the number of vortex nodes

$$\mathrm{CPU}_{\mathrm{cost}} \sim N_{\mathrm{vortices}} \times N_{\mathrm{nodes}} \tag{9}$$

Because all the evaluations of Eq. (2) can be performed independent of each other, multithreading can reduce the computational time significantly. In QBLADE, multithreading is implemented in the form of the OPENMP API [18].

In cases of long simulated time series, the vortex lines and nodes that are tracked can use up a considerable amount of memory and in cases of short simulations, the memory usage can be very low. Because the amount of memory needed varies from one simulation to the next, the line and node elements are dynamically allocated at runtime. While this has a slight negative impact on the performance, it is ensured that the simulation will never run out of memory (given the hardware is sufficient) and only uses up as much memory as needed for a given simulation.

Besides multithreading, other strategies to reduce computational cost always evolve around limiting or reducing the number of free line vortices and vortex nodes. To reduce the number of vortex nodes in the wake, adjacent line vortices share common vortex nodes. The connectivity and topology of the wake is shown in Fig. 9. If for any reason, a vortex element is to be removed from the wake it is important to also remove the associated vortex nodes—if they are not connected to other vortex line elements. As a simple way to track this connectivity, functions for attaching and detaching vortex lines to vortex nodes have been implemented. A vortex node always has an array that lists the IDs of all attached vortex line elements. Whenever a line element is removed from the domain, it first detaches from its vortex nodes, by removing its ID from the vortex nodes lists. If there is a vortex node in the domain, without any vortex line element in its list, it is automatically removed.

Vortex Concentration. One strategy that is often applied to reduce the number of free vortex elements is the concentration of wake vorticity into a lesser number of line vortices. In Ref. [19], it is proposed to integrate at the last row of the vortex sheet from the radial position of maximum circulation to the tip and the hub and then shed the vortices from the tip and positions of the last wake row. However, this is not accurate in cases where there is more than one local circulation maximum on the blade, which can often be the case in simulations that are off the rotors design point. In this implementation, the circulation is integrated from one local circulation minimum to the next local maximum, which better captures the flow field in many off design positions where more than two concentrated counter-rotating vortices are present in the wake (see Fig. 10).

The concentrated circulation for a vortex is by integrating the circulation from local minimum to local maximum or vice versa

$$\Gamma_{\mathrm{con}} = \int_{r_{\Gamma_{l,\min}}}^{r_{\Gamma_{l,\max}}} \Gamma_{\mathrm{trailing}}(r)dr \tag{10}$$

The radial positions (r_{em}) where the concentrated vortex lines originate from are computed from the positions of the contributing vortex lines that are converted, weighted by the contributed vortex strength

$$r_{\mathrm{em}} = \sum (r_i \cdot \Delta\Gamma_i)^1 \Big/ _{\Gamma_{\mathrm{con}}} \tag{11}$$

With this methodology implemented, the full wake sheet, which includes shed and trailing vortex lines, is lumped into fewer concentrated trailing vortices. During this concentration, the shed

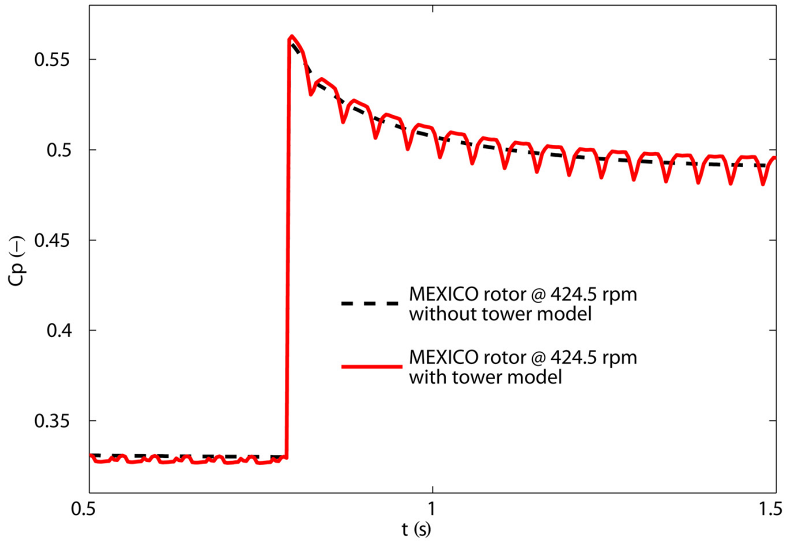

Fig. 7 MEXICO rotor C_p with and without tower model, during a step change in velocity from 20 m/s to 15 m/s

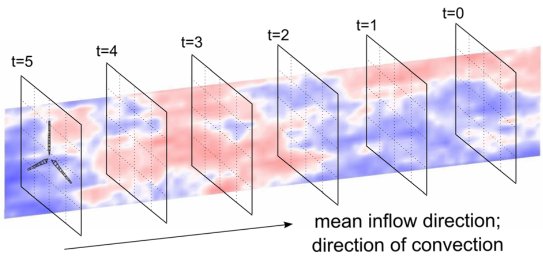

Fig. 8 Qualitative sketch of rotor in a turbulent wind field with frozen turbulent structures

vortex lines are omitted and removed from the simulation, while the circulation of the trailing vortices is fully conserved. The free parameter N_{con} defines after which time the line vortices are concentrated. It is made dimensionless with the time a rotor needs for one full revolution, so N_{con} determines that all vortex elements are transformed into concentrated vortex lines N_{con} full rotor revolutions after they were released from the TE. To investigate, how this parameter affects the accuracy of the simulation, the power output of the two-bladed NREL PHASE VI [20] wind turbine rotor was compared for three different tip-speed ratios (TSRs). Power output was chosen for this comparison because it represents an integral value to which all blade stations contribute.

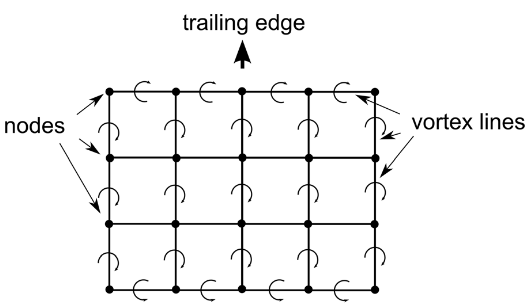

Fig. 9 Example of wake topology and connectivity

Figure 11 shows the relative error (from the converged value) of the computed power output, over the number of full rotor revolutions after which the wake sheet is converted into concentrated vortex lines. It can be seen that for all cases of TSRs that were simulated, the relative error drops below 1% after $N_{con} = 2.5$. A value of 2.5 already allows limiting the number of free wake elements drastically without a great effect on accuracy. Even though not shown in here, the relative error was also investigated for simulations of a yawed rotor, where the shed vortex lines have more significance than in steady inflow conditions. However, no larger error on the rotor performance could be found.

To limit the maximum amount of free vortex elements in the wake and to prevent the computational costs of growing exponentially during the simulation of long time series, it is necessary to truncate the wake at some point and remove vortex elements from the domain. This can either be done after a vortex element has reached a certain distance to the rotor origin or after it has reached a certain age. It was decided to implement the wake truncation after a certain vortex age, made dimensionless by the time the rotor needs for a full revolution (similar to N_{con}).

Figure 12 shows the relative error on a logarithmic scale over the number of full rotor revolutions, N_{trunc}, after which a wake

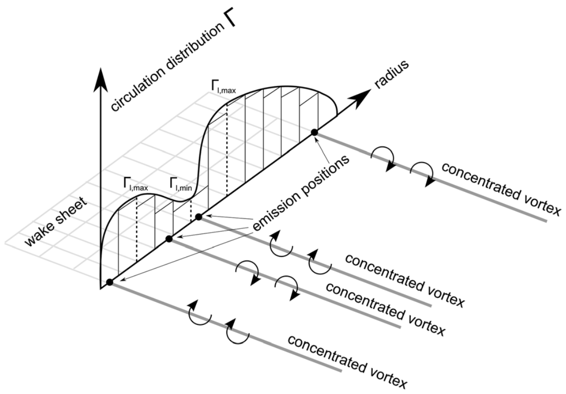

Fig. 10 Illustration of implemented vortex concentration approach

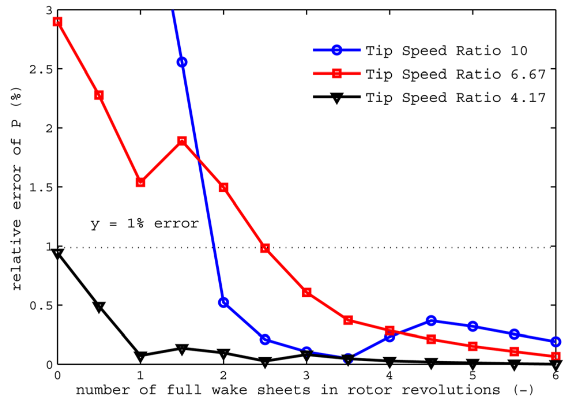

Fig. 11 Relative error of power output over full rotor revolutions before wake concentration for 3 TSRs

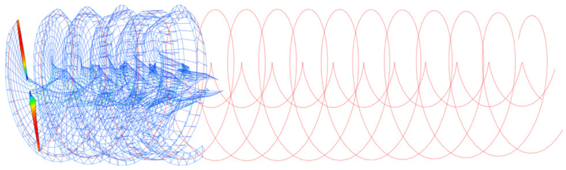

Fig. 13 Case 1: $N_{con} = 2.5$, $N_{trunc} = 8$, and shed and trailing vortices

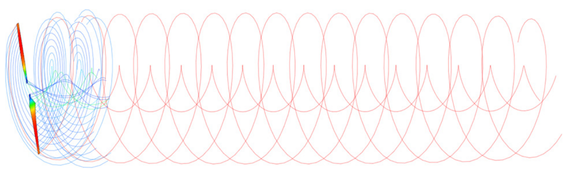

Fig. 14 Case 2: $N_{con} = 1$, $N_{trunc} = 8$, and only trailing vortices

element is completely removed from the simulation. It can be seen that the value for a parameter N_{trunc} with an acceptable error depends highly on the TSR. The reason for this is that the wake sheets at a high TSR are only convected away very slowly from the rotor disk. Instead, they accumulate in the vicinity of the rotor disk where their induction, even after a large number of rotor revolutions, still has a large influence on rotor performance. The N_{trunc} parameter, therefore, should always be adjusted to the range of TSRs, which is currently simulated to achieve an optimal performance.

An example for the computational time that is needed for a time-step is given for an Intel® Core™ i5 with four cores running at 3.2 GHz each. The NREL Phase VI rotor [20] is simulated with a 10 deg annular discretization. Each blade is discretized with 18 bound vortices. The parameters $N_{con} = 2.5$ and $N_{trunc} = 8$ were used. The number of free vortex elements, after the truncation starts limiting their number, is 7096 with 4076 vortex nodes (Fig. 13). Equation (2) is, therefore, evaluated about 29×10^6 times per time-step. The total central processing unit (CPU) time for 500 time-steps was 360 s—averaging to 0.72 s for a single time step. To demonstrate the sensitivity of the computational costs to these parameters, a second exemplary simulation (Fig. 14) was performed, with the same setup, but $N_{con} = 1$ and shed vortex lines disabled. This reduced the number of wake elements to 2308 and nodes to 2348 resulting in only 5.5×10^6 evaluations of Eq. (2) per time-step. One time-step was computed in 0.14 s. While the difference in calculated rotor C_P is below 1%, the saving in computational cost scales with a factor of 5.

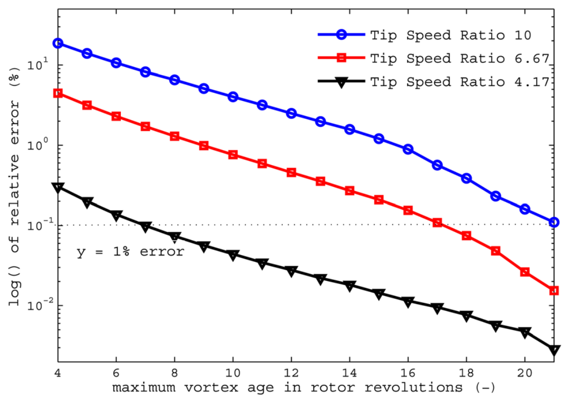

Fig. 12 Log of the relative error of power output over full rotor revolutions before wake truncation for 3 TSRs

Validation

To validate the implemented LLT algorithm, it is compared to the experimental data from the NREL Phase VI and the MEXICO experiment and simulations that were performed during various code benchmarks with these experimental results. During all validation calculations with QBLADE, the parameters $N_{con} = 2.5$ and $N_{trunc} = 8$ were used. Both shed and trailing vortices were enabled. A steady, uniform wind field was used as inflow and tower shadow effects were disabled.

NREL Phase VI Experiment. The NREL Phase VI rotor (Fig. 15) is a two-bladed, stall regulated rotor that was investigated in the NASA Ames Wind Tunnel. For all comparisons, the rotational speed is at a constant 72 rpm. To compare the results for simple, steady-state simulations of different operational points, the power curve of the Phase VI rotor is compared to the experimental data from Ref. [20] and the SMARTROTOR code [21], a panel method code that was implemented in GENUVP [22] and includes the ONERA [23] dynamic stall model. Figure 16 shows that there is a very good agreement between the BEM and LLT method of QBLADE, which is not surprising since both methods use the exact same

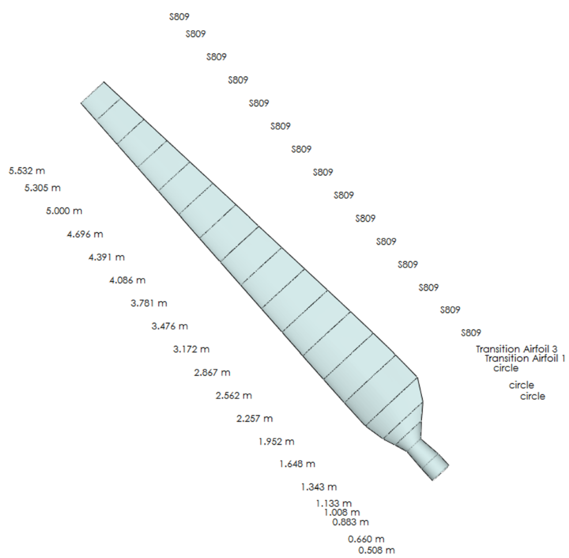

Fig. 15 NREL Phase VI geometry created in QBLADE

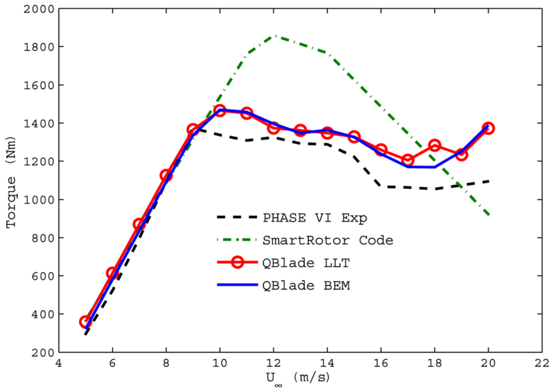

Fig. 16 Power curve of the Phase VI rotor, comparison between QBLADE BEM/LLT and SMARTROTOR panel method

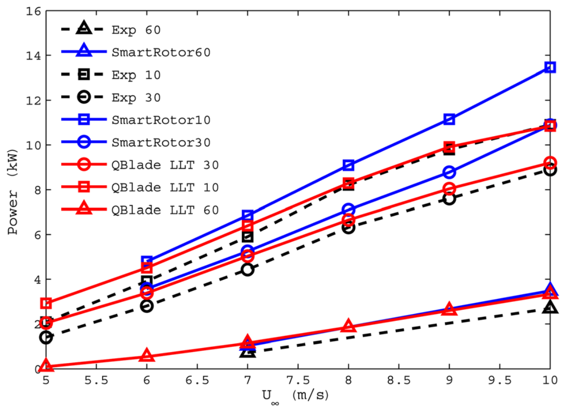

Fig. 17 Azimuthally averaged power curves for three different cases of yaw (10 deg, 30 deg, and 60 deg) of the MEXICO rotor

blade definition and polar data. The LLT predicts the stall much better than the SMARTROTOR code and overall shows very good performance in the whole operational range, for both high and low TSRs. To benchmark the LLT performance under more complex inflow conditions, the power curve was simulated for three different yaw cases. For comparison, the power output was averaged over one rotor revolution. In Fig. 17, it can be seen that the experimental result is predicted with a slightly higher accuracy by the QBLADE LLT, the BEM method of QBLADE cannot be used as a comparison here because it does not include a yaw correction model. Figure 18 shows the free wake structure for the three yaw cases.

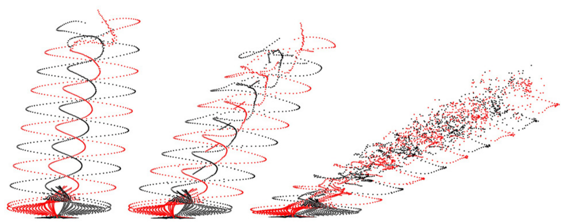

Fig. 18 Free wake structure for three different yaw cases, showing wake nodes only; from left to right: 10 deg yaw, 30 deg yaw, and 60 deg yaw

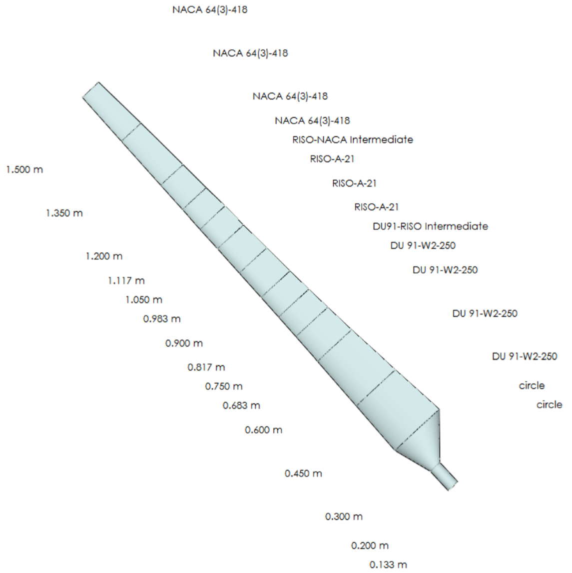

Fig. 19 MEXICO geometry created in QBLADE

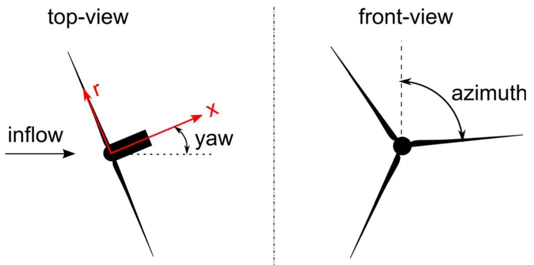

Fig. 20 Coordinate system used during MEXICO validation

MEXICO Experiment. The MEXICO [5] experiment was performed by ECN in the large German–Dutch wind tunnel DNW. The main objective during testing was to create a detailed database of aerodynamic and load measurements for validation and improvement of computational methods. All experiments and simulations in this section have been performed at 424.5 rpm. The

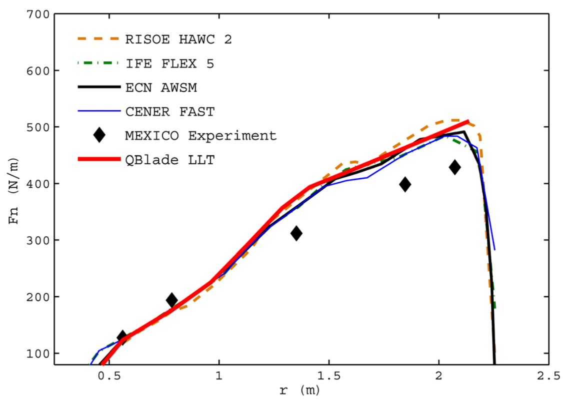

Fig. 21 IEA Task 29 Mexnext: normal force variation over blade radius at 15 m/s, yaw = 0 deg

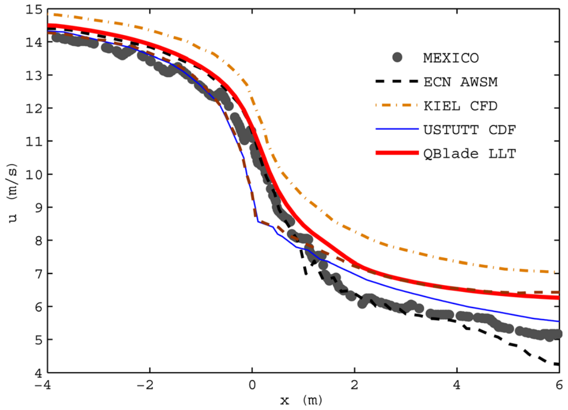

Fig. 22 IEA Task 29 Mexnext: axial velocity decay at 80% span, yaw = 0 deg, and 0 deg rotor azimuth

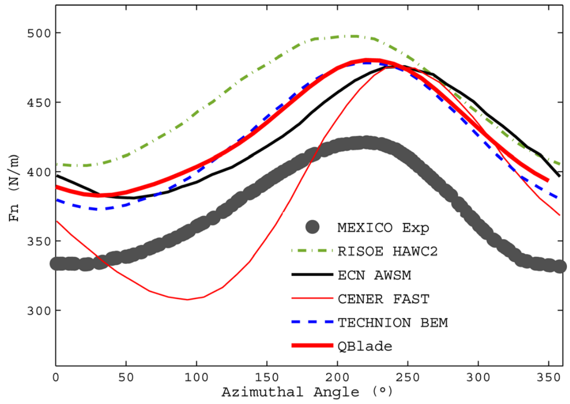

Fig. 25 IEA Task 29 Mexnext: azimuthal variation of normal force at *U* = 15 m/s, yaw = 30 deg, and pitch = −2.3 deg

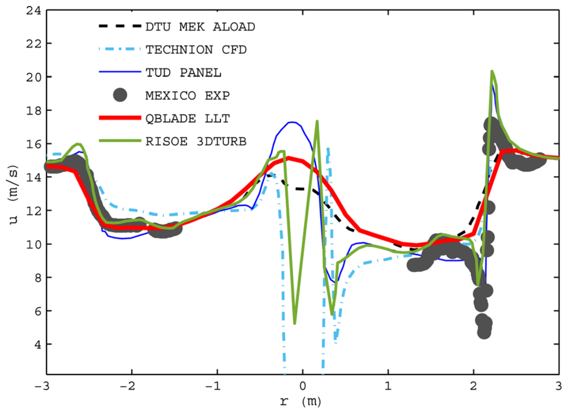

Fig. 23 IEA Task 29 Mexnext: axial velocity traverse parallel to rotor at *x_m* = 0.15, yaw = 30 deg, and rotor azimuth = 60 deg

rotor is shown in Fig. 19. In Ref. [5], the final results of Mexnext-I have been presented. Among other things, many different computational tools were compared with the experimentally obtained data. For this validation, the results of the LLT algorithm were added to this comparison. In the blade definition within QBLADE, the "officially" distributed polars of the MEXICO project were used. This is important to enable a comparison between the QBLADE implementation and the other BEM and LLT codes that were benchmarked that does not depend on the used polars.

The coordinate system, showing the local rotor coordinates (r and x) and the conventions used for yaw and azimuthal angle, is depicted in Fig. 20. The first case (Fig. 21) compares the variation of normal force on the blade at a constant, inflow of 15 m/s without rotor yaw. It can be seen that all the codes overpredict the normal force at outboard blade stations. The QBLADE LLT follows the general trend of the other codes. The blade discretization in QBLADE, however, is not fine enough at the blade tips to capture the drop in normal force.

In Fig. 22, the axial velocity decay at an 80% span wise position is compared for another case without yaw. The rotor plane is located at $x = 0$ m. It can be seen that the LLT code follows the experimental velocity distribution quite well, however, downstream of the rotor plane the velocity deficit is underestimated. ECN's vortex code AWSM achieves the best result. Compared to all other codes, of which some are high fidelity CFD codes, the result of the LLT is still acceptable.

Figures 23 and 24 show the axial wake velocity over the rotor span, 15 cm behind the rotor plane at 30 deg rotor yaw and at rotor positions of 60 deg and 100 deg azimuth, respectively. Experimental values are only available at outboard radial positions. QBLADE shows very good agreement to the experimental values, compared to the other codes. The reason for the large deviations between the

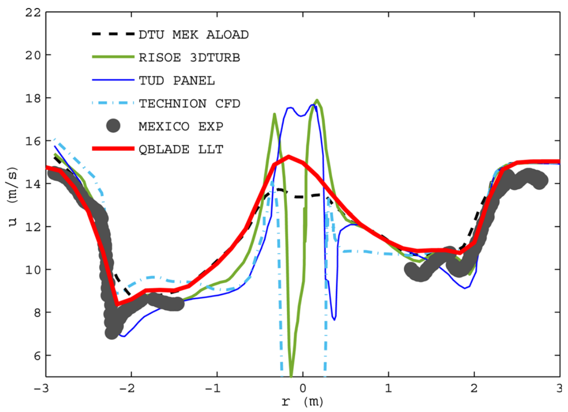

Fig. 24 IEA Task 29 Mexnext: axial velocity traverse parallel to rotor at *x_m* = 0.15, yaw = 30 deg, and rotor azimuth = 100 deg

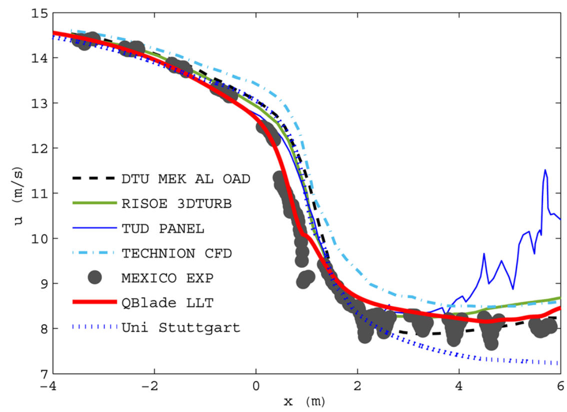

Fig. 26 IEA Task 29 Mexnext: axial velocity traverse at *y* = −1.4 m, yaw = 30 deg, and 60 deg rotor azimuth

simulation results at the inner board region is that in some setups, the nacelle is included and in some it is not included.

In Fig. 25, the azimuthal variation of the blades normal force under yawed inflow is compared. The QBLADE LLT and the Technion BEM code reproduce the phase with the highest accuracy among the engineering codes while the normal force is largely overpredicted by all codes. Again, as already seen in Fig. 1, the AERODYN method implemented in FAST has troubles accurately predicting the phase of the normal force variation.

Figure 26 shows the axial velocity, traversing through the rotor plane (at $x=0$) for a 30 deg rotor yaw case with the rotor at 60 deg azimuth position. In this test case, QBLADE reproduces the experimentally measured velocity decay through the rotor plane with the best accuracy out of all codes that were used in this comparison.

Conclusion and Future Work

A lifting line-free vortex wake algorithm has been implemented into the open source wind turbine simulator QBLADE. The integrated code allows the time-accurate simulation of wind turbine rotors in turbulent wind fields under the influence of tower blockage. The algorithm was optimized for computational efficiency as provision for a coupling with a structural simulator. By integration with QBLADE and its database of airfoils, polars, and wind fields, the setup of simulations is greatly facilitated. Results were thoroughly validated against a number of other codes and experimental data and show good agreement in all cases. Integration and testing of the algorithm have been completed and the source code will be made publicly available. A new version of QBLADE, v0.9, including the new LLT module, has been released under an open source license.

As a next step, the LLT code will be coupled with FAST to enable aeroelastic simulations with the LLT providing the aerodynamic forces. To simulate vertical axis wind turbines, the LLT has been adapted and integrated into the VAWT module of QBLADE. Successively, a structural model for VAWT rotors will be integrated to also enable aeroelastic simulations for vertical axis wind turbine rotors.

Acknowledgment

The authors gratefully acknowledge the support of the German Science Foundation (DFG), funding this research through the PAK 780 research focus: "Wind Turbine Load Control Under Realistic Inflow Conditions."

Nomenclature

AoA; α = angle of attack
BEM = blade element momentum method
C_P = power coefficient
LLT = lifting line theory
r = radial position
r_c = vortex core radius
S_c = time offset parameter
t = time
TSR = tip-speed ratio
V_{rel}, V_{ind} = relative velocity, induced velocity
$\mathbf{x}_t$ = wake node position vector
Γ = circulation
δ_v = turbulent viscosity coefficient
ε = strain rate
ν = kinematic viscosity

References

[1] Moriarty, P. J., and Hansen, C., 2005, "AeroDyn Theory Manual," National Renewable Energy Laboratory, Golden, CO.
[2] Juul, T., 2009, "How 2 HAWC2, the User's Manual," Risø National Laboratory, Technical University of Denmark, Roskilde, Denmark, Risø-R-1597.
[3] Winkelaar, D., 1991, "Fast Three-Dimensional Wind Simulation and the Prediction of Stochastic Blade Loads," 14th Annual Energy Sources Technology Conference and Exhibition, Houston, TX, Jan. 20–23, Vol. 11, pp. 5–14.
[4] Bossanyi, E. A., 2003, *GH Bladed Theory Manual*, GH and Partners, Bristol, UK.
[5] Snel, H., Schepers, G., and Siccama, N., 2009, "Mexico Project: The Database and Results of Data Processing and Interpretation," 47th AIAA Aerospace Sciences Meeting, Orlando, FL, Jan. 5–8, AIAA Paper No. 2009-1217.
[6] Marten, D., Wendler, J., Pechlivanoglou, G., Nayeri, C. N., and Paschereit, C. O., 2013, "QBlade: An Open Source Tool for Design and Simulation of Horizontal and Vertical Axis Wind Turbines," IJETAE, **3**(S3), pp. 264–269.
[7] Marten, D., Wendler, J., Pechlivanoglou, G., Nayeri, C., and Paschereit, C., 2013, "Development and Application of a Simulation Tool for Vertical and Horizontal Axis Wind Turbines," ASME Paper No. GT2013–94979.
[8] Drela, M., 1989, "XFOIL: An Analysis and Design System for Low Reynolds Number Airfoils," *Low Reynolds Number Aerodynamics* (Lecture Notes in Engineering, Vol. 54), Springer, Berlin, pp. 1–12.
[9] Montgomerie, B., 2004, "Methods for Root Effects, Tip Effects and Extending the Angle of Attack Range to ±180, With Application to Aerodynamics for Blades on Wind Turbines and Propellers," FOI, Swedish Defence Research Agency, Stockholm, Sweden, Report No. FOI-R-1305-SE.
[10] Viterna, L. A., and Janetzke, D. C., 1981, "Theoretical and Experimental Power From Large Horizontal-Axis Wind Turbines," NASA Lewis Research Center; Cleveland, OH, NASA Report No. TM-82944.
[11] Lennie, M. D., 2013, "Development of the QFEM Solver," Master's thesis, TU Berlin, Berlin.
[12] Veers, P. S., 1988, "Three-Dimensional Wind Simulation," Sandia National Laboratories, Albuquerque, NM, Report No. SAND88-0152, UC-261.
[13] Jonkman, J., 2013, "FAST Theory Manual," National Renewable Energy Laboratory, Golden, CO.
[14] Grasso, F., Van Garrel, A., and Schepers, J. G., 2011, "Development and Validation of Generalized Lifting Line Based Code for Wind Turbine Aerodynamics," 49th AIAA Aerospace Sciences Meeting, Orlando, FL, Jan. 4–7, AIAA Paper No. 2011-146.
[15] van Garrel, A., 2003, "Development of a Wind Turbine Aerodynamics Simulation Module," ECN Wind Energy, Petten, The Netherlands, Technical Report ECN-C–03-079.
[16] Sant, T., 2007, "Improving BEM-Based Aerodynamic Models in Wind Turbine Design Codes," Ph.D. thesis, TU Delft, Delft, The Netherlands.
[17] Leishman, J. G., Bhagwat, M. J., and Bagai, A., 2002, "Free-Vortex Filament Methods for the Analysis of Helicopter Rotor Wakes," J. Aircr., **39**(5), pp. 759–775.
[18] Chapman, B., Jost, G., and Van Der Pas, R., 2008, *Using OpenMP: Portable Shared Memory Parallel Programming*, Vol. 10, MIT Press, Cambridge, MA, p. 353.
[19] Qiu, Y.-X., Wang, X.-D., Kang, S., Zhao, M., and Liang, J.-Y., 2014, "Predictions of Unsteady HAWT Aerodynamics in Yawing and Pitching Using the Free Vortex Method," Renewable Energy, **70**, pp. 93–106.
[20] Simms, D., Schreck, S., Hand, M., and Fingersh, L. J., 2001, "NREL Unsteady Aerodynamics Experiment in the NASA-Ames Wind Tunnel: A Comparison of Predictions to Measurements," National Renewable Energy Laboratory, Golden, CO, Report No. NREL/TP-500-29494.
[21] McTavish, S., Feszty, D., and Nitzsche, F., 2009, "Aeroelastic Simulations of the NREL Phase VI Wind Turbine Using a Discrete Vortex Method Coupled With a Nonlinear Beam Model," 17th Propulsion Symposium of the Canadian Aeronautics & Space Institute Conference (AERO 2009) Kanata, ON, Canada, May 5.
[22] Opoku, D. G., Triantos, D. G., Nitzsche, F., and Voutsinas, S. G., 2002, "Rotorcraft Aerodynamic and Aeroacoustic Modelling Using Vortex Particle Methods," 23rd International Congress of Aeronautical Sciences (ICAS 2002), Toronto, ON, Canada, Sept. 8–13, Paper No. ICAS 2002-2.1.3.
[23] Tang, D., and Dowell, E., 1996, "Comments on the ONERA Stall Aerodynamic Model and Its Impact on Aeroelastic Stability," J. Fluids Struct., **10**(4), pp. 353–366.

Chapter 3 | Application

This chapter shows different examples of applications and validations of the aeroelastic model that has been presented in Chapter 2. The following three examples, that are included in this work have been published in Journals, and are included in this thesis with a brief introduction:

- Three-Dimensional Aerodynamic Analysis of a Darrieus Wind Turbine Blade Using Computational Fluid Dynamics and Lifting Line Theory
- Benchmark of a Novel Aero-Elastic Simulation Code for Small Scale VAWT Analysis
- Predicting Wind Turbine Wake Breakdown Using a Free Vortex Wake Code

Furthermore, additional examples for the application of the simulation framework are given. Some of the work has already been conducted and applied within a range of projects. The presented examples are only briefly touched, without going too much into detail. The purpose is to demonstrate the wide range of possible applications of the QBlade-Chrono coupling, that go beyond the scope of solely wind turbine aero-elasticity:

- Wind Park Simulations
- Modeling of Airborne Wind Energy Systems
- Wind Turbine Ice Throw Simulations
- Simulations of Floating Offshore Wind Turbines
- Earthquake Simulations

3.1. Publication II: Three-Dimensional Aerodynamic Analysis of a Darrieus Wind Turbine Blade Using Computational Fluid Dynamics and Lifting Line Theory

Balduzzi, F., Marten, D., Bianchini, A., Drofelnik, J., Ferrari, L., Campobasso, M. S.,Pechlivanoglou, G., Nayeri, C. N., Ferrara, G. & Paschereit, C. O. (2017). Three-Dimensional Aerodynamic Analysis of a Darrieus Wind Turbine Blade Using Computational Fluid Dynamics and Lifting Line Theory. Journal of Engineering for Gas Turbines and Power, 140(2), 022602. https://doi.org/10.1115/1.4037750

In this publication a detailed comparison between a high fidelity CFD RANS simulation and the medium fidelity LLFVW simulation of a vertical axis wind turbine is carried out.

Compared are the overall predicted performance, time resolved blade performance characteristics and the highly complex flow-fields inside several cross-sectional planes. The RANS simulations, with a mesh size of 64 million cells, were carried out over 8640 time steps (with 0.5° azimuthal increments) to obtain a periodic solution of the flow. Using $16,000$ processor cores, the resulting wall-clock time of the CFD simulations was approximately 30 days. The corresponding LLFVW simulations, using QBlade, were performed within a wall clock time of approximately 200s on a single workstation. For the difference in computational cost, in between 6-7 orders of magnitude, the similarity of results is remarkable.

Overall, the results shown in this publication present the most detailed cross-validation of QBlade's LLFVW method that has been performed to date. On the other hand the consistency in the results, using two complete different computational methods, also proves the capability of the employed RANS framework to reliably predict the unsteady aerodynamics in the near field of a VAWT with high detail.

Francesco Balduzzi
Department of Industrial Engineering,
University of Florence,
Via di Santa Marta 3,
Firenze 50139, Italy
e-mail: balduzzi@vega.de.unifi.it

David Marten
Hermann-Föttinger-Institut,
Technische Universität Berlin,
Müller-Breslau-Straße 8,
Berlin 10623, Germany
e-mail: david.marten@tu-berlin.de

Alessandro Bianchini
Department of Industrial Engineering,
University of Florence,
Via di Santa Marta 3,
Firenze 50139, Italy
e-mail: bianchini@vega.de.unifi.it

Jernej Drofelnik
School of Engineering,
University of Glasgow,
James Watt Building South,
University Avenue,
Glasgow G12 8QQ, UK
e-mail: j.drofelnik.1@research.gla.ac.uk

Lorenzo Ferrari
Department of Energy, Systems, Territory
and Construction Engineering,
University of Pisa,
Largo Lucio Lazzarino,
Pisa 56122, Italy
e-mail: lorenzo.ferrari@unipi.it

Michele Sergio Campobasso
Department of Engineering,
Lancaster University,
Gillow Avenue,
Lancaster LA1 4YW, UK
e-mail: m.s.campobasso@lancaster.ac.uk

Georgios Pechlivanoglou
Hermann-Föttinger-Institut,
Technische Universität Berlin,
Müller-Breslau-Straße 8, Berlin 10623, Germany
e-mail: george@pechlivanoglou.com

Christian Navid Nayeri
Hermann-Föttinger-Institut,
Technische Universität Berlin,
Müller-Breslau-Straße 8,
Berlin 10623, Germany
e-mail: christian.nayeri@tu-berlin.de

Giovanni Ferrara
Department of Industrial Engineering,
University of Florence,
Via di Santa Marta 3,
Firenze 50139, Italy
e-mail: giovanni.ferrara@unifi.it

Christian Oliver Paschereit
Hermann-Föttinger-Institut,
Technische Universität Berlin,
Müller-Breslau-Straße 8,
Berlin 10623, Germany
e-mail: oliver.paschereit@tu-berlin.de

Three-Dimensional Aerodynamic Analysis of a Darrieus Wind Turbine Blade Using Computational Fluid Dynamics and Lifting Line Theory

Due to the rapid progress in high-performance computing and the availability of increasingly large computational resources, Navier–Stokes (NS) computational fluid dynamics (CFD) now offers a cost-effective, versatile, and accurate means to improve the understanding of the unsteady aerodynamics of Darrieus wind turbines and deliver more efficient designs. In particular, the possibility of determining a fully resolved flow field past the blades by means of CFD offers the opportunity to both further understand the physics underlying the turbine fluid dynamics and to use this knowledge to validate lower-order models, which can have a wider diffusion in the wind energy sector, particularly for industrial use, in the light of their lower computational burden. In this context, highly spatially and temporally refined time-dependent three-dimensional (3D) NS simulations were carried out using more than 16,000 processor cores per simulation on an IBM BG/Q cluster in order to investigate thoroughly the 3D unsteady aerodynamics of a single blade in Darrieus-like motion. Particular attention was paid to tip losses, dynamic stall, and blade/wake interaction. CFD results are compared with those obtained with an open-source code based on the lifting line free vortex wake model (LLFVW). At present, this approach is the most refined method among the "lower-fidelity" models, and as the wake is explicitly resolved in contrast to blade element momentum (BEM)-based methods, LLFVW analyses provide 3D flow solutions. Extended comparisons between the two approaches are presented and a critical analysis is carried out to identify the benefits and drawbacks of the two approaches. [DOI: 10.1115/1.4037750]

Contributed by the Turbomachinery Committee of ASME for publication in the Journal of Engineering for Gas Turbines and Power. Manuscript received July 5, 2017; final manuscript received July 19, 2017; published online October 3, 2017. Editor: David Wisler.

Introduction

The deployment of Darrieus-type vertical axis wind turbines (VAWTs) is rapidly growing due to the significant benefits in comparison to more conventional horizontal-axis rotors in applications such as delocalized power production in the urban environment, offshore floating turbines, and tidal energy applications. In highly turbulent flows like those encountered in the built environment, they can benefit from the independence of the performance on wind direction, the lower structural stress due to the generator often positioned on the ground [1], the low noise emissions [2], and the enhanced performance in skewed flows [3]. On the other hand, the continuous variation of the incidence angle to the rotor blades during the revolution generates an extremely complex flow field and the resulting unsteady phenomena have a significant impact on the overall performance of the machine. If experimental testing is often difficult and expensive, increasingly more accurate and robust aerodynamic prediction tools can provide a versatile mean to improve the design of VAWTs [4].

Navier–Stokes (NS) computational fluid dynamics (CFD) has the potential of accurately predicting the unsteady blade-flow interaction, which is strongly affected by dynamic stall and flow separation, both extremely difficult to model. Broadly speaking, available analysis approaches can be divided in two main categories: low-fidelity and high-fidelity models. The two computationally efficient low-fidelity methods that are presently thought capable of properly modeling VAWT aerodynamics are the blade element momentum (BEM) theory, based on momentum balances, and the lifting line theory coupled to a free vortex wake model (LLFVW) [5]. Their main advantages rely on the setup simplicity and the short simulation time, even on conventional workstations. Moreover, the LLFVW model also provides a solution of the three-dimensional (3D) flow field past the rotor, making the method particularly attractive for complex analyses like turbine/wake interactions in wind farms. The fact that the LLFVW method computes the 3D flow field past the turbine enables fairly straightforward comparisons with higher-fidelity approaches (e.g., unsteady Reynolds-averaged Navier–Stokes or large eddy simulations (LES) and CFD), as shown later in this study. To guarantee an adequate accuracy of the LLFVW, however, a careful selection of parameters for the various models implemented in the method is needed [6]. Among others, the availability of highly reliable airfoil force data is pivotal [7–9] and, unfortunately, such data are often not readily available.

High-fidelity numerical models belong to the family of CFD models. Even if the present frontier of the research is leading to the massive use of LES, Reynolds-averaged Navier–Stokes (RANS) approaches are still the benchmark for Darrieus applications due to their more affordable computational cost with respect to LES. Moreover, the majority of the studies available in the literature made use of a two-dimensional (2D) approach [10], as this offers a good tradeoff between computational cost and reliability of the overall turbine performance. However, 2D simulations discard some important aerodynamic features, such as tip flow effects, downwash, and secondary flows. In the light of this, 3D fully unsteady CFD can be considered as the most suitable numerical approach for a complete resolution of these rotor flow fields. Unsteady 3D NS simulations of Darrieus rotor aerodynamics is often unaffordable, due to the very large temporal and spatial grid refinement needed for obtaining reliable results [11,12]. In the past few years, some 3D studies have been carried out to characterize the turbine wake [13] and the flow field around the blades [14], to study the start-up of small rotors [15], and to assess the impact of the effects of finite aspect ratio [16], supporting arms [17], and different blade shapes [18] on turbine performance. Other studies focused on the turbine performance in skewed flow conditions [19]. In almost all the cases, however, the limited availability of computational resources imposed the use of fairly coarse spatial and temporal resolution, introducing uncertainty on the extent to which these results can be considered time-step or grid-independent. More specifically, the common approach found in literature was to progressively coarsen the 2D mesh sections for the 3D analyses with respect to the relatively fine mesh used for 2D analyses so as to limit the total number of cells of the 3D grid to values between 1,000,000 and 10,000,000. Most recent 2D parametric CFD analyses of Darrieus rotors (e.g., see Ref. [10]) showed conversely that the simulation reliability is tremendously affected by the quality and refinement level of the meshing and time-stepping strategies. As an example, one of the previous studies based on 2D RANS CFD for a three-blade rotor showed that temporal and spatial grid-independent solutions are obtained provided that grids with at least 400,000 elements are used [9]. To preserve the same accuracy level in a 3D simulation of the same turbine (modeling only half of the rotor making use of symmetry boundary conditions on the plane at rotor midspan), the 3D mesh would consist of about 90,000,000 cells, which is almost ten times the size of the finest meshes used in the 3D RANS studies of Darrieus rotor flows published to date.

In this paper, the results of a fairly unique time-dependent 3D Navier–Stokes simulation of a single-bladed Darrieus rotor, carried out using a 98,304-core IBM BG/Q cluster and characterized by a very high level of spatial and temporal refinement, are reported. To the best of the authors' knowledge, the present case study represents the most detailed numerical solution of the flow field past a Darrieus rotating blade to date. The 3D Navier–Stokes solution is used as a benchmark to validate an open-source code based on the lifting line free vortex wake model. Moreover, important 3D effects such as the torque reduction due to finite blade effect, the tip vortices' structure and the wake propagation are analyzed in detail. The cross-comparison of the phenomena occurring during the cyclic motion of the considered one-blade rotor configuration is thought to be of great value for understanding the prediction capabilities of the LLFVW model and to validate its performance for future analyses of Darrieus wind turbines.

Case Study

The numerical models used in this study focus on a one-blade H-Darrieus rotor using a NACA 0021 airfoil. The blade has a chord c of 0.0858 m, is 1.5 m long, is positioned at a radius R of 0.515 m from the central shaft, and is attached at midchord. The turbine model is created based on the experimental full-scale three-blade rotor used in the experimental tests of Refs. [7] and [14]. The decision of simulating a single blade was based both on physical considerations and on hardware limitations. First, a one-blade model is sufficient to investigate all the desired 3D flow structures that lead to an efficiency reduction of a finite blade; at the same time, the use of a single blade allows one to isolate and analyze fundamental aerodynamic phenomena of finite length blade aerodynamics, removing additional aerodynamic effects due to multiple blade/wake interactions occurring in a multibladed rotor. From a more practical viewpoint, the need of ensuring an adequate level of spatial refinement both in the grid planes normal to the rotor axis and in the axial direction would have required a grid with more than 100 million elements for a three-blade rotor, which was beyond the resources available for this project. Given these prerequisites, the one-blade model allows one to both maintain computational costs within the bounds imposed by the available resources and keep the desired accuracy of the targeted analysis.

The complete power curve of the rotor was calculated with the LLFVW code and is reported in Fig. 1. Due to the large burden associated with running the 3D time-dependent Navier–Stokes simulation, only a single operating condition was simulated with the CFD code, namely, that associated with a tip-speed ratio (TSR) of 3.3 (circle mark in the figure). This condition is of particular interest because: (a) it is one of fairly high efficiency and thus one where the rotor is expected to work more often than at other TSRs and (b) it features several complex aerodynamic phenomena (e.g., stall and strong tip vortices [20,21]) posing a significant modeling challenge to the considered methods. All RANS

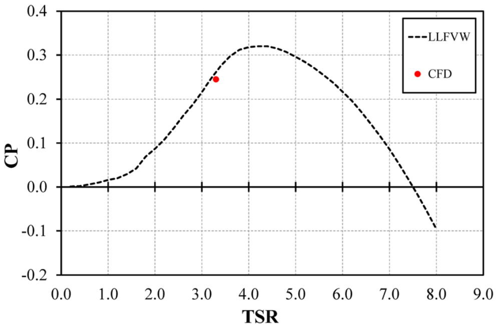

Fig. 1 Power curve as a function of the TSR

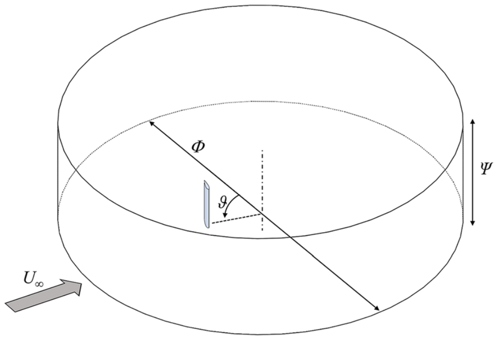

Fig. 2 Computational domain

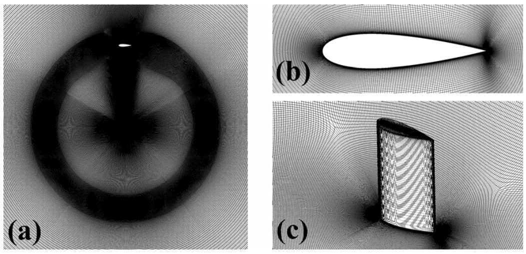

Fig. 3 Some details of the computational mesh

and LLFVW cross-comparison reported later refer to this working point.

Numerical Techniques

Two different numerical techniques were applied and compared in this study. The main features of the different approaches are presented in this section.

CFD RANS Simulations. All the CFD simulations have been performed using the COSA CFD system for general renewable energy applications. COSA is a structured multiblock finite volume massively parallel RANS code, which uses the compressible formulation of the RANS equations, and features Menter's k–ω shear stress transport (SST) turbulence model [22]. It features a steady flow solver, a time domain solver for the solution of general unsteady problems [23,24], and a frequency-domain harmonic balance solver for the rapid calculation of unsteady periodic flows [25,26]. The RANS equations are obtained by averaging the Navier–Stokes equations on the turbulence time-scales using the Reynolds–Favre averaging approach. The discretization of the convective fluxes of both the RANS and SST equations uses a second-order upwind discretization, based on Van Leer's MUSCL extrapolations and Roe's flux difference splitting. The discretization of the diffusive fluxes is instead based on central finite differencing. The integration of the RANS and SST equations is performed in a fully coupled fashion, using an explicit solution strategy based on full approximation scheme multigrid featuring a four-stage Runge–Kutta smoother. Convergence acceleration is further enhanced using local time-stepping and variable-coefficient central implicit residual smoothing. Time-dependent problems are solved using a second-order dual-time stepping approach. For unsteady problems with moving bodies, such as the Darrieus rotor configuration investigated herein, the governing equations are solved in the absolute frame of reference using an arbitrary Lagrangian–Eulerian approach and body-fitted grids.

For the present study, this implies that the entire computational grid rotates about the rotational axis of the rotor during the simulation. The COSA solvers have been extensively validated, interested readers may refer to Refs. [25] and [26], while its suitability for the simulation of Darrieus wind turbines has been recently assessed through comparative analyses with both commercial research codes and experimental data [12].

The central symmetry of H-Darrieus rotors was exploited, allowing to simulate only a half of the blade rather than the entire blade length of $H = 1.5$ m. Thus, the aspect ratio of the simulated blade portion is 8.74, which is half that of the actual blade. The computational domain (Fig. 2) is a cylinder centered on the rotational axis and containing the rotating blade. A domain radius $\Phi = 240R$ was chosen to guarantee a full development of the wake [12]. The height of the domain was instead set to $\Psi = 2.53H$, corresponding to half of the height (due to the aforementioned symmetry condition) of the wind tunnel where the original model was tested [7]; experimental data from these tests were used for the validation of the 2D variant of the 3D RANS approach considered herein [12,27].

The 3D mesh (detail reported in Fig. 3) was obtained by first generating a 2D mesh past the airfoil using the optimal mesh settings identified in Refs. [12] and [28], extruding this mesh in the spanwise (z) direction, and filling up with grid cells the volume between the blade tip and the circular farfield boundary. The 3D grid is structured multiblock. Its 2D section normal to the z-axis (within the z-interval occupied by the blade—Fig. 3(a)) consisted of 4.3×10^5 quadrilateral cells. The airfoil was discretized with 580 nodes and the first element height was set to $5.8 \times 10^{-5}c$ to guarantee a dimensionless wall distance y^+ lower than 1 throughout the revolution. As recommended in Ref. [10], a proper refinement of both leading and the trailing edge regions was adopted (Fig. 3(b)) as well as a globally high refinement in the region around the airfoil within one chord from the walls in order to properly resolve the detached flow regions at high angle of attack [29].

After extrusion in the z direction, 80 layers in the half-blade span were formed (Fig. 3(c)), with progressive grid clustering from midspan to the tip in order to ensure an accurate description of tip flows.

A high grid refinement level was used in the whole tip region above the blade in order to properly capture the flow separation and the tip vortices. The final mesh was made of 64 million hexahedral cells.

The free stream wind speed was set to $U_\infty = 9.0$ m/s. The turbulence farfield boundary conditions were a turbulent kinetic energy (k) based on 5% turbulence intensity and a characteristic length of 0.07 m (limiters of the production of k and ω were used with a cut-off l_k of ten [30]).

The 3D RANS simulations reported later have been performed on an IBM BG/Q cluster [31] featuring 8144 16-core nodes with a total of 98,304 cores. Exploiting the high linear scalability of the COSA solvers, verified up to 20,000 processor cores, the RANS simulation reported later has been performed using about 16,000 cores. Using 720 intervals per revolution, the simulation required

12 revolutions to achieve a fully periodic state. The flow field was considered to be periodic once the maximum difference between the torque over the last two revolutions was smaller than 0.1% of the maximum value of torque over the last revolution. The wall-clock time required for the complete simulation was about 653 h (27.2 days). The numerical settings used for this RANS simulation ensure a highly accurate RANS solution, as they were selected (even if not as accurate as an LES approach), fulfilling all the key requirements of temporal and spatial discretization. Indeed, although not reported in this paper for brevity, numerical tests pointed to grid-independence of the solution obtained with the grid used in this study.

LLFVW Model. As discussed, two different numerical models were considered here to assess the influence of poststall polars, a BEM model, and a lifting line theory free vortex wake method.

The BEM model is represented by the VARDAR code of the University of Florence, Florence, Italy [8,11], which has been used in the last few years to design several industrial models of small Darrieus turbines. The VARDAR code is based on an improved version of the *Double Multiple Streamtubes Approach With Variable Interference Factors*, originally proposed by Paraschivoiu [24]. The Glauert's correction for the BEM theory has been taken into account with the most recent improvements based on experimental data [25], together with the corrections due to blades finite aspect ratio, using the Lanchester–Prandtl model [26].

In order to increase the accuracy of the aerodynamic estimations, the code is embedded with several dynamic stall models (i.e., those proposed by Berg, Strickland, and Paraschivoiu [1]) and with the stream tube expansion model presented in Ref. [1], although the incidence of this latter on the simulation of small turbines like those investigated in this work is reduced.

The prediction capabilities of the VARDAR code have been validated during a several-years' experience in the design of three H-Darrieus rotors, having swept areas of 1, 2.5, and 5 m^2, respectively, and two or three blades, either straight or helix-shaped [11,19,27]. The 1:1 models of all the rotors were tested in different wind tunnels (both with closed and open-jet). In all cases, the code was able to predict correctly both the power curves at different wind speeds and the starting ramps of rotor and is then considered predictive for the turbine typology investigated in this study.

Lifting Line Theory Model. The LLFVW computations in this study have been performed with the wind turbine design and simulation tool QBlade [32,33], which is developed by some of the authors at the Technical University of Berlin. The LLFVW algorithm is loosely based on the nonlinear lifting line formulation as described by van Garrel [34] and its implementation in QBlade can be used to simulate both horizontal-axis wind turbine and VAWT rotors.

Rotor forces are evaluated from tabulated lift and drag airfoil data. The wake is discretized with vortex line elements, which are shed at the blades trailing edge during every time step and then undergo free convection behind the rotor (Fig. 4). The vortex elements are desingularized using the van Garrel's cut-off method [35] with the vortex core size, taking into account viscous diffusion via the vortex core size that is modeled through the kinematic viscosity ν, a turbulent vortex viscosity coefficient δ_v, and a time offset parameter S_c using the below equation:

$$r_c = \left(\frac{5.03\delta_v \nu (t + S_c)}{1 + \varepsilon}\right)^{1/2} \tag{1}$$

The effects of unsteady aerodynamics and dynamic stall are introduced via the ATEFlap aerodynamic model [36,37] that reconstructs lift and drag hysteresis curves from a decomposition of the lift polars. The implemented ATEFlap formulation has

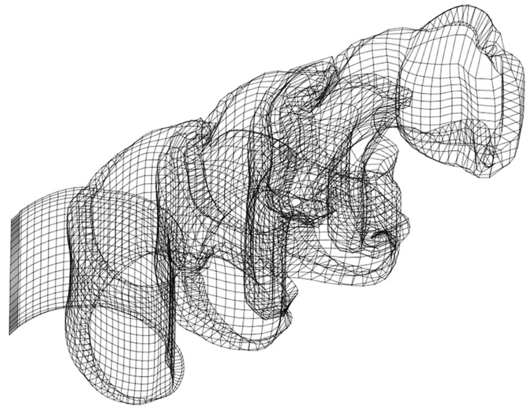

Fig. 4 Snapshot of the LLFVW simulation after 12 rotor revolutions

been further adapted to work under the intricate conditions of VAWT exhibiting large fluctuations of the angle of attack when rotating at low TSR [38].

To increase computational efficiency, the wake convection step is GPU parallelized using the OpenCL framework. To prevent the computational cost from growing exponentially over time, different wake reduction schemes (for VAWT and horizontal-axis wind turbine) are implemented [36–39].

The main parameters used in the LLFVW simulation of this study are given in Table 1. The azimuthal discretization was chosen to achieve a compromise between computational efficiency and accuracy. The wake was fully resolved for 12 revolutions, to obtain high-quality results in the wake region, after which it was truncated. The blade was discretized into 21 panels using sinusoidal spacing to obtain a higher resolution in the tip region where the largest gradients in circulation are to be expected. The vortex time offset and the turbulent viscosity parameters were chosen so that the initial core size is large enough to prevent the simulation from diverging during the blade/wake interaction around the 270 deg azimuthal position, but small enough not to dampen the free wake induction onto the rotor blades and large enough not to cause the simulation to blow up due to the singularity in the Biot–Savart equation. Such an internal calibration of the vortex parameters is necessary for each turbine that is simulated and is achieved by comparing azimuthal distributions of induced velocities and blade forces over a range of these parameters.

The simulation was carried out over 16 revolutions resulting in 1152 time steps on a single workstation (3.3 GHz Intel Xeon 1230 v2, 8 GB RAM, NVidia GTX1070 GPU), the wall clock-time required for the simulation was 196 s, which reduces the runtime of the LLFVW simulation by more than 4 orders of magnitude over that of the CFD calculation. The ratio of the actual computational cost of the LLFVW and RANS simulations is probably more than 6orders, due to the use of 8144 cluster nodes for the RANS simulation. However, it is difficult to quantify this ratio more precisely because the processor type and architecture used by the two simulations are substantially different.

Table 1 Simulation parameters of LLFVW in QBlade

Inflow	9 m/s
Azimuthal discretization	5 deg
Blade discretization	21 (sinusoidal)
Full wake length	12
Vortex time offset	0.0001 s
Turbulent vortex viscosity	100

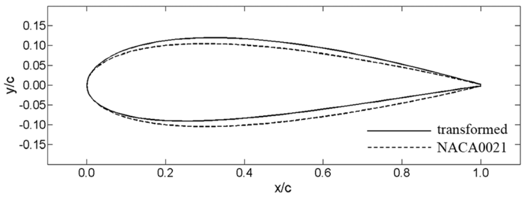

Fig. 5 Geometry of the virtual airfoil compensated for the virtual camber effect

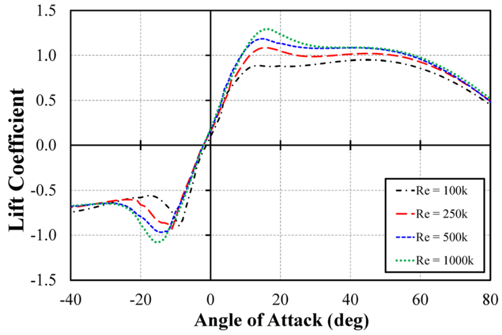

Fig. 6 Lift polars of the virtual airfoil extrapolated with the Montgomerie method

Airfoil Polar Data. Using accurate and high-quality airfoil, polar data are pivotal to obtain accurate results with the LLFVW method. Such data were obtained using the process explained in the following.

To account for the virtual camber effect [29], a virtual airfoil geometry was obtained from the NACA0021 geometry using the conformal transformation technique (Fig. 5) based on the chord-to-radius ratio, as described in Ref. [40].

Lift and drag polars (Fig. 6) of the virtual airfoil were then obtained in a Reynolds number range between 100,000 and 1,000,000 using XFoil [41] with an N_{Crit} value of nine and forced transition at the leading edge of the pressure and suction side.

In a different publication of the authors [5], it was shown that, besides modeling the dynamic stall, a smooth extrapolation of the polar data in the post stall region is critical to obtain high-quality simulation results (e.g., see Ref. [42]).

Results

In this section, the results of the 3D numerical simulations using both the CFD and the LLFVW approach are analyzed and cross-compared. In particular, CFD results are used here as a benchmark to verify the computationally less expensive LLFVW method. All the analyses refer to TSR = 3.3.

Torque Profile. The availability of the resolved flow field past the rotor with both approaches enables the investigation of both local flow phenomena, such as wake patterns behind the rotor, and the assessment of integral performance metrics key to design, such as the periodic torque profile over one revolution.

The impact of the effects due to finite length blade on the periodic torque profile is analyzed first. To this aim, the reduction of the torque coefficient moving from midspan toward the tip was evaluated in terms of instantaneous torque coefficient per unit blade length (C_{mz}), defined by the below equation, in which T_z denotes the instantaneous torque per unit blade length at the considered z position, and U_∞ and ρ_∞ denote the freestream values of wind speed and air density, respectively,

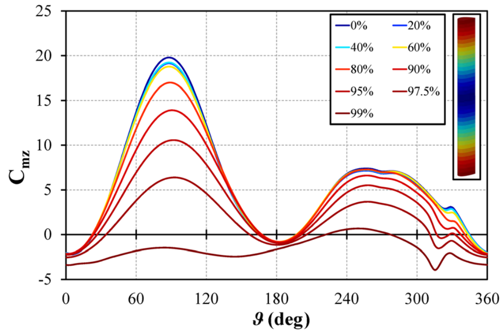

Fig. 7 CFD moment coefficient versus azimuthal angle: variation at different span lengths

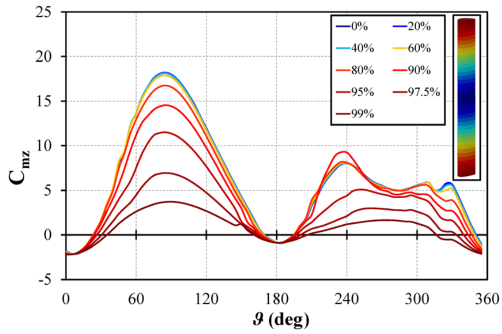

Fig. 8 LLFVW moment coefficient versus azimuthal angle: variation at different span lengths

$$C_{mz} = \frac{T_z}{\frac{1}{2}\rho_\infty U_\infty^2 c^2} \tag{2}$$

The periodic profiles of the torque coefficient per unit length at different span positions along the blade for the CFD and the LLFVW simulations are shown in Figs. 7 and 8, respectively. In the figures, the "0%" mark corresponds to midspan, while the "100%" mark corresponds to the tip section.

One notes that the agreement between the torque profiles obtained with the two approaches in the upwind part of the revolution (i.e., from $\vartheta = 0$ deg to $\vartheta = 180$ deg) is generally good.

The torque peak values are consistent both in terms of amplitude and angular location. The blades are characterized by a predominantly 2D flow with negligible impact of tip flow effects up to 60% of the semispan. The curves at 0%, 20%, 40%, and 60% are almost superimposed in both cases, while the efficiency reduction is clearly visible starting from 80% semispan. Moreover, in both cases the azimuthal position of the torque peak occurs later in the cycle as one moves toward the tip, with a shift between the 0% and 97.5% sections of about 5 deg. The torque reduction predicted by the two codes is comparable also at the spanwise positions closer to the tip, except for the section very close to the tip (99%), where the LLFVW is not able to predict the abrupt reduction of the torque and its negative values.

Two reasons for this discrepancy can be identified: One is that the spanwise discretization of LLFVW is much coarser than that of the CFD setup. Due to this, in the LLFVW simulation, the local moment coefficient, very close to the tip, is only interpolated and not explicitly calculated at the respective position. The other reason is that the flow in the tip region is highly three-dimensional due to the influence of the tip vortex. One of the main assumptions of the LLFVW method is that, when blade forces are evaluated

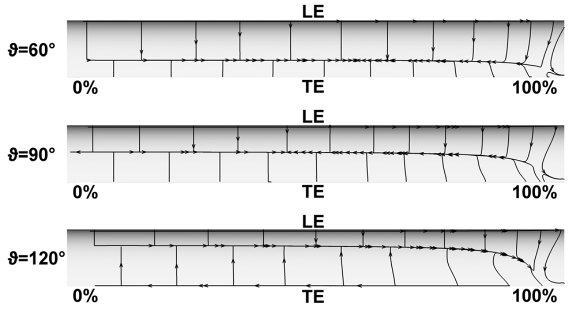

Fig. 9 Skin friction lines on the blade suction surface at different azimuthal positions

using airfoil data, the flow on the blade surface is two-dimensional. Even though the three-dimensional flow in the tip region affects the inflow vectors in the virtual airfoil planes of the LLFVW method and thereby has an effect on the generated lift and drag, the inherent simplification of the physics in this method leads to inaccurate estimates when assumptions are violated. To give an estimate of the 2D and 3D flow regions on the blade, Fig. 9 shows their extensions for three angular positions close to the torque peak. In the rear of the suction side, the region of separated flow increases moving from $\vartheta = 60\,\mathrm{deg}$ to $\vartheta = 120\,\mathrm{deg}$, and the downwash effect due to the tip flows increases as well.

As a result, at $\vartheta = 60\,\mathrm{deg}$ a highly 3D flow region covers about 7% of the blade length in the tip region, while this region increases up to 15% of the blade semispan at $\vartheta = 120\,\mathrm{deg}$.

In the downwind position of the blade trajectory, the agreement of the torque profiles of the two codes is slightly poorer, although the mean torque values are still comparable, similarly to the magnitude of the torque reduction along the blade span. More specifically, although a fairly good agreement of the two codes is observed in the profiles at the spanwise positions above 90% semispan (except for the section at 99% semispan, for the reasons provided earlier), significant discrepancies occur around $\vartheta = 240\,\mathrm{deg}$, where the LLFVW torque at 90% semispan is significantly higher than that of the RANS analysis, and $\vartheta = 270\,\mathrm{deg}$, where the LLFVW torque is instead visibly smaller. To assess the impact of 3D effects from an aggregate point of view, the overall torque coefficient C_m of the 3D rotor defined by the below equation was analyzed.

$$C_m = \frac{2}{H}\int_0^{\frac{H}{2}} C_{mz} dz \tag{3}$$

Figure 10 compares the mean 3D torque profiles obtained with the CFD analysis and the corresponding estimate obtained with the LLFVW code. The figure also provides the results of the 2D simulations of the same rotor [27], which were performed to provide the "ideal" torque of a blade with infinite span, i.e., without any secondary effects at the blade tip.

The comparison of these torque profiles shows that the ideal 2D torque and the 3D torque profiles are characterized by similar patterns. Since the tip losses affect only a marginal portion of the blade, no substantial modifications to the shape of the torque curve can be observed, but only a slight reduction in amplitude. For both numerical methods, the relative maxima occur at the same azimuthal positions, with a larger reduction in the upwind part of the revolution. Conversely, when the angle of attack to the airfoil is small (i.e., $0\,\mathrm{deg} < \vartheta < 40\,\mathrm{deg}$ and $150\,\mathrm{deg} < \vartheta < 210\,\mathrm{deg}$), the 2D and 3D curves are almost superimposed. An overall good agreement of CFD and LLFVW results in the estimation of the torque modification due to the finite blade span is noticed.

Detailed Flow Field Analyses. In this section, the 3D flow field resulting from the interaction of the rotor and the oncoming wind is analyzed in detail. Main flow structures are described in terms of velocity and vorticity, in order to highlight the main aerodynamic phenomena occurring during the revolution.

The planes used for the comparative analysis are schematically displayed in Fig. 11.

Fluid structures were investigated in the three Cartesian plane sets, at various distances from the rotor. More specifically, the following planes were considered:

- Horizontal X–Y planes: five positions along the blade semispan, starting from midspan ($z/H = 0$) to the tip ($z/H = 1$).
- Vertical Y–Z planes: four positions downstream the rotor, equally spaced by half rotor diameter ($0.5D$), starting from the rotor axis ($x/D = 0$).
- Vertical X–Z planes: three lateral positions at $0.6\,R$, $0.8\,R$, and $0.9\,R$ from the rotor axis.

In all of the following figures, LLFVW results are depicted in the left subplots, while the CFD ones are reported in the right subplots.

A comparison of the front views of the fields of the velocity modulus on the vertical Y–Z planes downstream of the rotor is shown in Fig. 12. Here, the blade is positioned at the azimuthal position of maximum C_m ($\vartheta \approx 90\,\mathrm{deg}$) and only half of the rotor height is shown, i.e., the upper blade semispan. The rectangular area swept by the blade is highlighted by light gray lines and the blade is shadowed in dark gray.

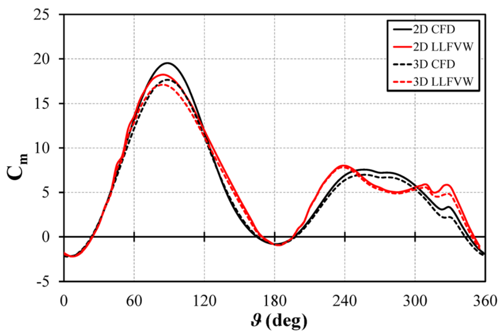

Fig. 10 Moment coefficient versus azimuthal angle: 2D simulations compared to the average 3D profiles

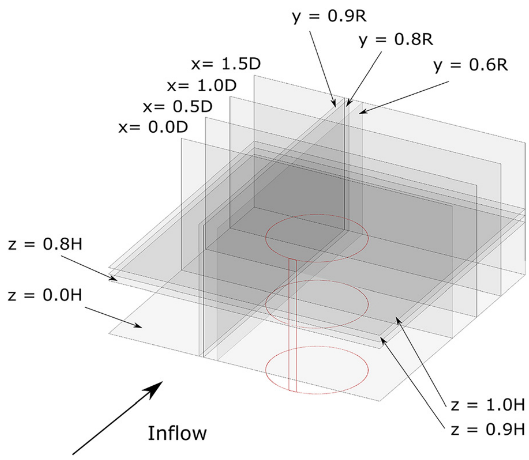

Fig. 11 Planes used for the comparative analysis of velocity and vorticity contours

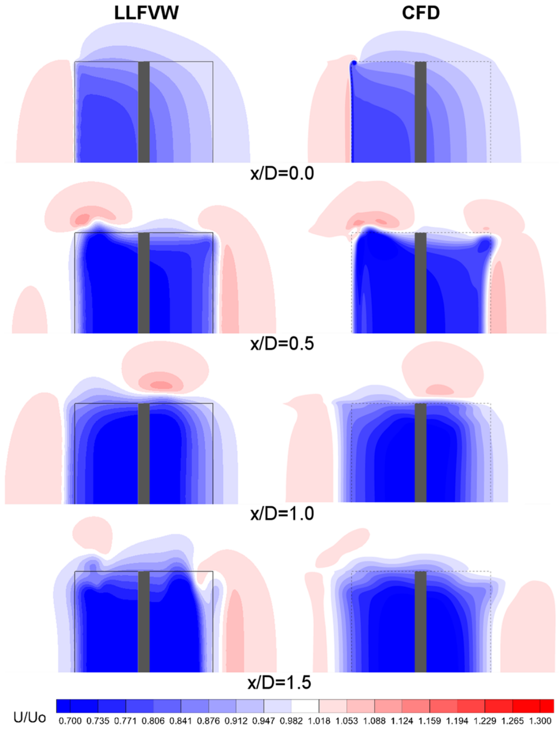

Fig. 12 Comparison of velocity contours between LLFVW (left) and CFD (right) on Y–Z planes at $\vartheta = 90\,\text{deg}$ for different distances downstream of the axis

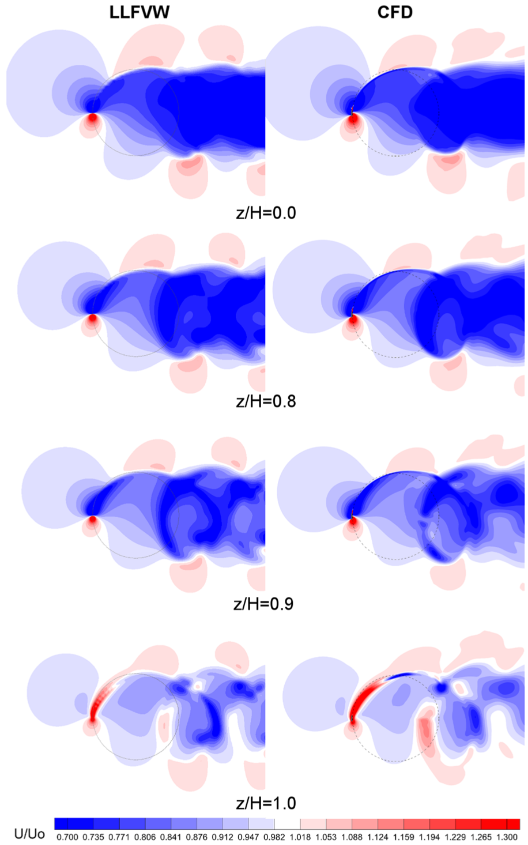

Fig. 13 Comparison of velocity contours between LLFVW (left) and CFD (right) on X–Y planes at $\vartheta = 90\,\text{deg}$ for different span positions

As expected from the analysis of the torque profiles comparison, the velocity contours predicted by the CFD and the LLFVW models show coherent results. The wake patterns confirm the consistency of the two approaches, since many similarities in the flow features can be observed. A significant reduction of velocity can be observed in the wake, whose shape becomes more regular, symmetric, and similar to the rotor swept area moving away from the rotor. At the streamwise position of the rotor axis ($x/D = 0$), the velocity deficit is asymmetric, with a higher deficit in the windward region of the wake, i.e., in the left side of the turbine frontal area.

At $x/D = 0$, the flow nonuniformity is marked also in the spanwise direction, since it affects about 40% of the blade semispan. At $x/D = 0.5$, the effects of the tip vortex at the top right corner can be also noticed, which determines a distortion of the wake. A notable similarity of the regions of accelerated flow can be observed at all the positions. Few discrepancies between the two solution sets can be, however, noticed, mainly related to a widening of the velocity deficit above the rotor with the LLFVW and a slightly larger instability of the wake at $x/D = 1.5$. Figure 13 shows the top views of the velocity fields on the horizontal X–Y planes at different semispan positions. The blade is again at $\vartheta = 90\,\text{deg}$ and its trajectory is indicated by the circular lines (the rotation is counter-clockwise). Remarkable agreement between the two solutions is observed again. At midspan, the wake is asymmetric, as already shown in Fig. 12, and remains almost unaltered up to 60% of the semispan.

The CFD results show a wider area of low-velocity upstream of the rotor in reason of the higher energy extraction by the turbine, as also indicated by the larger values of the torque coefficient C_{mz} in Fig. 7. At $z/H = 0.8$, a global attenuation of the velocity deficit behind the blade is visible, partly due to the fact that the outboard sections of the blade extract far less energy from the oncoming fluid and thus do not reduce the downstream velocity as much as the inboard sections do. In the tip proximity ($z/H = 1.0$), the strong acceleration of the flow leaking over the blade tip is also clearly visible. This produces a relevant asymmetry of the shape of the wake, which is more pronounced in CFD results.

To analyze the tip vortex flow and its interaction with the blade wake, the vorticity field is examined. Figure 14 shows contour slices of the z-component of the flow vorticity on the considered horizontal X–Y planes when the blade is at $\vartheta = 90\,\text{deg}$.

Overall, good agreement in the wake behavior was found when comparing LLFVW and CFD solutions. These vorticity contours show that, even though the resemblance of the wake behavior predicted by the two methods is good, the wakes of the CFD solution are initially thinner. One of the reasons for this could be that the LLFVW method does not take into account the shape of the blade, and also that the mesh density of the CFD setup is notably higher.

On the other hand, the vortices shed by the blade shortly after $\vartheta = 90\,\text{deg}$ appear to be resolved more sharply by the LLFVW method, since such approach has very low dissipation affecting the free convection of vorticity. Further inspection of the LLFVW and CFD solutions suggests that the differences between the two approaches increase from midspan toward the tip. The z-vorticity generated by the tip vortices appears to be stronger when using the CFD method rather than the LLFVW. This could be due to the much coarser grid used at the blade tip in the LLFVW simulation.

Figure 15 compares the contours of the y-component of the flow vorticity on different vertical X–Z planes at $\vartheta = 90\,\text{deg}$. Half of the rotor height is shown and the lateral view of the virtual

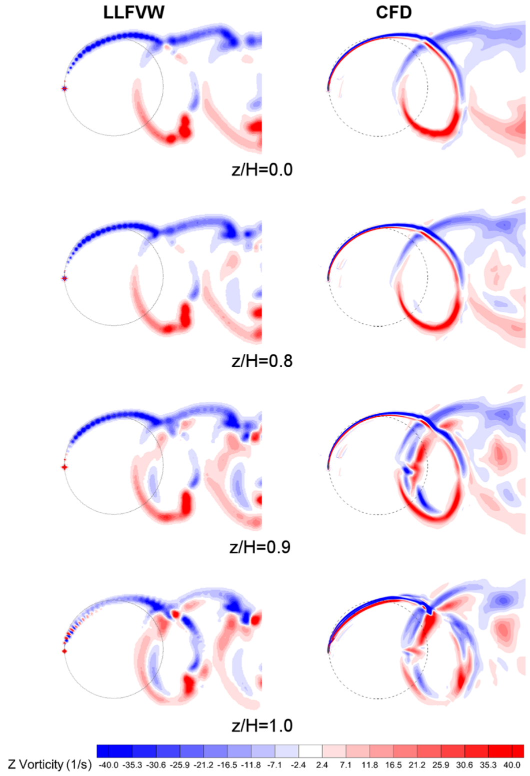

Fig. 14 Comparison of *Z*-vorticity contours between LLFVW (left) and CFD (right) on *X–Y* planes at $\vartheta = 90\,$deg for different span positions

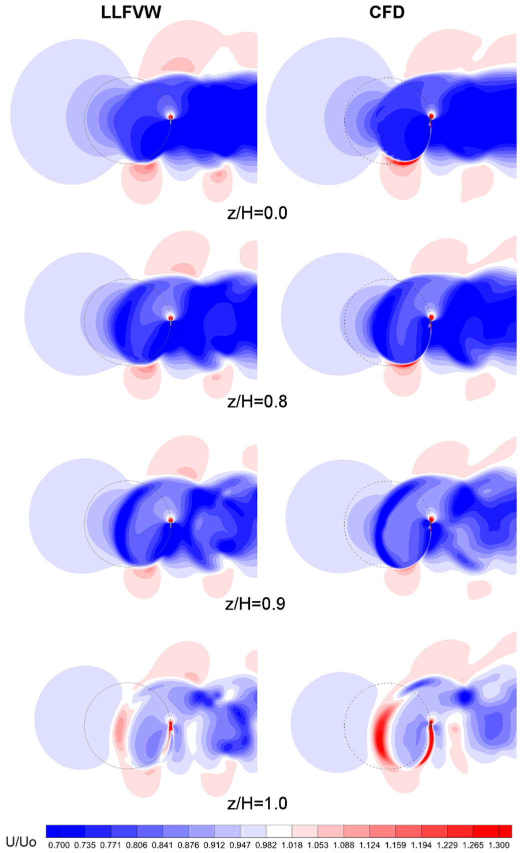

Fig. 16 Comparison of velocity contours between LLFVW (left) and CFD (right) on *X–Y* planes at $\vartheta = 270\,$deg for different span positions

cylinder swept by the blade is highlighted by horizontal and vertical black straight lines. A good similarity of the two simulations is observed in all the considered planes.

Note also that the fluid leaking at the tip generates a vortex that leaves the blade and is convected downstream. The vortex expansion due to its progressive deceleration makes it large enough to enter the virtual cylinder swept by the blade and affect a fairly large portion of the blade interacting with it in the downwind half of the revolution, as already shown in Figs. 7 and 8. Three different vortices, generated during as many revolutions, are visible in the results of both approaches.

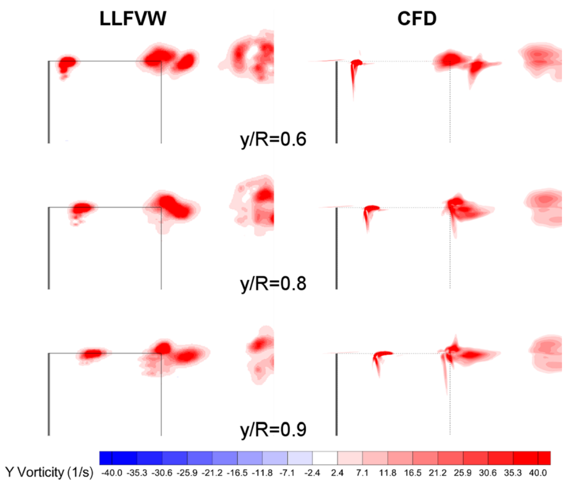

Fig. 15 Comparison of *Y*-vorticity contours between LLFVW (left) and CFD (right) on *X–Z* planes at $\vartheta = 90\,$deg for different lateral positions

As already highlighted in Fig. 14, the lower dissipation of the LLFVW method preserves the intensity of the vortices downstream the rotor, which are instead dissipated faster in the CFD solution.

The turbine wake was examined also at $\vartheta = 270\,$deg, where the larger mismatch in terms of torque output between the two codes was noticed. Figure 16 shows the top view of the velocity fields on the horizontal *X–Y* planes at different semispan positions. All the main flow features are reproduced fairly well by both codes, even though some discrepancies can be noticed, particularly in the blade wake prediction.

The CFD solution shows a high-velocity zone in the blade wake at all span heights, which is not present in the LLFVW solution.

Also in this circumstance, the reason should be related to the physical thickness of the airfoil, which is accounted for only in the CFD method.

Figure 17 shows contour slices of the z-component of the flow vorticity at five spanwise positions at the azimuthal position $\vartheta = 270\,$deg. Similarly to the $\vartheta = 90\,$deg case, good agreement on the behavior of the blade's wake is generally found between the LLFVW and CFD solutions. As soon as they are detached from the blades, wakes predicted by the CFD solution are sharper than those of LLFVW, suggesting a slower wake diffusion of the wake

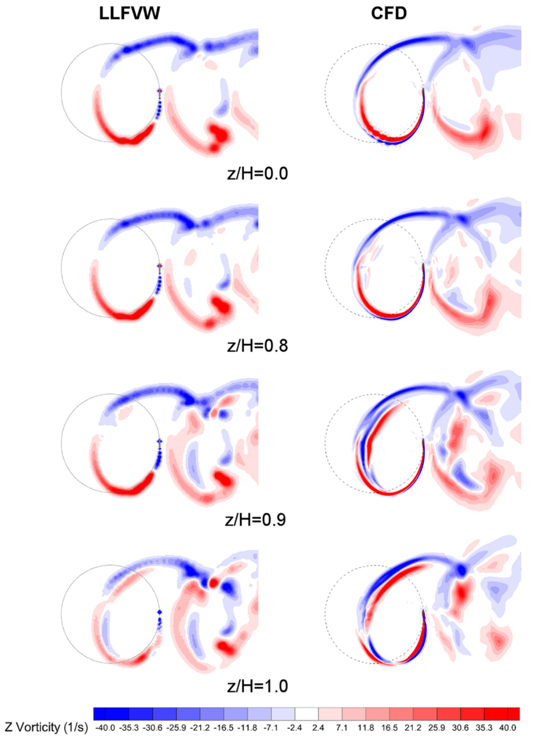

Fig. 17 Comparison of *Z*-vorticity contours between LLFVW (left) and CFD (right) on *X*–*Y* planes at $\vartheta = 270$ deg for different span positions

predicted by CFD. On the other hand, the shed vortices behind the trailing edge are resolved more sharply by the LLFVW, which limits their coalescence.

Overall, the *z*-vorticity generated by the tip vortices is stronger when using the CFD method, thus generating a stronger wake. Finally, the differences between the two approaches increase from midspan toward the tip.

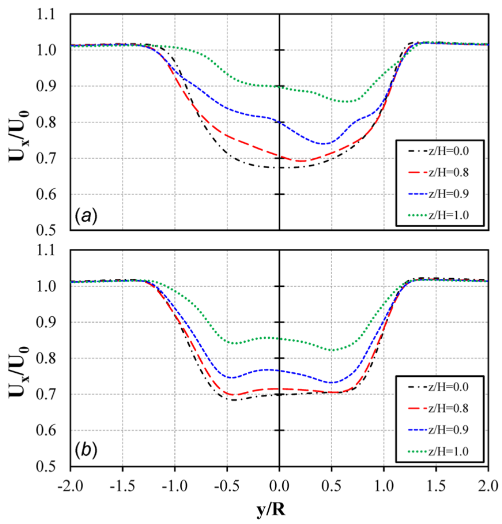

Fig. 18 Average velocity profile comparison between LLFVW and CFD on *X*–*Y* planes at different span heights at $X/D = 0$ (*a*) and $X/D = 1$ (*b*)

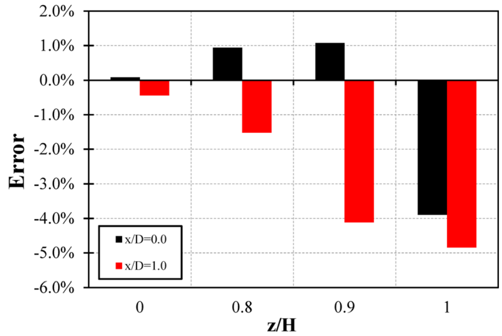

Fig. 19 Relative error of average velocity predicted by CFD and LLFVW along the span height at $X/D = 0$ and $X/D = 1$

Finally, the velocity profiles along the *y*-direction at four different spanwise positions were extracted and averaged along the whole revolution. Figure 18 reports the comparison between the results of the two numerical approaches for $x/D = 0$ (Fig. 18(*a*)) and $x/D = 1$ (Fig. 18(*b*)). It is apparent that the matching is very coherent for the half-rotor location ($x/D = 0$), while some discrepancies exist for the location downstream the rotor ($x/D = 1$), as also highlighted by the error analysis reported in Fig. 19. Beside possible differences in the resolution of the wake evolution, this behavior can be physically related to what already pointed out for the profiles of the torque coefficient of Figs. 7 and 8.

The predicted torque in the upwind half of the rotation is very similar, leading to similar predictions of the energy extraction and similar velocity deficit at $x/D = 0$. Conversely, the discrepancies in the torque prediction at the angular position of $\vartheta = 240$ deg and $\vartheta = 270$ deg lead to an analogous behavior of the wake profiles. Indeed, the differences are significant for $y/D < 0$, while similar trends are obtained for $y/D > 0$, corresponding to the windward half of the rotation. Notwithstanding this, it can be pointed out that the overall amplitudes of the velocity deficit are coherent for all the analyzed locations.

The level of agreement between the velocity predictions in the wake was assessed quantitatively by calculating the percentage difference between the CFD and LLFVW profiles.

The values were averaged along the *y*-direction in the range $-1 < y/R < 1$ and the percentage differences at various blade heights are reported in Fig. 19. These results confirm that the differences between the two predictions are very low (below 1.5%) for most of the wake region and tend to increase up to roughly 5% only in proximity of the tip. At each span position, the difference between the two codes is lower at $x/D = 0$ than at $x/D = 1$.

Conclusions

In this study, the 3D numerical simulation of a single blade in Darrieus-like motion was carried out with both a highly refined, time-dependent CFD model and an LLFVW code.

A CFD mesh featuring a very fine discretization level was used to accurately solve the flow field, in order to provide highly resolved data to assess the prediction capabilities of the LLFVW method.

The comparison showed an extremely promising agreement between the results. In particular, the investigation of the torque reduction due to finite-blade effect confirmed the consistency on the two approaches in predicting the efficiency reduction as a function of the blade span. The discrepancies in the LLFVW curves are related to a slight underestimation of the torque peak and to the presence of a torque deficit at the azimuthal position $\vartheta = 270$ deg. A comparative analysis of the velocity and vorticity contours was then carried out to better highlight the capability of predicting the most relevant flow features. The rotor wake analysis showed similar velocity patterns and fairly good agreement of the vorticity fields.

The results demonstrated that the LLFVW model can provide accurate results and a good prediction of most 3D flow features with a great advantage in terms of low computational cost. Indeed, the computational cost of the LLFVW calculation is more than 6 orders of magnitude lower than the one of the CFD simulation. However, thanks to the constant increase of the hardware performance, the possibility of performing accurate 3D CFD simulations is, and will be, pivotal to provide high-quality data for the validation and calibration of such low-order models.

Acknowledgment

The authors acknowledge the use of Hartree Centre resources in this work. Part of the reported simulations was also performed on two other clusters. One is POLARIS (coordinated by the Universities of Leeds and Manchester) part of the N8 HPC facilities provided and funded by the N8 consortium and EPSRC (Grant No. EP/K000225/1). The other resource is the HEC cluster of Lancaster University, which is also kindly acknowledged. Finally, thanks are due to Professor Ennio Antonio Carnevale of the Università degli Studi di Firenze for supporting this research.

Nomenclature

BEM = blade element momentum
c = blade chord (m)
C_{mz} = moment coefficient around the z-axis
CFD = computational fluid dynamics
CP = power coefficient
k = turbulence kinetic energy (m^2/s^2)
LLFVW = lifting line free vortex wake
NS = Navier–Stokes
R, D = turbine radius, diameter (m)
RANS = Reynolds-averaged Navier–Stokes
S_c = vortex time offset parameter (s)
SST = shear stress transport
t = time (s)
TSR = tip-speed ratio
U = wind speed (m/s)
VAWT = vertical axis wind turbine
X, Y, Z = reference axes
y^+ = dimensionless wall distance

Greek Symbols

δ_v = turbulent viscosity parameter
ε = vortex strain
ν = kinematic viscosity (m^2/s)
ρ = fluid density (kg/m^3)
Φ = computational domain diameter (m)
Ψ = computational domain height (m)
ω = specific turbulence dissipation rate (1/s)
ϑ = azimuthal position of the blade (rad)

Subscript

∞ = value at infinity

References

[1] Paraschivoiu, I., 2002, *Wind Turbine Design With Emphasis on Darrieus Concept*, Polytechnic International Press, Montreal, QC, Canada.
[2] Mohamed, M. H., 2014, "Aero-Acoustics Noise Evaluation of H-Rotor Darrieus Wind Turbines," Energy, **65**(1), pp. 596–604.
[3] Balduzzi, F., Bianchini, A., Carnevale, E. A., Ferrari, L., and Magnani, S., 2012, "Feasibility Analysis of a Darrieus Vertical-Axis Wind Turbine Installation in the Rooftop of a Building," Appl. Energy, **97**, pp. 921–929.
[4] Bianchini, A., Ferrari, L., and Magnani, S., 2012, "Energy-Yield-Based Optimization of an H-Darrieus Wind Turbine," ASME Paper No. GT2012-69892.
[5] Marten, D., Bianchini, A., Pechlivanoglou, G., Balduzzi, F., Nayeri, C. N., Ferrara, G., Paschereit, C. O., and Ferrari, L., 2016, "Effects of Airfoil's Polar Data in the Stall Region on the Estimation of Darrieus Wind Turbines Performance," ASME J. Eng. Gas Turbines Power, **139**(2), p. 022606.
[6] Marten, D., Lennie, M., Pechlivanoglou, G., Nayeri, C. D., and Paschereit, C. O., 2016, "Nonlinear Lifting Line Theory Applied to Vertical Axis Wind Turbines: Development of a Practical Design Tool," International Symposium on Transport Phenomena and Dynamics of Rotating Machinery (ISROMAC), Honolulu, HI, Apr. 10–15, pp. 1–7.
[7] Dossena, V., Persico, G., Paradiso, B., Battisti, L., Dell'Anna, S., Brighenti, A., and Benini, E., 2015, "An Experimental Study of the Aerodynamics and Performance of a Vertical Axis Wind Turbine in Confined and Non-Confined Environment," ASME Paper No. GT2015-42827.
[8] Bachant, P., and Wosnik, M., 2015, "Characterising the Near-Wake of a Cross-Flow Turbine," J. Turbul., **16**(4), pp. 392–410.
[9] Bianchini, A., Balduzzi, F., Bachant, P., Ferrara, G., and Ferrari, L., 2017, "Effectiveness of Two-Dimensional CFD Simulations for Darrieus VAWTs: A Combined Numerical and Experimental Assessment," Energy Convers. Manage., **136**, pp. 318–328.
[10] Balduzzi, F., Bianchini, A., Maleci, R., Ferrara, G., and Ferrari, L., 2016, "Critical Issues in the CFD Simulation of Darrieus Wind Turbines," Renewable Energy, **85**(1), pp. 419–435.
[11] Balduzzi, F., Bianchini, A., Ferrara, G., and Ferrari, L., 2016, "Dimensionless Numbers for the Assessment of Mesh and Timestep Requirements in CFD Simulations of Darrieus Wind Turbines," Energy, **97**, pp. 246–261.
[12] Balduzzi, F., Bianchini, A., Gigante, F. A., Ferrara, G., Campobasso, M. S., and Ferrari, L., 2015, "Parametric and Comparative Assessment of Navier–Stokes CFD Methodologies for Darrieus Wind Turbine Performance Analysis," ASME Paper No. GT2015-42663.
[13] Lam, H. F., and Peng, H. Y., 2016, "Study of Wake Characteristics of a Vertical Axis Wind Turbine by Two- and Three-Dimensional Computational Fluid Dynamics Simulations," Renewable Energy, **90**, pp. 386–398.
[14] Raciti Castelli, M., Pavesi, G., Battisti, L., Benini, E., and Ardizzon, G., 2010, "Modeling Strategy and Numerical Validation for a Darrieus Vertical Axis Micro-Wind Turbine," ASME Paper No. IMECE2010-39548.
[15] Untaroiu, A., Wood, H. G., Allaire, P. E., and Ribando, R. J., 2011, "Investigation of Self-Starting Capability of Vertical Axis Wind Turbines Using a Computational Fluid Dynamics Approach," ASME J. Solar Energy Eng., **133**(4), p. 041010.
[16] Alaimo, A., Esposito, A., Messineo, A., Orlando, C., and Tumino, D., 2015, "3D CFD Analysis of a Vertical Axis Wind Turbine," Energies, **8**(4), pp. 3013–3033.
[17] De Marco, A., Coiro, D. P., Cucco, D., and Nicolosi, F., 2014, "A Numerical Study on a Vertical-Axis Wind Turbine With Inclined Arms," Int. J. Aerosp. Eng., **2014**, pp. 1–14.
[18] Raciti Castelli, M., and Benini, E., 2012, "Effect of Blade Inclination Angle on a Darrieus Wind Turbine," ASME J. Turbomach., **134**(3), p. 031016.
[19] Orlandi, A., Collu, M., Zanforlin, S., and Shires, A., 2015, "3D URANS Analysis of a Vertical Axis Wind Turbine in Skewed Flows," J. Wind Eng. Ind. Aerodyn., **147**, pp. 77–84.
[20] Bianchini, A., Balduzzi, F., Ferrara, G., Ferrari, L., Persico, B., Dossena, V., and Battisti, L., 2017, "Detailed Analysis of the Wake Structure of a Straight-Blade H-Darrieus Wind Turbine by Means of Wind Tunnel Experiments and CFD Simulations," ASME Paper No. GT2017-64733.
[21] Bianchini, A., Balduzzi, F., Ferrara, G., Ferrari, L., Persico, B., Dossena, V., and Battisti, L., 2017, "A Combined Experimental and Numerical Analysis of the Wake Structure and Performance of a H-Shaped Darrieus Wind Turbine," First GPPS Forum, Zürich, Switzerland, Jan. 16–18, pp. 1–8.
[22] Menter, F. R., 1994, "Two-Equation Turbulence-Models for Engineering Applications," AIAA J., **32**(8), pp. 1598–1605.
[23] Campobasso, M. S., Piskopakis, A., Drofelnik, J., and Jackson, A., 2013, "Turbulent Navier–Stokes Analysis of an Oscillating Wing in a Power Extraction Regime Using the Shear Stress Transport Turbulence Model," Comput. Fluids, **88**, pp. 136–155.
[24] Drofelnik, J., and Campobasso, M. S., 2016, "Comparative Turbulent Three-Dimensional Navier–Stokes Hydrodynamic Analysis and Performance Assessment of Oscillating Wings for Renewable Energy Applications," Int. J. Mar. Energy, **16**, pp. 100–115.
[25] Campobasso, M. S., Gigante, F., and Drofelnik, J., 2014, "Turbulent Unsteady Flow Analysis of Horizontal Axis Wind Turbine Airfoil Aerodynamics Based on the Harmonic Balance Reynolds-Averaged Navier–Stokes Equations," ASME Paper No. GT2014-25559.
[26] Campobasso, M. S., and Baba-Ahmadi, M. H., 2012, "Analysis of Unsteady Flows Past Horizontal Axis Wind Turbine Airfoils Based on Harmonic Balance Compressible Navier–Stokes Equations With Low-Speed Preconditioning," ASME J. Turbomach., **134**(6), p. 061020.
[27] Bianchini, A., Balduzzi, F., Ferrara, G., and Ferrari, L., 2017, "Aerodynamics of Darrieus Wind Turbines Airfoils: The Impact of Pitching Moment," ASME J. Eng. Gas Turbines Power, **139**(4), p. 042602.
[28] Gigante, F. A., Balduzzi, F., Bianchini, A., Minghan, Y., Ferrara, G., Campobasso, M. S., and Ferrari, L., 2017, "Low-Speed Preconditioning for Strongly Coupled Integration of Reynolds-Averaged Navier-Stokes Equations and Two-Equation Turbulence Models," Comput. Fluids (submitted).
[29] Rainbird, J., Bianchini, A., Balduzzi, F., Peiro, J., Graham, J. M. R., Ferrara, G., and Ferrari, L., 2015, "On the Influence of Virtual Camber Effect on Airfoil Polars for Use in Simulations of Darrieus Wind Turbines," Energy Convers. Manage., **106**, pp. 373–384.
[30] Campobasso, M. S., Drofelnik, J., and Gigante, F., 2016, "Comparative Assessment of the Harmonic Balance Navier–Stokes Technology for Horizontal and

Vertical Axis Wind Turbine Aerodynamics," Comput. Fluids, **136**, pp. 354–370.
[31] The Hartree Centre, 2017, "Hartree Centre," The Hartree Centre, Warrington, UK, accessed May 10, 2016, http://community.hartree.stfc.ac.uk/wiki/site/admin/resources.html
[32] Marten, D., Pechlivanoglou, G., Nayeri, C. N., and Paschereit, C. O., 2010, "Integration of a WT Blade Design Tool in XFOIL/XFLR5," German Wind Energy Conference (DEWEK), Bremen, Germany, Nov. 17–18, pp. 1–4.
[33] Marten, D., Wendler, J., Pechlivanoglou, G., Nayeri, C. N., and Paschereit, C. O., 2013, "QBlade: An Open Source Tool for Design and Simulation of Horizontal and Vertical Axis Wind Turbines," Int. J. Emerging Technol. Adv. Eng., **3**(3), pp. 264–269.
[34] Van Garrel, A., 2003, *Development of a Wind Turbine Aerodynamics Simulation Module*, Energy Research Centre of the Netherlands, Petten, The Netherlands, Report No. ECN-C-01-099.
[35] Marten, D., 2016, "QBlade Guidelines v0.95," Technical University of Berlin, Berlin, Germany.
[36] Marten, D., Lennie, M., Pechlivanoglou, G., Nayeri, C. D., and Paschereit, C. O., 2015, "Implementation, Optimization and Validation of a Nonlinear Lifting Line Free Vortex Wake Module Within the Wind Turbine Simulation Code QBlade," ASME J. Eng. Gas Turbines Power, **138**(7), p. 072601.
[37] Marten, D., Pechlivanoglou, G., Nayeri, C. N., and Paschereit, C. O., 2016, "Nonlinear Lifting Line Theory Applied to Vertical Axis Wind Turbines: Development of a Practical Design Tool," International Symposium on Transport Phenomena and Dynamics of Rotating Machinery (ISROMAC), Honolulu, HI, Apr. 10–15, pp. 1–7.
[38] Bergami, L., and Gaunaa, M., 2012, "ATEFlap Aerodynamic Model: A Dynamic Stall Model Including the Effects of Trailing Edge Flap Deflection," Technical University of Denmark, Kongens Lyngby, Denmark, Report No. Risø-R-1792(EN).
[39] Wendler, J., Marten, D., Pechlivanoglou, G., Nayeri, C. N., and Paschereit, C. O., 2016, "An Unsteady Aerodynamics Model for Lifting Line Free Vortex Wake Simulations of HAWT and VAWT in QBlade," ASME Paper No. GT2016-57184.
[40] Bianchini, A., Balduzzi, F., Rainbird, J., Peiro, J., Graham, J. M. R., Ferrara, G., and Ferrari, L., 2015, "An Experimental and Numerical Assessment of Airfoil Polars for Use in Darrieus Wind Turbines. Part I—Flow Curvature Effects," ASME J. Eng. Gas Turbines Power, **138**(3), p. 032602.
[41] Drela, M., and Giles, M., 1989, "Viscous-Inviscid Analysis of Transonic and Low Reynolds Number Airfoils," AIAA J., **25**(10), pp. 1347–1355.
[42] Montgomerie, B., 2004, "Methods for Root Effects, Tip Effects and Extending the Angle of Attack Range to ±100 deg, With Application to Aerodynamics for Blades on Wind Turbines and Propellers," FOI Swedish Defence Research Agency, Stockholm, Sweden, Report No. FOI-R-1035-SE.

3.2. Publication III: Benchmark of a Novel Aero-Elastic Simulation Code for Small Scale VAWT Analysis

Marten, D., Lennie, M., Pechlivanoglou, G., Paschereit, C. O., Bianchini, A., Ferrara, G., & Ferrari, L. (2018). Benchmark of a Novel Aero-Elastic Simulation Code for Small Scale VAWT Analysis. Journal of Engineering for Gas Turbines and Power, 141(4), 041014. https://doi.org/10.1115/1.4041519

In this publication the capability of the complete aero-elastic model, that is outlined in Chapter 2 of this work is demonstrated through aeroelastic simulations of a small scale helical VAWT. The helical VAWT that was simulated is a commercial of-the-shelf turbine. Its aerodynamic and structural properties were obtained from the manufacturers blueprints and sketches.

At first, purely aerodynamic LLFVW calculations of the VAWT are compared to the results of a Double-Multiple-Streamtube (DMST) code. An analysis of the near rotor flow field is then carried out to highlight the sources of inaccuracies found in the DMST predictions. Subsequently a modal analysis of the structural VAWT model in QBlade is performed and the resulting Campbell diagram is compared to the results of a commercial tool. Finally, an aeroelastic start-up simulation of the VAWT is carried out. Due to the increasing rotational speed of the VAWT, and a thereby increasing excitation frequency, resonance at the first tower eigenmode, as previously predicted during the modal analysis, is observed.

David Marten[1]
Chair of Fluid Dynamics,
HFI TU Berlin,
Müller Breslau Strasse 8,
Berlin 10623, Germany
e-mail: david.marten@tu-berlin.de

Matthew Lennie
Chair of Fluid Dynamics,
HFI TU Berlin,
Müller Breslau Strasse 8,
Berlin 10623, Germany

George Pechlivanoglou
Chair of Fluid Dynamics,
HFI TU Berlin,
Müller Breslau Strasse 8,
Berlin 10623, Germany

Christian Oliver Paschereit
Chair of Fluid Dynamics,
HFI TU Berlin,
Müller Breslau Strasse 8,
Berlin 10623, Germany

Alessandro Bianchini
Department of Industrial Engineering,
Università degli Studi di Firenze,
Via di Santa Marta 3,
Firenze 50139, Italy

Giovanni Ferrara
Department of Industrial Engineering,
Università degli Studi di Firenze,
Via di Santa Marta 3,
Firenze 50139, Italy

Lorenzo Ferrari
DESTEC,
Università di Pisa Largo Lucio Lazzarino,
Pisa 56122, Italy

Benchmark of a Novel Aero-Elastic Simulation Code for Small Scale VAWT Analysis

After almost 20 years of absence from research agendas, interest in the vertical axis wind turbine (VAWT) technology is presently increasing again, after the research stalled in the mid 90's in favor of horizontal axis wind turbines (HAWTs). However, due to the lack of research in past years, there are a significantly lower number of design and certification tools available, many of which are underdeveloped if compared to the corresponding tools for HAWTs. To partially fulfill this gap, a structural finite element analysis (FEA) model, based on the Open Source multiphysics library PROJECT::CHRONO, was recently integrated with the lifting line free vortex wake (LLFVW) method inside the Open Source wind turbine simulation code QBlade and validated against numerical and experimental data of the SANDIA 34 m rotor. In this work, some details about the newly implemented nonlinear structural model and its coupling to the aerodynamic solver are first given. Then, in a continuous effort to assess its accuracy, the code capabilities were here tested on a small-scale, fast-spinning (up to 450 rpm) VAWT. The study turbine is a helix shaped, 1 kW Darrieus turbine, for which other numerical analyses were available from a previous study, including the results coming from both a one-dimensional beam element model and a more sophisticated shell element model. The resulting data represented an excellent basis for comparison and validation of the new aero-elastic coupling in QBlade. Based on the structural and aerodynamic data of the study turbine, an aero-elastic model was then constructed. A purely aerodynamic comparison to experimental data and a blade element momentum (BEM) simulation represented the benchmark for QBlade aerodynamic performance. Then, a purely structural analysis was carried out and compared to the numerical results from the former. After the code validation, an aero-elastically coupled simulation of a rotor self-start has been performed to demonstrate the capabilities of the newly developed model to predict the highly nonlinear transient aerodynamic and structural rotor response. [DOI: 10.1115/1.4041519]

Introduction

Despite a long absence from research agendas, a growing interest into the study of Darrieus-type vertical axis wind turbines (VAWTs) can be observed [1], after the research stalled in the mid 90's in favor of the horizontal axis wind turbines (HAWTs) [2] that were adopted by the industry emerging at that time. This choice was due the higher power coefficients achievable with the horizontal-axis configuration, and a much better capability of self-starting, even in low winds, which was instead missing for the very first VAWT prototypes. There are two main fields of application where the Darrieus concept seems to offer some undisputed advantages in comparison to HAWTs. The first one is represented by deep water offshore applications with floating structures [3,4], where more favorable structural loads of the Darrieus architecture could lead to smaller floating structures, reduced logistics and capital cost and ultimately to a lower cost of energy. On the other hand, a significant growth can be observed in the market for small wind turbines for decentralized energy production [5]. In these applications, the Darrieus concept is even more exploited thanks to the insensitivity of these rotors on changes in wind direction [6], misaligned flows [7], or turbulence [8], and to their lower design complexity. In addition, they are almost noiseless [9] and with a lower visual impact [10].

However, due to the lack of a systematic research in past years, there are a significantly lower number of design and certification tools available, many of which are underdeveloped when compared to the corresponding tools for HAWTs. Numerical techniques based on computational fluid dynamics are considered to be the most accurate tools, since they are able to provide a detailed and comprehensive representation of the flow field around the blades in cycloidal motion (e.g., see Ref. [11]). On the other hand, these kinds of simulations are characterized by an enormous calculation cost, due to the strict requirements in terms of spatial and temporal discretizations [12]. From the above, one can argue that the massive use of computational fluid dynamics is presently prohibitive for routine application in industrial design, which instead makes use of low-and medium-fidelity models, like the blade element momentum (BEM) method [13] or the lifting line free vortex wake (LLFVW) method [14].

Even if these lower-order methods can show inaccuracies in some cases (e.g., see Ref. [15]), with respect to the prediction of aerodynamic performance, recent studies (e.g., see Ref. [16]) demonstrated that—if corrected to account for higher-order

[1]Corresponding author.

Manuscript received July 13, 2018; final manuscript received August 31, 2018; published online November 28, 2018. Editor: Jerzy T. Sawicki.

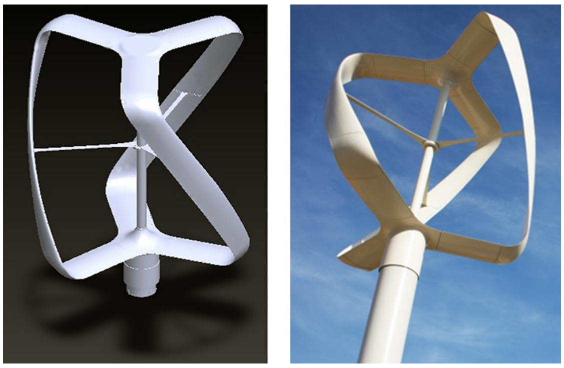

Fig. 1 Computer-aided design model (left) and on field picture (right) of the WT1 KW (courtesy of Pramac Spa)

phenomena like flow curvature effects [17–19] and dynamic stall [20]—they can provide reliable estimations of the overall turbine performance and the torque profiles for a wide range of operating conditions.

To really enable a diffusion of Darrieus rotors, however, increasing attention must be devoted to their structural design, for which whether an established constructive technology or common choice of materials is present yet. In further detail, proper aero-structural models are especially needed to model floating platforms (where the loads are pivotal for the dynamic floating behavior) and small rotors, which are forced to spin fast to get to the typical functioning tip-speed ratios (TSRs).

Moreover, robust and reliable structural tools also have an important application in turbine certification, following the standards of the IEC 61400-2 [21] and 64100-3 [22], for small and offshore turbines, respectively. When being applied in a turbine certification context, a high numerical efficiency is of principal importance as the needed number of converged aeroelastic timesteps is in the range of 10,000,000 when all design load cases are evaluated. To fulfill this requirement for an efficient aeroelastic model, the optimal balance between its accuracy and its numerical cost must be found when choosing the temporal and spatial discretization of the coupled aerodynamic and structural simulations.

To this end, a structural finite element analysis (FEA) model, based on the Open Source multiphysics library CHRONO [23], was recently integrated with the lifting line free vortex wake method inside the Open Source wind turbine simulation code QBlade [24–26]. The aero-elastic capabilities of this new simulation tool have been already benchmarked with numerical and experimental data of the SANDIA 34 m turbine in Ref. [27].

In this paper, a second benchmark will demonstrate the code capabilities to model a small-scale, fast-spinning (up to 450 rpm) Darrieus VAWT, for which structural simulations were available from a previous study [28].

Study Turbine

The turbine used as a benchmark for the present study is the PRAMAC (PR INDUSTRIAL s.r.l., Siena, Italy) *Revolutionair* WT1 KW (Fig. 1), a real industrial H-Darrieus rotor [29],[2] whose features are reported in Table 1.

The electric rated power of the turbine (1 kW) is declared by the manufacturer at a wind speed of 15 m/s and a TSR of 2.1 corresponding to a revolution speed of approximately 415 rpm.

As already discussed by some of the authors in Ref. [28], the structural layout of the turbine consists of a metal structure (i.e., the central tower plus six small appendixes to support the struts) to which other plastic components are connected [29]. The plastic material used to produce the rotor is a custom mix of high-resistance polypropylene and reinforcing fibers, whose characteristics have been calculated based on the general criteria proposed in Refs. [31] and [32]. The blades are made of two halves linked at middle span by metal plates sustained by the tie-rods, realized with metal profiles [28]. The internal structure of the blades includes several stiffening ribs, closed by thin plastic covers which can be hypothesized not to provide any influence on the structural behavior of the rotor.

[2] http://it.wikipedia.org/wiki/Revolutionair

Table 1 Main feature of the study turbine

Blade number (N)	3
Blade shape	Helix-shaped 60 deg
Airfoil	Symmetric custom [30]
Diameter, D (m)	1.45
Height, H (m)	1.45
Blade chord, c (m)	0.22
Moment of inertia, I_z (kg m^2)	7.6
AR	6.6
Solidity ($\Sigma = N_c/D$)	0.45

Aerodynamic Analysis

Before going into the structural simulation of the rotor, an aerodynamic analysis of the same was carried out, in order to assess the proper forces to be used within the following analyses. In a previous study [28] that involved the PRAMAC turbine, the rotor was simulated by some of the authors using a BEM method. Due to some recent findings in the accuracy improvements of low-order methods (e.g., see Refs. [13] and [16–18]), however, a cross-comparison between the BEM research code VARDAR and the nonlinear lifting line free vortex wake module in QBlade was carried out preliminary.

Vardar Aerodynamic Model Formulation

The VARDAR research code of the University of Firenze (Italy) [13,33] is based on an improved version of a *Double Multiple Streamtubes Approach with Variable Interference Factors* originally proposed by Professor Paraschivoiu in Ref. [6]. With respect to the "standard" formulation, the Glauert's correction for the BEM theory has been modified based on recent experimental data [34]. To increase the accuracy of the aerodynamic estimations, several submodels have been embedded within the code, including the corrections due to the finite aspect ratio of the blades (using the Lanchester–Prandtl model [35]), several dynamic stall models (in the present study the one by Gormont–Berg with AM = 6 was used [6]), and the stream tube expansion model presented in Ref. [6], although the incidence of this latter on the simulation of small turbines—like those investigated in this work—is limited. Furthermore, for the analyses presented in this study, some of the recent corrections available in the VARDAR code were used. In further detail, the corrections aim at modifying the tabulated polars in order to account for:

- Virtual Camber Effect: This effect, originally postulated from a theoretical point of view in Ref. [36], has been recently demonstrated with experiments [37] and numerical simulations [17]. In a cycloidal motion, the blade indeed behaves aerodynamically (i.e., in terms of lift, drag and moment coefficients) like a virtually transformed equivalent airfoil with a camber line defined by its arc of rotation. From the perspective of the code, this means that the coefficients of the virtually cambered airfoil must be used as tabulated inputs if proper results are about to be achieved. The consistency of this correction has been widely demonstrated recently in Ref. [19].

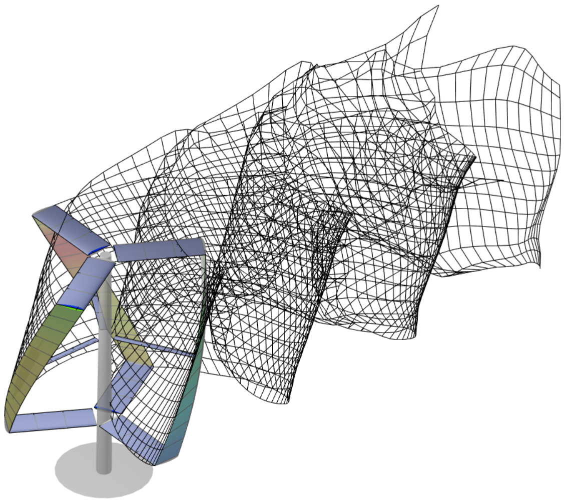

Fig. 2 Overview about blade, strut and wake discretization for the aerodynamic LLFVW method in QBlade

- Virtual Incidence Effect: In addition to the virtual cambering, the airfoils in cycloidal motion may also experience extra-incidence due to flow curvature [18]. Some of the authors, showed in Ref. [19] that in BEM codes a constant mean virtual incidence can correctly predict the impact of such an effect on the power curve. In a first approximation, this value can be assumed to correspond to the average virtual incidence along the revolution, calculated by means of the simplified kinematic analysis proposed in Ref. [36].
- Smoothing of Lift and Drag Polars in the Stall Region: A recent study [16] showed that, in order to increase the accuracy of low-order models, it is pivotal to provide a smoothing of the airfoil polars (especially of the lift one) in proximity of the stall region. This precaution is needed since airfoils in motion experience a progressive and continuous variation of the angle of attack, which does not originate the abrupt drop in the lift force just after the static stall angle [38]. According to Ref. [16], the polars in this study were smoothed with the Viterna model [39].
- Accurate Poststall Data: Due to their intrinsic functioning principle, airfoils in Darrieus motion experience a wide range of angles of attack, which commonly exceed the static stall angle. The use of accurate poststall data is then extremely beneficial for improving the prediction capabilities of low-order models [16]. For this reason, the experimental full-360 deg polars of the airfoil were here provided [40].

QBlade Aerodynamic Model Formulation

QBlade uses the lifting line free vortex wake [14] method to calculate the aerodynamics of wind turbines.

The blade is discretized into panels, to which the circulation is assigned from tabulated lift and drag airfoil data. The spanwise oriented Lifting Line at the blades is connecting the quarter chord positions of the panels. Chordwise oriented bound vorticity at the blades accounts for the circulation gradient in the spanwise direction. Blade struts are included in the model through aerodynamic panels for which only the drag influence is calculated. The wake is modeled through free vortex line elements that are convected with the local point velocities during every timestep. An overview of the blade, the strut, and the wake discretization is given in Fig. 2.

All point velocities in the model are calculated using a Biot–Savart kernel for the combined influences of all the vortex elements in the simulation setup. The employed Biot–Savart kernel is regularized using a vortex core model that also accounts for vortex viscosity and stretching. To reduce the calculation time per timestep, which scales proportionally to the square of the total number of vortex elements, the evaluations are carried out in parallel on the graphics processing unit using the OpenCL framework. The Gormont–Berg (using AM = 6) method is used to model dynamic stall during the calculations. The airfoil polars in the simulation setup have been "smoothed" in the poststall region by an interpolation between the original lift and drag data and the Viterna extrapolation and are the same polars that the VARDAR code used in this study.

Rotor Performance Analysis

Figure 3 first shows a comparison of the power coefficient curves of the rotor at three relevant wind speeds of 4, 8, and

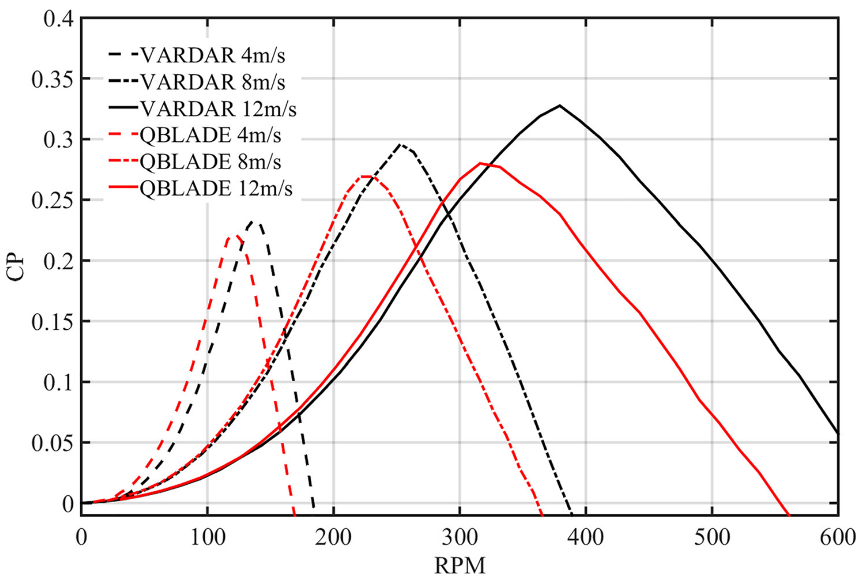

Fig. 3 Power coefficient versus rotational speed for three wind velocities

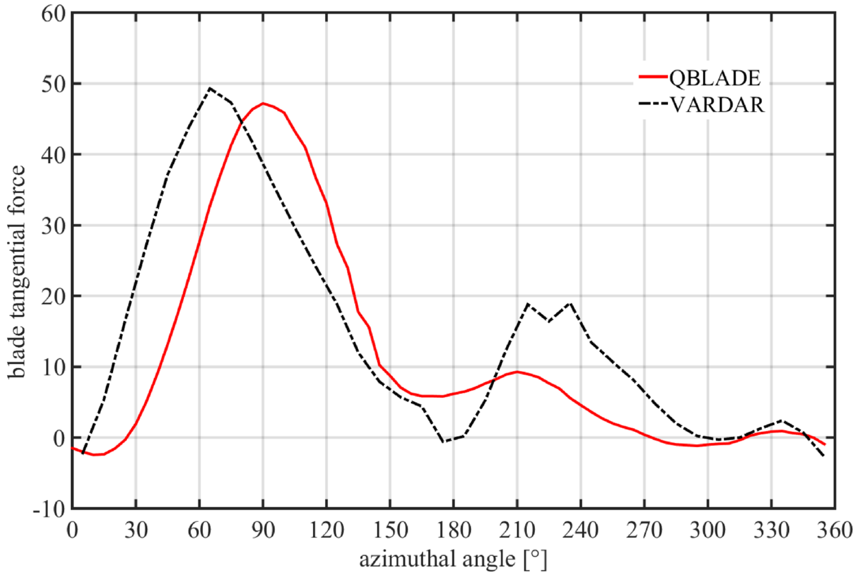

Fig. 4 Tangential force of one blade versus azimuthal angle

12 m/s, respectively. It is apparent that good agreement between the two theories was found for low tip-speed ratios, i.e., in the left-hand side of the curves. As soon as the energy extracted from the flow increases, however, i.e., the rotor behaves like a lesser porous media for the flow, the efficiency reduction predicted by QBlade becomes more relevant in comparison to that predicted by the BEM theory, leading to lower power coefficients and a steeper right-hand side of the curve. As will be shown later, this behavior can be related to the high solidity of the present rotor, which makes the interactions between the blades very strong. The presence of vortices and other flow macrostructures cannot be accounted for by the very simplified BEM approach, but are captured by the LLFVW method. In a previous study [16], the two theories indeed showed a much better agreement in case of a simplified 1-blade only test case, where the mutual blade influences were reduced. Taking a closer look at the variation of relevant quantities along a revolution, Figs. 4 and 5 report the comparisons of tangential and normal forces versus azimuthal angle for the maximum operating condition of the rotor (i.e., TSR = 2.2 at $U = 15$ m/s), respectively. Decent agreement can be noticed in terms of curve trends, especially for the tangential force. A significant shift is noticed in the first part of the curve, where a mismatch of the predicted angles of attack can be seen (Fig. 6). Indeed, this discrepancy can be likely related to the high solidity of the rotor, which is thought to generate a deflection of the oncoming flow [18], which is barely reproducible with the BEM theory, which only accounts for streamwise variation of momentum [13]. Based on the above, the Lifting Line model of QBlade was thought to be more suitable for use in predicting the aerodynamic forces produced by the present rotor.

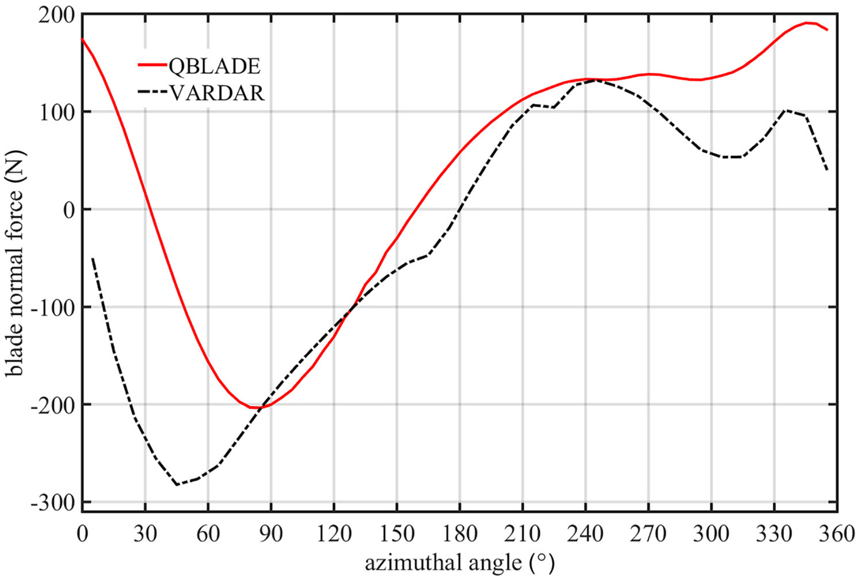

Fig. 5 Normal force of one blade versus azimuthal angle

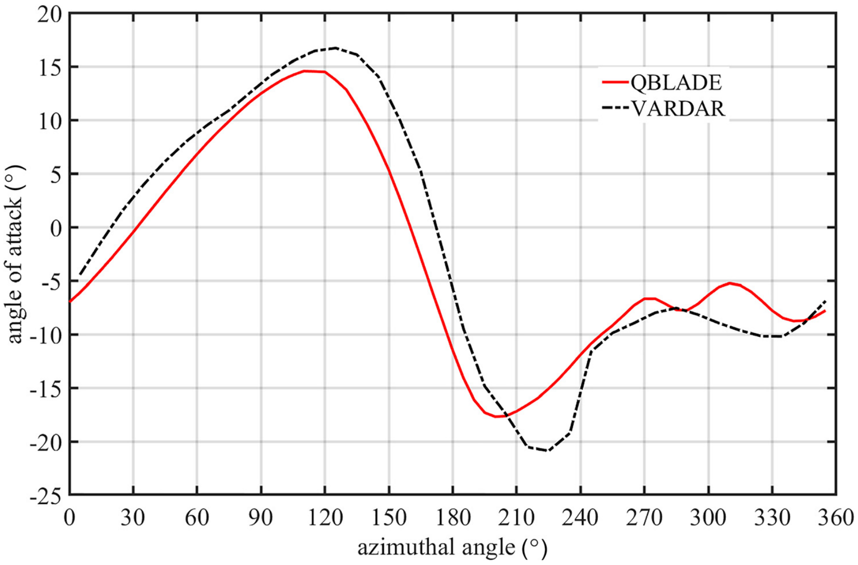

Fig. 6 Angle of attack at the blade midspan position versus azimuthal angle

Flow field Analysis

To support the conclusions of the Rotor Performance Analysis section, a detailed study of the predicted flow field around the turbine was carried out. Figure 7 reports the vorticity contours predicted by QBlade for the optimal operating condition, i.e., that with the maximum power coefficient of the rotor (TSR = 2.2 at $U = 15$ m/s). Upon examination of the figure, the generation of extended vortex structures is apparent from the zones of increased vorticity. Their intensity is even higher for the present study rotor, since the helix shape of the blades also induces flow gradients along the span (not reproducible with the BEM theory). Moreover, especially in the bottom right view, a strong interaction of these

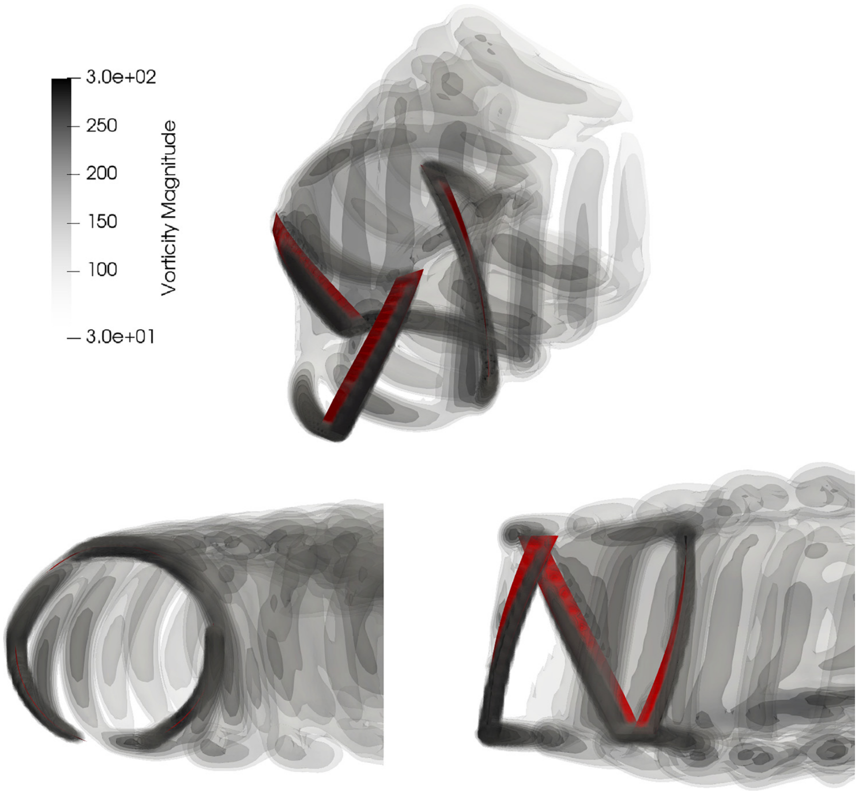

Fig. 7 Vorticity iso contours from the QBlade simulation; TSR 2.2, 15 m/s inflow

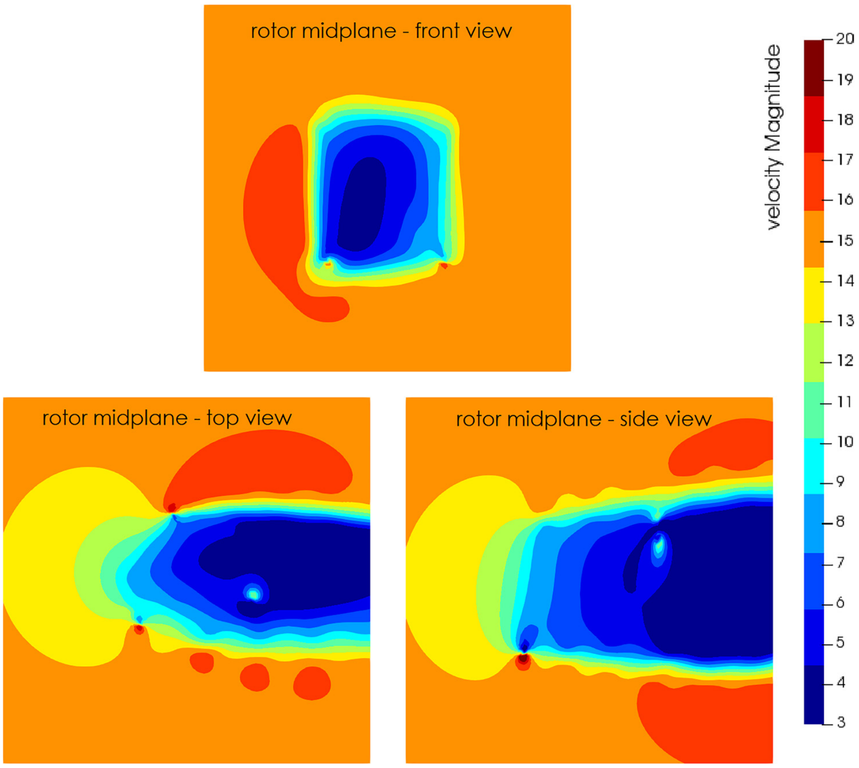

Fig. 8 Velocity iso contours from the QBlade simulation; TSR 2.2, 15 m/s inflow

high-vorticity areas with the passing blades is clearly observable, together with a strong tip-vortex.

The high rotor solidity is also visible from the massive flow induction, testified by the velocity contours reported in Fig. 8. The high energy extraction in the upwind region induces a strong deceleration to the flow entering the downwind region.

Moreover, the flow deflection is clearly distinguishable by the area of accelerated flow around the rotor for azimuthal angles up to 60 deg. This deflection is responsible for the already discussed discrepancies between the codes seeable from Figs. 4 and 5.

QBlade Structural Model Formulation

The structural model in QBlade is based on the FEA module of the open source multiphysics engine PROJECT::CHRONO [23]. CHRONO is distributed as an open source object oriented library with a C++ API, which has been fully integrated with the source code of QBlade.

The FEA module of CHRONO contains a multitude of structural elements in a corotational formulation [41,42] for a nonlinear evaluation of the structural dynamics including large deflections and rotations. A brief validation of the corotational formulation in CHRONO is given in Ref. [41].

Corotational, six degrees-of-freedom, Euler-beam elements are used to model the main components of the turbine model in QBlade (blades, tower, struts and support structures) while guy, or interblade connecting cables are modeled with cable elements in an absolute nodal coordinate formulation. The total turbine structure is assembled through specific constraints which limit individual degrees-of-freedom between beam or cable nodes or enforce boundary conditions where the turbine components are connected.

Furthermore, a preprocessor was designed that automatically constructs the complete turbine assembly from a rotor geometry defined within QBlade and a set of input files, in which the tower, the support structure, and guy cables are specified and the structural properties for each individual component are assigned. The structural properties that were used in to model the PRAMAC turbine were provided by the authors of the previously mentioned comparative study [28] to ensure consistency in the setup of the beam models.

Time Domain and Modal Analysis. During time domain analysis, the simulation is advanced using an implicit Hilber–Hughes–Taylor (HHT) time integrator [43], while the solution for the current structural dynamic system state is obtained using the direct MKL-PARDISO solver.

To perform a modal analysis of the turbine structure, the linearized tangent mass (m), stiffness (k), damping (d), and constraint (C_q) matrices are exported from the CHRONO system and reordered into a generalized Eigenvalue problem. The constraint matrices are included in the augmented stiffness matrix (K). The augmented stiffness, damping (D), and mass (M) matrices are

$$K = \begin{bmatrix} k & C_q{}' \\ C_q & 0 \end{bmatrix}, \quad D = \begin{bmatrix} d & 0 \\ 0 & 0 \end{bmatrix} \quad \text{and} \quad M = \begin{bmatrix} m & 0 \\ 0 & 0 \end{bmatrix} \tag{1}$$

From the augmented matrices, a generalized Eigenvalue problem of the form:

$$Ax = \lambda Bx \tag{2}$$

with

$$A = \begin{bmatrix} K & 0 \\ 0 & I \end{bmatrix} \quad \text{and} \quad B = \begin{bmatrix} D & M \\ I & 0 \end{bmatrix} \tag{3}$$

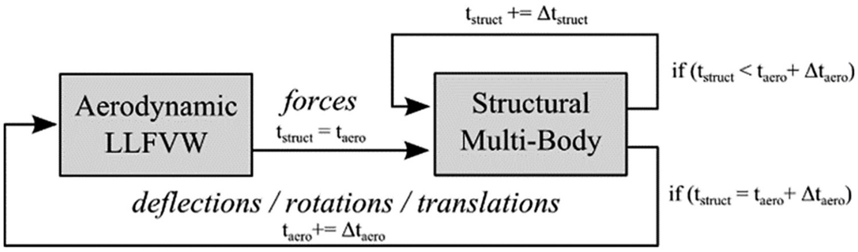

Fig. 9 Overview of the loose coupling scheme

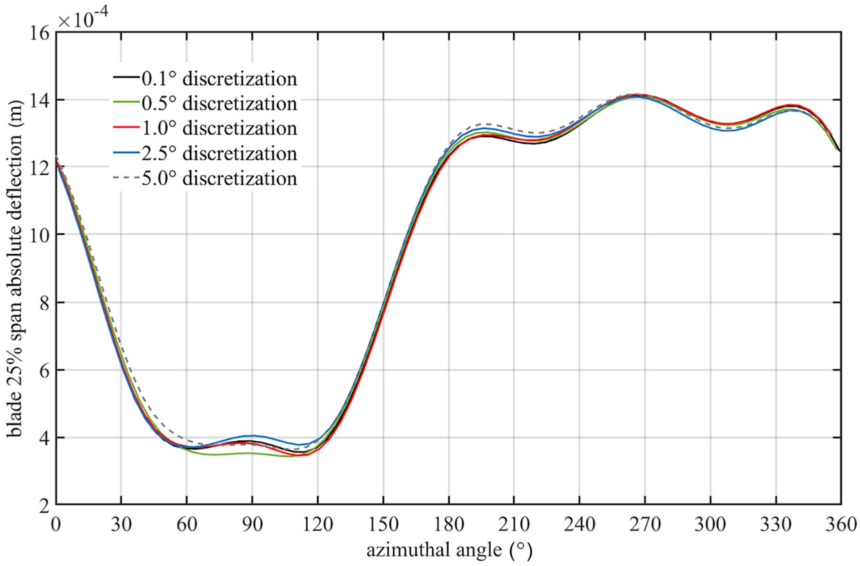

Fig. 10 Total displacement at a 25% spanwise position over the azimuthal blade angle

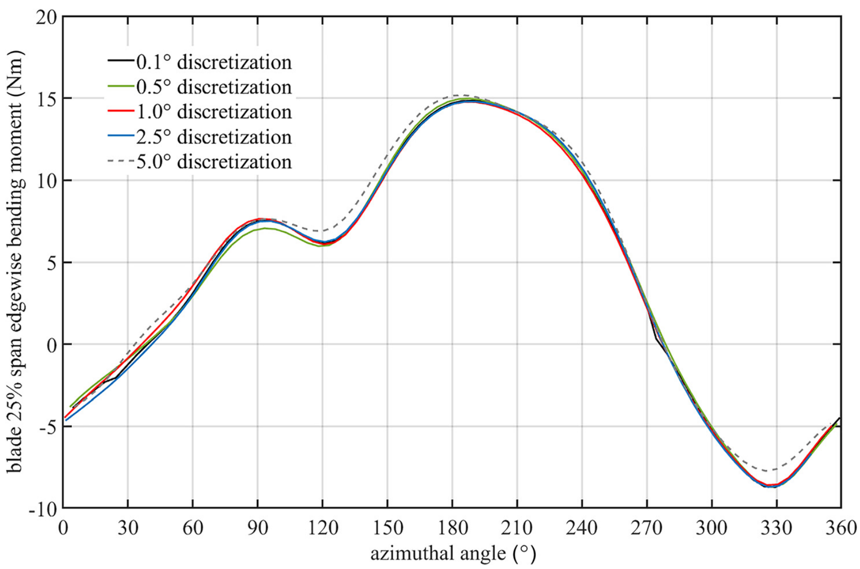

Fig. 11 Edgewise bending moment at a 25% spanwise position over the azimuthal blade angle

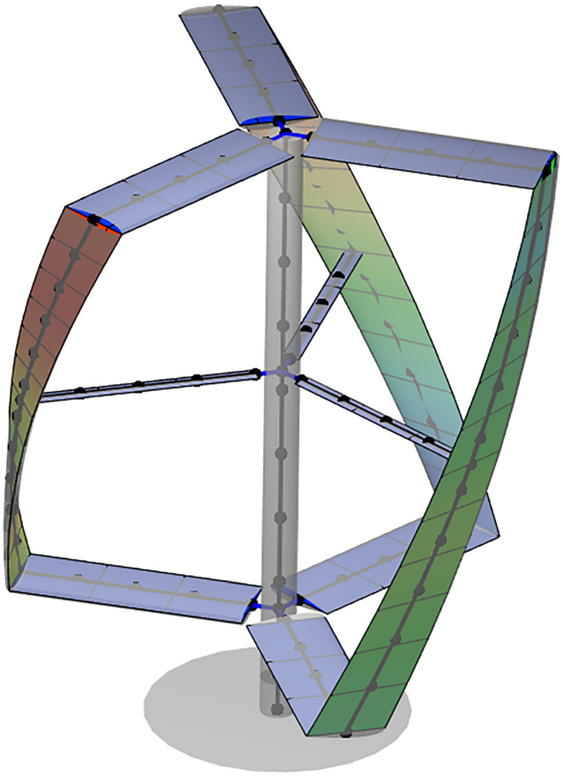

Fig. 12 The aero-elastic turbine model in QBlade showing aerodynamic panels and structural beams and nodes

where I is the identity matrix, and is solved using the *DGGEV* function from the *LAPACK* library. When the modal analysis is performed for a spinning turbine, for which geometric stiffness terms (that lead to spin stiffening and softening effects) play an important role, the rotor is brought up to the desired rotational speed in a time domain simulation and snapshots of the linearized tangent matrices are taken at distinct azimuthal angles, transformed back to an initial frame of reference, and then averaged. In the same way, aerodynamic forces can be included into the modal analysis.

Aeroelastic Coupling. The scheme that is used to couple the aerodynamic to the structural simulation is a *loose coupling scheme*. The main reason for employing the loose scheme is its simple implementation, as both solvers can operate in their own frameworks, and no details of the simulation process need to be communicated between them. Additionally, the loose scheme allows using independent timestep sizes for both subsimulations, which is particularly beneficial for a reduction of the computational cost of the overall simulation. By using independent time steps, each subsimulation can be optimized on its own in terms of computational cost versus desired accuracy. Generally, the aerodynamic analysis is not only computationally more demanding than the structural simulation, but it can also be run at larger timesteps without losing too much accuracy (from previous work [27] an azimuthal discretization of 5 deg is recommended). After an aerodynamic timestep is finished, the evaluated forces are interpolated from the aerodynamic onto the structural mesh and the structural simulation advances with its own timestep until it reaches the next aerodynamic timestep. When the next aerodynamic timestep is reached, the aerodynamic mesh is reconstructed from the beam coordinate systems and information about rotations and velocities is passed to the aerodynamic solver. The process is illustrated in Fig. 9.

Temporal Discretization. The sensitivity of the structural model to the variation of timestep size is shown in Figs. 10 and 11. For both figures, the aerodynamic simulation was performed at a fixed azimuthal discretization of 5 deg. To reduce the discontinuities that may arise in the structural simulation due to the coarser aerodynamic timestep, the aerodynamic forces, which remain constant during the structural subtime steps, are rotated around the rotor axis with the azimuthal increment by which the turbine rotation is advancing for each structural subtime-step.

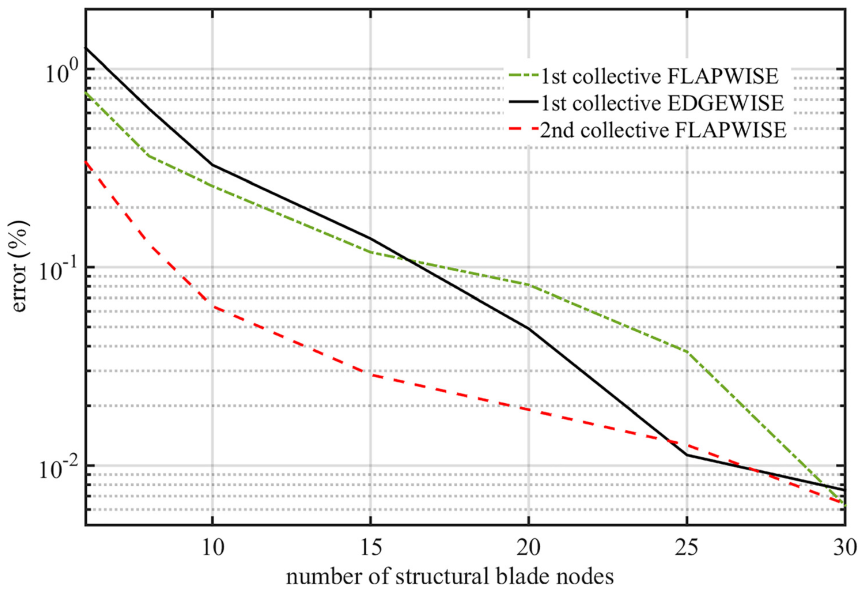

Fig. 13 Convergence of calculated Eigen frequencies for different structural discretization levels

Table 2 Eigen frequencies of the turbine, predicted by the SHELL model and the BEAM model of Ref. [28] and the QBlade model, error shown for comparison to SHELL model

Mode number	Shell freq. (Hz)	Beam freq. (Hz)	Beam error (%)	QBlade freq. (Hz)	QBlade error (%)
1	7.85	7.95	1.27	7.67	2.29
2	13.9	15.1	8.63	16.01	15.17
4	16.1	15.7	2.48	16.19	0.55
5	23.2	22.8	1.72	23.75	2.37
7	25.7	25.4	1.16	26.48	3.03

Figure 10 shows the total displacement at a 25% spanwise position on the blade during one revolution at 10 m/s uniform inflow and 200 rpm. The displacement variation shows almost no sensitivity toward the size of the structural timestep. Even for a structural discretization equivalent to 5 deg azimuthal angle, a good accuracy is achieved.

The resulting edgewise bending moment, shown in Fig. 11, shows a very similar behavior, and almost no sensitivity to the size of the structural timestep can be observed.

These results can be attributed to the behavior of the HHT time integrator, which can improve stability by suppressing instabilities of lightly damped high frequency modes via numerical damping.

A fixed discretization of 2.5 deg will be used in the structural model for the following simulations, which translates into 2 structural subtimesteps for each aerodynamic timestep.

Spatial Discretization. Similar to the individual timestep sizes of the models, their spatial discretization is also independent in this implementation. Figure 12 shows an example for a coarser aerodynamic mesh mapped onto the finer structural mesh. The simulations were performed with 14 aerodynamic panels per blade, four aerodynamic panels per strut and a total of 110 structural nodes.

Modal Analysis

In preparation for the modal analysis, a sensitivity study on the spatial discretization of the structural model was carried out. Figure 13 shows the convergence of the first three calculated blade Eigen frequencies for different numbers of blade nodes, with which the blade structure was discretized. As expected, the evaluated frequencies converge for a finer spatial discretization. It is remarkable that even for a discretization with only seven panel elements, the evaluated frequencies showed a maximum of 1.3% deviation from the converged result.

A structural discretization of 16 nodes was chosen for all subsequent simulations as the error was found to be below 0.1%.

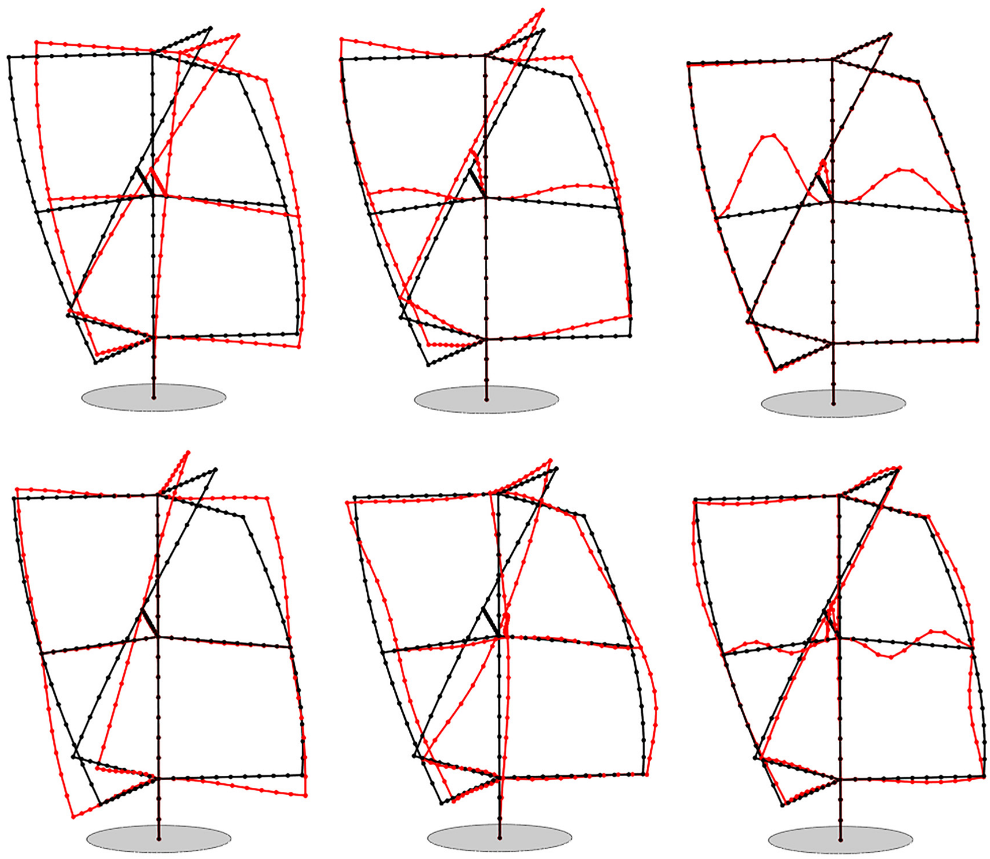

Fig. 14 Mode-shapes for the first six eigenmodes as calculated with QBlade

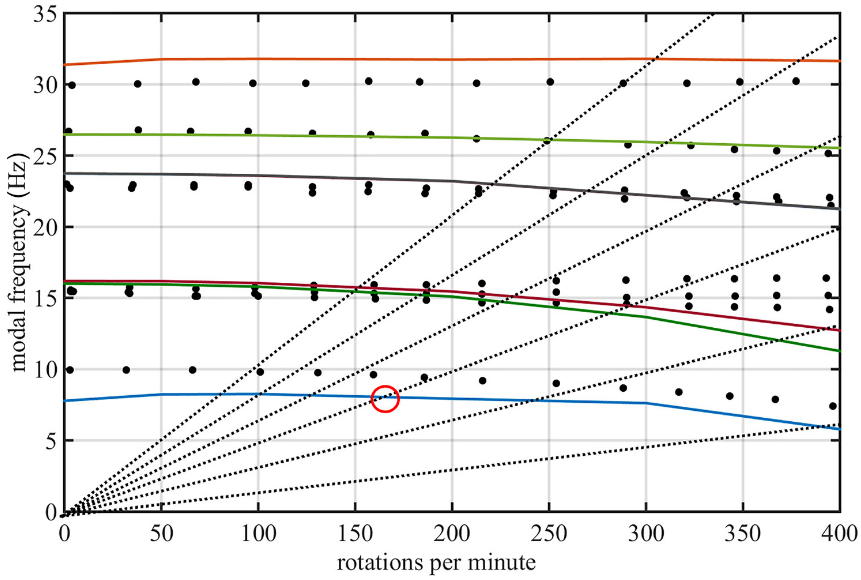

Fig. 15 Campbell diagram including 1p–6p excitation lines, colored line data from QBlade, point data calculated with GAROS [44] software

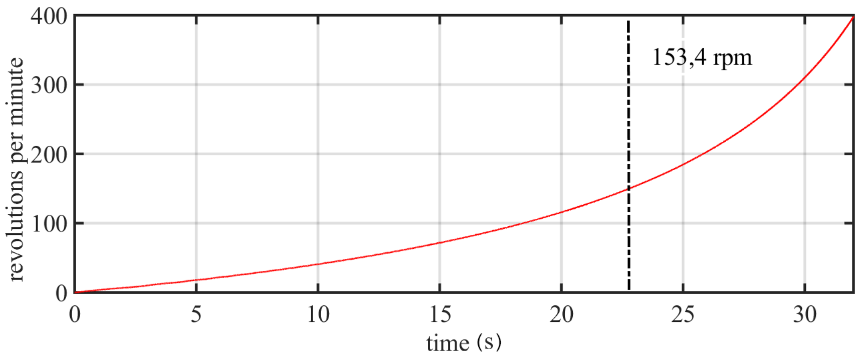

Fig. 16 Rotor revolutions per minute over time during transient rotor self-start simulation

Table 2 shows a comparison of the first five Eigen frequencies between the *NX-NASTRAN* shell model and *NX-NASTRAN* beam model that were originally presented in Ref. [28] and the beam model in QBlade. The error in Table 2 is shown in reference to the shell model results from *NX-NASTRAN*.

The agreement for the compared frequencies is good; however, a maximum deviation of 15% is found at the first flap wise blade mode. This can be attributed to the sparse information with which the geometry of the structural model has been set up in QBlade. While accurate data for the structural properties of the individual turbine components were available, the geometrical information was lacking. The blade structure was reconstructed from rotor images and the information that is given in Table 1. For instance, the curvature at the top and bottom of the blades (see Fig. 1) was not accounted for, and instead modeled as a sharp edge. Furthermore, also the NX-NASTRAN beam model shows the largest difference to the NX-NASTRAN shell model for first flap wise blade mode, suggesting that these large differences are also caused by the approximation of the structure via beam elements.

The first six Eigen mode shapes, as calculated with QBlade, are shown in Fig. 14. Figure 15 instead shows the Campbell diagram for the first five distinct Eigen frequencies and rotational speeds from 0 to 400 rpm. In this case, the results from QBlade are compared to an analysis carried out by the GAROS software [44] that was also presented in the former study [28]. In Ref. [28], it is mentioned that the discrepancies, such as the overprediction of the first tower mode by GAROS, are "*…mainly due to some simplifications that were needed to fit the model to the GAROS requirement….*" [28]. The analysis in GAROS is based on a modal coupling method, which employs precalculated mode shapes of substructures obtained *NX-NASTRAN* and thus does cannot resolve the nonlinearities that may be present in the assembled structure.

In this view, as we are comparing models of vastly different fidelity, the agreement in Fig. 14 is remarkable, and both codes predict the centrifugal softening to dominate over the centrifugal stiffening for high rotational speeds. The most critical crossing in the Campbell diagram is shown by the red circle in Fig. 15. Here, the first tower Eigen mode crosses the 3p excitation, which in case of the three bladed PRAMAC rotor is the blade passing frequency at 153.3 rpm. This point is subject of an aeroelastic analysis in Aeroelastic Startup Analysis section.

Aeroelastic Startup Analysis

As a second benchmark, for the correct functioning of the aeroelastic simulation, a self-starting simulation with a constant

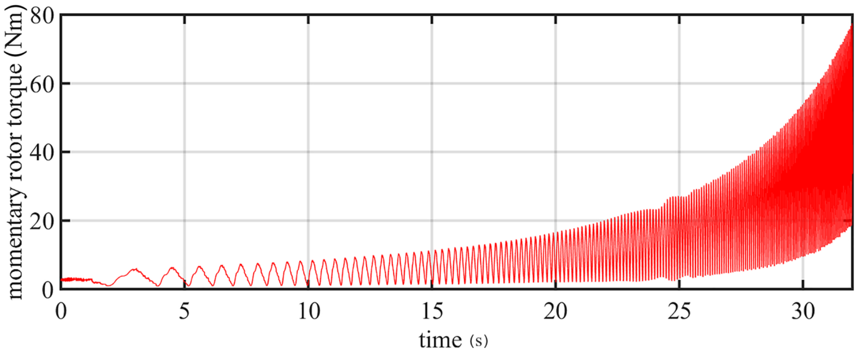

Fig. 17 Torque evolution over time during transient rotor self-start simulation

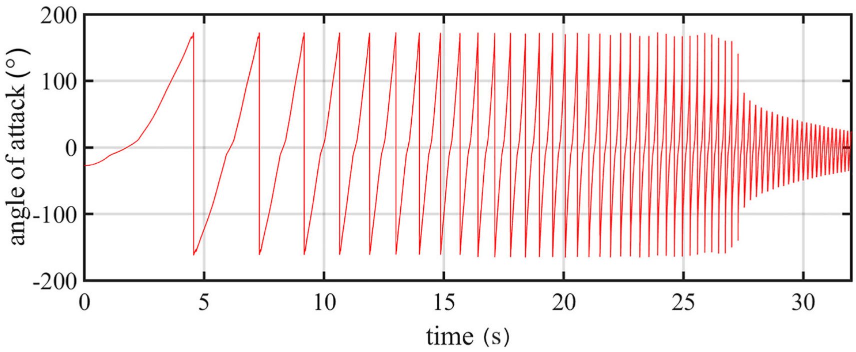

Fig. 18 Angle of attack evolution over time during transient rotor self-start simulation

inflow of 15 m/s was carried out to give insight into the interaction between structure and aerodynamics for this complex case, and to also confirm the findings that were obtained in the frequency domain during the modal analysis. In this simulation, the rotor bearings were modeled as frictionless and no resisting torque was applied onto the main shaft.

The highly transient self-starting of a VAWT is already a challenging test case from a purely aerodynamic point of view since the rotor, during speedup, operates over a wide range of tip-speed ratios and Reynolds numbers and, especially during the initial startup phase, is experiencing a large variation of the angle of attack. Thus, the poststall polar data plays a crucial role and it is important to accurately predict unsteady aerodynamic effects, such as dynamic stall.

From an aeroelastic standpoint, the startup is equally interesting because, due to the varying rotation of the rotor, the structure is excited over a wide range of frequencies. In Fig. 16, the rotational speed of 153.3 rpm was identified as the first occurrence of a critical excitation of the structure due to the blade passing.

Figure 16 shows the ramp up of the rotational speed over time, driven by a slowly increasing aerodynamic torque that grows due to the speedup of the rotor, as shown in Fig. 17. First, the acceleration is rather small, and the rotational speed stays low, with high angle of attack variations, as seen in Fig. 18.

As soon as the rotational frequency (153.4 rpm) reaches the vicinity of the first tower bending mode at 7.67 Hz (marked by the black line in Fig. 19), the tower starts to oscillate. Figure 20 shows

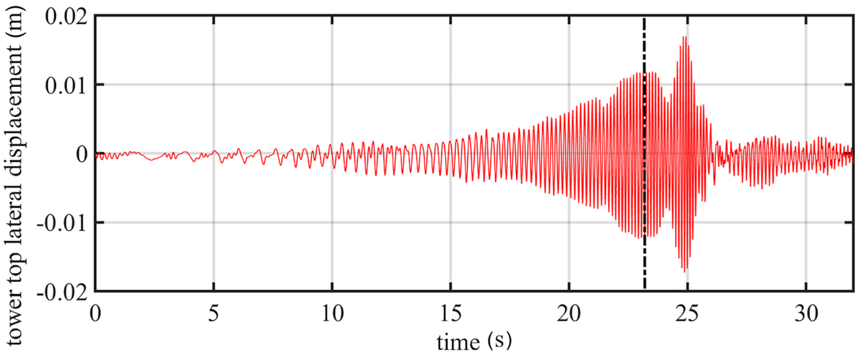

Fig. 19 Tower top position lateral deflection over time during transient rotor self-start simulation

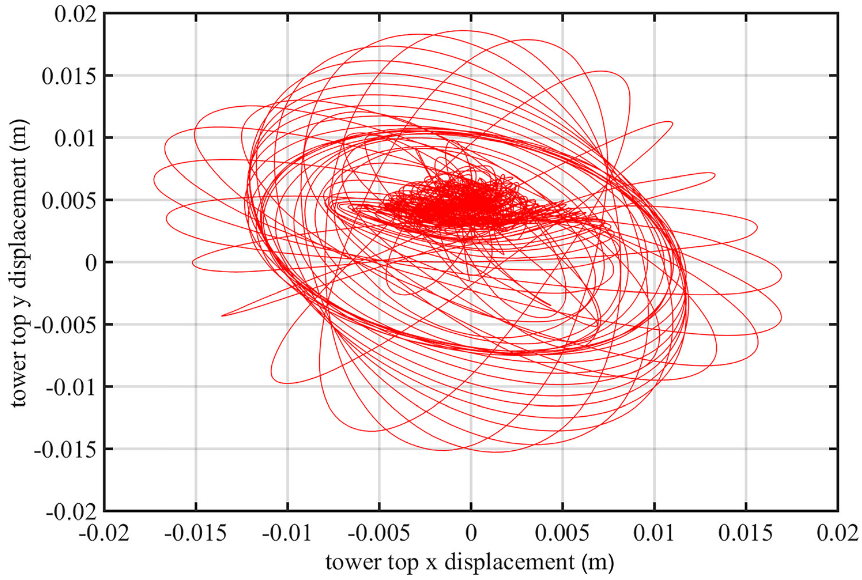

Fig. 20 Trajectories of the tower top position for the transient rotor self-start simulation

the full trajectory of the tower top node as seen from a top-down view, recorded during the simulation. The distinct "thick" circle in Fig. 20 shows the phase lock between the excitation and the tower oscillation. At the time of phase lock, the tower top node lateral displacement forms a plateau (Fig. 19). After the rotational speed further increases, leaving the range of resonance, and the phase between excitation and tower oscillation starts to shift more and more, the tower oscillations first start to decline and are then amplified by a constructive out-of-phase interference followed by a destructive interference, after which they are vastly reduced for the rest of the simulated time.

This phenomenon is clearly visible in Fig. 20 when looking at the trajectories whose x- and y-components are exceeding the "thick circle." Generally, the trajectories shown in Fig. 20 visualize quite well the large degree of nonlinearity that is present in this simulation and the necessity for the aerodynamic and the structural models to be able to accurately model such conditions.

Runtime. The self-start simulation was carried out over 32 s simulated time, with an aerodynamic time-step size of 0.005 s and a structural timestep of 0.0025 s, resulting in 6400 aerodynamic and 12,800 structural timesteps. The aerodynamic calculation was carried out on a NVIDIA GTX 1070 graphics processing unit, the structural simulation on an Intel Xeon E3-1230 v3 CPU. The total calculation time was 600 s.

Conclusions

In the present study, a novel aero-elastic simulation tool for wind turbines has been presented. Its aerodynamic model is based on a state-of-the-art free-wake formulation and can also deal with, for BEM models often problematic, high solidity multiblade VAWT rotors. The structural model is based on a multibody formulation, which employs structural elements in a corotational formulation to deal with large deflections and rotations. The dependency of the loosely coupled model accuracy as a function of different discretization settings has been investigated to find the optimal settings to balance accuracy and numerical cost. Both submodels were successfully validated and the resulting aeroelastic model is able to predict the complex, highly nonlinear dynamics of a Darrieus VAWT during self-starting, even if it is temporally operating in resonance.

Nomenclature

AM = constant of the Berg model
AR = blade aspect ratio
c = blade chord, m
C_q = constraints matrix
d = damping matrix
D = turbine diameter, m
H = turbine height, m
I = identity matrix
I_z = momentum of inertia, kg m^2
k = stiffness matrix
m = mass matrix
N = blade number

Acronyms

BEM = blade element momentum
HAWT = horizontal axis wind turbine
LLFVW = lifting line free vortex wake
VAWT = vertical axis wind turbine

Greek Symbols

ϑ = azimuthal position of the blade, deg
Σ = turbine solidity

Subscript

∞ = value at infinity

References

[1] Damota, J., Lamas, I., Couce, A., and Rodríguez, J., 2015, "Vertical Axis Wind Turbines: Current Technologies and Future Trends," International Conference on Renewable Energies and Power Quality (ICREPQ'15), La Coruña, Spain, Mar. 25–27, pp. 530–535.
[2] Sutherland, H. J., Berg, D. E., and Ashwill, T. D., 2012, "A Retrospective of VAWT Technology," Sandia National Laboratorie, Alburquerque, NM, Report No. SAND2012-0304.
[3] Blonk, D. L., 2010, "Floating Vertical Axis Wind Turbines," MSc thesis, Delft University of Technology, Delft, The Netherlands.

[4] Schmidt Paulsen, U., Madsen, H. A., Hattel, J. H., Baran, I., and Nielsen, P. H., 2013, "Design Optimization of a 5 MW Floating Offshore Vertical-Axis Wind Turbine," Energy Procedia, **35**, pp. 22–32.
[5] Aslam Bhutta, M. M., Hayat, N., Farooq, A. U., Ali, Z., Jamil, S. R., and Hussain, Z., 2012, "Vertical Axis Wind Turbine—A Review of Various Configurations and Design Techniques," Renewable Sustainable Energy Rev., **16**(4), pp. 1926–1939.
[6] Paraschivoiu, I., 2002, *Wind Turbine Design With Emphasis on Darrieus Concept*, Polytechnic International Press, Montreal, QC, Canada
[7] Bianchini, A., Ferrara, G., Ferrari, L., and Magnani, S., 2012, "An Improved Model for the Performance Estimation of an H-Darrieus Wind Turbine in Skewed Flow," Wind Eng., **36**(6), pp. 667–686.
[8] Carbó Molina, A., Bartoli, G., and De Troyer, T., 2017, "Generation of Uniform Turbulence Profiles in the Wind Tunnel for Urban VAWT Testing," *Wind Energy Exploitation in Urban Environment. TUrbWind 2017 Colloquium*, Springer, Berlin.
[9] Möllerström, E., Larsson, S., Ottermo, F., Hylander, J., and Bååth, L., 2014, "Noise Propagation From a Vertical Axis Wind Turbine," International Congress on Noise Control Engineering, Melbourne, Australia, Nov. 16–19.
[10] Sharpe, T., and Proven, G., 2010, "Crossflex: Concept and Early Development of a True Building Integrated Wind Turbine," Energy Build., **42**(12), pp. 2365–2375.
[11] Balduzzi, F., Drofelnik, J., Bianchini, A., Ferrara, G., Ferrari, L., and Campobasso, M. S., 2017, "Darrieus Wind Turbine Blade Unsteady Aerodynamics: A Three-Dimensional Navier-Stokes CFD Assessment," Energy, **128**, pp. 550–563.
[12] Balduzzi, F., Bianchini, A., Ferrara, G., and Ferrari, L., 2016, "Dimensionless Numbers for the Assessment of Mesh and Timestep Requirements in CFD Simulations of Darrieus Wind Turbines," Energy, **97**, pp. 246–261.
[13] Bianchini, A., Balduzzi, F., Ferrara, G., Ferrari, L., Persico, B., and Dossena, V., 2018, "A Critical Analysis on Low-Order Simulation Models for Darrieus VAWTs: How Much Do They Pertain to the Real Flow?," ASME Paper No. GT2018-76623.
[14] Marten, D., Lennie, M., Pechlivanoglou, G., Nayeri, C. D., and Paschereit, C. O., 2015, "Implementation, Optimization and Validation of a Nonlinear Lifting Line Free Vortex Wake Module Within the Wind Turbine Simulation Code QBlade," ASME J. Eng. Gas Turbines Power, **138**(7), p. 072601.
[15] Simão Ferreira, C., Aagaard Madsen, H., Barone, M., Roscher, B., Deglaire, P., and Arduin, I., 2014, "Comparison of Aerodynamic Models for Vertical Axis Wind Turbines," J. Phys.: Conf. Ser., **524**, p. 012125.
[16] Marten, D., Bianchini, A., Pechlivanoglou, G., Balduzzi, F., Nayeri, C. N., Ferrara, G., Paschereit, C. O., and Ferrari, L., 2016, "Effects of Airfoil's Polar Data in the Stall Region on the Estimation of Darrieus Wind Turbines Performance," ASME J. Eng. Gas Turbines Power, **139**(2), p. 022606.
[17] Rainbird, J., Bianchini, A., Balduzzi, F., Peiro, J., Graham, J. M. R., Ferrara, G., and Ferrari, L., 2015, "On the Influence of Virtual Camber Effect on Airfoil Polars for Use in Simulations of Darrieus Wind Turbines," Energy Convers. Manage., **106**, pp. 373–384.
[18] Bianchini, A., Balduzzi, F., Ferrara, G., and Ferrari, L., 2016, "Virtual Incidence Effect on Rotating Airfoils in Darrieus Wind Turbines," Energy Convers. Manage., **111**, pp. 329–338.
[19] Balduzzi, F., Bianchini, A., Maleci, R., Ferrara, G., and Ferrari, L., 2014, "Blade Design Criteria to Compensate the Flow Curvature Effects in H-Darrieus Wind Turbines," ASME J. Turbomach., **137**(1), p. 011006.
[20] Bianchini, A., Balduzzi, F., Ferrara, G., and Ferrari, L., 2016, "Critical Analysis Of Dynamic Stall Models In Low-Order Simulation Models For Vertical-Axis Wind Turbines," Energy Procedia, **101**, pp. 488–495.
[21] IEC, 2013, "Design Requirements for Small Wind Turbines," International Electrotechnical Commission, Geneva, Switzerland, Standard No. IEC 61400-2.
[22] IEC, 2009, "Design Requirements for Offshore Wind Turbines," International Electrotechnical Commission, Geneva, Switzerland, Standard No. IEC 61400-3.
[23] Tasora, A., Serban, R., Mazhar, H., Pazouki, A., Melanz, D., Fleischmann, J., Taylor, M., Sugiyama, H., and Negrut, D., 2016, "CHRONO: An Open Source Multi-Physics Dynamics Engine," *High Performance Computing in Science and Engineering: Second International Conference, HPCSE 2015, Soláň, Czech Republic, May 25–28, 2015, Revised Selected Papers (pp. 19–49)* (Lecture Notes in Computer Science 9611), Springer, Berlin, pp. 19–49.
[24] Marten, D., Wendler, J., Pechlivanoglou, G., Nayeri, C. N., and Paschereit, C. O., 2013, "QBlade: An Open Source Tool for Design and Simulation of Horizontal and Vertical Axis Wind Turbines," Int. J. Emerging Technol. Adv. Eng., **3**(3), pp. 264–269.
[25] Marten, D., Lennie, M., Pechlivanoglou, G., Nayeri, C. D., and Paschereit, C. O., 2017, "Nonlinear Lifting Line Theory Applied to Vertical Axis Wind Turbines: Development of a Practical Design Tool," ASME J. Fluids Eng., **140**(2), p. 021107.
[26] Marten, D., 2015, "QBlade Guidelines v0.95," Technical University of Berlin, Berlin, Technical Report No. TUB-2015-1.
[27] Marten, D., Lennie, M., Pechlivanoglou, G., Paschereit, C. O., Dy, N. V., Paraschivoiu, I., and Saeed, F., 2017, "Validation and Comparison of a Newly Developed Aeroelastic Design Code for VAWT," AIAA Paper No. AIAA 2017-0452.
[28] Bianchini, A., Cangioli, F., Papini, S., Rindi, A., Carnevale, E. A., and Ferrari, L., 2015, "Structural Analysis of a Small H-Darrieus Wind Turbine Using Beam Models: Development and Assessment," ASME J. Turbomach., **137**(1), p. 011003.
[29] PRAMAC S.p.A., 2018, "Revolution Air Wind Turbines," PRAMAC S.p.A., Siena, Italy, Technical Report, accessed Oct. 29, 2018, http://www.liberamente.tv/img/pramac.pdf
[30] Bianchini, A., Ferrari, L., and Schneider, A., 2008, "First Steps in the Design and Optimization of Darrieus VAWTs for Microeolic Applications," World Renewable Energy Congress (WREC) X, Glasgow, Scotland, July 19–25.
[31] Lowe, A. C., Moore, D. R., and Robinson, I. M., 1994, "Data for Designing With Continuous-Glass-Fibre-Reinforced Polypropylene," Compos. Sci. Technol., **52**(2), pp. 205–216.
[32] Pandit, S. N., Gupta, V. B., and Subramanian, K., 1981, "Compounding of Glass Fiber-Reinforced Polypropylene and Investigation of Its Mechanical Properties Under Simple and Complex Loading," Polym. Compos., **2**(2), pp. 68–74.
[33] Bianchini, A., Ferrara, G., and Ferrari, L., 2015, "Design Guidelines for H-Darrieus Wind Turbines: Optimization of the Annual Energy Yield," Energy Convers. Manage., **89**, pp. 690–707.
[34] Marshall, L., and Buhl, J., Jr., 2005, "A New Empirical Relationship Between Thrust Coefficient and Induction Factor for the Turbulent Windmill State," National Renewable Energy Laboratory, Golden, CO, Technical Report No. NREL/TP-500-36834.
[35] Abbott, I. H., and Von Doenhoff, A. E., 1959, *Theory of Wing Sections*, Dover Publications, New York.
[36] Migliore, P. G., Wolfe, W. P., and Fanucci, J. B., 1980, "Flow Curvature Effects on Darrieus Turbine Blade Aerodynamics," J. Energy, **4**(2), pp. 49–55.
[37] Bianchini, A., Balduzzi, F., Rainbird, J., Peiro, J., Graham, J. M. R., Ferrara, G., and Ferrari, L., 2015, "An Experimental and Numerical Assessment of Airfoil Polars for Use in Darrieus Wind Turbines—Part 1: Flow Curvature Effects," ASME J. Eng. Gas Turbines Power, **138**(3), p. 032602.
[38] Linn, A. B., 1999, "Determination of Average Lift of a Rapidly Pitching Airfoil," MSc thesis, Worcester Polytechnic Institute, Worcester, MA.
[39] Viterna, L. A., and Janetzke, D. C., 1982, "Theoretical and Experimental Power From Large Horizontal-Axis Wind Turbines," NASA Lewis Research Center, Cleveland, OH, Technical Report No. NASA-TM-82944.
[40] Bianchini, A., 2011, "Performance Analysis and Optimization of a Darrieus VAWT," Ph.D. thesis, School of Energy Engineering and Innovative Industrial Technologies/University of Florence, Florence, Italy.
[41] Tasora, A., 2016, "Euler-Bernoulli Corotational Beams in CHRONO::Engine," CHRONO::Engine Technical Documentation, Università di Parma, Parma, Italy, accessed Feb. 19, 2018, http://www.projectchrono.org/assets/white_papers/FEA/euler_beams.pdf
[42] Recuero, A., and Negrut, D., 2016, "Co-Rotational Formulation in CHRONO," ProjectCHRONO, Technical documentation, Università di Parma, Parma, Italy, accessed Feb. 19, 2018, http://www.projectchrono.org/assets/white_papers/FEA/WhitePaper_Co-rotational.pdf
[43] Tasora, A., 2017, "Time Integration in CHRONO::Engine," Project::Chrono Technical Documentation, Università di Parma, Parma, Italy, accessed Feb. 19, 2018, http://www.projectchrono.org/assets/white_papers/ChronoCore/integrator.pdf
[44] Vollan, A., and Komzsik, L., 2012, *Computational Techniques of Rotor Dynamics with the Finite Element Method* (Series of Computational Techniques of Engineering), 1st ed., CRC Press Taylor and Francis Group, Boca Raton, FL.

3.3. Publication IV: Predicting Wind Turbine Wake Breakdown Using a Free Vortex Wake Code

Marten, D., Paschereit, C. O., Huang, X., Meinke, M. H., Schroeder, W., Mueller, J., & Oberleithner, K. (2019). Predicting Wind Turbine Wake Breakdown Using a Free Vortex Wake Code. AIAA Journal, Published 24.09.2020 in Article in Advance, https://doi.org/10.2514/1.J058308

This paper, published the AIAA Journal, is a purely aerodynamic study. The LLFVW method is used for detailed simulations of the helical near wake structure of a HAWT that is perturbed through actuation of a trailing edge flap. Previous studies, using LES CFD, demonstrated that through the excitation at certain frequencies, the breakdown of the stable helical wake structure can be promoted. This can be beneficial in practice, as an earlier wake breakdown results in a faster wake recovery that can potentially increase the overall energy extraction of tightly packed wind farms. The underlying process is a mutual induction instability, where the interaction of neighboring vortex filaments in the wake can lead to an exponential growth of small spatial perturbations of the vortex positions. The aim of this work was threefold:

At first, the general applicability of the LLFVW formulation to investigate such detailed aerodynamic phenomena should be demonstrated. The topic of helical wake instability was well suited for this task due to the availability of comparable studies in the literature.

Secondly, the capability of the LLFVW formulation and the associated implementation of the AFC model (Section 2.4.6) to accurately predict the flap induced perturbations to the helical vortex structure should be validated. This could be realized through the comparison to a highly resolved CFD simulation that was carried out by one of the co-authors.

Finally, the validated framework was applied to predict the influence of periodic trailing edge flap actuations on the wake structure of a wind turbine. In previously published work the vortex perturbations were introduced only artificially, or purely numerically. The present publication is the first work in which the concept of wind turbine wake destabilization by means of a real world control device is evaluated.

Check for updates

Predicting Wind Turbine Wake Breakdown Using a Free Vortex Wake Code

D. Marten* and C. O. Paschereit†
Technical University of Berlin, 10623 Berlin, Germany
X. Huang,‡ M. Meinke,§ and W. Schröder¶
RWTH Aachen University, 52062 Aachen, Germany
and
J. Müller** and K. Oberleithner††
Technical University of Berlin, 10623 Berlin, Germany

https://doi.org/10.2514/1.J058308

When modeling wind turbine wake recovery, the location of wake breakdown plays a crucial role. The breakdown is caused by a rapid deformation of the helical near-wake vortex structure that is triggered by the pairing of successive blade tip vortices. In this paper, the capability of a cost-efficient lifting-line free vortex wake code to accurately predict the wake breakdown location and its underlying mechanisms is demonstrated and validated against simulation results of a large-eddy simulation solver and additional data from the literature. Furthermore, this work investigates a technique to accelerate the breakdown of wind turbine wakes. The onset of wake breakdown is caused by perturbations that travel along the helical structure of the wake and grow via mutual-induction interaction between neighboring vortex filaments. To accelerate wake breakdown, the blade tip vortices are perturbed at different frequencies via trailing-edge flaps located in the outboard region of the rotor blades. Through the evaluation of the perturbation growth rates and the analysis of velocity fields, it is shown that for a multi-megawatt wind turbine operating in a turbulent wind field, the wake breakdown position can be significantly affected by a moderate flap actuation amplitude if excited at an appropriate frequency.

Nomenclature

f_c = normalized flap actuation frequency ($f_{\text{flap}}/f_{\text{rotor}}$)

I. Introduction

DUE to spatial constraints, wind turbines are often installed within large clusters, or wind parks, to reduce infrastructure and installation costs and to optimize maintenance. Depending on the spacing of the wind park and the prevalent wind directions, this wind turbine clustering often leads to wind turbine wake interaction, in which the wakes of upstream turbines partially or fully impinge on the rotors of downstream turbines. This wake impingement leads to an increased turbulence level and a reduced mean velocity for the downstream rotor. As a result, the power production of the downstream turbine is usually reduced because the kinetic energy in the wind is lower and fatigue loads are increased by the larger velocity fluctuations resulting from the convected vortical structures, especially during partial wake impingement.

Recent strategies to reduce the problems associated with wake impingement include steering the wake away from downstream rotors through wake tracking and active turbine yawing [1]; optimized spacing of turbines [2]; or low induction rotors [3], which generally reduce the magnitude of the wake deficit. Another strategy is to accelerate the turbulent breakdown of the helical vortex system, and thereby facilitate the recovery of the wake.

Presented as Paper 2019-2080 at the AIAA SciTech 2019, San Diego, CA, January 7–11, 2019; received 8 April 2019; revision received 7 May 2020; accepted for publication 19 June 2020; published online 25 September 2020.

*Research Group Leader, Fluid Dynamics.
†Professor of Fluid Dynamics.
‡Research Associate, Institute of Aerodynamics.
§Senior Research Associate, Institute of Aerodynamics.
¶Professor of Institute of Aerodynamics.
**Research Associate, Flow Instabilities and Dynamics.
††Professor of Flow Instabilities and Dynamics.

Observations show that helical vortex systems of wind turbines are highly stable structures, and a significant wake deficit can still be observed at up to 18 diameters [4] behind a wind turbine (under uniform inflow conditions with 10% ambient turbulence) long after the turbulent breakdown of the wake vortex structure. Facilitating the breakdown of the helical wake structure by introducing perturbations that instigate the helical wake's natural instability can promote an early wake recovery and ultimately reduce the wake deficit.

To develop effective wind park control and optimization strategies, there need to be efficient and accurate numerical tools that are capable of multiturbine simulations and fast enough for parametric investigations of long-time series simulations to test different control algorithms.

To date, the majority of wind park simulations are conducted via immersed lifting-line large-eddy simulations (LESs), which allow investigating the near- and far-wake development and possess a reasonable efficiency because the blade surfaces do not need to be resolved. However, due to their Eulerian approach, the whole domain of interest still needs to be discretized with a reasonably fine volume mesh to avoid excessive numerical dissipation of the dominant vortex structures. This approach leads to computational costs that are prohibitive for rapidly evaluating the parametric studies of a large number of design iterations.

An alternative method for simulating the wind turbine wake involves modeling the flowfield with a Lagrangian approach by assuming an inviscid flowfield and only discretizing the vorticity within the domain. Free vortex wake methods have been applied for the simulation of wind turbine wakes numerous times [5–7] and possess a good accuracy while reducing computational costs significantly. The majority of these studies model the wake with vortex filaments and only deal with the induction caused by the near wake on an isolated wind turbine rotor. To model the interaction between an upstream and a downstream turbine in a wind park, accurate modeling of the wake breakdown and recovery is crucial, with the latter being far more challenging to model. Generally, vortex filament methods are not suitable for modeling the turbulent mixing, which occurs after the wake breakdown: the random fluctuations lead to a heavy three-dimensional distortion of the free wake filaments (see Fig. 1), and the resulting velocity fields are not representative for the actual flow physics; they are merely an artifact of the simulation.

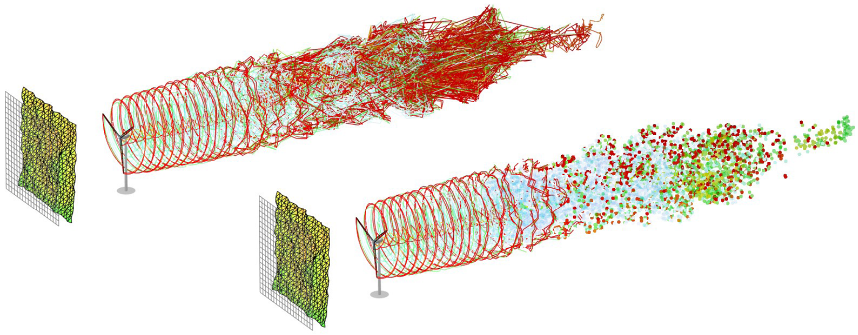

Fig. 1 LLFVW simulation of a turbine in turbulent inflow: vortex lines only, showing heavy wake distortion after wake breakdown (top); and conversion into particles after 6.5 revolutions (bottom).

These shortcomings can be overcome by using vortex particles, or blobs, instead of filaments. By using vortex particles and grid-based remeshing techniques in combination with a Poisson solver, the turbulent mixing in the wake occurring on subgrid scales can be effectively modeled by LES methods [8]. The drawback of using vortex particles is the higher computational costs. In opposition to vortex lines, wake particles do not possess any connectivity and the self-induced velocity in the wake has to be evaluated at twice the number of points, which increases the computational costs by a factor of two. While the computational costs of free wake methods generally scale with $O(N^2)$ (where N is the number of particles or filaments), tree code methods can reduce the cost to $O(N\log(N))$ and multilevel approaches even to $O(N)$, at the cost of additional overhead for remeshing and the Poisson solver step. When using Lagrangian vortex methods, a numerically efficient approach would be to convert the computationally more efficient vortex filaments into particles after the point of wake breakdown. This limits the region in which the remeshing has to be carried out, reduces the matrix size for the Poisson solver, and correspondingly the particle count N. As a continuation of this work, such a treatment is a promising method for performing accurate and efficient aeroservoelastic simulations of multiple full-scale turbines in wind park settings with computational costs that are several orders of magnitude lower than state-of-the-art Eulerian computational fluid dynamics (CFD) solvers.

However, the main goal of this work is to validate the capability of a free vortex filament method for accurately predicting vortex system perturbations and the point of wake breakdown after which the filaments can potentially be converted into vortex particles (see an illustration of this concept in Fig. 1).

A. Stability of Helical Vortex Systems

The features of helical wakes originating from propellers or turbines have been studied as early as 1912, when Joukowsky [9] developed a model description based on horseshoe vortices. Roughly six decades later, in 1970, Crow [10] investigated the stability of a pair of trailing vortices behind the wings of an aircraft.

The first work on the stability of a helical vortex system, simplified as a single helical vortex filament, was performed by Widnall in 1972 [11], who discovered and characterized the long wave mode, the short wave mode, and mutual-inductance instability. Soon afterward, in 1974, Gupta and Loewy found [12] that axial perturbations within a helical vortex system promote mutual-inductance instability, whereas radial perturbations have a much smaller effect. Furthermore, they characterized the influence of the helix pitch, helix number, and vortex filament core size.

Leishman and Bhagwat [13] introduced the next advancement in 2004 by applying a free vortex method for investigating the stability of helicopter wakes in static flight conditions. In this study, they identified wave numbers for stable and unstable conditions of the mutual-induction instability. Unstable conditions are observed at wave numbers equal to $K = N^*_{\mathrm{blade}}\ (i + 0.5)$, whereas stable conditions appear at wave numbers of $K = N^*_{\mathrm{blade}}(i)$, where i is a positive integer and N_{blade} is the number of blades.

The next enhancement came in 2010 when a numerical study focusing on wind turbine wakes was conducted by Ivanell et al. [14]. Employing an LES solver combined with the actuator line technique (ACL) for a 120 deg rotor segment with periodic boundary conditions, Ivanell et al. found that the mutual inductance, or pairing instability, is the main cause for the breakdown of wind turbine wakes.

The study of Ivanell et al. [14] was later continued by Sarmast et al. in 2014 [15], who confirmed the dominant effect of the mutual-induction instability for wind turbine wakes. Similar to Ivanell et al. [14], Sarmast et al. [15] also performed simulations using an LES solver combined with the ACL technique. In their study, though, the simulation results were analyzed with the proper orthogonal decomposition and dynamic mode decomposition methods. Furthermore, Sarmast et al. derived a semiempirical relationship for the stable wake length of a wind turbine operating in turbulent inflow conditions.

The year 2015 saw two seminal studies. First, Quaranta et al. [16] performed experimental investigations of the long wave instability of a single helical vortex through periodic modulation of the rotor rotation, partly correcting and extending the work of Widnall and Gupta [11,12] from four decades ago. Second, Carrión et al. [17] compared a Reynolds-averaged Navier–Stokes simulation with the detailed aerodynamic experiments of the Model Experiments in Controlled Conditions (MEXICO) project [18]. Both the simulation and the experiment also included the turbine tower. In their comparison, Carrión et al. [17] juxtaposed the frequency content of the wake between the experiment and the CFD. At far downstream positions, a higher-frequency content was observed than the blade passing frequency, which indicates the onset of wake breakdown.

B. Structure of This Paper

This work presents a comparison between a lifting-line free vortex wake (LLFVW) method and an LES code in which near- and midwake properties related to the mutual-induction stability mechanisms are contrasted against each other. The more efficient LLFVW method is then applied in a parametric study on the mutual-induction instability, comparing these results to literature data. Finally, the impact of flap actuation on a multi-megawatt turbine operated in a turbulent wind field is assessed. This paper is organized as follows:

1) Section II gives a brief overview of the two numerical simulation methods (LLFVW and LES) that are applied in this study.

2) Section III focuses on a comparison of the near-wake vortex perturbations that are caused by flap deflections. The main purpose is to validate the general applicability of the highly simple polar-interpolation-based flap model employed by the LLFVW through a comparison with a fully blade-resolved LES.

3) Section IV compares midwake vortex trajectories between the LES and the LLFVW at different flap actuation frequencies to validate the LLFVW's capability for predicting the mutual-induction instabilities. Velocity fields are compared up to the point of vortex pairing.

4) In Section V, a parametric study over a range of flap actuation frequencies is conducted with the LLFVW method. Growth rates are calculated via fast Fourier transformation (FFT) and then compared to data from the literature.

5) In Sec. VI, the National Renewable Energy Laboratory (NREL) 5 MW turbine, equipped with an active flap, is simulated in turbulent inflow conditions. The stable wake length observed in these simulations is compared to the semiempirical relationship of Sarmast et al. [15]. Furthermore, the influence of the flap deflection amplitude on the stable wake length is shown.

II. Validation Setup and the Compared Numerical Methods

A. Simulated Rotor Geometry and Method of Wake Perturbation

The rotor geometry employed in this study is from the Berlin Research Turbine (BERT): a 3-m-diameter wind turbine model equipped with active trailing-edge flaps. Within the research project titled “Wind Turbine Load Control Under Realistic Turbulent Inflow Conditions” [19], conducted by four universities in Germany, the BERT model [20] has been extensively simulated and experimentally investigated [21,22] by the project partners as a common test bench for load control investigations (see Fig. 2 for an illustration of the rotor and its characteristics). Recently, the concept of a wind turbine load control by means of active trailing-edge flaps has been the topic within numerous research publications [22–24].

While the BERT geometry including active flaps has been designed as a test bench for active load control, in this study, the flaps are used to promote wake breakdown by introducing harmonic perturbations into the helical tip vortex system (as shown in a recent publication by Huang et al. [25]). While the outboard flap induces the perturbations, the inboard flap is deflected with a 180 deg phase shift to reduce the overall blade load fluctuations that result from the outboard flap movement. The advantages of using the BERT rotor geometry in this present study are that the existing CFD infrastructure applied by the authors can be reused and numerical findings can potentially be confirmed by wind tunnel experiments (although not within the scope of this paper). Generally, the BERT geometry is suitable for demonstrating and cross validating the concept of wake excitation through flaps and the propagation and growth of perturbation, because these mechanisms depend more on the operating state of the rotor (defined by the thrust and power coefficients) than on its actual geometry.

B. Lifting-Line Free Vortex Wake Simulations

Lifting-line free vortex wake simulations of the BERT rotor are performed using the QBlade wind turbine simulation code [5]. The formulation of QBlade’s aerodynamic model calculates the blade forces from tabulated lift and drag airfoil data. The wake is discretized with constant circulation straight vortex line filaments, which are shed at the blade’s trailing edge during each time step and then experience free convection under the influence of mutual induction behind the rotor. The vortex elements are desingularized through a cutoff method as proposed by van Garrel [26]. The vortex core size is used as a cutoff parameter. Viscous diffusion in the wake is accounted for through a vortex core growth model that also includes the effects of vortex strain (calculated from changes in filament length). The core size of each vortex filament is updated each time step according to the following equation:

$$r_c = r_0 + \sqrt{\frac{4a\delta_v \nu \Delta t}{1+\varepsilon}} \tag{1}$$

where $a = 1.25643$ is a constant, δ_v is the turbulent viscosity coefficient, ν is the kinematic viscosity, and r_0 is the initial vortex core size that is usually assumed to be a fixed fraction of the local blade chord. Also, ε is the vortex filament strain that is evaluated from the change in vortex filament length relative to its initial length l_0 as

$$\varepsilon = \frac{l - l_0}{l_0} \tag{2}$$

The on-blade effects of unsteady aerodynamics and dynamic stall are introduced via the Adaptive trailing edge flap (ATEFlap) aerodynamic model [27]. Massive graphics processing unit (GPU) parallelization within the Open Computing Language (OpenCL) framework is employed to accelerate the free wake convection step. Recently, within QBlade, a method for modeling trailing-edge flaps was implemented [12] that is based on the interpolation of polar data from different flap angles. Unsteady aerodynamic effects are taken into account through the ATEFlap model [27]. Within this paper, the flap model will be applied to perturb the wake in the vicinity of the rotor by augmenting the blade circulation via dynamic flap deflections. More detailed information on the LLFVW implementation can be found in Ref. [5].

C. Large-Eddy Simulations in the Arbitrary-Lagrangian–Eulerian Formulation

The Navier–Stokes equations in the arbitrary Lagrangian–Eulerian formulation are spatially filtered assuming an implicit grid filter defined by the finite volume method and are discretized on a structured body-fitted mesh. The monotonic integrated large-eddy simulation approach [28] is used; i.e., the dissipative part of the truncation error is assumed to mimic the effect of the dissipation of the unresolved subgrid scales. The convective fluxes are formulated by a low dissipation variant of the advection upstream splitting method scheme [29] and a monotonic upstream-centered scheme for conservation laws interpolation of second-order accuracy is used. The discretization of the viscous fluxes is performed by a second-order-accurate central difference scheme [30]. An explicit second-order-accurate five-step Runge–Kutta formulation is used for the temporal integration. This solution method has been extensively

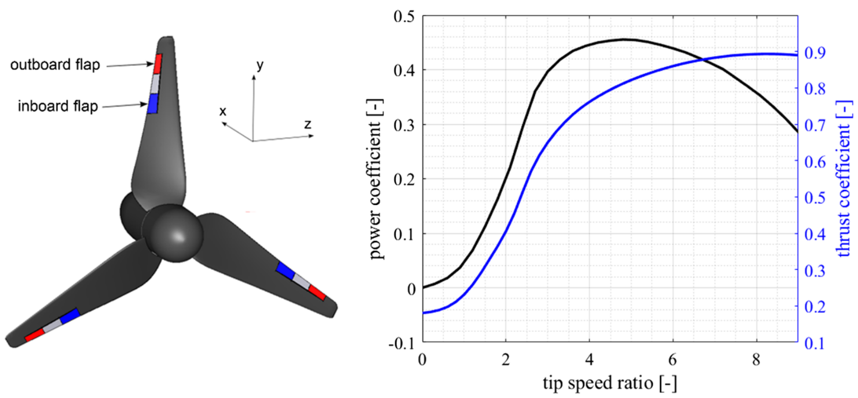

Fig. 2 BERT rotor geometry and coordinate system (left), and rotor characteristics of BERT (right).

validated for various internal and external subsonic and transonic turbulent flow problems; see Refs. [31,32].

III. Comparison Between an LLFVW Simulation and LES in Near Wake

The flowfields over the BERT rotor without and with oscillating flaps are simulated by LLFVW and LES [25]. The operating conditions of the simulated rotor are shown in Table 1. The perturbations of the tip vortex are achieved by the synchronous deflection of each blade's outboard flap (see Fig. 2) at a certain oscillation frequency. To mitigate the flap-induced rotor loads, the inboard flaps of each blade are actuated at the same frequency with a 180 deg phase difference. The amplitude of deflection of the outboard and inboard flaps is 10 deg. The dimensionless flap oscillation frequency f_c for the flaps (see Fig. 2) is selected to be 4.5, i.e., 4.5 periods of flap oscillation per rotation of the blade. This frequency is associated with a local maximum of the growth rate of the helical instability in the study of Ivanell et al. [14] and is large enough to be resolved by a 120 deg segment with periodic boundary conditions as used by the LES. The perturbation of the tip vortex system through the oscillation of the flaps is evaluated by comparing the tip vortex core positions in the near wake of the rotor in a blade-fixed plane (as illustrated in Fig. 3) between the cases with and without the oscillating flaps. The unperturbed vortex positions are taken here as the reference position around which the tip vortex displacements are evaluated. The vortex center positions in the LLFVW simulation and LES are obtained by dividing the first moment of vorticity by the total vorticity in the vicinity of the vortex core.

Table 1 Operating conditions for the near-wake simulations

Operating parameter	Value
Revolutions per minute (RPMs)/tip speed ratio/rotor radius	180/4.6/1.5 m
Inflow velocity	6 m/s, uniform
Dimensionless flap actuation frequency	4.5
Flap actuation amplitude	10 deg

A. Numerical Setup of LES Near-Wake Simulations

The computational domain of the LES consists of a 120 deg sector using periodic boundary conditions in the circumferential direction, such that the flow over one blade is simulated. The structured body-fitted mesh consists of 49 blocks with approximately 248 million cells. The minimum cell sizes in the blade tip and flap region are $\Delta y^+ = 2$, $\Delta z^+ = 30$ and $\Delta x^+ = 50$. The flaps are modeled as a continuous geometry variation such that the influence of the flap gap is not considered. After being initialized with the fully developed flowfield of a precursor simulation, the simulation is evaluated over seven million time steps, resulting in approximately two full rotor revolutions. More details of the LES setup and results can be found in Ref. [25]. Figure 4 shows the highly resolved flowfield around the BERT rotor as simulated by the LES.

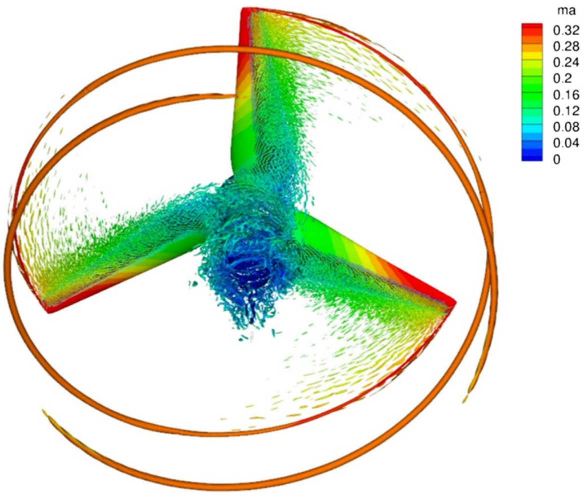

Fig. 4 Isosurfaces of the second invariant of the velocity gradient tensor ($Q = 30$) colored by the local Mach number illustrating flowfield around BERT rotor simulated with LES: reproduced from Ref. [25].

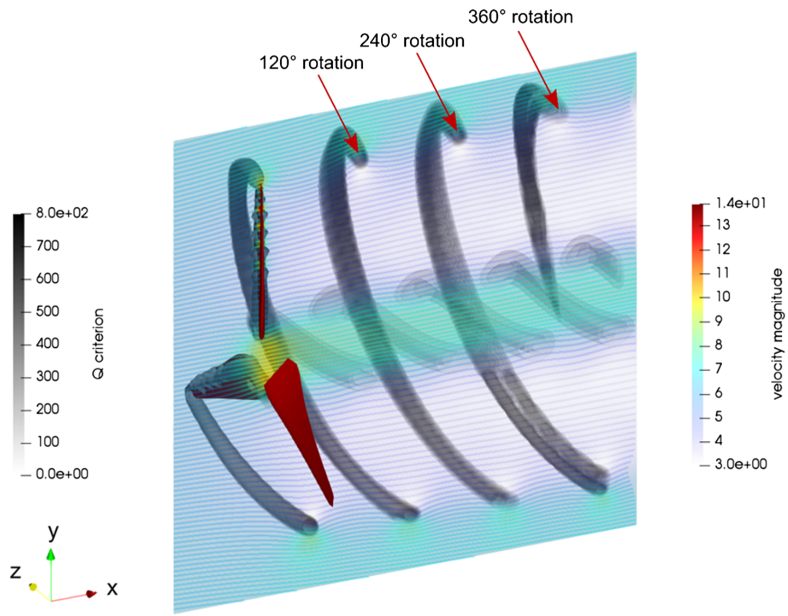

Fig. 3 Visualization of the LLFVW simulation, showing the blade-fixed plane of vortex position evaluations; the helical vortex system is visualized by the Q criterion.

B. Numerical Setup of LLFVW Near-Wake Simulations

The full rotor is simulated with the LLFVW method in QBlade. Each blade is discretized with 28 evenly spaced panels (each flap is made of three panels). The time-step size is equivalent to an azimuthal rotor advancement of 5 deg. The initial vortex core size is set to 10% of the local chord and the turbulent vortex viscosity coefficient [33] is set to five. The simulation is calculated for 12 full rotor revolutions, whereas the wake is truncated after two full revolutions, resulting in a maximum of ~24,000 free vortex line elements at a time.

C. Results and Comparison

Figure 5 shows a comparison of the unperturbed and perturbed vortex core positions over one flap oscillation period. Distances are given in relation to the unperturbed vortex location of the LLFVW simulation and the LES, respectively, and are normalized with the rotor radius. X is oriented in the streamwise direction, and Y is oriented along the radial direction of blade 1 (see Fig. 3). The top-left graph in Fig. 5 shows the trajectory of the vortex displacement over one full flap oscillation cycle in a blade-fixed plane after the rotor has travelled through a rotation of 120 deg. The top-right and bottom-left graphs show the trajectories at the positions after 240 and 360 deg rotations, respectively. The arrows highlight the maximum displacement (normalized by the rotor radius R) of the vortex core position for one full flap oscillation cycle, with respect to its unperturbed reference position. The growth of the maximum displacements over the three positions in the wake (120, 240, and 360 deg) is shown in the bottom-right graph of Fig. 5. The linear slope in this semilog graph denotes the growth rate of the displacements. For reference, it is compared with the universal growth rate of $\pi/2$.

Overall, similar magnitudes are predicted for the flap-induced vortex core displacements. When comparing the resulting growth rates (bottom right in Fig. 5), it can be seen that the universal growth rate of $\pi/2$ is slightly underpredicted by the LES results, whereas it is slightly overpredicted by the LLFVW results. However, when comparing the vortex core trajectories, no good agreement can be obtained at the different vortex locations. While the LLFVW simulation consistently predicts the radial, or Y, direction as the prevalent direction of the vortex path (at the three locations and for all consecutive rotations of the rotor), the trajectories show a somewhat randomized behavior in the LESs. The slightly stochastic trajectory paths can be attributed to the much higher complexity of the unsteady three-dimensional flowfield that evolves from the boundary-layer-generated turbulence, which is shed from the blade surfaces in the highly resolved LESs. Details about the CFD mesh and the extraction of the vortex core positions can be found in Ref. [25].

Overall, this comparison shows that the simple flap model of the LLFVW method is reasonably suitable for obtaining an estimate of the magnitude and growth of tip vortex perturbations caused by trailing-edge flap deflections.

IV. Comparison Between an LLFVW Simulation and LES in Midwake

Since the structured body-fitted mesh of the LES employed in the near-wake comparison becomes progressively coarser downstream, it cannot accurately resolve the tip vortices. Thus, to perform a validation of the LLFVW method's capability for predicting the midwake dynamics, the body-fitted mesh of the LES was replaced by an actuator line model (ACL). The time-varying tangential and

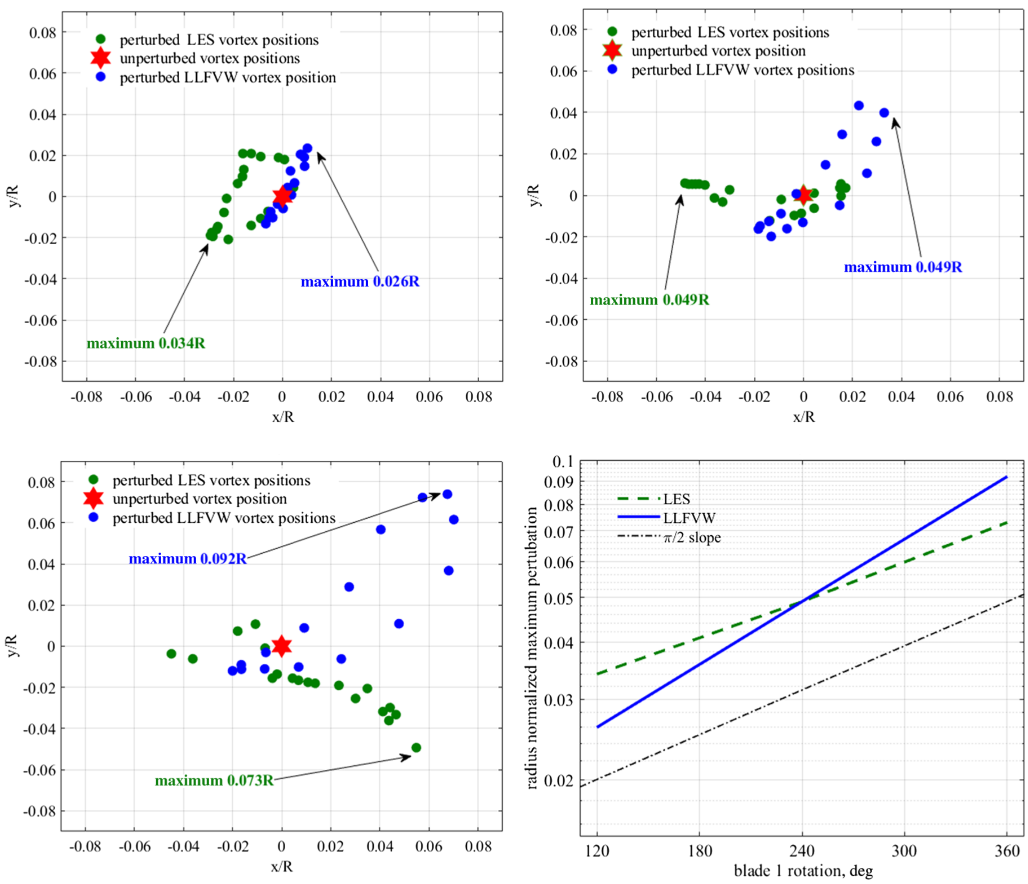

Fig. 5 Comparison of unperturbed and perturbed vortex core positions over one flap oscillation period as computed by LES in Ref. [25] and LLFVW.

Table 2 Operating conditions for the midwake simulations

Operating parameter	Value
RPMs/tip speed ratio/rotor radius	180/4.31/1.5 m
Inflow velocity	6.5 m/s, uniform
Dimensionless actuation frequency f_c	1.5; 3.0
Flap actuation amplitude	0; 2 deg

normal blade forces corresponding to the flap deflections that are interpolated onto the actuator line are taken from fully converged LLFVW simulations (see Fig. 6).

The results between LLFVW and LES are then compared in the midwake region up to three rotor diameters behind the rotor plane. A baseline case without flap actuation and two perturbed cases with a 2 deg flap actuation at $f_c = 1.5$ and 3.0 are compared at the operating conditions shown in Table 2.

A. Numerical Setup of LES

The actuator line method [34] is used to model the turbine blade. The influence of the flap motion can be achieved by adding a force oscillation on the actuator line where the tip and midspan flap are located. The magnitude of the force oscillations and their radial distribution has been precomputed by LLFVW simulations. The precomputed forces are interpolated on the actuator line and imposed into the source term of the Navier–Stokes equations. Figure 6 shows the precomputed normal and tangential force distributions (relative to the rotor plane) from the LLFVW with 0 deg flap deflection. The computational domain (see Fig. 7) has a streamwise extent of 30R. The inflow plane is positioned 10R upstream of the rotor, and the outflow cross section is located 20R downstream of the rotor. Most cells are concentrated in the equidistant region near the actuator lines. Approximately 50 mesh points discretize each actuator line. In total, the grid consists of approximately 36×10^6 cells.

B. Numerical Setup of LLFVW Midwake Simulations

The full rotor is simulated with the LLFVW method in QBlade. Each blade is discretized with 14 evenly spaced panels, and each flap is made of two panels (in comparison to Sec. III, a coarser blade discretization was chosen to accelerate the midwake calculations). The azimuthal discretization is set to 5 deg. The initial vortex core size is set to 10% of the local chord, and a turbulent vortex viscosity coefficient [33] of 7.5 is used. The turbulent vortex viscosity coefficient of 7.5 was found by means of a sensitivity study to show best agreement with the LES vorticity contours. The simulation is calculated for 22 full rotor revolutions, whereas the wake is truncated after nine full revolutions, resulting in a maximum of ~52,000 free vortex line elements at a time.

C. Results and Comparison

Figure 8 shows the comparison of the results from the LLFVW simulation and the LES for a case without flap actuation and two cases with flap actuation at the dimensionless frequencies f_c of 1.5 and 3. The result that are illustrated here are time averaged over four rotor revolutions. The time averaged Q criterion in the globally fixed rotor mid-plane is a good indicator for the averaged vortex core trajectories.

The baseline case without flap actuation (top of Fig. 8) shows particularly good agreement for the time averaged Q criterion. No flap actuation is present, and no wake breakdown can be observed. The LLFVW method exhibits a slightly lower diffusion of the

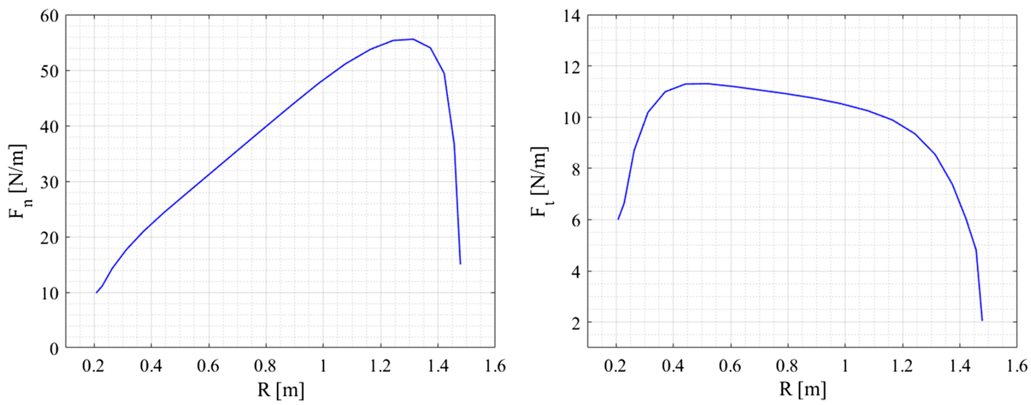

Fig. 6 Normal and tangential forces of the BERT blade without oscillating flap calculated with the LLFVW method and used in the LES-ACL simulation.

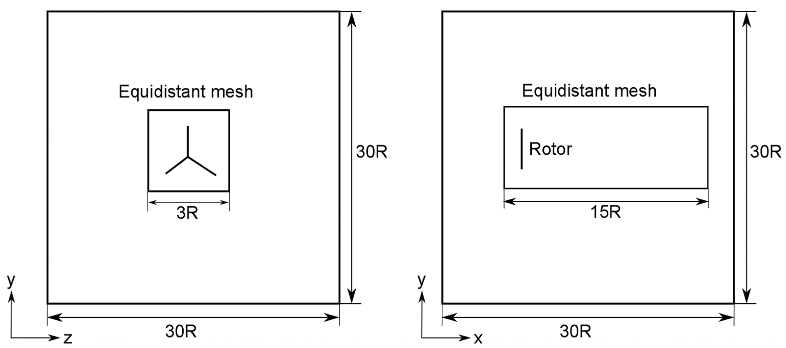

Fig. 7 Computational domain of the LES-ACL simulations.

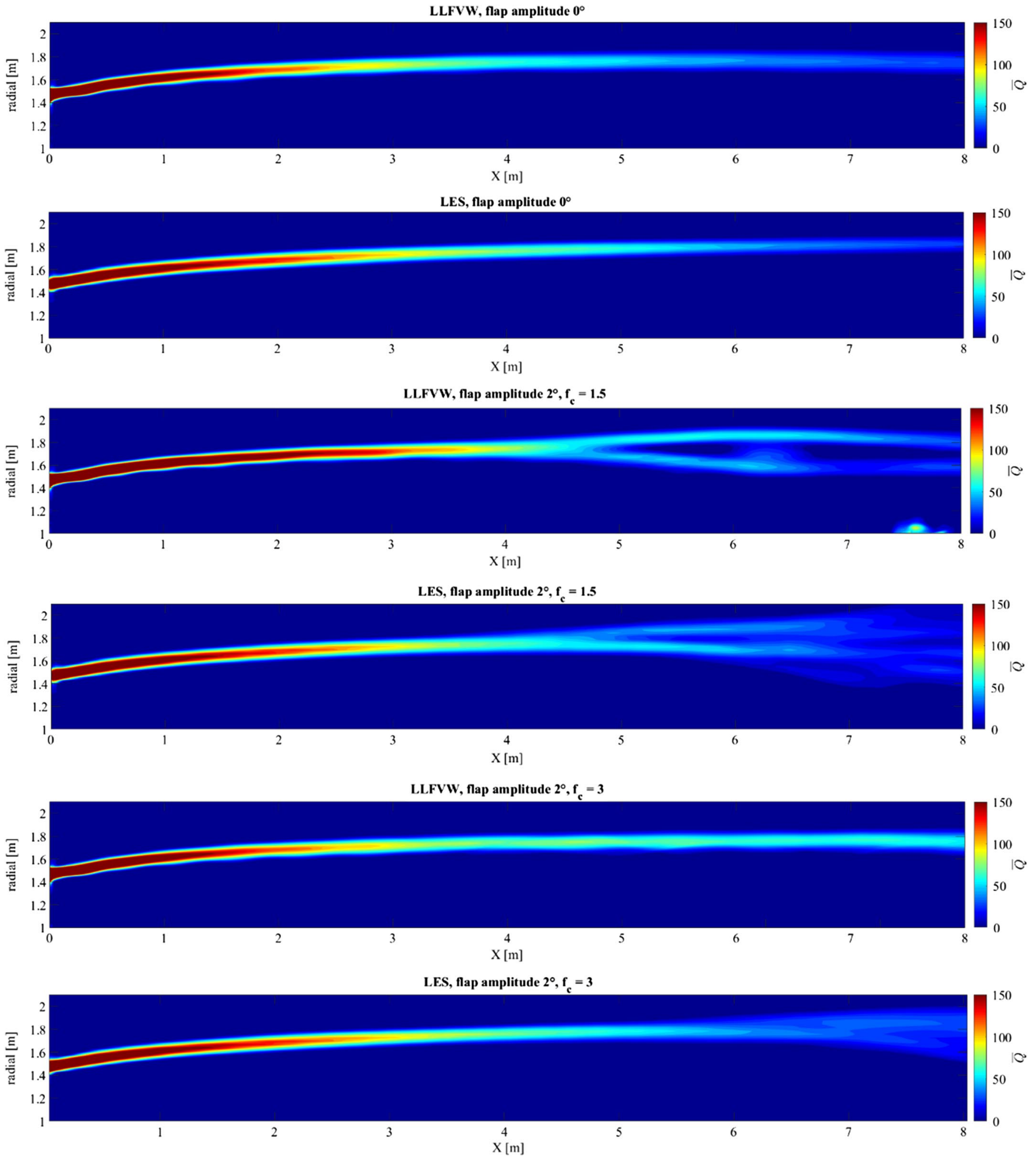

Fig. 8 Comparison between LLFVW and LES results for three different cases showing the time-averaged Q criterion of the tip vortices.

vortices when compared to the LES. Such differences can be expected since the diffusion in the LLFVW method, realized through a vortex core growth function that is implemented in the filament formulation, relies on semiempirical factors for the initial core size and the core size growth rate. In the second case with a flap oscillation frequency f_c of 1.5, shown in the middle of Fig. 8, the onset of wake breakdown is visible in both the LES and the LLFVW simulation. In the time averaged Q-criterion field, a "separation" of the vortex trajectories starting at around $x = 4.8$ is clearly visible. This apparent separation is due to vortex pairing that starts to occur in this region.

At the bottom of Fig. 8, where the flap is actuated at $f_c = 3.0$, no clear wake breakdown is visible in either the LES or the LLFVW results. Although the LES code shows a significantly more smeared time averaged Q criterion around $x = 8$ m, this is not an effect of vortex pairing but can be attributed to viscous effects that are not resolved by the LLFVW method.

Overall, the comparison shows consistent agreement between the LES and the LLFVW simulation results. Minor differences can be attributed to the inability of the LLFVW method for modeling small-scale viscous effects that the LES can resolve.

V. Wake Stability Investigations Using the LLFVW

To compare the capability of the LLFVW method for correctly predicting the wake dynamics of vortex pairing and the associated wake breakdown for a range of different wake excitation frequencies, a comparison to literature data was performed. A detailed analysis of the inductance instability in a wind turbine wake has been undertaken by Ivanell et al. in Ref. [14], Carrión et al. in Ref. [17], and Sarmast et al. in Ref. [15]. Through the modal decomposition technique and Fourier analysis, the growth rate of perturbations at different excitation frequencies and the mechanisms of the underlying vortex dynamics have been investigated. The analyses in Refs. [14,15] are based on actuator line LESs of the Tjaereborg wind turbine rotor. Further theoretical work on wake stability has been conducted in the past by many researchers [10–17]. This work forms an excellent dataset for the validation of the wind turbine wake-related vortex dynamics predicted by the LLFVW code. The LLFVW simulations were performed with the BERT rotor geometry and the operating conditions shown in Table 3.

A. Numerical Setup of LLFVW Wake Simulations

Each blade is discretized with 14 evenly spaced panels, and each flap is made of two panels. The azimuthal discretization is set to 5 deg. The initial vortex core size is set to 10% of the local chord, and the turbulent vortex viscosity coefficient [33] is set to 7.5. The simulation is calculated for 22 full rotor revolutions, whereas the wake is truncated after nine full revolutions, resulting in a maximum of ~52,000 free vortex line elements at a time. To facilitate the analysis of the growth of wake perturbations over a larger downstream distance, a reduced flap amplitude of only 0.2 deg was employed in this comparison. Due to the smaller flap amplitude, the linear region of the growth stretches further downstream until a nonlinear state is eventually reached. However, when reducing the amplitude of flap actuation, care must be taken to not select too small amplitudes that are in the same order as numerical truncation errors.

For this analysis, the wake was excited harmonically at frequencies f_c equal to multiples of the rotor rotational frequency, as shown in Table 3. The last four rotor revolutions from a simulation after the rotor loading is sufficiently converged were recorded and evaluated at a rate of 72 samples per rotor revolution. This is sufficient for the FFT to resolve dimensionless frequencies f_c of up to 36 with a frequency resolution of 0.25.

B. Analysis of Perturbation Growth Rates

The flow snapshots obtained from the numerical simulations are transformed into cylindrical coordinates with the origin being aligned with the wind turbine hub centerline. In addition, the snapshots are recorded in a rotating frame of reference to decouple the flowfield from the uniform rotation of the blades. This enables tracking the tip vortices at a constant rotor phase angle, eliminating the streamwise convection and keeping track of the vortex displacements at fixed streamwise positions.

Successively, the snapshots $\boldsymbol{u}_n$ are Reynolds decomposed into a mean and a fluctuation part $\boldsymbol{u}_n = \bar{\boldsymbol{u}} + \boldsymbol{u}'_n$. In the corotating frame of reference, the mean part includes the induced velocities of the vortices since they are stationary, apart from the periodic displacements. Conversely, the fluctuation part describes these very displacements. For analyzing the displacements ranked by frequency, the N snapshots of the fluctuation part $\boldsymbol{u}'_n$ are Fourier transformed into the frequency domain via

Table 3 **Operating conditions for the parametric study**

Operating parameter	Value
RPMs/tip speed ratio/rotor radius	180/4.31/1.5 m
Inflow velocity	6.5 m/s, uniform
Dimensionless actuation frequency f_c	0.5 to 7.5 in steps of 0.5
Flap actuation amplitude	0.2 deg

$$\hat{\boldsymbol{u}}'_k = \frac{1}{N}\sum_{n=0}^{N-1} \boldsymbol{u}'_n e^{-ink(2\pi/N)} \tag{3}$$

where $\hat{\boldsymbol{u}}_k$ is the vector of the Fourier coefficients of the kth mode at frequency $f_k = k/(N\Delta t)$ with $k = [0, 1, 2, \dots, N/2 - 1]$. Subsequently, each of the k Fourier modes are integrated over the radial coordinate at each streamwise position in order to obtain the specific energy for each cross section:

$$E_k = \frac{\rho}{2}\int_{r_1}^{r_2} |\hat{\boldsymbol{u}}'_k|^2 \,\mathrm{d}r \tag{4}$$

where r_1 and r_2 denote the limits of integration for the region of interest, i.e., the section comprising the tip vortices.

For a perturbed case, the strongest and initial response occurs at the fundamental frequency of the perturbation frequency, followed by the first harmonic. The first harmonic starts to grow, spatially shifted in the downstream direction, and only becomes significant in the nonlinear stage of the wake breakdown. This is in line with previous studies [14]. Since this paper focuses on the predictive capability of LLFVW for perturbation growth in the linear stage until vortex pairing occurs (excluding the wake breakdown region downstream), only the response at the fundamental frequency is considered in the following.

As mentioned before, the vortices have discrete positions. Therefore, the bulk of the fluctuation energy occurring at the fundamental perturbation frequency is accumulated at these locations, leading to localized narrow peaks at each streamwise vortex position. These peaks correspond to the magnitude of the vortex displacements, fixed at this specific rotor phase angle. The envelope of these peaks provides the overall growth of the vortex displacements over all rotor phase angles, i.e., along the entire helical vortex filament.

From the specific energy of the Fourier coefficient vector, the local growth rates can be calculated. The exponential growth rate that occurs in the linear region of the induction instability [14,15] is particularly interesting. The linear region can be readily identified in a semilog scaled plot. The exponential growth of the energy is then described by the ansatz

$$\frac{E_{k,2}}{E_{k,1}} = e^{\sigma(x_2 - x_1)} \tag{5}$$

where indices 1 and 2, respectively, denote an upstream and a downstream position in the linear region; and where σ denotes the growth rate. The growth rate over all streamwise positions in the linear region is obtained by solving a nonlinear least-squares problem with the previously mentioned exponential ansatz as the model function. The resulting growth rate is normalized with

$$\sigma_{\mathrm{Norm}} = \sigma \frac{2h^2 U_c}{\Gamma} \tag{6}$$

where σ is the nonnormalized growth rate, h is the axial distance between two vortices, U_c is the convective velocity of the vortices, and Γ is the circulation of a vortex. The convective velocity of the vortices was evaluated from the flowfields to be $U_c = 4.23$ m/s, the axial vortex distance is $h = 0.791$ m, and the circulation of the tip vortex is $\Gamma = 1.9$ m^2/s.

C. Results and Comparison to Literature

Figure 9 shows the calculated Fourier coefficients for the fundamental frequency with which the flaps were deflected. The growth rate is evaluated in the linear region. The linear region has objectively identified from this dataset as the region in which linear growth is observed for all excitation frequencies. The wake breakdown can be observed at the position where the Fourier coefficient of the excited fundamental frequency reaches its maximum.

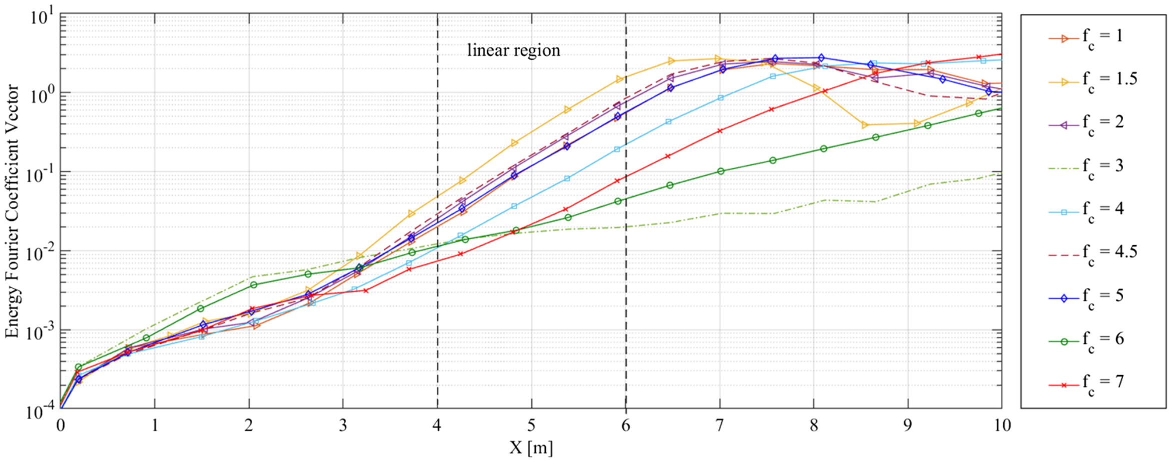

Fig. 9 Fourier coefficients for selected perturbation frequencies, calculated at discrete vortex positions.

In Fig. 10, the growth rates for different frequencies are compared to data that were evaluated from simulations of the Tjaerborg turbine in Refs. [14,15]. In these publications, the perturbations were injected into the wake by directly modifying the streamwise component of the freestream velocity in the vicinity of the tip vortices with a harmonic signal. The Tjaerborg turbine was simulated at a tip speed ratio of 7.07 with 10 m/s inflow and a thrust coefficient of $C_t = 0.79$. The operating conditions of the BERT rotor shown in Table 3 lead to a thrust coefficient of $C_t = 0.78$; thus, a similar operating state is ensured.

The results obtained from the LLFVW simulations follow the overall trend very well and exhibit their minima and maxima at the frequencies that were also predicted by Leishman et al. in a previous study [13]. Maxima of the growth rate are found at $f_c = 1.5, 4.5$, and 7.5, whereas minima exist at $f_c = 3$ and 6.

The general trend is that the LLFVW predicts slightly larger growth rates than corresponding LESs, especially when compared to the result from Ivanell et al. in Ref. [14]. This confirms the trend that was already observed in Sec. III of this work where the simulation of tip vortex displacements was compared between LLFVW and LES.

One reason for this could be the Lagrangian treatment of the vorticity in the LLFVW simulation where diffusion is only included via empirically tuned core growth rates, and no numerical diffusion occurs. However, some of the LESs also predict growth rates larger than $\pi/2$. This is partially explained in Ref. [15] by a potential subharmonic excitation in these cases. In Ref. [14], it is mentioned that a finer grid leads to larger growth rates.

Overall, this comparison shows that the free vortex wake method implemented in QBlade is suitable for evaluating the onset of wake breakdown. An advantage, when compared to LES tools, is the high numerical efficiency. Using the LLFVW method, a single simulation for one excitation frequency over 22 rotor revolutions could be evaluated in 260 s on a single workstation. The comparable LES shown in Sec. IV required about 4 h on 1800 CPU cores for 22 rotor revolutions. This demonstrates that the difference in computational cost between the two methods is roughly in between four and five orders of magnitude.

Figure 11 shows the tip vortices via the Q criterion in a blade-fixed plane for a baseline case without flap deflection and two exemplary frequencies. The Q-criterion plots are time averaged over four rotor revolutions. The rotor is located at the (0,0) coordinate. The shown extension in the X direction equals three rotor diameters. When the wake is not perturbed, no breakdown can be observed in the region that is shown.

For an excitation at $f_c = 1.5$, at which the growth rate has a maximum, wake breakdown can be observed at a position of

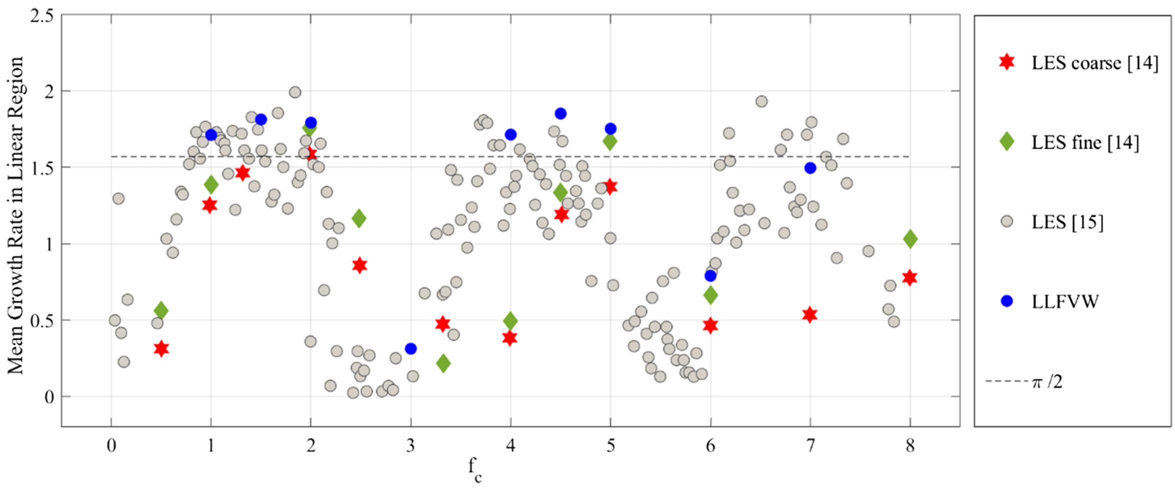

Fig. 10 Comparison to literature of mean perturbation growth rates over dimensionless perturbation frequencies calculated in the linear region of Fig. 9.

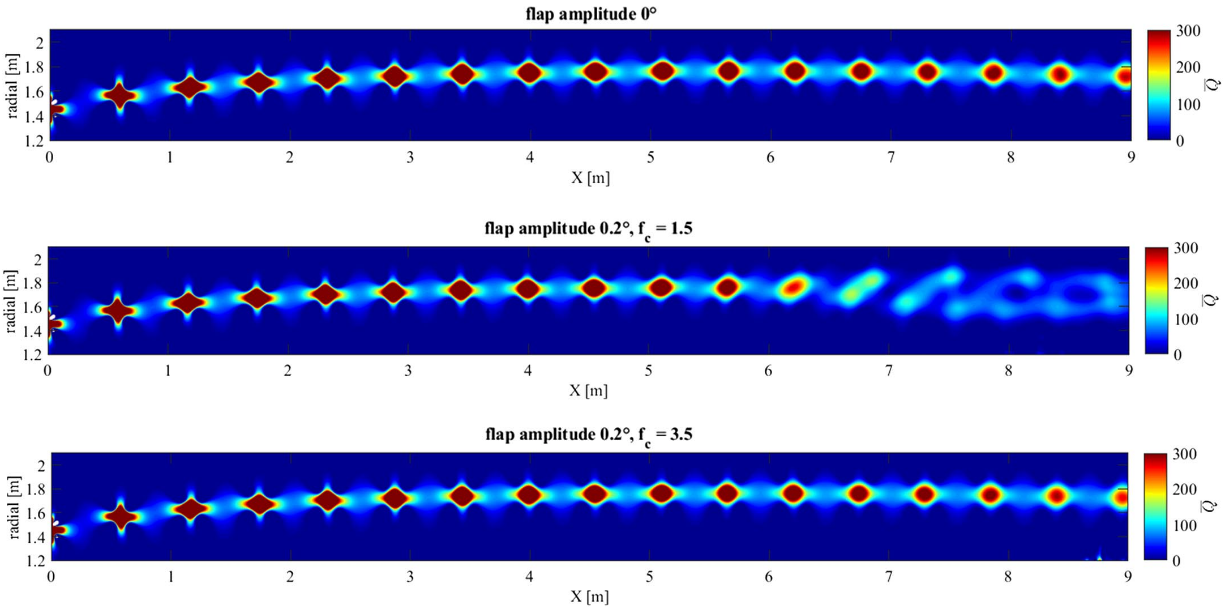

Fig. 11 ***Q*** **criterion of the blade tip vortices in a blade-fixed plane: no perturbation (top), perturbed with 0.2 deg flap deflection $f_c = 1.5$ (middle), and perturbed with 0.2 deg flap deflection $f_c = 3.5$ (bottom).**

$X = \sim 7$ m; this can also be confirmed when looking at the maximum of the Fourier coefficient for $f_c = 1.5$ in Fig. 9. The perturbation waves of neighboring vortex rings pass each other out of phase, and small perturbations are amplified due to a change in relative distance and mutual-induction interaction in the velocity field. Ultimately, the growing perturbation leads to a pairing of two successive vortex rings (see Fig. 12), the kinetic energy content of the wake rapidly increases, and a three-dimensional breakdown of the helical wake structure follows [35].

When exciting the wake at $f_c = 3.5$, where the growth rate is near a minimum, no breakdown can be observed. The perturbation waves of neighboring vortex rings pass each other almost in phase, which inhibits the growth of the perturbation because the relative distances between successive vortex rings and the induced velocities do not change significantly. Examples for general wake shapes at different actuation frequencies are shown in Fig. 13.

VI. Effect of Flap Actuation on Wake Breakdown in a Turbulent Wind Field

For a practical application, the key question is the following: How effective is the flap actuation to promote wake breakdown in turbulent wind conditions? To give an example, the NREL 5 MW reference wind turbine [36] is equipped with an active trailing-edge flap and

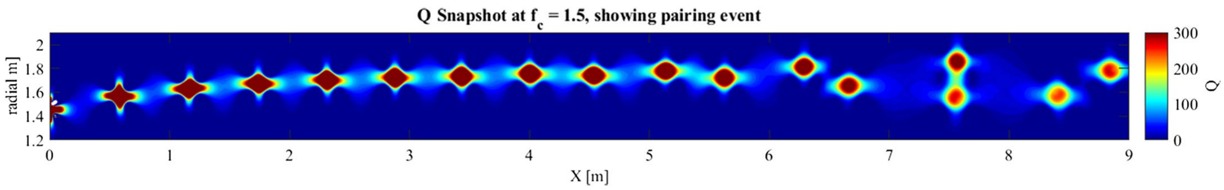

Fig. 12 **Snapshot of** ***Q*** **criterion, showing vortex pairing.**

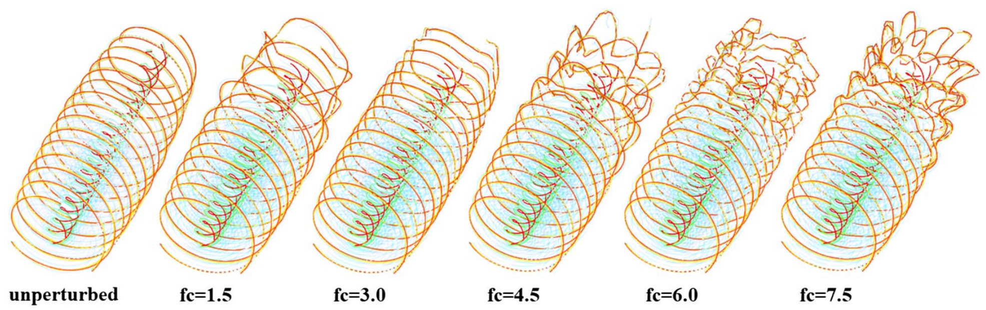

Fig. 13 **Exemplary wake shapes at different perturbation frequencies for a harmonic flap actuation, with vortex filaments colored by vorticity magnitude.**

simulations are conducted under turbulent inflow conditions. A trailing-edge flap was applied to the outer 5% of the NREL 5 MW baseline blade geometry (see Fig. 14). At these outboard positions, the NREL 5 MW turbine uses the NACA 64618 airfoil geometry, to which a flap hinged at the 70% chordwise position was added.

Simulations are performed under turbulent inflow conditions using a three-dimensional turbulent wind box generated with the Veers [37] method (see Fig. 15). The generated turbulence has a power spectral density after the Kaimal model and a turbulence intensity of 12%, representative of a lower-turbulence type-C wind class according to the IEC-61400-1 standard [38]. For the wind box, Taylor's frozen turbulence hypothesis is assumed.

The turbulent structures in the inflow are advected with the mean flow, and no two-way interaction between the wake and the inflow vortices is considered. The frozen turbulence hypothesis is a typical assumption in Lagrangian flow formulations and is valid for small turbulence intensities. The operating conditions of the simulation are given in Table 4. The flap actuation frequency is constant at $f_c = 1.5$, for which the perturbation growth rate exhibits a maximum. In Ref. [15] Sarmast et al. found that the maximum growth rate of the perturbation (equal to $\pi/2$) is universal for the vortex pairing instability. As $f_c = 1.5$ is the lowest frequency at which the maximum growth rate appears, this frequency is chosen because it requires the smallest number of flap actuations over the lifetime of the turbine.

As the rotor wake is constantly perturbed through velocity fluctuations when operating in turbulent wind, the wake breakdown occurs much earlier than in an idealized laminar inflow setting. So, how sensitive is the wake breakdown location to the flap actuation in such a scenario?

In Ref. [15], Sarmast et al. developed a semiempirical model to predict the stable wake length of a wind turbine in turbulent inflow of varying turbulence intensity:

Table 4 Operating conditions for the turbulent wind field simulations of the NREL 5 MW wind turbine

Operating parameter	Value
RPMs/tip speed ratio/rotor radius	$9/7.42/63$ m
Inflow velocity	8 m/s, $T_i = 0.12$, Veers generated [37]
Dimensionless actuation frequency f_c	1.5
Flap actuation amplitude	0; 2.5; 5; 7.5; 10; 15 deg

$$\left(\frac{l}{R}\right) = -\frac{16\left(1 + C_2\left(\sqrt{1 - C_T} - 1\right)\right)^3}{N_b \lambda C_T} \ln(C_1 T_i) \tag{7}$$

In a publication by Sørensen et al. [39], the constant C_1, which links the tip vortex perturbations to the turbulence intensity, has been calibrated to $C_1 = 0.33$. The constant $C_2 = 0.5$ corresponds to the roller bearing analogy of Okulov and Sørensen [40], which assumes U_c, (the convective velocity of the vortices) to be the average between the freestream velocity and the wake velocity. Inserting the operating conditions of the simulated NREL 5 MW turbine, which were obtained by averaging over the instantaneous inflow conditions ($N_b = 3$; $\lambda = 7.42$; $C_T = 0.77$; $T_i = 0.12$), in Eq. (7) yields the vortex pairing position as $l = 73.68$ m.

In the following, the results of the analysis are presented. For each flap actuation amplitude, the contour plots of the Q criterion are time averaged over six rotor revolutions (or 432 individual snapshots) in a plane that is fixed to the blade rotation. The results are shown in Fig. 16. In the blade-fixed rotating frame of reference, the flowfield is decoupled from the rotation of the rotor and the streamwise convection of the tip vortices is eliminated. Thus, the smearing of the Q criterion be directly linked to the inflow turbulence and the growing oscillations of the tip vortices (as previously discussed in Sec. V.B). The top graph in

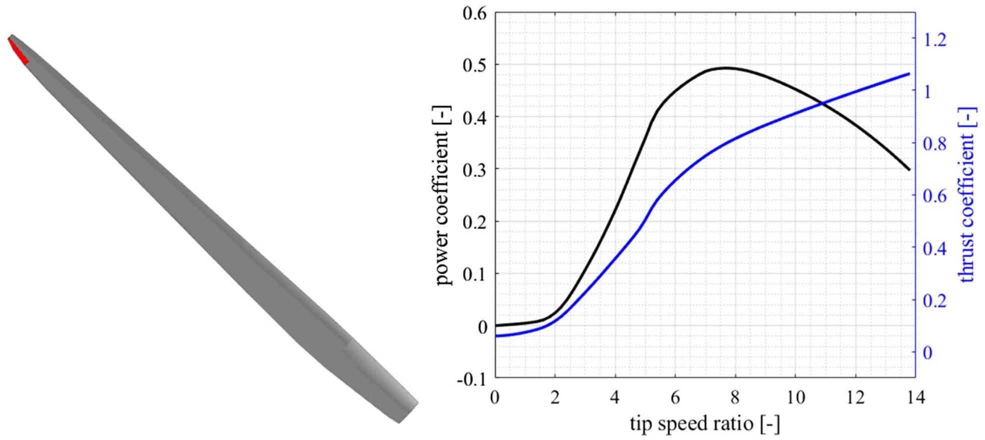

Fig. 14 Illustration of NREL 5 MW blade geometry and flap location (in red) (left), and rotor characteristics of the NREL 5 MW turbine (right).

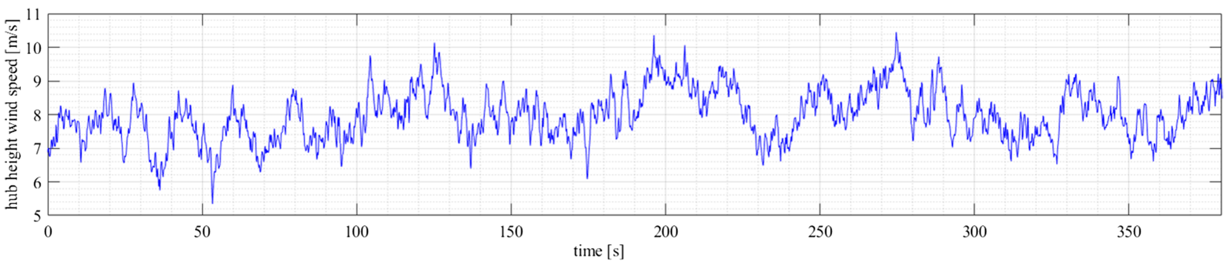

Fig. 15 Wind speed sampled at the hub during the simulations with 12% turbulence.

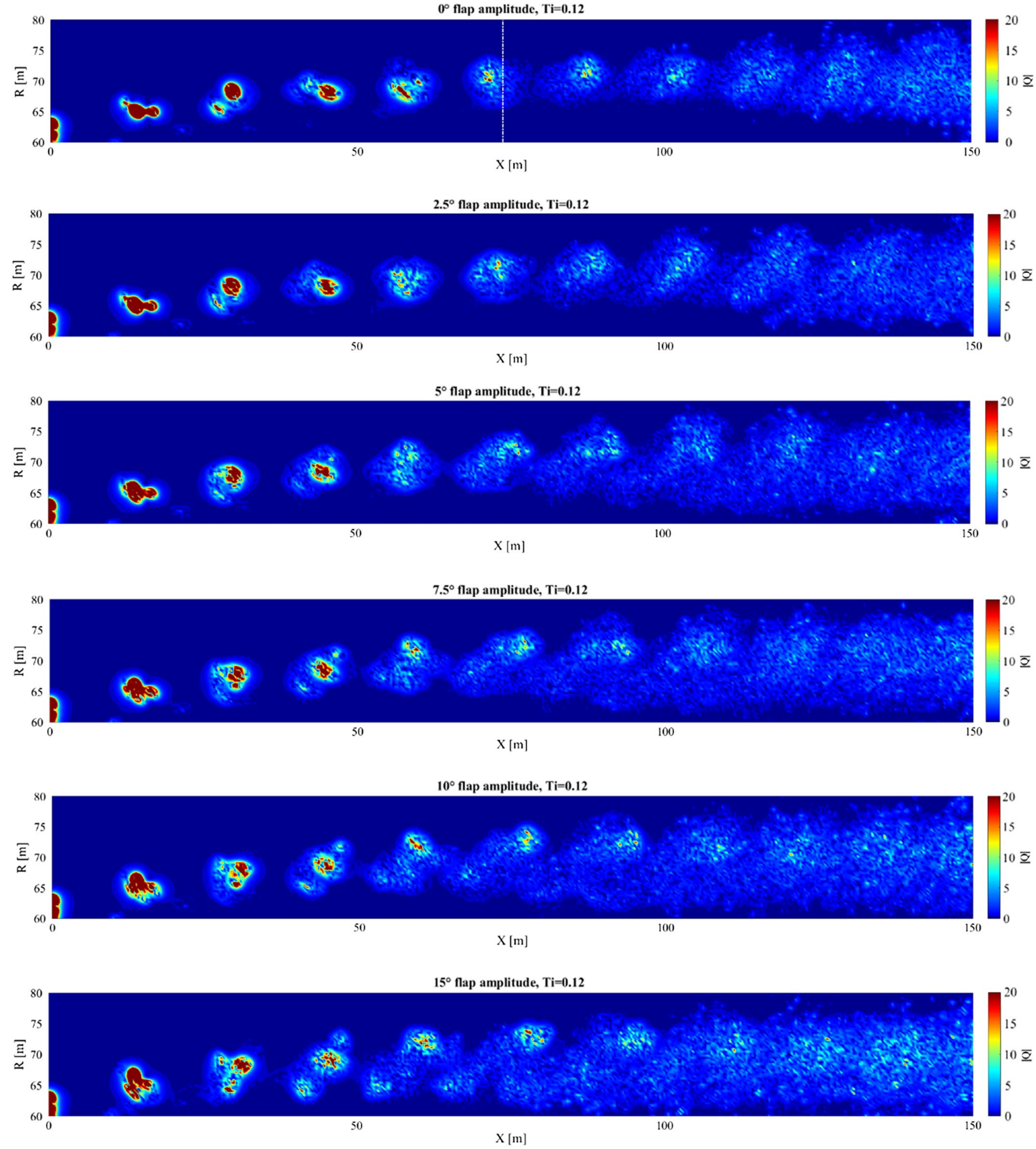

Fig. 16 Onset of wake breakdown locations in a turbulent wind field for different flap actuation amplitudes at a constant excitation frequency of $f_c = 1.5$, shown as the Q-criterion magnitude.

Fig. 16 shows the case without flap actuation, where vortex pairing occurs solely due to the inflow turbulence induced perturbations. The white dotted line shows the location for vortex pairing that was predicted by using the formulation of Sarmast et al. [15] given in Eq. (7). The simulation results confirm that this location marks the onset of vortex pairing because the following vortex cross section in the downstream direction already shows a significant amount of spatial oscillations. Generally, Fig. 16 shows that the larger the flap oscillations, the earlier the onset of wake breakdown is occurring.

Figure 17 shows the calculated wake breakdown positions over the flap actuation angle. The smallest actuation amplitude already significantly affects the wake breakdown location. While the breakdown location is consequently shifted upstream for larger flap deflection amplitudes, the gain in the shift of breakdown location grows smaller. It can therefore be concluded that even under turbulent inflow conditions, the introduction of a small perturbation in the vicinity of the tip vortex has a significant effect on the location of wake breakdown.

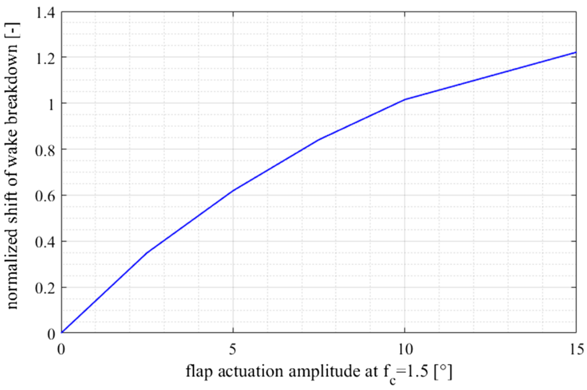

Fig. 17 Upstream shift of wake breakdown normalized with rotor radius over the flap actuation amplitude.

VII. Conclusions

By comparing LESs to data from the literature, it was shown that the LLFVW method (based on straight line vortex filaments) is a cost-efficient and consistent technique for modeling the near wake and predicting the breakdown location of wind turbine wakes. Under idealized conditions, the predicted perturbation growth rate and the mechanism of vortex pairing agree well with the theory and the results obtained from literature. Furthermore, in an exemplary study, the effect of flap actuation on the wake breakdown of a 5 MW reference turbine operating in a realistic turbulent wind field could be demonstrated.

An intended application of this work will be to integrate a hybrid vortex line/particle formulation into the open-source QBlade simulation tool. The more computationally efficient vortex line filaments will be used to model the near wake and will then be converted into vortex particles at the detected wake breakdown location. Vortex particles can significantly improve the modeling of three-dimensional turbulent mixing and the process of wake recovery that is taking place after the wake breakdown. The resulting simulation tool could perform accurate aeroservoelastic multiturbine simulations in wind park settings with a computational cost that is several magnitudes lower than those of comparable CFD solvers.

Acknowledgments

The authors gratefully acknowledge the support of the German Science Foundation (DFG) for funding this research through the research project PAK 780 "Wind Turbine Load Control Under Realistic Inflow Conditions." Furthermore, the authors would like to acknowledge the NVIDIA Corporation for providing an NVIDIA Quadro P6000 graphics processing unit on which the QBlade lifting-line free vortex wake simulations have been performed. The authors gratefully acknowledge the Gauss Centre for Supercomputing e.V. (GCS) for funding this project by providing computing time on two GCS supercomputers: Hazel Hen at the High Performance Computing Center Stuttgart (HLRS), and the supercomputer JUQUEEN at the Jülich Supercomputing Centre.

References

[1] Fleming, P., Annoni, J., Shah, J. J., Wang, L, Ananthan, S., Thang, Z., Hutchings, K., Wang, P., Chen, W., and Chen, L., "Field Test of Wake Steering at an Offshore Wind Farm," *Wind Energy Science*, Vol. 2, No. 1, 2017, pp. 229–239.
https://doi.org/10.5194/wes-2-229-2017

[2] Feng, J., and Shen, W. Z., "Solving the Wind Farm Layout Optimization Problem Using Random Search Algorithm," *Renewable Energy*, Vol. 78, June 2015, pp. 182–192.
https://doi.org/10.1016/j.renene.2015.01.005

[3] Madsen, H. A., Bergami, L., and Rasmussen, F., "New Aerodynamics Rotor Concepts Specifically for Very Large Offshore Wind Turbines," Innwind TR D2.11, Europe, 2013.

[4] Ajormand Kermani, A., Andersen, S. J., Sørensen, J. N., and Shen, W. Z., "Analysis of Turbulent Wake Behind a Wind Turbine," *Proceedings of the 2013 International Conference on Aerodynamics of Offshore Wind Energy Systems and Wakes (ICOWES2013)*, Technical Univ. of Denmark, Lyngby, Denmark, June 2013, pp. 1–16.

[5] Marten, D., Lennie, M., Pechlivanoglou, G., Nayeri, C. D., and Paschereit, C. O., "Implementation, Optimization and Validation of a Nonlinear Lifting Line Free Vortex Wake Module Within the Wind Turbine Simulation Code QBlade," *Journal of Engineering for Gas Turbines and Power*, Vol. 138, No. 7, 2016, Paper 072601.
https://doi.org/10.1115/1.4031872

[6] Shapiro, C. R., Gayme, D. F., and Meneveau, C., "Modelling Yawed Wind Turbine Wakes: A Lifting Line Approach," *Journal of Fluid Mechanics*, Vol. 841, April 2018, Paper R1.
https://doi.org/10.1017/jfm.2018.75

[7] Jeon, M., Lee, S., Kim, T., and Lee, S., "Wake Influence on Dynamic Load Characteristics of Offshore Floating Wind Turbines," *AIAA Journal*, Vol. 54, No. 11, 2016, pp. 3535–3545.
https://doi.org/10.2514/1.J054584

[8] Branlard, E., "Analysis of Wind Turbine Aerodynamics and Aeroelasticity Using Vortex-Based Methods," Ph.D. Thesis, DTU Wind Energy Phd-0052(EN), 2015, p. 219.

[9] Joukowsky, N. E., "Vortex Theory of Screw Propeller, I," *Trudy Otdeleniya Fizicheskikh Nauk Obshchestva Lubitelei Estestvoznaniya*, Vol. 16, No. 1, 1912, pp. 1–31 (in Russian); also *Théorie Tourbillonnaire de l'Hélice Propulsive*, Gauthier–Villars, Paris, 1929, pp. 1–47 (in French).

[10] Crow, S. C., "Stability Theory for a Pair of Trailing Vortices," *AIAA Journal*, Vol. 8, No. 12, 1970, pp. 2172–2179.
https://doi.org/10.2514/3.6083

[11] Widnall, S. E., "The Stability of a Helical Vortex Filament," *Journal of Fluid Mechanics*, Vol. 54, No. 4, 1972, pp. 641–663.
https://doi.org/10.1017/S0022112072000928.

[12] Gupta, B. P., and Loewy, R. G., "Theoretical Analysis of the Aerodynamic Stability of Multiple Interdigitated Helical Vortices," *AIAA Journal*, Vol. 12, No. 10, 1974, pp. 1381–1387.
https://doi.org/10.2514/3.49493

[13] Leishman, G., Bhagwat, M. J., and Ananthan, S., "The Vortex Ring State as a Spatially and Temporally Developing Wake Instability," *Journal of the American Helicopter Society*, Vol. 49, No. 2, 2004, pp. 160–175.
https://doi.org/10.4050/JAHS.49.160

[14] Ivanell, S., Mikkelsen, R., Sorensen, J. N., and Henningson, D., "Stability Analysis of the Tip Vortices of a Wind Turbine," *Wind Energy*, Vol. 13, No. 8, 2010, pp. 705–715.
https://doi.org/10.1002/we.391

[15] Sarmast, S., Dadfar, R., Mikkelsen, R. F., Schlatter, P., Ivanell, S., Sørensen, J. N., and Henningson, D. S., "Mutual Inductance Instability of the Tip Vortices Behind a Wind Turbine," *Journal of Fluid Mechanics*, Vol. 755, Sept. 2014, pp. 705–731.
https://doi.org/10.1017/jfm.2014.326

[16] Quaranta, H. U., Bolnot, H., and Leweke, T., "Long-Wave Instability of a Helical Vortex," *Journal of Fluid Mechanics*, Vol. 780, Oct. 2015, pp. 687–716.
https://doi.org/10.1017/jfm.2015.479

[17] Carrión, M., Woodgate, M., Steijl, R., Barakos, G. N., Gomez-Iradi, S., and Munduate, X., "Understanding Wind-Turbine Wake Breakdown Using Computational Fluid Dynamics," *AIAA Journal*, Vol. 53, No. 3, 2015, pp. 588–602.
https://doi.org/10.2514/1.J053196

[18] Schepers, J. G., and Snel, H., "Final Report of IEA Task 29, MexNext (Phase I): Analysis of Mexico Wind Tunnel Measurements," Energy Research Center of the Netherlands TR-ECN-E-12-004, Petten, The Netherlands, Feb. 2012.

[19] Nayeri, C. N., Vey, S., Marten, D., Pechlivanoglou, G., Paschereit, C. O., Huang, X., Meinke, M., Schöder, W., Kampers, G., Hölling, M., Peinke, J., Fischer, A., Lutz, T., Krämer, E., Cordes, U., Hufnagel, K., Schiffmann, K., Spiegelberg, H., and Tropea, C., "Collaborative Research on Wind Turbine Load Control under Realistic Turbulent Inflow Conditions," *12th German Wind Energy Conference*, UL DEWI, May 2015.

[20] Pechlivanoglou, G., Fischer, J., Eisele, O., Vey, S., Nayeri, C., and Paschereit, C. O., "Development of a Medium Scale Research Hawt for Inflow and Aerodynamic Research in the Tu Berlin Wind Tunnel," UL DEWI, 2015.

[21] Klein, A. C., Bartholomay, S., Marten, D., Lutz, T., Pechlivanoglou, G., Nayeri, N. C., Paschereit, C. O., and Krämer, E., "About the Suitability of Different Numerical Methods to Reproduce Model Wind Turbine Measurements in a Wind Tunnel with a High Blockage Ratio," *Wind Energy Science*, Vol. 3, June 2018, pp. 349–460.

[22] Marten, D., Bartholomay, S., Pechlivanoglou, G., Nayeri, C. N., and Paschereit, C. O., "Numerical and Experimental Investigation of Trailing Edge Flap Performance on a Model Wind Turbine," *2018 Wind Energy Symposium, AIAA SciTech Forum*, AIAA Paper 2018-1246, 2018.
https://doi.org/10.2514/6.2018-1246

[23] Barlas, T. K., and van Kuik, G. A. M., "Review of State of the Art in Smart Rotor Control Research for Wind Turbines," *Progress in Aerospace Sciences*, Vol. 46, No. 1, 2010, pp. 1–27.
https://doi.org/10.1016/j.paerosci.2009.08.002.

[24] Barlas, T., "Active Aerodynamic Load Control on Wind Turbine Blades: Aeroservoelastic Modelling and Wind Tunnel Experiments," Ph.D. Thesis, Delft Univ. of Technology, Delft, The Netherlands, 2011.

[25] Huang, X., Alavi Moghadam, S. M., Meysonnat, P. S., Meinke, M., and Schröder, W., "Numerical Analysis of the Effect of Flaps on the Tip Vortex of a Wind Turbine Blade," *International Journal of Heat and Fluid Flow*, Vol. 77, June 2019, pp. 336–351.
https://doi.org/10.1016/j.ijheatfluidflow.2019.05.004

[26] Van Garrel, A., "Development of a Wind Turbine Aerodynamics Simulation Module," Tech. Rept., ECN, Petten, Netherlands, 2003.

[27] Bergami, L., and Gaunaa, M., "ATEFlap Aerodynamic Model, a Dynamic Stall Model Including the Effects of Trailing Edge Flap Deflection," Tech. Rept., DTU, Copenhagen, Denmark, 2012.

[28] Boris, J. P., Grinstein, F. F., Oran, E. S., and Kolbe, R. L., "New Insights into Large Eddy Simulation," *Fluid Dynamics Research* Vol. 10, Nos. 4–6, 1992, pp. 199–228.
https://doi.org/10.1016/0169-5983(92)90023-P

[29] Liou, M. S., and Steffen, C. J., Jr., "A New Flux Splitting Scheme," *Journal of Computational Physics* Vol. 107, No. 1, 1993, pp. 23–39.
https://doi.org/10.1006/jcph.1993.1122

[30] Meinke, M., Schröder, W., Krause, E., and Rister, T., "A Comparison of Second and Sixth-Order Methods for Large-Eddy Simulations," *Computers and Fluids*, Vol. 31, Nos. 4–7, 2002, pp. 695–718.

[31] König, D., Koh, S. R., Meinke, M., and Schröder, W., "Two-Step Simulation of Slat Noise," *Computers and Fluids*, Vol. 39, No. 3, 2010, pp. 512–524.

[32] Feldhusen-Hoffmann, A., Statnikov, V., Klaas, M., and Schröder, W., "Investigation of Shock-Acoustic-Wave Interaction in Transonic Flow," *Experiments in Fluids*, Vol. 59, No. 1, 2018, Paper 15.
https://doi.org/10.1007/s00348-017-2466-z

[33] Xu, H., and Ryckaert, J. P., "On the Coupling Between the Intrinsic Angular Momentum of Molecules and the Fluid Vorticity," *Microscopic Simulations of Complex Flows*, edited by M. Mareschal, Vol. 236, NATO ASI Series (Series B: Physics), Springer, Berlin, 1990.

[34] Sørensen, J. N., and Shen, W. Z., "Numerical Modelling of Wind Turbine Wakes," *Journal of Fluids Engineering*, Vol. 124, No. 1, 2002, pp. 393–399

[35] Lignarolo, L. E. M., Ragni, D., Scarano, F., Simao Ferreira, C. J., and van Bussel, G. J. W., "Tip-Vortex Instability and Turbulent Mixing in Wind-Turbine Wakes," *Journal of Fluid Mechanics*, Vol. 781, Oct. 2015, pp. 467–493.
https://doi.org/10.1017/jfm.2015.470

[36] Jonkman, J., Butterfield, S., Musial, W., and Scott, G., "Definition of a 5-MW Reference Wind Turbine for Offshore System Development," National Renewable Energy Laboratory (NREL) TP-500-38060, Boulder, Colorado, 2009.

[37] Veers, P. S., "Three-Dimensional Wind Simulation," Sandia National Labs. TR SAND88–0152, UC–261, Livermore, CA, 1988.

[38] International Electrotechnical Commission, "IEC 61400-1, Wind Turbines—Part 1," 2005.

[39] Sørensen, J. N., Mikkelsen, R., Sarmast, S., Ivanell, S., and Henningson, D., "Determination of Wind Turbine Near-Wake Length Based on Stability Analysis," *Journal of Physics: Conference Series*, Vol. 524, No. 1, 2014, Paper 012155.
https://doi.org/10.1088/1742-6596/524/1/012155

[40] Okulov, V. L., and Sørensen, J. N., "Stability of Helical Tip Vortices in a Rotor Far Wake," *Journal of Fluid Mechanics*, Vol. 576, April 2007, pp. 1–25.
https://doi.org/10.1017/S0022112006004228

M. M. Choudhari
Associate Editor

3.4. Wind Park Simulations

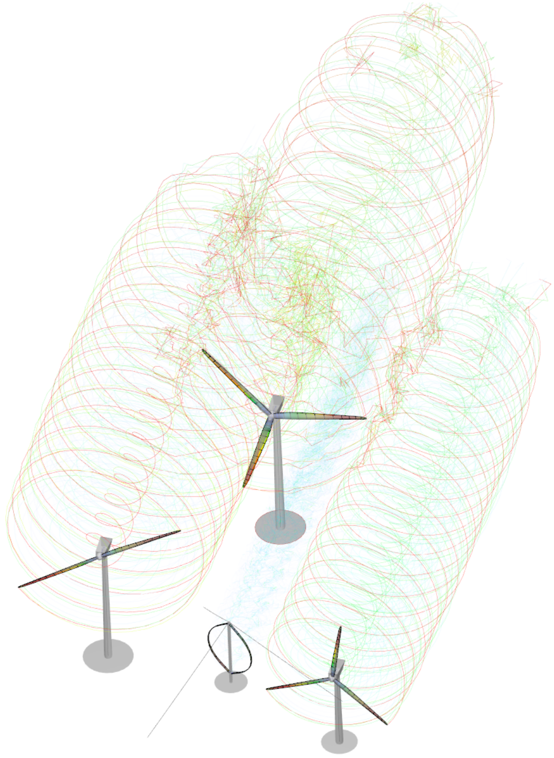

Figure 3.1.: Visualization of a wind park simulation of four different turbines

A current research topic in wind energy is the development and implementation of real-time wind park level control [206, 207, 208]. The main concept is, instead of optimizing only the performance of individual wind turbines through their own controllers, to optimize the overall operation of the whole wind park with the objectives to reduce operation and maintenance cost, increase the overall power production and thereby to lower the overall LCoE. To test wind park controllers, computational efficient simulation tools are needed that can take into account the mutual interactions of all turbines in operation. At present, the common practice is to model such interactions through expensive LES simulations [209, 210], or via reduced order models [211, 212]. As already mentioned in Sections 4.3 and 1.3.2, the free vortex wake formulation is generally suited to simulate the mutual interaction of wind turbines in wind parks with comparably high detail and low computational cost. To enable the application of QBlade for multi-turbine simulations, the complete evaluation of the aeroelastic simulation steps (shown in Figure 2.34) has been parallelized. Multiple turbine instances, each containing their own structural model and supervisory controller, are evaluated in parallel (for an example see Figure 3.1). The individual simulations are advanced with a global time step and the interaction between the rotors and wakes is realized through a global wake array, where the wake elements of all simulated turbines are stored. First results of the multi-turbine simulation capabilities have been presented in [213][53] where multi-turbine simulations for the NTUA blind tests [214, 215] were carried out.

An additional example for the application of the multi-turbine capabilities is shown in Figure 3.3. Two NREL 5MW turbines are separated by $150m$ along the x (downstream) direction and $45m$ along the y (crossstream). It can be seen that the power generation of the downstream turbine starts to undergo large fluctuations (Figure 3.2) about 15% once the wake of the upstream turbine starts to partially impinge onto its rotor. Figure 3.3 shows the interacting wakes. Notice the area of wake interaction, downstream of the second turbine, where the wake structure breaks down. The simulation could be carried out at real-time speed, with an azimuthal discretization of 10° for both rotors[54].

53 One of the associated publications

54 The azimuthal discretization has a large impact on the real time capabilities, the number of wake elements scales linearly with $\Delta\Phi$, 10° is a reasonably fine step for load assessments, similar to what is used for DLC's

In the near future it is planned to further improve the work for multi-turbine simulations in the following aspects:

- When wake breakdown is detected, automatically convert vortex filaments to vortex particles
- Improve the representation of turbulent dissipation and mixing through re-meshing and sub-grid turbulence models within the regions which contain vortex particles
- Implement individual time stepping for each turbine instance, limit turbine interaction to global time steps

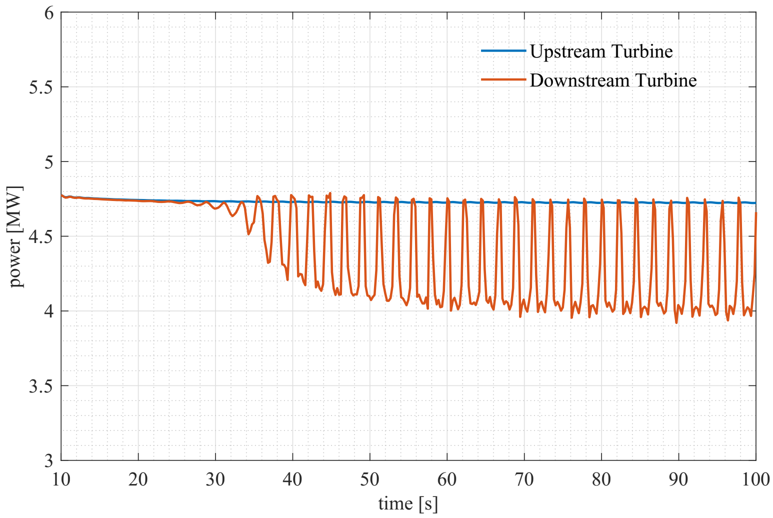

Figure 3.2.: The effect of partial wake impingement on power production of the NREL 5MW

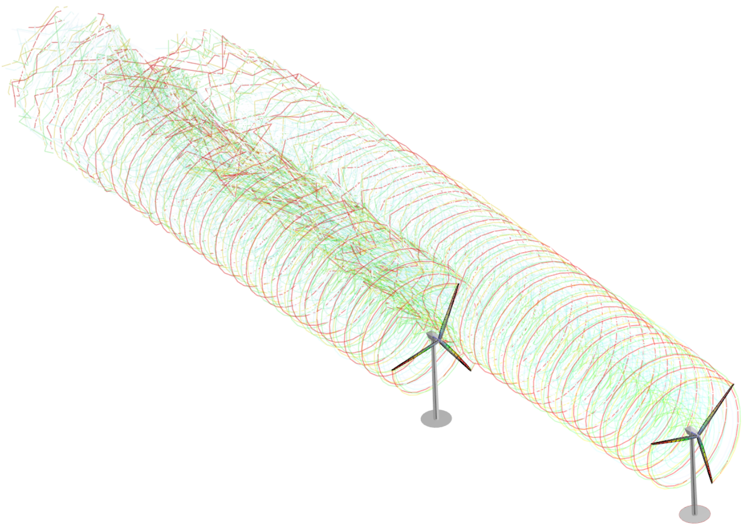

Figure 3.3.: Visualization of the partial wake impingement

3.5. Modeling of Airborne Wind Energy Systems

A recent trend in wind energy is the investigation and conceptualization of Airborne Wind Energy Systems (AWES) [216]. The main benefit of these concepts is the accessibility of strong high altitude winds, with a need for a comparatively low amount of material. Due to the massive potential to reduce the LCoE, a number of startups, pursuing a range of different concepts [217], such as EnerKite, Ampyx or Makani, is emerging on the market. Broadly, these concept are distinguished by either on-board- or ground-based generation of electricity. The on-board generation requires the generator to be aloft and a method to transmit the generated power to the ground[55]. Ground based concepts usually drive a ground based generator by reeling-out a tether that is connected to a rigid or flexible wing. One of the main challenges in this area is the autonomous flight control of the AWES, enabling a reliable long term operation, that is capable of self-starting and landing when required by hazardous weather conditions or other occurrences. Most aeroelastic computer models that have been developed for the simulation of AWES are either quasi steady [218], or rely on the assumption of rigid kites with highly simplified aerodynamic models [219, 220, 221].

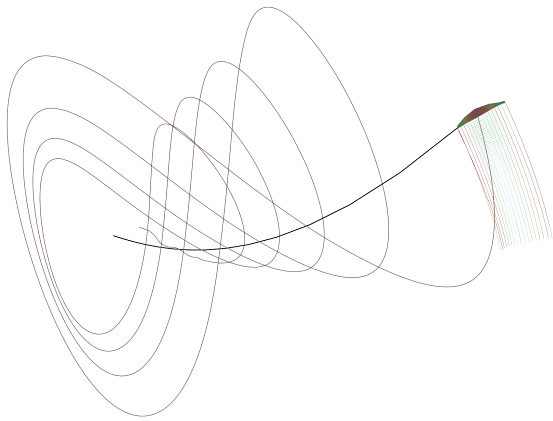

Figure 3.4.: Visualization of a generic AWES simulation, showing rigid kite, wake, tether and the trajectory

The aeroelastic formulation in the QBlade-Chrono coupling is general enough to be used for the simulation of such systems. While the aerodynamics of the AWES system can be modeled by the LLFVW formulation in QBlade, the Newtonian flight mechanics of the airborne and its structural dynamics can be represented by the co-rotational formulation in Chrono. Such simulation models can also include an explicit structural modeling of the tether. To assess the performance of QBlade's aerodynamic formulation for the simulation of kite geometries, the characteristics of a generic kite geometry (Figure 3.5) have been compared between the XFLR5 computer code and QBlade.

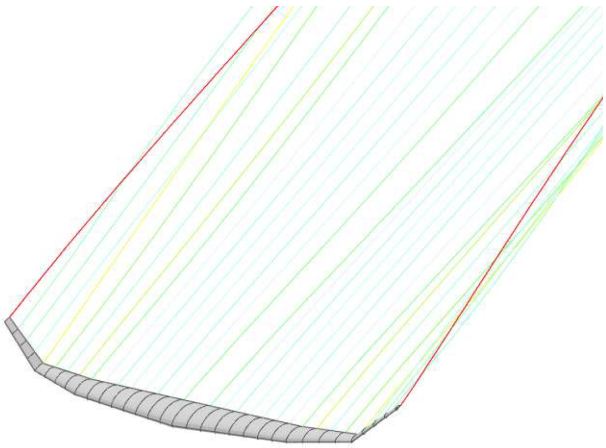

Figure 3.5.: Generic kite model for the validation of performance coefficients

55 Current concepts involve a conductive tether, microwave or laser transmission

Good agreement could be observed when comparing various kite performance characteristics over different angles of attack (see Figures 3.6 and 3.7). Furthermore, free flight studies and simulations of a tethered AWES along predefined trajectories (see Figure 3.4) have been investigated. The initial test conducted confirm the usability of the QBlade-Chrono coupling as a real-time capable test-bed and design tool for AWES controllers[56].

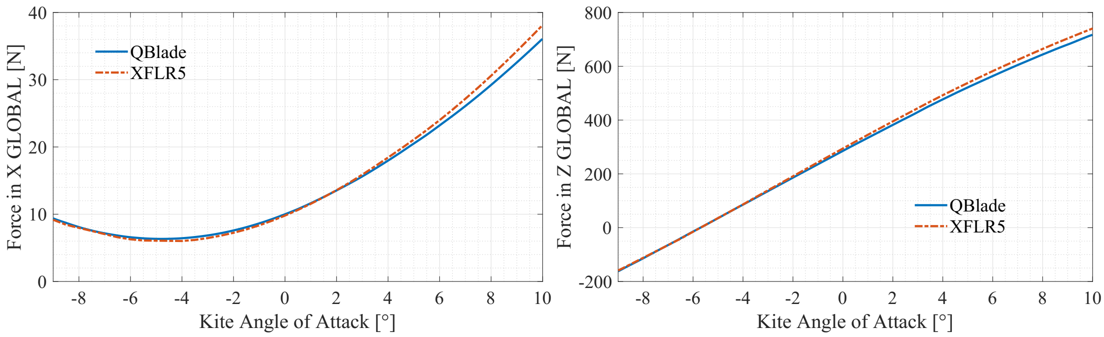

Figure 3.6.: Left: kite force along x (roll-axis), right: kite force along z (pitch) axis, comparison between QBlade and XFLR5

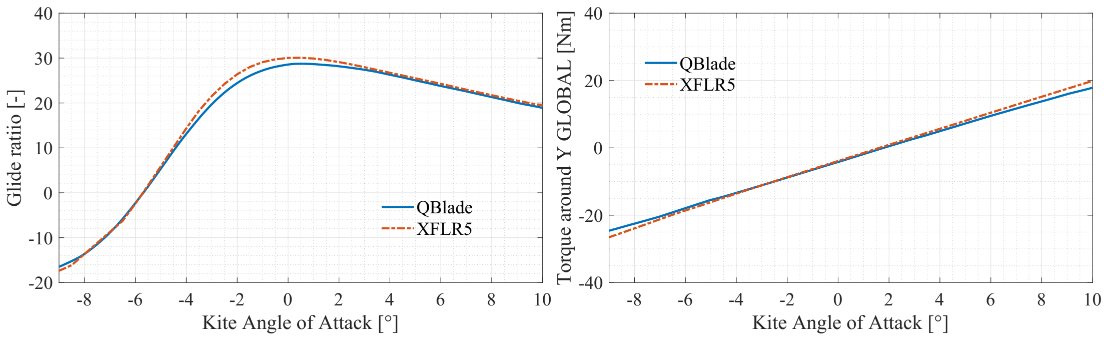

Figure 3.7.: Left: kite glide ratio, right: kite moment coefficient, comparison between QBlade and XFLR5

56 The AWES simulations outlined here are currently being applied within an industry project

3.6. Wind Turbine Ice Throw Simulations

Another application originating from the multi-physics capabilities of the Chrono integration in QBlade is the simulation of wind turbine ice throw. It is a common approach in literature to apply the empirical Seifert formula [222] to establish a safety perimeter, which estimates the maximum throwing distance of an ice fragment shed from a rotor blade as 1.5 times the combined hub-height and rotor diameter. However, this is a highly conservative approach and more accurate models, taking into account the driving physics, will yield more realistic data, resulting in higher quality estimates [223][57].

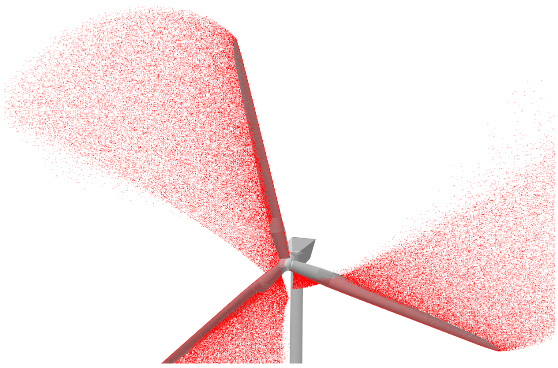

Figure 3.8.: Detailed view of randomized ice particles being shed from the rotor blade

The capability of Chrono, to efficiently model the Newtonian dynamics of a large number of rigid bodies, is here employed for the purpose of ice risk assessments. During a regular wind turbine simulation in QBlade rigid bodies, each representing an ice fragment, are released from randomized rotor blade locations (see Figure 3.8). The ice fragment properties, such as density, size and drag coefficient or initial radial position for each ice fragment are randomized within user defined bounds. The position of each ice fragment is then updated once during each time step, taking into account Newtonian dynamics, gravitational and drag forces, while lift is neglected. Once an ice fragment has landed on the ground, its position is stored along other quantities such as its impact energy. Ice throw simulations may include turbulent wind fields and can also account for the effect of wake induction.

A single simulation is then carried out for a representative range of operating conditions[58], which are prescribed through the 'Simulation Input File Format' (see Section 2.5.4). The overall distribution of landed particles (see Figure 3.9) is then analyzed using Monte Carlo (importance) sampling. Through the sampling process the probability distribution of the initially randomized particle properties and the prescribed operating conditions[59] can be adjusted as part of the post-processing of the data set. Data for different wind conditions is obtained through a simple rotation of the data set. Finally, ice throw risk maps can be generated that are based on the Weibull wind distribution and wind rose at the turbines site. Through sensitivity analysis, it was found that the sampling process requires $\approx 100,000$ landed particles for the statistics to converge.

Figure 3.10 shows an exemplary iso-risk contour for localized individual risk that was evaluated based on the ice particle data obtained from the NREL 5MW wind turbine for a single wind direction, wind speed and rotational speed. The 10^{-7} contour marks the minimum distance of the turbine from highly frequented facilities, such as shopping malls, schools or hospitals (see IEA Wind TCP Task 19 [224]).

57 One of the associated publications
58 Combinations of rotational speed, wind speed and yaw offsets
59 The operating conditions are stored as particle information upon its release at the rotor blade

The advantage of the proposed physics based approach, when compared to simple analytical ballistics curves, is its ability to quickly adapt to different turbine geometries and types[60] and that the physical properties can easily be adjusted. Furthermore, the fidelity of the model can be continuously increased, for example by including lift terms into the calculation of the particle trajectories. In addition, the sampling based post-processing only requires a single calculation of a particle distribution for a turbine type, from which the risk-maps for arbitrary site conditions can be generated[61]

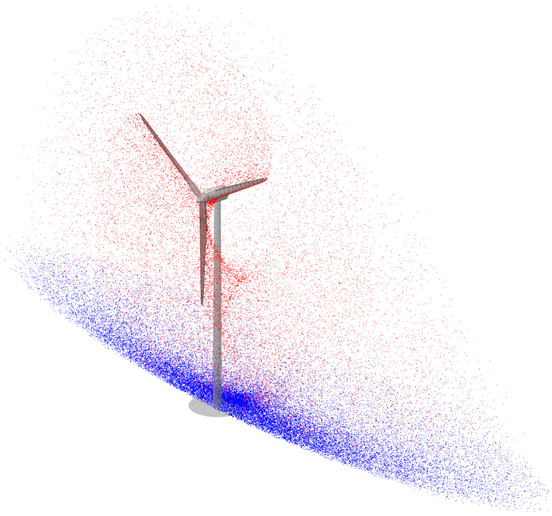

Figure 3.9.: Visualization of the ice throw model showing flying (red) and landed (blue) particles

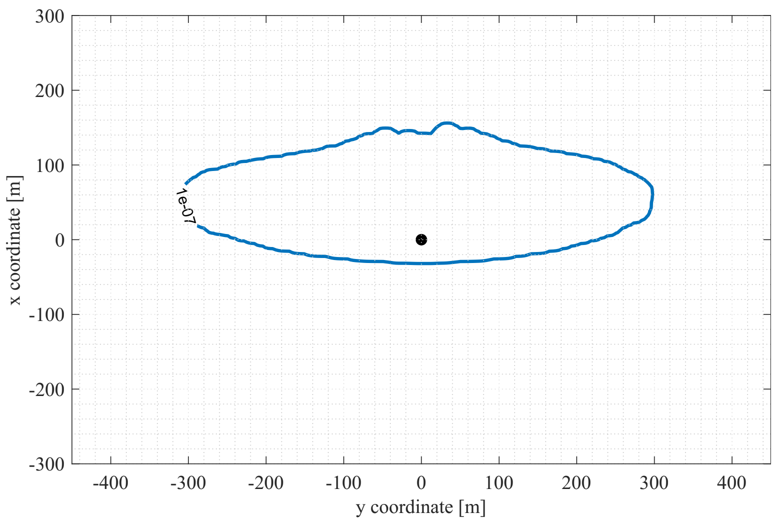

Figure 3.10.: Ice throw iso-risk contour (10^{-7}) for localized individual risk (LIRA), the tower bottom is situated at the origin (0,0)

60 Such as swept blades, coned blades, VAWT, ...
61 Currently within an industry project the presented ice throw model is applied and training is provided

3.7. Simulations of Floating Offshore Wind Turbines

The integration of Chrono into QBlade has also been used to setup and simulate floating platform wind turbines. Figure 3.11 shows a simulation of the NREL 5MW wind turbine operating on the OC3-Hywind [225] spar buoy platform. The floating platform is modeled through rigid bodies in Chrono, whose mass and inertia properties are assigned according to the OC3-Hywind platform specifications, given in [225]. Based on the current location and velocity of the body elements gravitational, buoyancy, inertia and wave forces (currently only Airy waves) are evaluated. Mooring lines are explicitly modeled as Absolute Nodal Coordinate Formulation (ANCF) cable elements that are connected to the platform via relative positional constraints and to the seabed via fixed positional constraints. The platform model is then loosely coupled to QBlade-Chrono's aeroelastic simulations. After the aeroelastic simulations are finished, the forces and torques acting on the tower bottom are communicated to the platform model whereas the platform model communicates the position of its attachment point to the wind turbine simulation.

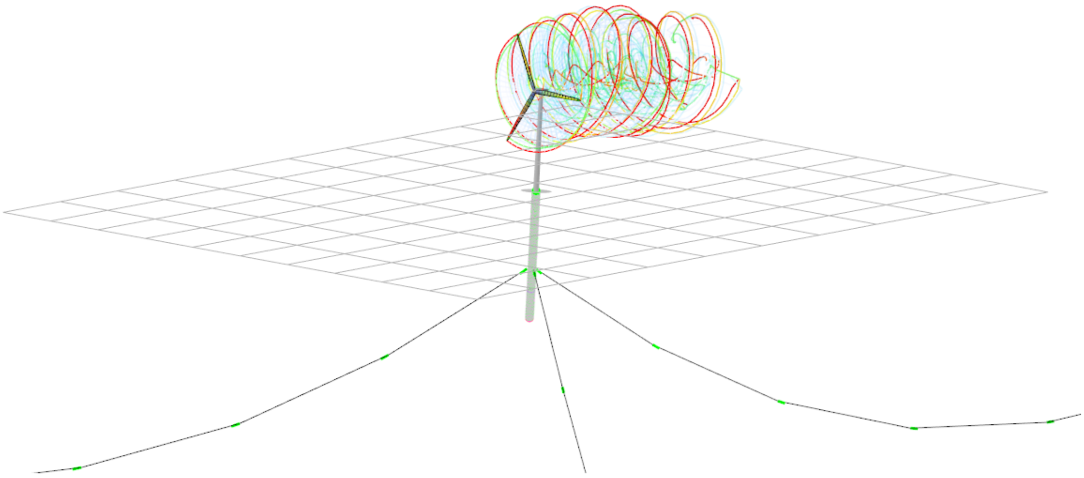

Figure 3.11.: Visualization of a floating wind turbine including mooring lines, simulated with QBlade; notice the skewed wake shape due to platform oscillations

Employing the platform model described above, a range of simulations has been conducted and compared against data from the *Offshore code comparison (IEA wind task 23)* [226]. Figure 3.12 shows exemplary results, for the decaying heave and yaw oscillations of a displaced platform. It can be seen that, while the decay of the oscillations is well predicted, some differences occur in the predicted frequencies. This is also visible when comparing the platform eigenfrequencies (Table 3.1) between the QBlade calculations and the reference results. Reasons for these differences might be associated with the explicit modeling of mooring lines or inconsistencies in the application of the additional damping coefficients that are provided in [225].

Table 3.1.: Comparison of platform eigenfrequencies between QBlade-Chrono and [225]

	x	**y**	**z**	**roll**	**pitch**	**yaw**
QBlade-Chrono	0,010	0,010	0,033	0,040	0,040	0,125
Reference frequency	0,008	0,008	0,03	0,03	0,03	0,13

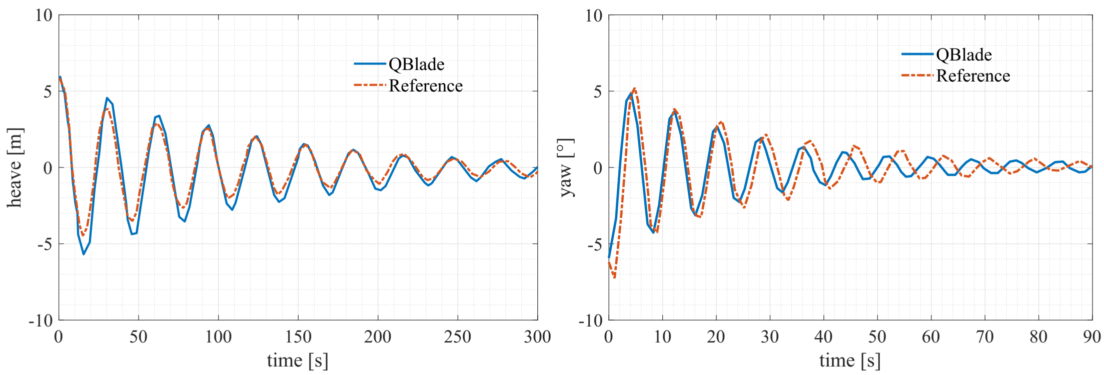

Figure 3.12.: Left: Comparison of heave oscillations, right: comparison of yaw oscillations

Planned improvements and future work associated with the integration of floating platform models into the QBlade-Chrono coupling concerns the following points:

- Implementation of a generalized pre-processor for floating platforms, similar to the pre-processors presented in Section 2.5.3
- Implementation of a boundary element method to calculate added mass and damping coefficients for floating platforms based on geometry to calculate radiation and diffraction forces
- Calculation of wave forces using the Morison equation [227]

3.8. Earthquake Simulations

Besides wind induced fatigue and extreme loads (turbulence, storms) or wave induced loads for offshore turbines, seismic loads (depending on the site) can have a detrimental influence on the turbines lifetime. Katsanos recommends in his review of seismic hazards for wind turbines [228] that: *"...the seismic hazard has a significant role to play in the structural analysis, design and/or assessment of wind turbines, since response quantities and reliability over the lifetime of these infrastructures were found to be severely affected by the earthquake strong ground motions"*. While seismic loads were previously often analyzed within the frequency domain, the advantage of time-domain methods is the inclusion of geometrical nonlinearities and the dynamic interactions between tower and rotor blades that influence the dynamic response [229] of the turbine to seismic excitation. In addition, the recent increase in computational power is another factor why time-domain analysis is now commonly used in this context.

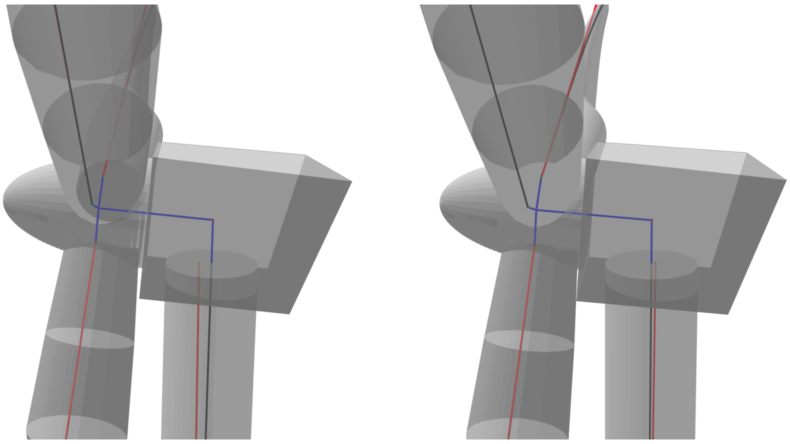

Figure 3.13.: Earthquake simulation, showing maximum nacelle deflections

Within the QBlade-Chrono coupling time series for seismic loads of wind turbines during operation can be simply simulated using the *Simulation Input File* format that was discussed in Section 2.5.4. As a proof of concept, a simulation of the NREL 5MW under the seismic loads of the Chile Earthquake of the 27th February in 2010 was carried out (see Figure 3.13). The time domain displacement data[62], which is used to translate the tower base, was obtained from the U.S. Geological Survey (USGS) database [230]. The structural data of the simulated NREL 5MW turbine can be found in Appendix A.2. The turbine operates at rated power in a laminar inflow of $20\frac{m}{s}$ at $12.1rpm$ with a fixed blade pitch of $17.5°$. Exemplary results of the simulations can be seen in Figure 3.14, 3.15 and 3.16.

Figure 3.14 shows the ground displacement along the x direction. It can be seen that the earthquake starts at $t = 60s$. Figure 3.15:left shows the displacement of the nacelle. As the earthquake excitation is close to the tower eigenfrequency of $0.316Hz$, the tower bottom displacements (max. peak to peak 0.4m) are amplified and the nacelle is oscillating with a peak to peak magnitude of more than 1m. The mean position of the nacelle results the wind forces acting on the rotor disc. Figure 3.15:right shows the global acceleration of the nacelle.

62 See Figure 3.14:left for the ground x-displacement, starting after $60s$

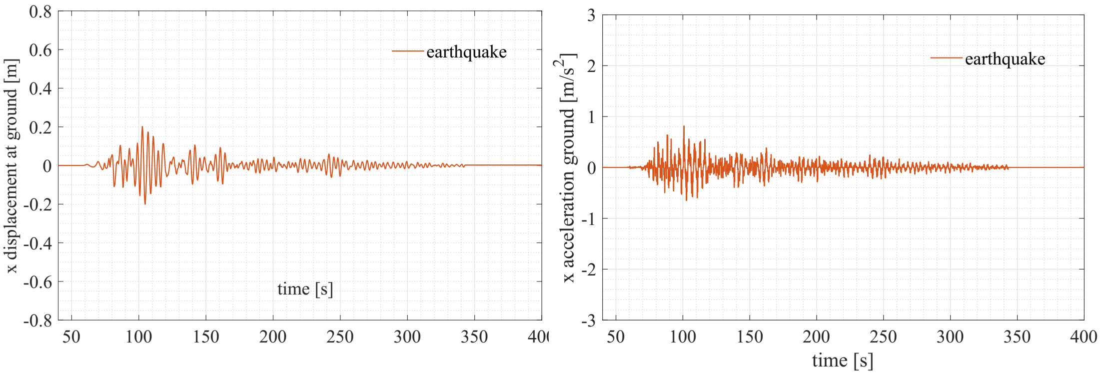

Figure 3.14.: Left: ground x displacement, right: ground x acceleration

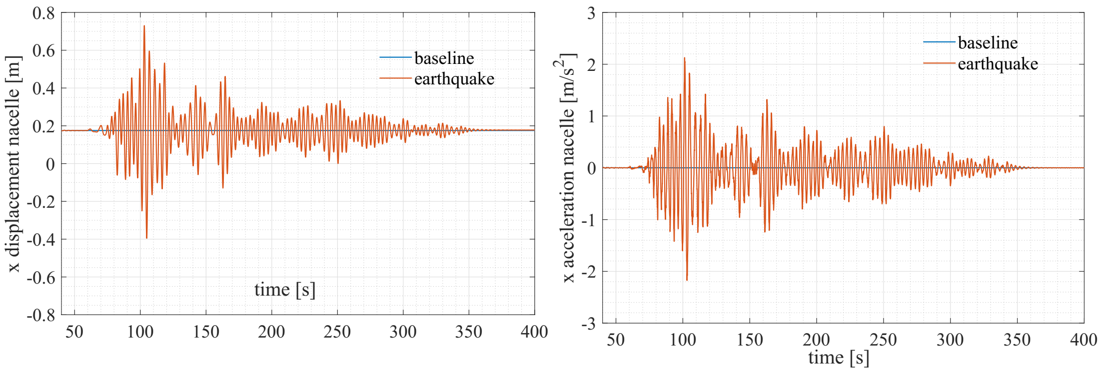

Figure 3.15.: Left: nacelle x displacement, right: nacelle x acceleration

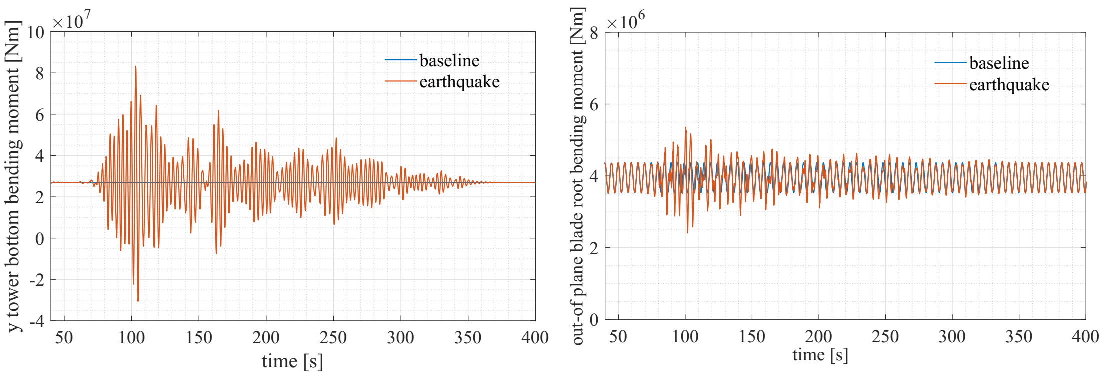

Figure 3.16.: Left: tower bottom bending moment around y, right: blade out-of plane deflection

The maximum accelerations are approximately $+-2\frac{m}{s^2}$ (0.2g). Figure 3.16:left shows the tower bottom bending moment around the y-axis (parallel to ground, lateral to x). It can be seen that the bending moment is significantly affected, with a maximum peak to peak magnitude of around $11 \times 10^7 Nm$. Figure 3.16:right shows the out-of-plane blade root bending moment of one rotor blade. It is apparent that the contribution of the seismic oscillations to the baseline bending moment oscillations, caused shaft tilt and cone angle, is relatively small.

Chapter 4 | Discussion

Previously in Chapter 3, examples of possible areas of application were given. The discussion will focus on highlighting the shortcomings of the current status of the aeroelastic formulation, discuss areas for improvements, and give recommendations for future work. The structure of this discussion is loosely based on the different model components of the aeroelastic formulation in QBlade.

4.1. Practicality of the developed tool within the context of design and certification

While the general applicability of the chosen methods for blade- and wake aerodynamics and the structural formulation have been demonstrated in terms of accuracy and computational efficiency, the term applicability also implies the level of readiness of the simulation tool for professional utilization. Essentially, the applicability is the difference between a research- and a professional tool. To reach this level of readiness, the requirement is to provide a tool whose usability is not prohibitive. A fast and efficient performance of the code is futile when these gains are lost in practice due to a cumbersome pre- and post-processing.

The stochastic wind input requires a large number of simulations[63] to be carried out for a full turbine simulation. The exact number differs according to the respective interpretation of the IEC 61400 design requirements [185]. All these simulations need to be setup according to the type of turbine and design load case (DLC) that they represent. This involves the definition of boundary conditions, by generating turbulent wind fields, the setting of control parameters when simulating failures, startup or shutdown conditions, and the permutation of pitch and yaw misalignment with different seeds for the turbulent wind field generator. Setting up all these simulations manually is prone to errors and too cumbersome for a practical application.

Once all simulations have been evaluated, the resulting data requires intensive post-processing to arrive at the design relevant results for the ultimate and the fatigue loads. The data that is usually generated for an evaluation of a complete DLC set is in the order of several gigabytes, which is too large for manual evaluation.

Thus, for a professional application, the coupling with, or integration of a pre- and a post-processor within the aeroelastic tool is required. While the work that is necessary is certainly not as interesting or intricate as the development of aerodynamic or structural models the task is not trivial and generally requires the following steps:

- **Parametrization of DLCs**: The whole set of DLCs from [185] needs to be parameterized into as variables as possible, such as DLC number, wind class, wind speed-, pitch error-

63 in the order of several hundred 10 minute simulations

and yaw error increments, number of turbulent seed, yaw and pitch variations and others. After all DLCs, or a subset, have been defined using this scheme, simulation templates are automatically generated that contain all the needed information for the complete definition of each $10min$ turbine simulation.

- **Batch capability and interface**: An interface to QBlade needs to be generated where simulations can be automatically defined and evaluated from the command line using the template files.
- **Integration of a cluster management framework**: A cluster management framework, such as the open source framework Apache Helix [231], could be implemented to distribute the individual DLCs (*jobs*) over a range of available workstations (*nodes*) to reduce the computational time that is needed. Another option would be to outsource the calculations by integrating them with an external cloud service such as AWS [232].
- **File system**: An auto-generated, hierarchical file system needs to be established where the resulting data is stored in a clearly arranged manner, in a commonly used format.
- **Automatic post-processing**: Post processing, based on the hierarchical file system, should be automated with the ability to adapt the exact post-processing algorithms within their bounds. Alternatively data can be exported to be used with existing post-processors.

4.2. The Blade Element Method

The blade element method is a highly cost-efficient method to model blade aerodynamics. In practice, this simple model, based on purely two-dimensional airfoil polar data, removes the need to model the highly challenging smallest scales (see Table 1.1) in the flow. The aerodynamics manifested at the level of the boundary layer and the airfoils surface are replaced by a simple and highly robust model that is based on integrated, non-dimensionalized force coefficients. The main benefits are that both friction drag and induced drag are included in the performance coefficients and that experimental data is easily included in a simulation. Even the bold assumption that the flow is two-dimensional at the airfoil cross sections is not critical during most operating conditions that a rotor experiences.

However, the most critical issue when using two-dimensional airfoil data, is the reliability of this data for very high angles of attack. For low angles of attack, in the linear region of the lift curve, both XFoil simulations and experiments are quite reliable. The situation changes for high angles of attack, beyond the static stall point. Neither XFoil, due to its viscous-inviscid coupling, nor wind tunnel experiments, due to blockage effects, yield reliable results at high angles of attack. Furthermore, it is questionable if static polar data is representative at all in a situation where the flow is fully separated and unsteady effects, such as vortex shedding, are prevalent [233]. In practice, the static polar data is simply extrapolated, using the rather simple extrapolation methods proposed by Viterna [234] or Montgomerie [235], assuming that most wind turbines likely won't ever operate at such high angles of attack. The unsteadiness of the flow is then modeled by letting one of the available dynamic stall model formulations operate on the static polar data. Each of the dynamic stall models has been carefully validated against experimental data, however the validations themselves involved fine tuning of the model time constants and the polar data decomposition. Thus, their successful validation under laboratory conditions cannot be generalized to be valid for the large number of different airfoils that exists, the large fluctuations in polar data quality that wind turbine designers deal with, and the large variability of the simulated turbine's operating conditions.

To give two examples where the dynamic stall models that we use today fall short:

VAWT during their initial startup experience drastic changes in the angle of attack[64] and reduced frequency. It is commonly accepted that dynamic stall effects have a significant influence on a VAWT's startup behavior. But existing dynamic stall models completely fail at these high angles of attack and are better fully switched off under these conditions to prevent numerical artifacts from contaminating the simulation. This results in the assumption of quasi-static aerodynamics for a highly unsteady case.

For HAWT, standstill vibrations pose a serious problem that can cause the complete failure of the whole rotor [236]. These vibrations originate from a lock-in between the frequency of vortex induced vibrations and eigenfrequencies of the blade structure. The vortex shedding can start at moderate angles through a roll-up of the shear layer into large-scale structures, or represent typical bluff-body shedding at higher angles of attack. Being able to model this process is completely out-of scope of today's dynamic stall models and still requires a fully blade-resolved CFD simulation coupled to a structural model.

Summing up, there is still more room for improvement in the unsteady aerodynamic models that are used in all of today's wind turbine aeroelastic codes. However, obtaining and generalizing the data that is needed to form a basis for such a model development is a highly challenging task.

4.3. The Free Vortex Wake Formulation

The free wake formulation that is employed using straight vortex filaments has proven its accuracy within many validation studies. The fact that the overall wake geometry and the resulting induction field is explicitly solved leads to more coherent results and an improved accuracy, especially in unsteady operating conditions, compared to BEM based methods. Its rather simple implementation, using straight line vortex filaments with a simple core growth model, has a sufficient computational efficiency for practical use and includes the first-order effects of wake diffusion. Another benefit is the method's general applicability, regardless of geometrical assumptions. Furthermore, as complete velocity fields can be obtained, the free wake method can be used for multi-turbine simulations in wind farm settings.

Such settings, where the wakes of multiple turbines are interacting, also illustrate the largest problem that is associated with a Lagrangian description of the flow field: the problem of flow field divergence. In any simulation, regardless of the initial vortex element density, the flow field eventually looses its divergence free nature and the accuracy of the simulation deteriorates. This problem does not manifest itself when simulating only a single wind turbine, as the area where divergence issues arise is sufficiently far away from the rotor location from which the wake originates. If simulating multiple turbines however the non-divergence free vorticity field might also directly impact the downstream rotor. Additionally, the correct estimation of wake recovery, which is a process associated with highly three-dimensional turbulent mixing, is also crucial for accurate wind farm simulations. Generally, and in part due to their underlying connectivity,

64 Up to 180°

vortex filaments are not very well suited to predict such phenomena. A possible solution to this problem, as already highlighted in Publication IV (Section 3.3), would be to transform the vortex filaments into vortex particles when the vorticity field starts to become divergent. While vortex particles share the same issues of eventually loosing their divergence-free nature due to particle clustering, grid-based re-meshing techniques are easily applicable. Using a grid based Poisson solver the vorticity field can be interpolated onto the underlying Eulerian grid and periodically re-meshing can be applied. In addition, the underlying grid can be used to implement sub-grid scale turbulence models, in a similar fashion that LES is used to resolve the wake's turbulent dissipation. Such a model can be a highly cost efficient alternative to the currently used, LES based, wind park simulation tools, such as NREL's open source CFD toolbox SOWFA [237].

Another inherent issue with Lagrangian methods is the scaling of the computational cost with $O(N^2)$. A range of possible solutions to remedy this issue exists. Tree-codes [238, 239] can leverage the spatial hierarchy of the vortex element distribution to reduce the computational cost to $O(NlogN)$ while maintaining complete control of the upper error bounds. Multi-level-grid methods [46, 102], employing interpolation and anterpolation, can reduce the computational cost down to $O(N)$. In practice, due to the computational overhead that is associated with these methods when constructing and updating the grid hierarchy, the savings in computational cost only start to materialize when the number of free wake elements is sufficiently large. The exact number is hardware dependent, but from experience, multi-level methods start to overtake massive GPU parallelization at a element count of approximately $50,000$. For the simulation of a single wind turbine in a DLC scenario, this element count is rarely reached. However, when considering the application of free vortex methods to wind farm simulations, much larger vortex element numbers can be expected. As an Eulerian grid is already required for the re-meshing of free vortex simulations, the already existing grid can very well be reused to construct the required hierarchical structure. Such a combined formulation, ensuring divergence-free nature through re-meshing and a reduction of the computational cost through a multi-level hierarchy could potentially rival the currently used LES codes in both accuracy and computational cost.

4.4. The Structural Multi-Body Beam Formulation

With the present day computational hardware, a multi-body beam based formulation is the only method that is cost-efficient enough for the simulation of large time series that is required for wind turbine design evaluations. The co-rotational formulation in Project Chrono's FEA module allows one to consider arbitrarily large deformations while retaining the linear formulations for the individual Euler-Bernoulli beams that are employed.

As mentioned before, the Euler-Bernoulli beams do not consider shear, which is a valid assumption for slender structures but is not well suited for thick or short components with a low aspect ratio. However, even if the assumption of slender structures is valid, it is challenging to accurately model the three dimensional anisotropic elastic behavior resulting from the complex geometrical features and structural properties of modern blades, due to the kinematic assumptions that are inherent in classical beam theory [240]. Especially for oscillations with wavelengths that are shorter than the blade length the assumption of planar beam sections, after the blade has undergone deformation, is problematic. With the trend towards larger, more flexible rotors, the need to adopt non-linear beam models arises [135]. Using generalized Timoshenko beam formulations combined with cross-sectional analysis, such as Variational Asymptotical Beam Section Analysis (VABS), can address the issues of classical beam theory with the non-classical effects of composite slender structures [241].

While out of scope for the presented work, the possibility exists to integrate new element types into the modular source code of the Chrono framework. While this requires the work of a specialist in the field, such an extension of the Chrono module is a realistic avenue for a further extension of the QBlade-Chrono capabilities with respect to its underlying structural formulation.

4.5. Concluding Words

Within this work, an overview of the employed models, their implementation, and the application of the QBlade-Chrono aero-elastic framework was given. The computational efficiency[65], accuracy[66] and versatility was demonstrated. While the methods used in the presented simulation framework are by no means new, but rather established, their robust and efficient implementation and coupling is what enables their application to a wide range of problems[67].

Most features of the presented framework will be integrated and successively released with the Open Source version of QBlade in the near future. The hope is that this work, and the resulting tool, enables interested researchers and designers to design innovative, robust and efficient wind turbines and thereby contributes to the overall reduction of greenhouse gas emissions. This update replaces the previous open-source version of QBlade (v0.963), that was released in 2016. The integration of a structural dynamics model and a controller interface greatly increases the applicability of the software and will further promote its use for teaching and research.

In terms of professional or industrial application this software serves as a proof of concept that the widespread BEM codes can be replaced with a higher order method that is robust and efficient enough for industrial purposes. Overall, very few reasons remain why design codes should still be BEM based. Certainly, using vortex methods requires more user involvement and generating results is slightly less automatic. Suitable parameters for the wake discretization need to be set to balance computational accuracy and cost[68]. Also, care must be taken when specifying the vortex settings for initial core size and vortex viscosity[69]. However setting up vortex simulations requires by far less involvement than CFD simulations and over time the process could be more and more automated. In addition, the essential knowledge to handle such simulations and to interpret its results can be taught to wind turbine load analysts in relatively short amount of time.

I am confident that in a matter of years, free wake vortex methods will be included within the majority of professional design tools and will play a crucial role in the design of the next generation of wind turbines.

65 Section 2.6.1
66 Sections 3.1, 3.2 and 3.3
67 Section 3
68 Section 2.4.10
69 Section 2.4.3

Bibliography

(excluding bibliography of publications I-IV)

[1] D. M. Etheridge, L. P. Steele, R. L. Langenfelds, R. J. Francey, J.-M. Barnola, and V. I. Morgan. Natural and anthropogenic changes in atmospheric CO2 over the last 1000 years from air in Antarctic ice and firn. *J. Geophys. Res.*, 101:4115–4128, 1996. doi:doi:10.1029/95JD03410.

[2] Charles D Keeling, Robert B Bacastow, Arnold E Bainbridge, Carl A Ekdahl, Peter R Guenther, and L E E S Waterman. Atmospheric carbon dioxide variations at Mauna Loa Observatory, Hawaii. *Tellus*, 28:538–551, 1976. doi:doi:10.1111/j.2153-3490.1976.tb00701.x.

[3] IPCC. Special Report on 1.5 degrees: Summary for Policymakers. 2018. URL `https://www.ipcc.ch/site/assets/uploads/sites/2/2019/05/SR15{_}SPM{_}version{_}report{_}LR.pdf`.

[4] Joeri Rogelj, Piers M Forster, Elmar Kriegler, Christopher J Smith, and Roland Séférian. Estimating and tracking the remaining carbon budget for stringent climate targets. pages 3–10. doi:10.1038/s41586-019-1368-z.

[5] IEA. Global Energy & CO2 Status Report, 2019. URL `https://www.iea.org/geco/emissions/`.

[6] IEA. Tracking Clean Energy Progress, 2019. URL `https://www.iea.org/tcep/`.

[7] Lazard. Levelized Cost of Energy and Levelized Cost of Storage 2018. Technical report, 2018. URL `https://www.lazard.com/media/450784/lazards-levelized-cost-of-energy-version-120-vfinal.pdf`.

[8] IEA. Next generation turbine, power-train and system management technology, 2019. URL `https://www.iea.org/topics/innovation/renewables/gaps/next-generation-turbine-power-train-and-system-management-technology.html`.

[9] IEA. Tapping deeper offshore wind resources through floating wind turbines, 2019. URL `https://www.iea.org/topics/innovation/renewables/gaps/tapping-deeper-offshore-wind-resources-through-floating-wind-turbines.html`.

[10] A. R. Collar. The expanding domain of aeroelasticity. *Journal of the Royal Aeronautical Society*, pages 613–636, 1946.

[11] Jessica Gabriëlle Holierhoek. *Aeroelasticity of Large Wind Turbines*. Number november. 2008. ISBN 9789090236278.

[12] Gerard Schepers. *Engineering models in wind energy aerodynamics: Development, implementation and analysis using dedicated aerodynamic measurements*. 2012. ISBN 9789461915078.

[13] C. Breitsamter. Wake vortex characteristics of transport aircraft, 2011. ISSN 03760421.

[14] G. a. M. van Kuik, J Peinke, R Nijssen, D Lekou, J Mann, J. N. Sørensen, C Ferreira, J. W. van Wingerden, D Schlipf, P Gebraad, H Polinder, a Abrahamsen, G. J. W. van Bussel, J. D. Sørensen, P Tavner, C L Bottasso, M Muskulus, D Matha, H J Lindeboom, S Degraer, O Kramer, S Lehnhoff, M Sonnenschein, P. E. Sørensen, R. W. Künneke, P E Morthorst, and K Skytte. Long-term research challenges in wind energy – a research agenda by the European Academy of Wind Energy. *Wind Energy Science*, 1(1):1–39, 2016. ISSN 2366-7451. doi:10.5194/wes-1-1-2016. URL http://www.wind-energ-sci.net/1/1/2016/wes-1-1-2016.pdf{%}5Cnhttp://www.wind-energ-sci.net/1/1/2016/.

[15] Hannes Frank, Andrea Beck, Thomas Bolemann, Florian Hindenlang, and Claus-dieter Munz. High order simulation of transitional flow over the SD7003 airfoil with the Discontinuous Galerkin Spectral Element Method. 2013.

[16] Adam C. DeVoria and Kamran Mohseni. On the mechanism of high-incidence lift generation for steadily translating low-aspect-ratio wings. *Journal of Fluid Mechanics*, 813:110–126, 2017. ISSN 0022-1120. doi:10.1017/jfm.2016.849.

[17] Walid Chakroun, Issa Al-Mesri, and Sami Al-Fahad. Effect of Surface Roughness on the Aerodynamic Characteristics of a Symmetrical Airfoil. *Wind Engineering*, 28(5): 547–564, 2005. ISSN 0309-524X. doi:10.1260/0309524043028136.

[18] Tuncer Cebeci. Effects of Environmentally on Airfoil Imposed Roughness Performance. *Nasa*, pages NASA–CR–179639, 1987.

[19] O. Pires, X. Munduate, K. Boorsma, O. Ceyhan Yilmaz, H. Aa Madsen, and W. A. Timmer. Experimental investigation of Surface Roughness effects and Transition on Wind Turbine performance. *Journal of Physics: Conference Series*, 1037(5), 2018. ISSN 17426596. doi:10.1088/1742-6596/1037/5/052018.

[20] Matthias Schramm, Hamid Rahimi, Bernhard Stoevesandt, and Kim Tangager. The influence of eroded blades on wind turbine performance using numerical simulations. *Energies*, 10(9):1–15, 2017. ISSN 19961073. doi:10.3390/en10091420.

[21] David C. Maniaci, Edward B. White, Benjamin Wilcox, Christopher M. Langel, C. P. Van Dam, and Joshua A. Paquette. Experimental Measurement and CFD Model Development of Thick Wind Turbine Airfoils with Leading Edge Erosion. *Journal of Physics: Conference Series*, 753(2), 2016. ISSN 17426596. doi:10.1088/1742-6596/753/2/022013.

[22] Earl P N Duque, Moffett Field, Wayne Johnson, Rotorcraft Aeromechanics Branch, Regina Cortes, Karen Yee, and Aeronautical Engineering. Numerical Predictions of Wind Turbine Power and Aerodynamic Loads for the Nrel Phase Ii Combined Experiment Rotor. *Wind Energy*, 2000.

[23] Srinivas Guntur. A Detailed Study of the Rotational Augmentation and Dynamic Stall Phenomena for Wind Turbines. *DTU Wind Energy*, 0022(December):111, 2013. URL https://findit.dtu.dk/en/catalog/2389472254.

[24] K Boorsma, A Muñoz, B Mendez, S Gomez, A Irisarri, X Munduate, Vres Sieros, P Chaviaropoulos, S Voutsinas, J Prospathopoulos, M Manolesos, WZ Shen, WJ Zhu, and H Madsen. INNWIND Deliverable 2.12: New airfoils for high rotational speed wind turbines. (September):1–165, 2015.

[25] Erich Hau. *Fundamentals, Technologies, Application, Economics*. Springer Berlin Heidelberg, 2013. ISBN 978-3-642-27150-2. doi:10.1007/978-3-642-27151-9.

[26] C. B. Merz, C. C. Wolf, K. Richter, K. Kaufmann, A. Mielke, and M. Raffel. Spanwise Differences in Static and Dynamic Stall on a Pitching Rotor Blade Tip Model. *Journal of the American Helicopter Society*, 62(1):1–11, 2016. ISSN 2161-6027. doi:10.4050/jahs.62.012002.

[27] Karen Mulleners, Arnaud Le Pape, Benjamin Heine, and Markus Raffel. The Dynamics of Static Stall. In *16th International Symposium on Applications of Laser Techniques to Fluid Mechanics*, volume 6, pages 9–12, Lisbon, Portugal, 2012.

[28] Thomas C. Corke and Flint O. Thomas. Dynamic Stall in Pitching Airfoils: Aerodynamic Damping and Compressibility Effects. *Annual Review of Fluid Mechanics*, 47(1):479–505, 2014. ISSN 0066-4189. doi:10.1146/annurev-fluid-010814-013632.

[29] M. A. Khan. Dynamic Stall Modeling for Wind Turbines. 2018.

[30] Thomas T. Rice, Keith Taylor, and Michael Amitay. Wind tunnel quantification of dynamic stall on an S817 airfoil and its control using synthetic jet actuators. *Wind Energy*, 22(1): 21–33, 2019. ISSN 10991824. doi:10.1002/we.2266.

[31] Y. El Khchine and M. Sriti. Tip Loss Factor Effects on Aerodynamic Performances of Horizontal Axis Wind Turbine. *Energy Procedia*, 118:136–140, 2017. ISSN 18766102. doi:10.1016/j.egypro.2017.07.028. URL `http://dx.doi.org/10.1016/j.egypro.2017.07.028`.

[32] W. Z. Shen, W. J. Zhu, and J. N. Sørensen. Study of tip loss corrections using CFD rotor computations. *Journal of Physics: Conference Series*, 555(1), 2014. ISSN 17426596. doi:10.1088/1742-6596/555/1/012094.

[33] Iván Herráez, Bernhard Stoevesandt, and Joachim Peinke. Insight into rotational effects on a wind turbine blade using navier-stokes computations. *Energies*, 7(10):6798–6822, 2014. ISSN 19961073. doi:10.3390/en7106798.

[34] Horia Dumitrescu and Vladimir Cardos. Inboard Stall Delay due to Rotation. *Journal of Aircraft*, 49(1):101–107, 2012. ISSN 0021-8669. doi:10.2514/1.c031329.

[35] J. Bosscher, B. Montgomerie, A J. Brand, and R.P.J.O.M. van Rooy. Influence of blade rotation on the sectional aerodynamics of rotational blades. *The twenty-second European Rotorcraft Forum*, 1996.

[36] M.O.L. Hansen. *Aerodynamics of Wind Turbines*. Earthscan, 2nd edition, 2008. ISBN 978-1-84407-438-9.

[37] Tony Burton Nick Jenkins David Sharpe Ervin Bossanyi. *Wind Energy Handbook*. John Wiley & Sons, Ltd, 2011. ISBN 9780470699751. doi:10.1002/9781119992714.

[38] Tonio Sant. *Improving BEM - based Aerodynamic Models in Wind Turbine Design Codes Improving BEM - based Aerodynamic Models Tonio Sant Tonio Sant Improving BEM-based Aerodynamic Models in Wind Turbine Design Codes*. 2007. ISBN 978-99932-0-483-1.

[39] C. J. Simão Ferreira, H. Bijl, G. Van Bussel, and G. Van Kuik. Simulating Dynamic Stall in a 2D VAWT: Modeling strategy, verification and validation with Particle Image Velocimetry data. *Journal of Physics: Conference Series*, 75(1), 2007. ISSN 17426596. doi:10.1088/1742-6596/75/1/012023.

[40] Alessandro Bianchini, Francesco Balduzzi, Giovanni Ferrara, and Lorenzo Ferrari. Critical Analysis of Dynamic Stall Models in Low-Order Simulation Models for Vertical-Axis Wind Turbines. *Energy Procedia*, 101(September):488–495, 2016. ISSN 18766102. doi:10.1016/j.egypro.2016.11.062. URL `http://dx.doi.org/10.1016/j.egypro.2016.11.062`.

[41] Nathan Hill, R. Dominy, G. Ingram, and J. Dominy. Darrieus turbines: The physics of self-starting. *Proceedings of the Institution of Mechanical Engineers, Part A: Journal of Power and Energy*, 223(1):21–29, 2009. ISSN 09576509. doi:10.1243/09576509JPE615.

[42] Michael Davies and Joseph Saverin. Implementation of Adaptive Gaussian Quadrature for Improved Accuracy of Boundary Element Methods Applied to Three Dimensional Geometries. In *Proceedings of the ASME Turbo Expo 2019*, 2019.

[43] L Erickson. NASA Technical Paper Panel Methods–An Introduction. 2018.

[44] J. Katz and A. Plotkin. *Low-Speed Aerodynamics*. Cambridge University Press, 2nd edition, 2001. ISBN 978-0-521-66219-2.

[45] David J. Willis, Jaime Peraire, and Jacob K. White. A combined pFFT-multipole tree code, unsteady panel method with vortex particle wakes. *International Journal for Numerical Methods in Fluids*, 53(8):1399–1422, 2007. ISSN 02712091. doi:10.1002/fld.1240.

[46] Arne van Garrel. *Multilevel panel method for wind turbine rotor flow simulations*. Number December. 2016. ISBN 9789036542241. doi:10.3990/1.9789036542241. URL `http://purl.org/utwente/doi/10.3990/1.9789036542241`.

[47] Mark Drela. XFOIL - An analysis and design system for low reynolds number airfoils, 1989.

[48] Martin Hepperle. JAVAFOIL User's Guide. Technical report, 2017. URL `https://www.mh-aerotools.de/airfoils/java/JavaFoilUsersGuide.pdf`.

[49] R.P.J.O.M. Van Rooij. Modification of the boundary layer calculation in RFOIL for improved airfoil stall prediction. Technical report, IWE TU Delft, 1996.

[50] Bryan Nelson and Jen-Shiang Kouh. The Aerodynamic Analysis of a Rotating Wind Turbine by Viscous-Coupled 3D Panel Method. *Applied Sciences*, 7(6):551, 2017. doi:10.3390/app7060551.

[51] N. R. García, J. N. Sørensen, and W. Z. Shen. A quasi-3D viscous-inviscid interaction code: Q 3 UIC. *Journal of Physics: Conference Series*, 555(1), 2014. ISSN 17426596. doi:10.1088/1742-6596/555/1/012041.

[52] Mark Drela. Fast 3D Viscous Calculation Methods. Technical report, Boeing/MIT Strategic Research Review, 2014.

[53] A Van Garrel. Development of a Wind Turbine Rotor Flow Panel Method. (December), 2011.

[54] John D Anderson. *COMPUTATIONAL FLUID DYNAMICS The Basics with Applications*. McGraw-Hill, 1995. ISBN 0070016852.

[55] Randall J. LeVeque. *Finite Volume Methods for Hyperbolic Problems*. Cambridge University Press, 2002. ISBN 9780511791253. doi:https://doi.org/10.1017/CBO9780511791253.

[56] Parviz Moin and Krishnan Mahesh. DIRECT NUMERICAL SIMULATION: A Tool in Turbulence Research. *Annual Review of Fluid Mechanics*, 30(1):539–578, 2002. ISSN 0066-4189. doi:10.1146/annurev.fluid.30.1.539.

[57] P. Sagaut. *Large Eddy Simulation for Incompressible Flows*. Springer International Publishing, 2006.

[58] Francesco Balduzzi, Jernej Drofelnik, Alessandro Bianchini, Giovanni Ferrara, Lorenzo Ferrari, and Michele Sergio Campobasso. Darrieus wind turbine blade unsteady aerodynamics: a three-dimensional Navier-Stokes CFD assessment. *Energy*, 128: 550–563, 2017. ISSN 03605442. doi:10.1016/j.energy.2017.04.017. URL `http://dx.doi.org/10.1016/j.energy.2017.04.017`.

[59] Heng Xiao and Paola Cinnella. Quantification of model uncertainty in RANS simulations: A review. *Progress in Aerospace Sciences*, (June 2018):1–31, 2019. ISSN 03760421. doi:10.1016/j.paerosci.2018.10.001. URL `https://doi.org/10.1016/j.paerosci.2018.10.001`.

[60] P.A. Durbin and T.I-P. Shih. An overview of turbulence modeling. *Modelling and Simulation of Turbulent Heat Transfer*, 15:1–29, 2008. doi:10.2495/978-1-85312-956-8/01.

[61] Nikolaos Stergiannis, Jeroen van Beeck, and Mark C. Runacres. Full HAWT rotor CFD simulations using different RANS turbulence models compared with actuator disk and experimental measurements. *Wind Energy Science Discussions*, (February):1–20, 2017. doi:10.5194/wes-2017-6.

[62] A. P. Schaffarczyk, R. Boisard, K. Boorsma, B. Dose, C. Lienard, T. Lutz, H. Madsen, H. Rahimi, T. Reichstein, G. Schepers, N. Sorensen, B. Stoevesandt, and P. Weihing. Comparison of 3D transitional CFD simulations for rotating wind turbine wings with measurements. *Journal of Physics: Conference Series*, 1037(2), 2018. ISSN 17426596. doi:10.1088/1742-6596/1037/2/022012.

[63] Annette Claudia Klein, Sirko Bartholomay, David Marten, Thorsten Lutz, George Pechlivanoglou, Christian Navid Nayeri, Christian Oliver Paschereit, and Ewald Krämer. About the suitability of different numerical methods to reproduce model wind turbine measurements in a wind tunnel with a high blockage ratio. *Wind Energy Science*, 3(1): 439–460, 2018. doi:10.5194/wes-3-439-2018.

[64] Konrad Meister, Thorsten Lutz, and Ewald Krämer. Simulation of a 5MW wind turbine in an atmospheric boundary layer. *Journal of Physics: Conference Series*, 555(1), 2014. ISSN 17426596. doi:10.1088/1742-6596/555/1/012071.

[65] Amin Rasam, Zeinab Pouransari, Karl Bolin, and Ciarán J. O'Reilly. Detached-eddy simulation of a horizontal axis wind turbine. *Notes on Numerical Fluid Mechanics and Multidisciplinary Design*, 137:357–367, 2018. ISSN 16122909. doi:10.1007/978-3-319-70031-1_30.

[66] K. Rogowski, M. O.L. Hansen, R. Hansen, J. Piechna, and P. Lichota. Detached Eddy Simulation Model for the DU-91-W2-250 Airfoil. *Journal of Physics: Conference Series*, 1037(2), 2018. ISSN 17426596. doi:10.1088/1742-6596/1037/2/022019.

[67] N. Stergiannis, C. Lacor, J. V. Beeck, and R. Donnelly. CFD modelling approaches against single wind turbine wake measurements using RANS. *Journal of Physics: Conference Series*, 753(3), 2016. ISSN 17426596. doi:10.1088/1742-6596/753/3/032062.

[68] Andrea Da Ronch, Marco Panzeri, Jernej Drofelnik, and Roberto D'Ippolito. Sensitivity and calibration of turbulence model in the presence of epistemic uncertainties. *CEAS Aeronautical Journal*, (c), 2019. ISSN 1869-5582. doi:10.1007/s13272-019-00389-y. URL `https://doi.org/10.1007/s13272-019-00389-y`.

[69] A. Garbaruk, D. Niculin, M. Strelets, A. Dyadkin, A. Krylov, and K. Stekenius. Comparative study of different turbulence modeling approaches to prediction of transonic and supersonic flows past a reentry capsule with balance flaps. 5:3–22, 2013. doi:10.1051/eucass/201305003.

[70] Xiaoyu Yang and Paul G. Tucker. Assessment of turbulence model performance: Large streamline curvature and integral length scales. *Computers and Fluids*, 126:91–101, 2016. ISSN 00457930. doi:10.1016/j.compfluid.2015.11.010.

[71] L. J. Vermeer, J. N. Sørensen, and A. Crespo. Wind turbine wake aerodynamics. *Progress in Aerospace Sciences*, 39(6-7):467–510, 2003. ISSN 03760421. doi:10.1016/S0376-0421(03)00078-2.

[72] B Sanderse. Aerodynamics of wind turbine wakes Literature review. Technical report, ECN, 2009.

[73] Peter Graf, Katherine Dykes, George Scott, Jason Fields, Monte Lunacek, Julian Quick, and Pierre Elouan Rethore. Wind Farm Turbine Type and Placement Optimization. *Journal of Physics: Conference Series*, 753(6), 2016. ISSN 17426596. doi:10.1088/1742-6596/753/6/062004.

[74] J Feng and W Z Shen. Optimization of Wind Farm Layout : A Refinement Method by Random Search. (June):624–633, 2013.

[75] Nicolas Kirchner-Bossi and Fernando Porté-Agel. Realistic Wind Farm Layout Optimization through Genetic Algorithms Using a Gaussian Wake Model. *Energies*, 11(12):3268, 2018. doi:10.3390/en11123268.

[76] Rasmus Borrmann, Knud Rehfeld, Anna-Kathrin Wallasch, and Silke Lüers. CAPACITY DENSITIES OF EUROPEAN Report conducted by Deutsche WindGuard GmbH. page 83, 2018.

[77] Zhenzhou Shao, Ying Wu, Li Li, Shuang Han, and Yongqian Liu. Multiple Wind Turbine Wakes Modeling Considering the Faster Wake Recovery in Overlapped Wakes. *Energies*, 12(4):680, 2019. doi:10.3390/en12040680.

[78] O. Eriksson, K. Nilsson, S. P. Breton, and S. Ivanell. Analysis of long distance wakes behind a row of turbines-A parameter study. *Journal of Physics: Conference Series*, 524 (1), 2014. ISSN 17426596. doi:10.1088/1742-6596/524/1/012152.

[79] N. A. Kermani, Soren Juhl Andersen, Jens Nørkær Sørensen, and Wen Zhong Shen. Analysis of turbulent wake behind a wind turbine. In *Proceedings of the 2013 International Conference on aerodynamics of Offshore Wind Energy Systems and wakes*, number June, pages 53–68, 2013. URL `http://forskningsbasen.deff.dk/Share.external?sp=Sd3a48569-35d7-43f7-816a-3fb626dc40db{&}sp=Sdtu`.

[80] Rolf-Erik Keck, Martin de Maré, Matthew J. Churchfield, Sang Lee, Gunner Larsen, and Helge Aagaard Madsen. On atmospheric stability in the dynamic wake meandering model. *Wind Energ.*, 2013. doi:0.1002/we.1662.

[81] Matthew J. Churchfield, Sang Lee, Patrick J. Moriarty, Yujia Hao, Matthew A. Lackner, Rebecca Barthelmie, Julie K. Lundquist, and Gregory Oxley. A Comparison of the Dynamic Wake Meandering Model, Large-Eddy Simulation, and Field Data at the Egmond aan Zee Offshore Wind Plant. (December 2014), 2015. doi:10.2514/6.2015-0724.

[82] Gunner. C. Larsen, Helge.Aa. Madsen, Ferhat. Bingöl, Jakob. Mann, Søren Ott, Jens. Nørkær. Sørensen, Valery. Okulov, Niels. Troldborg, Morten. Nielsen, Kenneth. Thomsen, Torben.J. Larsen, and Robert. Mikkelsen. *Dynamic Wake Meandering Modeling*, volume 1607. 2007. ISBN 9788755036024. URL `http://orbit.dtu.dk/ws/files/7703042/ris{_}r{_}1607.pdf`.

[83] Stefan Ivanell, Robert Mikkelsen, Jens N. Sørensen, and Dan Henningson. Stability analysis of the tip vortices of a wind turbine. *Wind Energ.*, (13):705–715, 2010. doi:10.1002/we.391.

[84] Mahendra J. Bhagwat and J. Gordon Leishman. Stability Analysis of Helicopter Rotor Wakes in Axial Flight. *Journal of the American Helicopter Society*, 45(3):165, 2000. ISSN 00028711. doi:10.4050/jahs.45.165.

[85] Hugo Umberto Quaranta, Hadrien Bolnot, and Thomas Leweke. Long-wave instability of a helical vortex. *Journal of Fluid Mechanics*, 780:687–716, 2015. ISSN 0022-1120. doi:10.1017/jfm.2015.479.

[86] Francesco Viola, Giacomo Valerio Iungo, Simone Camarri, Fernando Porté-Agel, and François Gallaire. Instability of wind turbine wakes immersed in the atmospheric boundary layer. *Journal of Physics: Conference Series*, 625(1), 2015. ISSN 17426596. doi:10.1088/1742-6596/625/1/012034.

[87] Sasan Sarmast, Reza Dadfar, Robert F. Mikkelsen, Philipp Schlatter, Stefan Ivanell, Jens N. Sørensen, and Dan S. Henningson. Mutual inductance instability of the tip vortices behind a wind turbine. *Journal of Fluid Mechanics*, 755:705–731, 2014. ISSN 14697645. doi:10.1017/jfm.2014.326.

[88] Ion Paraschivoiu. Double-Multiple Streamtube Model for Studying VAWT's. *Journal of Propulsion and Power*, 4(4):370–378, 1988. URL `http://ci.nii.ac.jp/naid/80004153847/en/`.

[89] H. Aa. Madsen, T J Larsen, U S Paulsen, and L Vita. Implementation of the Actuator Cylinder Flow Model in the HAWC2 code for Aeroelastic Simulations on Vertical Axis Wind Turbines. (January):1–12, 2013.

[90] W. Yu, V. W. Hong, C. Ferreira, and G. A.M. Van Kuik. Validation of engineering dynamic inflow models by experimental and numerical approaches. *Journal of Physics: Conference Series*, 753(2), 2016. ISSN 17426596. doi:10.1088/1742-6596/753/2/022024.

[91] H. Snel and J.G. Schepers. Joint investigation of dynamic inflow effects and implementation of an engineering method, 1995. ISSN 0167-6105.

[92] H. Rahimi, M. Hartvelt, J. Peinke, and J. G. Schepers. Investigation of the current yaw engineering models for simulation of wind turbines in BEM and comparison with CFD and experiment. *Journal of Physics: Conference Series*, 753(2), 2016. ISSN 17426596. doi:10.1088/1742-6596/753/2/022016.

[93] Glauert. Airplane Propellers. *Aerodynamic Theory*, IV:169–360, 1935. URL `http://dx.doi.org/10.1007/978-3-642-91487-4{_}3`.

[94] S. J. Andersen, J. N. Sørensen, S. Ivanell, and R. F. Mikkelsen. Comparison of engineering wake models with CFD simulations. *Journal of Physics: Conference Series*, 524(1), 2014. ISSN 17426596. doi:10.1088/1742-6596/524/1/012161.

[95] T. Hommes, J. Bosschers, and H. W.M. Hoeijmakers. Evaluation of the radial pressure distribution of vortex models and comparison with experimental data. *Journal of Physics: Conference Series*, 656(1):7–11, 2015. ISSN 17426596. doi:10.1088/1742-6596/656/1/012182.

[96] A. Van Garrel. Development of a Wind Turbine Aerodynamics Simulation Module. *Technical Report ECN-C-03-079*, (August):106, 2003. ISSN 0040-5736. doi:10.13140/RG.2.1.2773.8000.

[97] G. S. Winckelmans. *Topics in vortex methods for the computation of three- and two-dimensional incompressible unsteady flows*. PhD thesis, California Institute of Technology, 1989.

[98] Emmanuel Branlard. *and aeroelasticity using vortex-based methods DTU Wind Energy PhD Thesis 2015*, volume 0052. 2015. ISBN 9788793278448.

[99] Francesco Balduzzi, David Marten, Alessandro Bianchini, Jernej Drofelnik, Lorenzo Ferrari, Michele Sergio Campobasso, Georgios Pechlivanoglou, Christian Navid Nayeri, Giovanni Ferrara, and Christian Oliver Paschereit. Three-Dimensional Aerodynamic Analysis of a Darrieus Wind Turbine Blade Using Computational Fluid Dynamics and Lifting Line Theory. *Journal of Engineering for Gas Turbines and Power*, 140(2):022602, 2017. ISSN 0742-4795. doi:10.1115/1.4037750.

[100] Rio Yokota and L. A. Barba. Comparing the treecode with FMM on GPUs for vortex particle simulations of a leapfrogging vortex ring. *Computers and Fluids*, 45(1):155–161, 2011. ISSN 00457930. doi:10.1016/j.compfluid.2010.11.029.

[101] P. Ploumhans, G. S. Winckelmans, and J. K. Salmon. Vortex particles and tree codes: I. flows with arbitrary crossing between solid boundaries and particle redistribution lattice; II. vortex ring encountering a plane at an angle. *ESAIM: Proceedings*, 7:335–348, 1999. doi:10.1051/proc:1999031.

[102] Joseph Saverin, David Marten, George Pechlivanoglou, Christian Oliver Paschereit, and Arne van Garrel. Implementation of the Multi-Level Multi-Integration Cluster Method to the Treatment of Vortex Particle Interactions for Fast Wind Turbine Wake Simulations. In *ASME Turbo Expo 2018: Turbomachinery Technical Conference and Exposition*, 2018.

[103] G. S. Winckelmans and A. Leonard. Contributions to Vortex Particle Methods for the Computation of Three-Dimensional Incompressible Unsteady Flows. *Journal of Computational Physics*, 109:247–273, 1993.

[104] P. Benard, A.C. Viré, V. Moureau, G. Lartigue, L. Beaudet, P. Deglaire, and L . Bricteux. Large-Eddy Simulation of wind turbines wakes including geometrical effects. *Computers & Fluids*, 173, 2018. doi:https://doi.org/10.1016/j.compfluid.2018.03.015.

[105] L A Martinez Tossas and S Leonardi. Wind Turbine Modeling for Computational Fluid Dynamics. *National Renewable Energy Laboratory*, (December 2010), 2013.

[106] Siri Kalvig, Eirik Manger, and Bjørn Hjertager. Comparing different CFD wind turbine modelling approaches with wind tunnel measurements. *Journal of Physics: Conference Series*, 555(1), 2014. ISSN 17426596. doi:10.1088/1742-6596/555/1/012056.

[107] Mandar Tabib, Adil Rasheed, and Trond Kvamsdal. LES and RANS simulation of onshore Bessaker wind farm: Analysing terrain and wake effects on wind farm performance. *Journal of Physics: Conference Series*, 625(1), 2015. ISSN 17426596. doi:10.1088/1742-6596/625/1/012032.

[108] Giacomo Valerio Iungo, Vignesh Santhanagopalan, Umberto Ciri, Francesco Viola, Lu Zhan, Mario A. Rotea, and Stefano Leonardi. Parabolic RANS solver for low-computational-cost simulations of wind turbine wakes. *Wind Energy*, 21(3):184–197, 2018. ISSN 10991824. doi:10.1002/we.2154.

[109] Hamid Sarlak Chivaee and Jens N. Sørensen. Large eddy simulation of wind turbine wakes in prescribed neutral and non-neutral atmospheric boundary layers. *Journal of Physics: Conference Series*, 555(1), 2014. ISSN 17426596. doi:10.1088/1742-6596/555/1/012087.

[110] Georgios Deskos, Sylvain Laizet, and Matthew D. Piggott. Turbulence-resolving simulations of wind turbine wakes. *Renewable Energy*, 134:989–1002, 2019. ISSN 18790682. doi:10.1016/j.renene.2018.11.084. URL `https://doi.org/10.1016/j.renene.2018.11.084`.

[111] Michael Hölling. *TOPICS IN WIND ENERGY 2 Wind Energy – Impact of*. ISBN 9783642546952.

[112] Yu Ting Wu and Fernando Porté-Agel. Large-Eddy Simulation of Wind-Turbine Wakes: Evaluation of Turbine Parametrisations. *Boundary-Layer Meteorology*, 138(3):345–366, 2011. ISSN 00068314. doi:10.1007/s10546-010-9569-x.

[113] J Bartl and P U Thamsen. A Detached-Eddy-Simulation study. pages 1–17, 2018.

[114] Boumehani Abdellah, Noura Belkheir, and Sofiane Khelladi. Effect of Computational Grid on Prediction of a Vertical axis Wind turbine Rotor Using Delayed Detached-Eddy Simulations. *2018 International Conference on Wind Energy and Applications in Algeria, ICWEAA 2018*, pages 1–5, 2019. doi:10.1109/ICWEAA.2018.8605048.

[115] Camilo A. Sedano, Frederik Berger, Hamid Rahimi, Omar D. Lopez Mejia, Martin Kühn, and Bernhard Stoevesandt. CFD validation of a model wind turbine by means of improved and delayed detached eddy simulation in openFoam. *Energies*, 12(7), 2019. ISSN 19961073. doi:10.3390/en12071306.

[116] R.F. Mikkelsen. *Actuator Disc Methods Applied to Wind Turbines*. 2003. ISBN 8774752960. URL `http://orbit.dtu.dk/files/5452244/Robert.PDF`.

[117] Niels Troldborg, Jens N. Sørensen, and Robert Mikkelsen. Actuator line simulation of wake of wind turbine operating in turbulent inflow. *Journal of Physics: Conference Series*, 75(1), 2007. ISSN 17426596. doi:10.1088/1742-6596/75/1/012063.

[118] Xiaolei Yang and Fotis Sotiropoulos. A new class of actuator surface models for wind turbines. *Wind Energy*, 21(5):285–302, 2018. ISSN 10991824. doi:10.1002/we.2162.

[119] Hugo Olivares-Espinosa, Simon-Philippe Breton, Karl Nilsson, Christian Masson, Louis Dufresne, and Stefan Ivanell. Assessment of Turbulence Modelling in the Wake of an Actuator Disk with a Decaying Turbulence Inflow. *Applied Sciences*, 8(9):1530, 2018. doi:10.3390/app8091530.

[120] Neal M. Chaderjian. Advances in Rotor Performance and Turbulent Wake Simulation Using DES and Adaptive Mesh Refinement. *7th International Conference on Computational Fluid Dynamics*, 3(1):1–25, 2012. URL `http://ntrs.nasa.gov/search.jsp?R=20130001604`.

[121] Jiangang Wang, Chengyu Wang, Filippo Campagnolo, and Carlo L. Bottasso. Scale-adaptive simulation of wind turbines, and its verification with respect to wind tunnel

measurements. *Wind Energy Science Discussions*, (July):1–26, 2018. doi:10.5194/wes-2018-47.

[122] David A. Peters and Cheng Jian He. Correlation of Measured Induced Velocities with a Finite-State Wake Model. *Journal of the American Helicopter Society*, 36(3):59–70, 1989. ISSN 21616027. doi:10.4050/jahs.36.59.

[123] Akihiro Suzuki. Generalized Dynamic Wake Model for YawDyn. In *37th Aerospace Sciences Meeting and Exhibit*, 1999.

[124] David A. Peters and Zhongyang Fei. Applications and data of generalised dynamic wake theory of the flow in a rotor wake. *IET Control Theory & Applications*, 9(7):1051–1057, 2015. ISSN 1751-8644. doi:10.1049/iet-cta.2014.0710.

[125] Moriarty and Hansen. AeroDyn Theory Manual. *Renewable Energy*, 15(January): 500–36313, 2005. ISSN 00664189. URL `http://www.nrel.gov/docs/fy05osti/36881.pdf`.

[126] Philippe Chatelain, Stéphane Bricteux, Laurent Backaert, Grégoire Winckelmans, Stefan Kern, and Petros Koumoutsakos. Vortex particle-mesh methods with immersed lifting lines applied to the Large Eddy Simulation of wind turbine wakes. In *Wake Conference, Gotland, Sweden*, 2011.

[127] Philippe Chatelain, Matthieu Duponcheel, Denis-Gabriel Caprace, Yves Marichal, and Grégoire Winckelmans. Vortex particle-mesh simulations of vertical axis wind turbine flows: from the airfoil performance to the very far wake. *Wind Energy Science*, 2(1): 317–328, 2017. doi:10.5194/wes-2-317-2017.

[128] S. Backaert, P. Chatelain, and G. Winckelmans. Vortex Particle-Mesh with Immersed Lifting Lines for Aerospace and Wind Engineering. *Procedia IUTAM*, 18:1–7, 2015. ISSN 22109838. doi:10.1016/j.piutam.2015.11.001. URL `http://dx.doi.org/10.1016/j.piutam.2015.11.001`.

[129] Stephen L Wood, Ralf Deiterding, and Flow Technology. A Lattice Boltzmann Method for Horizontal Axis Wind Turbine Simulation. pages 1–18, 2015.

[130] Ralf Deiterding and Stephen L. Wood. Predictive wind turbine simulation with an adaptive lattice Boltzmann method for moving boundaries. *Journal of Physics: Conference Series*, 753(8), 2016. ISSN 17426596. doi:10.1088/1742-6596/753/8/082005.

[131] M. Sbragaglia, L. Biferale, and S. Succi. Lattice Boltzmann Methods for Nanofluidics. *Encyclopedia of Nanotechnology*, pages 1771–1777, 2016. doi:10.1007/978-94-017-9780-1_100974.

[132] LS Luo and M Krafczyk. Lattice Boltzmann Method for Computational Fluid Dynamics. *Encyclopedia of Aerospace*, 2003. URL `http://onlinelibrary.wiley.com/doi/10.1002/9780470686652.eae064/full`.

[133] Louis-Charles Forcier and Simon Joncas. On the wind turbine blade loads from an aeroelastic simulation and their transfer to a three-dimensional finite element model

of the blade. *Wind Engineering*, page 0309524X1984986, 2019. ISSN 0309-524X. doi:10.1177/0309524X19849861. URL `http://journals.sagepub.com/doi/10.1177/0309524X19849861`.

[134] Wilfried Campbell. *Protection of steam turbine disk wheels from axial vibration*. 1924.

[135] M. O.L. Hansen, J. N. Sørensen, S. Voutsinas, N. Sørensen, and H. Aa Madsen. State of the art in wind turbine aerodynamics and aeroelasticity. *Progress in Aerospace Sciences*, 42(4):285–330, 2006. ISSN 03760421. doi:10.1016/j.paerosci.2006.10.002.

[136] Jan van der Tempel. Wind turbine structural dynamics - A review of the principles for modern power generation, onshore and offshore. *Wind Engineering*, 26(4):211–20, 2002.

[137] Lars Andersen and Johan Clause. Efficient Modelling of Wind Turbine Foundations. *Fundamental and Advanced Topics in Wind Power*, 2012. doi:10.5772/20176.

[138] K. Holm-Jørgensen and S. R.K. Nielsen. System reduction in multibody dynamics of wind turbines. *Multibody System Dynamics*, 21(2):147–165, 2009. ISSN 13845640. doi:10.1007/s11044-008-9132-4.

[139] Philipp Thomas, Xin Gu, Roland Samlaus, Claudio Hillmann, and Urs Wihlfahrt. The OneWind Modelica Library for Wind Turbine Simulation with Flexible Structure - Modal Reduction Method in Modelica. *Proceedings of the 10th International Modelica Conference, March 10-12, 2014, Lund, Sweden*, 96:939–948, 2014. doi:10.3384/ecp14096939.

[140] Long Wu and Paolo Tiso. Nonlinear model order reduction for flexible multibody dynamics: a modal derivatives approach. *Multibody System Dynamics*, 36(4):405–425, 2016. ISSN 1573272X. doi:10.1007/s11044-015-9476-5. URL `http://dx.doi.org/10.1007/s11044-015-9476-5`.

[141] K Branner, J P Blasques, T Kim, V A Fedorov, P Berring, R D Bitsche, C Berggreen, K Branner, J P Blasques, T Kim, and V A Fedorov. *Anisotropic beam model for analysis and design of passive controlled wind turbine blades*, volume 0001. 2012. ISBN 9788792896018.

[142] Lin Wang, Xiongwei Liu, and Athanasios Kolios. State of the art in the aeroelasticity of wind turbine blades: Aeroelastic modelling. *Renewable and Sustainable Energy Reviews*, 64:195–210, 2016. ISSN 18790690. doi:10.1016/j.rser.2016.06.007. URL `http://dx.doi.org/10.1016/j.rser.2016.06.007`.

[143] Angelo Simone. An Introduction to the Analysis of Slender Structures. Technical report, Delft University of Technology, 2011.

[144] S. P. Timoshenko. 0n the Correction for Shear of the Differential Equation for Transverse Vibrations of Prismatic Bars. *Philosophical Magazine*, 1921.

[145] Hui Chen, Wenbin Yu, and Mark Capellaro. A critical assessment of computer tools for calculating composite wind turbine blade properties. *Renewable Energy*, 2009. doi:10.1002/we.372.

[146] L. Arany, S. Bhattacharya, S. Adhikari, S. J. Hogan, and J. H.G. Macdonald. An analytical model to predict the natural frequency of offshore wind turbines on three-spring flexible foundations using two different beam models. *Soil Dynamics and Earthquake Engineering*, 74:40–45, 2015. ISSN 02677261. doi:10.1016/j.soildyn.2015.03.007. URL http://dx.doi.org/10.1016/j.soildyn.2015.03.007.

[147] M. A. Crisfield. A consistent co-rotational formulation for non-linear, three-dimensional, beam-elements. *Computer Methods in Applied Mechanics and Engineering*, 81(2): 131–150, 1990. ISSN 00457825. doi:10.1016/0045-7825(90)90106-V.

[148] J. Oliver and E. Onate. A total lagrangian formulation for the geometrically nonlinear analysis of structures using finite elements. Part I. Two-dimensional problems: Shell and plate structures. *International Journal for Numerical Methods in Engineering*, 20(12): 2253–2281, 1984. ISSN 10970207. doi:10.1002/nme.1620201208.

[149] Antonio M. Recuero and Dan Negrut. An Introduction to the Floating Frame of Reference Formulation for Small Deformation in Flexible Multibody Dynamics. page 11, 2016.

[150] M. Greco and H. B. Coda. Positional FEM formulation for flexible multi-body dynamic analysis. *Journal of Sound and Vibration*, 290(3-5):1141–1174, 2006. ISSN 10958568. doi:10.1016/j.jsv.2005.05.018.

[151] Thomas Forrister and Comsol. Von Mises Stress distribution in the wind turbine design, 2019. URL https://www.comsol.com/blogs/analyzing-wind-turbine-blades-with-the-composite-materials-module/.

[152] Philippe Couturier, Steen Krenk, and Jan Høgsberg. Beam section stiffness properties using 3D finite elements. 2013.

[153] Philippe Couturier and Steen Krenk. General Beam cross Section Analysis using a 3D Fnite Element Slice. In *Proceedings of the ASME 2014 International Mechanical Engineering Congress and Exposition IMECE2014*, 2014.

[154] Martin Arnold and Werner Schielen. *Simulation Techniques for Applied Dynamics*. Springer US, 2008. ISBN 978-3-211-89547-4.

[155] Michael Valasek, Jirı Maca, Pavel Steinbauer, Jan Spurny, Vıt Smilauer, and Ondrej Vaculın. Coupling of SImulation Tools for Simulation of Multiphysical Systems. *Engineering MECHANICS*, 13(3):2006, 2006.

[156] B Simeon and M Arnold. Mathematical and Computer Modelling of Dynamical Systems : Methods , Tools and Applications in Engineering and Related Sciences Coupling DAEs and PDEs for Simulating the Interaction of Pantograph and Catenary. (April 2015):37–41, 2010. ISSN 13873954. doi:10.1076/1387-3954(200006)6.

[157] Martin Arnold, Antonio Carrarini, Andreas Heckmann, and Gerhard Hippmann. Simulation Techniques for Multidisciplinary Problems in Vehicle System Dynamics, 2003.

[158] IRENA. Renewable Energy Technologies: Cost Anaylsis of Wind Power. *Cost Analysis Series*, 1(5), 2012. ISSN 18653537. doi:10.1016/B978-0-08-098330-1.00011-9. URL http:

//linkinghub.elsevier.com/retrieve/pii/B9780080983301000119{%}0Ahttps://www.irena.org/DocumentDownloads/Publications/RE{_}Technologies{_}Cost{_}Analysis-BIOMASS.pdf{%}5Cnwww.irena.org/Publications.

[159] K Boorsma, M Hartvelt, and L M Orsi. Application of the lifting line vortex wake method to dynamic load case simulations. In *Journal of Physics: Conference Series*, volume 753, 2016. doi:10.1088/1742-6596/753/2/022030.

[160] S. Hauptmann, M. Bülk, L. Schön, S. Erbslöh, K. Boorsma, F. Grasso, M. Kühn, and P. W. Cheng. Comparison of the lifting-line free vortex wake method and the blade-element-momentum theory regarding the simulated loads of multi-MW wind turbines. In *Journal of Physics: Conference Series*, volume 555, 2014. doi:10.1088/1742-6596/555/1/012050.

[161] Joseph Saverin, Juliane Peukert, David Marten, George Pechlivanoglou, Christian Oliver Paschereit, and David Greenblatt. Aeroelastic simulation of multi-MW wind turbines using a free vortex model coupled to a geometrically exact beam model. In *Journal of Physics: Conference Series*, volume 753, 2016. doi:10.1088/1742-6596/753/8/082015.

[162] E A Bossanyi. Bladed Theory Manual version 4.7. Technical report, DNV GL, 2003.

[163] C. L. Botasso and A. Croce. Cp-Lambda user manual. Technical report, Politecnico di Milano, 2009.

[164] Torben Juul Larsen and Anders Melchior Hansen. *How 2 HAWC2, the user's manual*. 2007. ISBN 9788755035836.

[165] WMC. WMC FOCUS6. URL https://wmc.eu/focus6.php.

[166] Jason M Jonkman and Marshall L Buhl Jr. FAST User ' s Guide. 2005.

[167] ADC. ADCoS - Aero Dynamik Consult. URL https://www.aero-dynamik.de/Leistungen/Windenergie/Simulation{_}66.html.

[168] B. M. Pedersen. 28th Meeting of Experts State of the Art of Aeroelastic Codes for Wind Turbine Calculations. Technical report, 1996. URL http://scholar.google.com/scholar?hl=en{&}btnG=Search{&}q=intitle:State+of+the+Art+of+Aeroelastic+Codes+for+Wind+Turbine+Calculations{#}5.

[169] V. A. Riziotis and S. G. Voutsinas. GAST: A general aerodynamic and structural prediction tool for wind turbines. In *EWEC-CONFERENCE*, pages 448–452, 1997.

[170] Mareike Leimeister and Philipp Thomas. The OneWind Modelica Library for Floating Offshore Wind Turbine Simulations with Flexible Structures. In *Proceedings of the 12th International Modelica Conference, Prague, Czech Republic, May 15-17, 2017*, volume 132, pages 633–642, 2017. doi:10.3384/ecp17132633.

[171] Modelica Association. Modelica - A Unified Object-Oriented Language for Systems Modeling. Language Specification. Version 3.4. page 308, 2017. URL https://www.modelica.org/documents/ModelicaSpec33Revision1.pdf.

[172] Paul E Thomassen, Per Ivar Bruheim, Loup Suja, and Lars Frøyd. A Novel Tool for FEM Analysis of Offshore Wind Turbines With Innovative Visualization Techniques. In *Proceedings of the Twenty-second (2012) International Offshore and Polar Engineering Conference*, volume 4, pages 374–379, 2012. URL `http://www.isope.org/publications/proceedings/isope/isope2012/data/papers/vol1/2012-TPC-226Thoma.pdf`.

[173] D Marten, J Wendler, G Pechlivanoglou, C N Nayeri, and C O Paschereit. QBlade : An Open Source Tool For Design And Simulation Of Horizontal And Vertical Axis Wind Turbines. *IJETAE*, 3(3):264–269, 2013.

[174] David Marten. QBlade v0.95 Guidelines for Lifting Line Free Vortex Wake Simulations. Technical Report June, TU Berlin, 2016.

[175] Bradley M Kuhn and Karen M Sandler. A Practical Guide to GPL Compliance Best Practices to Avoid Common Violations. pages 1–15, 2008.

[176] Jasmin Blanchette and Mark Summerfield. *C ++ GUI Programming with Qt 4*. Trolltech AS, 2006. ISBN 9780131872493.

[177] Mahendra J. Bhagwat and J. Gordon Leishman. Stability, Consistency and Convergence of Time-Marching Free-Vortex Rotor Wake Algorithms. *Journal of the American Helicopter Society*, 46(1):59–71, 2009. ISSN 21616027. doi:10.4050/jahs.46.59.

[178] Leonardo Bergami and Mac Gaunaa. ATEFlap Aerodynamic Model. Technical report, DTU, 2012.

[179] Juliane Wendler, David Marten, George Pechlivanoglou, Christian Oliver Paschereit, and Christian Navid Nayeri. An Unsteady Aerodynamics Model for Lifting Line Free Vortex Wake Simulations of HAWT and VAWT in QBlade. In *Proceedings of ASME Turbo Expo 2016: Turbomachinery Technical Conference and Exposition*, 2016.

[180] Morten Hartvig Hansen, Mac Gaunaa, and Helge Aagaard Madsen. A Beddoes-Leishman type dynamic stall model in state-space and indicial formulation. Technical report, DTU, 2004.

[181] Mac Gaunaa. Unsteady two-dimensional potential-fl ow model for thin variable geometry airfoils. *Wind Energ.*, 13(December 2005):167–192, 2010. doi:I: 10.1002/we.3.

[182] NREL. OSU Wind-Tunnel Test Data S809, 1999. URL `https://wind.nrel.gov/airfoils/OSU{_}data/data/`.

[183] David Marten, Sirko Bartholomay, George Pechlivanoglou, Christian Nayeri, Christian O. Paschereit, Annette Fischer, and Thorsten Lutz. Numerical and Experimental Investigation of Trailing Edge Flap Performance on a Model Wind Turbine. In *AIAA SciTech Forum, 2018 Wind Energy Symposium*, number January, pages 1–14, 2018. doi:10.2514/6.2018-1246.

[184] H. Snel, R. Houwink, and W. J. Piers. Sectional Prediction of 3D Effects for Separated Flow on Rotating Blades, 1993.

[185] IEC. IEC 61400-1:2019 Wind energy generation systems - Part 1: Design requirements, 2019.

[186] G Taylor. The spectrum of turbulence. *Proceedings of the Royal Society of London*, 313, 1938.

[187] Paul S. Veers. Three-Dimensional Wind Simulation. Technical report, Sandia, 1988. URL `https://prod.sandia.gov/techlib-noauth/access-control.cgi/1988/880152.pdf`.

[188] B. J. Jonkman. TurbSim User's Guide: Version 1.50. Technical Report September, NREL, 2009.

[189] J. G. Leishman. *Principles of Helicopter Aerodynamics*. Cambridge University Press, 2000.

[190] David Marten, Matthew Lennie, Christian Navid Nayeri, and Christian Oliver Paschereit. Implementation, Optimization and validation of a Nonlinear Lifting Line Free Vortex Wake Module within the Wind Turbine Simulation Code QBlade. In *Proceedings of ASME Turbo Expo 2015: Turbine Technical Conference and Exposition*, pages 1–11, 2016.

[191] John E Stone, David Gohara, and Guochun Shi. OpenCL: A Parallel Programming Standard for Heterogeneous Computing Systems. *Computing in Science & Engineering*, 2010.

[192] Alessandro Tasora, Hammad Mazhar Radu Serban2, Arman Pazouki, Daniel Melanz, Jonathan Fleischmann, Michael Taylor, Hiroyuki Sugiyama, and Dan Negrut. Chrono: An Open Source Multi-physics Dynamics Engine. *Tasora, A., Serban, R., Mazhar, H., Pazouki, A., Melanz, D., Fleischmann, J., . . . Negrut, D. (2016). Chrono: An Open Source Multi-physics Dynamics Engine. High Performance Computing in Science and Engineering, 19–49. doi:10.1007/978-3-319-40361-8_2*, 2016. doi:doi:10.1007/978-3-319-40361-8_2.

[193] Projectchrono.org. Project Chrono - An Open-Source Physics Engine, 2019. URL `https://projectchrono.org/about/`.

[194] Tuxfamily. EIGEN - a C++ template library for linear algebry: matrices, vectors, numerical solvers and related algorithms. URL `http://eigen.tuxfamily.org`.

[195] Dan Negrut. Co-rotational Formulation in Chrono Antonio Recuero Chrono. pages 1–10, 2016.

[196] DNVGL. Guideline for the Certification of Wind Turbines, 2010.

[197] Morten Hartvig Hansen and Lars Christian Henriksen. *Basic DTU Wind Energy controller Wind Energy Report 2013*. Number January. 2013. ISBN 9788792896278.

[198] Matthew Lennie, David Marten, George Pechlivanoglou, Christian Navid Nayeri, and Christian Oliver Paschereit. Modern methods for investigating the stability of a pitching floating platform wind turbine. *Journal of Physics: Conference Series*, 753(8), 2016. ISSN 17426596. doi:10.1088/1742-6596/753/8/082012.

[199] Netlib.org. LAPACK: dggev, . URL `http://www.netlib.org/lapack/explore-html/d9/d8e/group{_}{_}double{_}g{_}eeigen{_}ga4f59e87e670a755b41cbdd7e97f36bea.html`.

[200] Netlib.org. LAPACK — Linear Algebra PACKage, . URL `http://www.netlib.org/lapack/`.

[201] David Marten, Matthew Lennie, Georgios Pechlivanoglou, Christian O. Paschereit, Norbert V. Dy, Ion Paraschivoiu, and Farooq Saeed. Validation and comparison of a newly developed aeroelastic design code for VAWT. In *AIAA SciTech Forum*, 2017. doi:10.2514/6.2017-0452.

[202] Alessandro Tasora. Time integration in Chrono::Engine. pages 1–44, 2017.

[203] J Jonkman, S Butterfield, W Musial, and G Scott. Definition of a 5-MW Reference Wind Turbine for Offshore System Development. Technical Report February, 2009.

[204] M M Hand, D A Simms, L J Fingersh, D W Jager, J R Cotrell, S Schreck, and S M Larwood. Unsteady Aerodynamics Experiment Phase VI : Wind Tunnel Test Configurations and Available Data Campaigns Unsteady Aerodynamics Experiment Phase VI : Wind Tunnel Test Configurations and Available Data Campaigns. (December), 2001.

[205] J G Schepers, K Boorsma, T Cho, Sugoi Gomez-iradi, P Schaffarczyk, A Jeromin, W Z Shen, T Lutz, K Meister, B Stoevesandt, S Schreck, D Micallef, R Pereira, T Sant, H a Madsen, and Niels N. S{\o}rensen. Final report of IEA Task 29, Mexnext (Phase 1): Analysis of Mexico wind tunnel measurements. (Phase 1):312, 2012.

[206] Sara Siniscalchi-Minna, Fernando D. Bianchi, Mikel De-Prada-Gil, and Carlos Ocampo-Martinez. A wind farm control strategy for power reserve maximization. *Renewable Energy*, 131:37–44, 2019. ISSN 18790682. doi:10.1016/j.renene.2018.06.112. URL `https://doi.org/10.1016/j.renene.2018.06.112`.

[207] B. R. Karthikeya and Reiner Johannes Schutt. Overview of wind park control strategies. *IEEE Transactions on Sustainable Energy*, 5(2):416–422, 2014. ISSN 19493029. doi:10.1109/TSTE.2013.2285392.

[208] D. Astrain Juangarcia, I. Eguinoa, and T. Knudsen. Derating a single wind farm turbine for reducing its wake and fatigue. *Journal of Physics: Conference Series*, 1037(3), 2018. ISSN 17426596. doi:10.1088/1742-6596/1037/3/032039.

[209] B. M. Doekemeijer, S. Boersma, L. Y. Pao, and J. W. Van Wingerden. Joint state-parameter estimation for a control-oriented les wind farm model. *Journal of Physics: Conference Series*, 1037(3), 2018. ISSN 17426596. doi:10.1088/1742-6596/1037/3/032013.

[210] S. Boersma, B. M. Doekemeijer, S. Siniscalchi-Minna, and J. W. van Wingerden. A constrained wind farm controller providing secondary frequency regulation: An LES study. *Renewable Energy*, 134:639–652, 2019. ISSN 18790682. doi:10.1016/j.renene.2018.11.031. URL `https://doi.org/10.1016/j.renene.2018.11.031`.

[211] Sjoerd Boersma, Bart Doekemeijer, Mehdi Vali, Johan Meyers, and Jan-Willem van Wingerden. A control-oriented dynamic wind farm model: WFSim. *Wind Energy Science*, 3(1):75–95, 2018. doi:10.5194/wes-3-75-2018.

[212] Jennifer Annoni, Pieter Gebraad and Peter Seiler. Reduced-Order Modeling for Wind Farm Control. *Wind Energy*, 2010. doi:10.1002/we.

[213] Joseph R. Saverin, David Marten, Christian Nayeri, and Christian O. Paschereit. Simulation of Multiple Turbine Aerodynamic Interaction using a Multilevel Method. (January), 2019. doi:10.2514/6.2019-1574.

[214] Fabio Pierella, Per Age Krogstad, and Lars Saetran. Blind Test 2 calculations for two in-line model wind turbines where the downstream turbine operates at various rotational speeds. *Renewable Energy*, 70:62–77, 2014. ISSN 09601481. doi:10.1016/j.renene.2014.03.034. URL `http://dx.doi.org/10.1016/j.renene.2014.03.034`.

[215] Per Age Krogstad and Pal Egil Eriksen. "Blind test" calculations of the performance and wake development for a model wind turbine. *Renewable Energy*, 50:325–333, 2013. ISSN 09601481. doi:10.1016/j.renene.2012.06.044. URL `http://dx.doi.org/10.1016/j.renene.2012.06.044`.

[216] Roland Schmehl. *Airborne Wind Energy - Advances in Technology Development and Research*. Springer Singapore, 2018. ISBN 978-981-10-1946-3. doi:10.1007/978-981-10-1947-0.

[217] Antonello Cherubini, Andrea Papini, Rocco Vertechy, and Marco Fontana. Airborne Wind Energy Systems: A review of the technologies. *Renewable and Sustainable Energy Reviews*, 51:1461–1476, 2015. ISSN 18790690. doi:10.1016/j.rser.2015.07.053.

[218] Rolf van der Vlugt, Roland Schmehl, and Michael Noom. Quasi-Steady Model of a Pumping Kite Power System. *Renewable Energy*, (May):14, 2014. ISSN 0960-1481. doi:10.1016/j.renene.2015.04.028. URL `http://dx.doi.org/10.1016/j.renene.2015.04.028`.

[219] G. Sánchez-Arriaga, A. Pastor-Rodriguez, R. Borobia-Moreno, and R. Schmehl. A constraint-free flight simulator package for airborne wind energy systems. *Journal of Physics: Conference Series*, 1037(6), 2018. ISSN 17426596. doi:10.1088/1742-6596/1037/6/062018.

[220] Nathan Slegers. Modelling and Control of a Tethered Rotorcraft. 298(0704):1–24, 2010.

[221] M B Ruppert. Development and validation of a real time pumping kite model. page 124, 2012.

[222] H. Seifert, A. Westerhellweg, and J. Kroening. Risk analysis of ice throw from wind turbines. In *Paper Presented at Boreas VI*, number April 2003, pages 1–9, 2003.

[223] Matthew Lennie, Sean Dominin, David Marten, George Pechlivanoglou, and Christian O. Paschereit. Development of Ice Throw Model for Wind Turbine Simulation Software QBlade. pages 1–13, 2019. doi:10.2514/6.2019-1800.

[224] Andreas Krenn, Nina Weber, Sten Barup, Thorsten Weidl, Andre Hoffmann, Rolv Erlend Bredersen, Marine Lannic, Stefan Müller, Nicole Stoffels, Thomas Hahm, Felix Storck, and Frederik Lautenschlager. IEA Wind TCP Task 19: International Recommendations for Ice Fall and Ice Throw Risk Assessments. Technical report, 2018.

[225] J. Jonkman. Definition of the Floating System for Phase IV of OC3. (May), 2010. doi:10.2172/979456. URL http://www.osti.gov/servlets/purl/979456-qqFMGj/.

[226] J. Jonkman, I. Fylling, J. Nichols, T. Larsen, A. Hansen, M. Kohlmeier, T. Nygaard, K. Maus, J. Pascual Vergara, D. Merino, M. Karimirad, Z. Gao, T. Moan, W. Shi, and H. Park. Offshore code comparison collaboration within IEA wind task 23: Phase IV results regarding floating wind Turbine modeling. *European Wind Energy Conference and Exhibition 2010, EWEC 2010*, 3, 2010.

[227] J. R. Morison, J. W. Johnson, and S. A. Schaaf. The Force Exerted by Surface Waves on Piles. *Society of Petroleum Engineers*, 1950. doi:doi:10.2118/950149-G.

[228] Evangelos I. Katsanos, Sebastian Thöns, and Christos Georgakis. Wind turbines and seismic hazard: a state-of-the-art review. *Wind Energy*, 19(11):2113–2133, 2016. ISSN 10991824. doi:10.1002/we.1968.

[229] S. Thoens, M. H. Faber, and W. Ruuecker. Ultimate Limit State Model Basis for Assessment of Offshore Wind Energy Converters. *Journal of Offshore Mechanics and Arctic Engineering*, 134(3):031904, 2012. ISSN 08927219. doi:10.1115/1.4004513. URL http://offshoremechanics.asmedigitalcollection.asme.org/article.aspx?articleid=1457857.

[230] USGS. U.S. Geological Survey, Earthquake Hazards Reduction Program, 2019. URL https://strongmotioncenter.org/cgi-bin/CESMD/iqr{_}dist{_}DM2.pl?IQRID=Chile{_}27Feb2010{_}us2010tfan{&}SFlag=0{&}Flag=3.

[231] LinkedIn-Corporation. Apache Helix, 2019. URL https://helix.apache.org/.

[232] Amazon. Amazon Web Services, 2019. URL https://aws.amazon.com/?nc1=h{_}ls.

[233] M Lennie, J Steenbuck, B R Noack, and C O Paschereit. Cartographing dynamic stall with machine learning. *Wind Energy Science Discussions*, 2019:1–31, 2019. doi:10.5194/wes-2019-36. URL https://www.wind-energ-sci-discuss.net/wes-2019-36/.

[234] L. A. Viterna and D. C. Janetzke. Theoretical and Experimental Power From Large Horizontal-Axis Wind Turbines. Technical report, 1982.

[235] B Montgomerie. Methods for Root Effects, Tip Effects and Extending the Angle of Attack Range to 6180, With Application to Aerodynamics for Blades on Wind Turbines and Propellers. Technical report, FOI, Swedish Defence Research Agency, 2004.

[236] Matthew Lennie, Alireza Selahi-Moghaddam, David Holst, Georgios Pechlivanoglou, Christian Navid Nayeri, and Christian Oliver Paschereit. Vortex Shedding and Frequency Lock in on Stand Still Wind Turbines: A Baseline Experiment. In *Volume 9: Oil and Gas Applications; Supercritical CO2 Power Cycles; Wind Energy*, page V009T49A007, 2017. ISBN 978-0-7918-5096-1. doi:10.1115/GT2017-63653. URL `http://proceedings.asmedigitalcollection.asme.org/proceeding.aspx?doi=10.1115/GT2017-63653`.

[237] Matthew Churchfield and Patrick Moriarty. Overview of the Simulator for Offshore Wind Farm Application (SOWFA). *Nrel*, page 109, 2012.

[238] J. Barnes and P. Hut. A hierarchical O(N log N) force-calculation algorithm. *Nature*, 324 (4):446–449, 1986.

[239] Sandeep Bhatt, Pangfeng Liu, Victor Fernandez, and Norman Zabusky. Tree codes for vortex dynamics: Application of a programming framework. *In International Parallel Processing Symposium*, 1995.

[240] Alejandro D. Otero and Fernando L. Ponta. Structural Analysis of Wind-Turbine Blades by a Generalized Timoshenko Beam Model. *Journal of Solar Energy Engineering*, 132 (1):011015, 2010. ISSN 01996231. doi:10.1115/1.4000596.

[241] Xiandong Zhou, Kefu Huang, and Zheng Li. Geometrically nonlinear beam analysis of composite wind turbine blades based on quadrature element method. *International Journal of Non-Linear Mechanics*, 104(November 2017):87–99, 2018. ISSN 00207462. doi:10.1016/j.ijnonlinmec.2018.05.007. URL `https://doi.org/10.1016/j.ijnonlinmec.2018.05.007`.

Publications Included in this Dissertation

In the following an overview of the publications, that are included in this cumulative dissertation, is given:

Publication I, found in Section: 2.7

Marten, D., Lennie, M., Pechlivanoglou, G., Nayeri, C. N., & Paschereit, C. O. (2015). Implementation, Optimization, and Validation of a Nonlinear Lifting Line-Free Vortex Wake Module Within the Wind Turbine Simulation Code QBlade. Journal of Engineering for Gas Turbines and Power, 138(7), 072601. publishers version. `https://doi.org/10.1115/1.4031872`

Publication II, found in Section: 3.1

Balduzzi, F., Marten, D., Bianchini, A., Drofelnik, J., Ferrari, L., Campobasso, M. S.,Pechlivanoglou, G., Nayeri, C. N., Ferrara, G. & Paschereit, C. O. (2017). Three-Dimensional Aerodynamic Analysis of a Darrieus Wind Turbine Blade Using Computational Fluid Dynamics and Lifting Line Theory. Journal of Engineering for Gas Turbines and Power, 140(2), 022602. publishers version. `https://doi.org/10.1115/1.4037750`

Publication III, found in Section: 3.2

Marten, D., Lennie, M., Pechlivanoglou, G., Paschereit, C. O., Bianchini, A., Ferrara, G., & Ferrari, L. (2018). Benchmark of a Novel Aero-Elastic Simulation Code for Small Scale VAWT Analysis. Journal of Engineering for Gas Turbines and Power, 141(4), 041014. publishers version. `https://doi.org/10.1115/1.4041519`

Publication IV, found in Section: 3.3

Marten, D., Paschereit, C. O., Huang, X., Meinke, M. H., Schroeder, W., Mueller, J., & Oberleithner, K. (2020). Predicting Wind Turbine Wake Breakdown Using a Free Vortex Wake Code. AIAA Journal, Article in Advance. publishers version. `https://doi.org/10.2514/1.J058308`

Publications Associated with this Dissertation

First Author

Marten, D., Paschereit, C. O., Huang, X., Meinke, M. H., Schroeder, W., Mueller, J., & Oberleithner, K. (2019). Predicting Wind Turbine Wake Breakdown Using a Free Vortex Wake Code. AIAA Scitech 2019, (January), 1–16. https://doi.org/10.2514/6.2019-2080

Marten, D., Bartholomay, S., Pechlivanoglou, G., Nayeri, C., Paschereit, C. O., Fischer, A., & Lutz, T. (2018). Numerical and Experimental Investigation of Trailing Edge Flap Performance on a Model Wind Turbine. AIAA SciTech Forum, 2018 Wind Energy Symposium, (January), 1–14. https://doi.org/10.2514/6.2018-1246

Marten, D., Lennie, M., Pechlivanoglou, G., Paschereit, C. O., Dy, N. V., Paraschivoiu, I., & Saeed, F. (2017). Validation and comparison of a newly developed aeroelastic design code for VAWT. AIAA SciTech Forum. https://doi.org/10.2514/6.2017-0452

Marten, D., Pechlivanoglou, G., Navid Nayeri, C., & Paschereit, C. O. (2017). Nonlinear Lifting Line Theory Applied to Vertical Axis Wind Turbines: Development of a Practical Design Tool. Journal of Fluids Engineering, 140(2), 021107. https://doi.org/10.1115/1.4037978

Marten, D., Bianchini, A., Balduzzi, F., Ferrara, G., Paschereit, C. O., & Ferrari, L. (2017). Effects of Airfoil's Polar Data in the Stall Region on the Estimation of Darrieus Wind Turbine Performance. Proceedings of ASME Turbo Expo 2016: Turbomachinery Technical Conference and Exposition, 1–11.

Marten, D., Bianchini, A., Pechlivanoglou, G., Balduzzi, F., Nayeri, C. N., Ferrara, G., . . . Ferrari, L. (2016). Effects of Airfoil's Polar Data in the Stall Region on the Estimation of Darrieus Wind Turbine Performance. Journal of Engineering for Gas Turbines and Power, 139(2), 022606. https://doi.org/10.1115/1.4034326

Marten, D. (2016). QBlade v0.95 Guidelines for Lifting Line Free Vortex Wake Simulations. https://doi.org/10.13140/RG.2.1.1663.1929

Marten, D., Spiegelberg, H., Pechlivanoglou, G., Nayeri, C., Paschereit, C. O., & Tropea, C. D. (2015). Configuration and Numerical Investigation of the Adaptive Camber Airfoil as Passive Load Alleviation Mechanism for Wind Turbines. 33rd AIAA Applied Aerodynamics Conference, (June), 1–9. https://doi.org/10.2514/6.2015-3390

Marten, D. (2015). QBlade v0.9 Guidelines.

Marten, D., Pechlivanoglou, G., Nayeri, C. N., & Paschereit, C. O. (2015). Integration of an unsteady nonlinear lifting line free wake algorithm in a wind turbine design framework. EAWE, (November). https://doi.org/10.13140/RG.2.1.4041.3528

Marten, D. (2014). QBlade Short Manual v0.8. https://doi.org/10.13140/RG.2.1.4015.0241

Marten, D., Wendler, J., Pechlivanoglou, G., Nayeri, C. N., & Paschereit, C. O. (2013). QBlade

: An Open Source Tool For Design And Simulation Of Horizontal And Vertical Axis Wind Turbines. IJETAE, 3(3), 264–269.

Marten, D., & Wendler, J. (2013). QBlade Guidelines - v0.6. https://doi.org/10.13140/RG.2.1.3819.8882

Marten, D., Pechlivanoglou, G., Nayeri, C. N., & Paschereit, C. O. (2013). QBlade : OpenSource Horizontal and Vertical Axis Wind Turbine Design and Simulation. Renewable Energy 2030 - Experts' Visions -.

Marten, D., & Pechlivanoglou, G. (2010). Integration of a WT Blade Design tool in XFOIL/XFLR5. Proceedings of the DEWEK, (April 2015), 1–4.

Co Author

Lennie, M., Dominin, S., **Marten, D.**, Pechlivanoglou, G., & Paschereit, C. O. (2019). Development of Ice Throw Model for Wind Turbine Simulation Software QBlade. AIAA Scitech 2019 Forum, (January), 1–13. https://doi.org/10.2514/6.2019-1800

Bartholomay, S., **Marten, D.**, Martinez, M. S., Alber, J., Pechlivanoglou, G., Nayeri, C. N., . . . Kraemer, E. (2018). Cross-Talk Compensation for Blade Root Flap- and Edgewise Moments on an Experimental Research Wind Turbine and Comparison to Numerical Resulrs. ASME Turbo Expo 2018, 1–11.

Bianchini, A., **Marten, D.**, Tonini, A., Balduzzi, F., Nayeri, C. N., Ferrara, G., & Paschereit, C. O. (2018). Implementation of the "virtual Camber" Transformation into the Open Source Software QBlade: Validation and Assessment. Energy Procedia, 148(Ati), 210–217. https://doi.org/10.1016/j.egypro.2018.08.070

Klein, A. C., Bartholomay, S., **Marten, D.**, Lutz, T., Pechlivanoglou, G., Nayeri, C. N., . . . Krämer, E. (2018). About the suitability of different numerical methods to reproduce model wind turbine measurements in a wind tunnel with a high blockage ratio. Wind Energy Science, 3(1), 439–460. https://doi.org/10.5194/wes-3-439-2018

Perez-becker, S., Saverin, J., **Marten, D.**, Pechlivanoglou, G. & Paschereit, C. O., (2018). Investigations on the Fatigue Load Reduction Potential of Advanced Control Strategies for Multi-MW Wind Turbines Using a Free Vortex Wake Model. Proceedings of ASME Turbo Expo 2018 Turbomachinery Technical Conference and Exposition, 1–11.

Saverin, J. R., **Marten, D.**, Nayeri, C., Pechlivanoglou, G., & Paschereit, C. O. (2018). Multilevel Simulation of Aerodynamic Singularity Elements. AIAA SciTech Forum 8–12, (January), 1–25. https://doi.org/10.2514/6.2018-0254

Saverin, J., **Marten, D.**, Pechlivanoglou, G., & Oliver Paschereit, C. (2018). Advanced Medium-Order Modelling of a Wind Turbine Wake with a Vortex Particle Method Integrated within a Multilevel Code. Journal of Physics: Conference Series, 1037(6). https://doi.org/10.1088/1742-6596/1037/6/062029

Saverin, J., **Marten, D.**, Pechlivanoglou, G., Paschereit, C. O., & Garrel, A. van. (2018). Implementation of the Multi-Level Multi-Integration Cluster Method to the Treatment of

Vortex Particle Interactions for Fast Wind Turbine Wake Simulations. ASME Turbo Expo 2018: Turbomachinery Technical Conference and Exposition.

Saverin, J., **Marten, D.**, Pechlivanoglou, G., Paschereit, C. O., Persico, G., & Dossena, V. (2018). Advanced Medium-Order Modelling for the Prediction of the Three-Dimensional Wake Shed by a Vertical Axis Wind Turbine. Proceedings of ASME Turbo Expo 2018 Turbomachinery Technical Conference and Exposition, V009T48A012. https://doi.org/10.1115/gt2018-76575

Saverin, J., **Marten, D.**, Pechlivanoglou, G., Nayeri, C. N., & Paschereit, C. O. (2017). Coupling of an Unsteady Lifting Line Free Vortex Wake Code to the Aeroelastic HAWT Simulation Suite FAST. Proceedings of ASME Turbo Expo 2016: Turbomachinery Technical Conference and Exposition, 1–10.

Saverin, J., **Marten, D.**, Holst, D., Pechlivanoglou, G., Paschereit, C. O., Persico, G., & Dossena, V. (2017). Comparison of Experimental and Numerically Predicted Three-Dimensional Wake Behaviour of a Vertical Axis Wind Turbine. Volume 9: Oil and Gas Applications; Supercritical CO2 Power Cycles; Wind Energy, 140(December 2018), V009T49A009. https://doi.org/10.1115/GT2017-64004

Lennie, M., Pechlivanoglou, G., **Marten, D.**, Nayeri, C. N., & Paschereit, O. (2016). A Review of Wind Turbine Polar Data and its Effect on Fatigue Load Simulation Accuracy. Proceedings of ASME Turbo Expo 2015: Turbine Technical Conference and Exposition, 1–13.

Lennie, M., **Marten, D.**, Pechlivanoglou, G., Nayeri, C. N., & Paschereit, C. O. (2016). Modern methods for investigating the stability of a pitching floating platform wind turbine. Journal of Physics: Conference Series, 753(8). https://doi.org/10.1088/1742-6596/753/8/082012

Lennie, M., **Marten, D.**, Pechlivanoglou, G., Nayeri, C. N., & Paschereit, C. O. (2016). Modern methods for investigating the stability of a pitching floating platform wind turbine. Wind Energy Science, 753(8), 671–683. https://doi.org/10.1088/1742-6596/753/8/082012

Lennie, M., **Marten, D.**, Pechlivanoglou, G., Nayeri, C. N., & Paschereit, C. O. (2016). Development and Validation of a Modal Analysis Code for Wind Turbine Blades. Proceedings of ASME Turbo Expo 2014: Turbine Technical Conference and Exposition, 1–10.

Saab, J. Y., Piquera, J. R. C., Pimenta, M., & **Marten, D.** (2016). Verification and Validation of the Airfoil Trailing-Edge Noise Prediction Module (PNoise). Technical Report, USP - TU Berlin

Saverin, J., Peukert, J., **Marten, D.**, Pechlivanoglou, G., Paschereit, C. O., & Greenblatt, D. (2016). Aeroelastic simulation of multi-MW wind turbines using a free vortex model coupled to a geometrically exact beam model. Journal of Physics: Conference Series, 753(8). https://doi.org/10.1088/1742-6596/753/8/082015

Wendler, J., **Marten, D.**, Pechlivanoglou, G., Nayeri, C. N., & Paschereit, C. O. (2016). An Unsteady Aerodynamics Model for Lifting Line Free Vortex Wake Simulations of HAWT and VAWT in QBlade. Proceedings of ASME Turbo Expo 2016: Turbomachinery Technical Conference and Exposition. Seoul, South Korea.

Niether, S., Bobusch, B., **Marten, D.**, Pechlivanoglou, G., Navid Nayeri, C., & Oliver Paschereit, C. (2015). Development of a Fluidic Actuator for Adaptive Flow Control on a Thick Wind Turbine Airfoil. Journal of Turbomachinery, 137(6), 061003. https://doi.org/10.1115/1.4028654

Vey, S., **Marten, D.**, Pechlivanoglou, G., Nayeri, C., & Paschereit, C. O. (2015). Experimental and Numerical Investigations of a Small Research Wind Turbine. In AIAA Aviation. 33rd AIAA Applied Aerodynamics Conference. https://doi.org/doi:10.2514/6.2015-3392

Chapter A | Appendix

A.1. Source Code of the Open-CL Biot-Savart Kernel

Listing A.1: The Biot-Savart Vortex Filament OpenCL Kernel

```
__kernel void biot_savart(__global float4 *Positions, __global float4 *Vort1,
__global float4 *Vort2, __global float4 *Velocities, __global int *elems, __global int *pos,
__local float4* localVort1, __local float4* localVort2) {

    unsigned int tid = get_local_id(0);
    unsigned int gid = get_global_id(0);
    unsigned int localSize = get_local_size(0);
    unsigned int globalSize = get_global_size(0);
    if (gid > *pos-1) gid = 0;
    unsigned int numTilesVortices = *elems / localSize + 1;
    float4 position = Positions[gid];
    float4 acc = (float4)(0.0,0.0,0.0,0.0);
    for(int i=0;i<numTilesVortices;++i)
    {
        int idx = i * localSize + tid;
        if (idx > *elems-1){
            localVort1[tid] = (float4)(1.0,2.0,3.0,10.0);
            localVort2[tid] = (float4)(1.0,2.0,3.0,0.0);}
        else{
            localVort1[tid] = Vort1[idx];
            localVort2[tid] = Vort2[idx];}
        float4 acc_aux = (float4)(0.0,0.0,0.0,0.0);
        barrier(CLK_LOCAL_MEM_FENCE);
        for (int j = 0; j < localSize; ++j)
        {
            float4 r1 = position-localVort1[j];
            float4 r2 = position-localVort2[j];
            r1.w = 0;
            r2.w = 0;
            float r1abs = length(r1);
            float r2abs = length(r2);
            float r1r2 = r1abs*r2abs;
            float mag = localVort2[j].w/4.0/3.14159*(r1abs + r2abs)/(r1r2*(r1r2+dot(r1, r2))+localVort1[j].w);
            if (!isnan(mag) && !isinf(mag)) acc_aux += cross(r1,r2) * mag;
        }
        acc += acc_aux;
        barrier(CLK_LOCAL_MEM_FENCE);
    }
    Velocities[gid] =  acc;
};
```

A.2. Structural Input Files for the NREL5MW Offshore turbine

Listing A.2: NREL 5MW Offshore Main Input File

```
---------------------- QBLADE STRUCTURAL MODEL INPUT FILE -----------------
NREL 5MW Turbine
------------------------------- CHRONO PARAMETERS -------------------------
0.2                 GLBGEOEPS   - Global geometry epsilon for node placement
9.80665             GRAVITY     - gravity constant

------------------------------- HAWT TURBINE CONFIGURATION ----------------
2.5                 PRECONE     - Rotor PreCone (deg) (HAWT only)
5                   SHFTTILT    - Turbine Shaft Tilt (deg) (HAWT only)
5.0191              OVERHANG    - Rotor Overhang (m) (HAWT only)
1.96256             TWR2SHFT    - Tower to Shaft distance (m) (HAWT only)

------------------------------- MASS AND INERTIA --------------------------
0.0                 YAWBRMASS   - Yaw Bearing Mass (kg) (HAWT only)
240000              NACMASS     - Nacelle Mass (kg) (HAWT only)
1.9                 NACCMX      - Downwind distance from the tower-top to the nacelle CM (m) (HAWT only)
0.0                 NACCMY      - Lateral  distance from the tower-top to the nacelle CM (m) (HAWT only)
1.75                NACCMZ      - Vertical distance from the tower-top to the nacelle CM (m) (HAWT only)
2607890             NACYINER    - Nacelle Yaw Inertia (kg*m^2) (HAWT only)
56780               HUBMASS     - Hub Mass (kg)
115926              HUBINER     - Hub Inertia (kg*m^2)

------------------------------- DRIVETRAIN MODEL --------------------------
97                  GBRATIO     - gearbox ratio (N)
1.0                 GBOXEFF     - gearbox efficiency (0-1)
true                DRTRDOF     - model drivetrain dynamics (true / false)
534.116             GENINER     - Generator side (HSS) Inertia (kg*m^2)
867637000           DTTORSPR    - Drivetrain torsional stiffness (N*m/rad)
6215000             DTTORDMP    - Drivetrain torsional damping (N*m*s/rad)

------------------------------- BRAKE MODEL -------------------------------
0                   BRKTORQUE   - maximum brake torque
0                   BRKDEPLOY   - brake deploy time (s) (only used with DTU style controllers)
0                   BRKDELAY    - brake delay time (s) (only used with DTU style controllers)

------------------------------- SENSOR ERRORS -----------------------------
0                   ERRORYAW        - yaw error (deg) (HAWT only)
0                   ERRORPITCH_1    - pitch error blade1 (deg)
0                   ERRORPITCH_2    - pitch error blade2 (deg)
0                   ERRORPITCH_3    - pitch error blade3 (deg)

------------------------------- BLADES ------------------------------------
3                   NUMBLD      - Number of blades
bladefileNREL.dat   BLDFILE_1   - Name of file containing properties for blade 1
bladefileNREL.dat   BLDFILE_2   - Name of file containing properties for blade 2
bladefileNREL.dat   BLDFILE_3   - Name of file containing properties for blade 3
20                  BLDDISC     - Number of structural nodes per blade

------------------------------- TOWER -------------------------------------
87.6                TWRHEIGHT   - Height of the tower (m)
towerfileNREL.dat   TWRFILE     - Name of file containing properties for the tower
20                  TWRDISC     - Number of structural nodes for the tower

------------------------------- DATA OUTPUT TYPES -------------------------
true                FOR_OUT - store (local) forces at all chosen locations
true                ROT_OUT - store (local) body rotations at all chosen locations
true                MOM_OUT - store (local) moments at all chosen locations
true                DEF_OUT - store (local) deflections at all chosen locations
true                POS_OUT - store (global) positions at all chosen locations
true                VEL_OUT - store (global) velocities at all chosen locations
true                ACC_OUT - store (global) accelerations at all chosen locations
true                LVE_OUT - store (local) velocities at all chosen locations
true                LAC_OUT - store (local) accelerations at all chosen locations


------------------------------- DATA OUTPUT LOCATIONS ---------------------
any number, or zero, user defined positions can be chosen as output locations.
locations can be assigned at any of the following components:
blades, struts, tower and guy cables.

See the following examples for the used nomenclature:

BLD_1_1.00       - exemplary position, blade 1 at 100% normalized radius
BLD_1_0.50       - exemplary position, blade 1 at  50% normalized radius
BLD_1_0.00       - exemplary position, blade 1 at  00% normalized radius
TWR_1.00         - exemplary position, tower at 100% normalized height
TWR_0.50         - exemplary position, tower at  50% normalized height
TWR_0.00         - exemplary position, tower at   0% normalized height
```

Listing A.3: NREL 5MW Blade Input File

```
0.0024  RAYLEIGHDMP
1.00    STIFFTUNER
1.00    MASSTUNER
        ADDMASS_0.00_0.00 - add a point mass at position 0.00 with 0.00kg mass
        ADDMASS_1.00_0.00 - add a point mass at position 1.00 with 0.00kg mass

LENGTH  BMASSD   FLAP      EDGE      GJ        EA        RGX     RGY     RGZ     XCM     YCM     STRPI   XCE     YCE     XCS     YCS     KX      KY      CHORD
0.00000 715.0200 1.812E+10 1.812E+10 5.560E+09 9.730E+09 0.32931 0.32936 0.79854 -0.0001 0.00000 0.00000 0.00000 0.00000 0.00000 0.00000 0.50000 0.50000 3.54200
0.00325 715.0200 1.812E+10 1.812E+10 5.560E+09 9.730E+09 0.32931 0.32936 0.79854 -0.0001 0.00000 0.00000 0.00000 0.00000 0.00000 0.00000 0.50000 0.50000 3.54200
0.01951 814.4600 1.942E+10 1.956E+10 5.430E+09 1.079E+10 0.32685 0.32307 0.74939 0.00701 0.00000 0.00000 0.00000 0.00000 0.00000 0.00000 0.50000 0.50000 3.54200
0.03577 779.9100 1.746E+10 1.950E+10 4.990E+09 1.007E+10 0.30601 0.31861 0.72427 0.00389 0.00000 0.00000 0.00550 0.00000 0.00550 0.00000 0.50000 0.50000 3.63710
0.05203 779.3700 1.529E+10 1.978E+10 4.670E+09 9.867E+09 0.28228 0.31667 0.68620 0.00547 0.00000 0.00000 0.01599 0.00000 0.01599 0.00000 0.50000 0.50000 3.75126
0.06829 623.9900 1.078E+10 1.485E+10 3.470E+09 7.608E+09 0.26375 0.30599 0.65374 0.01416 0.00000 0.00000 0.02846 0.00000 0.02846 0.00000 0.50000 0.50000 3.86545
0.08455 474.2100 7.230E+09 1.022E+10 2.320E+09 5.491E+09 0.24658 0.29224 0.61110 0.02535 0.00000 0.00000 0.04020 0.00000 0.04020 0.00000 0.50000 0.50000 3.97998
0.10081 446.5900 6.310E+09 9.145E+09 1.910E+09 4.971E+09 0.23129 0.28160 0.56642 0.03507 0.00000 0.00000 0.05129 0.00000 0.05129 0.00000 0.50000 0.50000 4.09450
0.11707 421.9300 5.529E+09 8.063E+09 1.570E+09 4.494E+09 0.21690 0.27057 0.52545 0.04628 0.00000 0.00000 0.06415 0.00000 0.06415 0.00000 0.50000 0.50000 4.20889
0.13333 402.3700 4.980E+09 6.884E+09 1.160E+09 4.035E+09 0.20504 0.25549 0.46408 0.05535 0.00000 0.00000 0.07634 0.00000 0.07634 0.00000 0.50000 0.50000 4.32302
0.14959 420.9000 4.936E+09 7.010E+09 1.000E+09 4.038E+09 0.19141 0.24658 0.41966 0.06722 0.00000 0.00000 0.08789 0.00000 0.08789 0.00000 0.50000 0.50000 4.43716
0.16585 448.9800 4.691E+09 7.168E+09 8.560E+08 4.169E+09 0.17635 0.24202 0.37251 0.06824 0.00000 0.00000 0.10107 0.00000 0.10107 0.00000 0.50000 0.50000 4.55129
0.18211 438.9700 3.949E+09 7.272E+09 6.720E+08 4.082E+09 0.16368 0.24883 0.33153 0.06696 0.00000 0.00000 0.11356 0.00000 0.11356 0.00000 0.50000 0.50000 4.57901
0.19837 427.7700 3.387E+09 7.081E+09 5.470E+08 4.087E+09 0.15436 0.25762 0.29745 0.05871 0.00000 0.00000 0.12168 0.00000 0.12168 0.00000 0.50000 0.50000 4.60218
0.21463 401.6900 2.934E+09 6.244E+09 4.490E+08 3.668E+09 0.14756 0.25220 0.28303 0.05978 0.00000 0.00000 0.12323 0.00000 0.12323 0.00000 0.50000 0.50000 4.62535
0.23089 371.5700 2.569E+09 5.048E+09 3.360E+08 3.147E+09 0.14153 0.24160 0.26300 0.06804 0.00000 0.00000 0.12262 0.00000 0.12262 0.00000 0.50000 0.50000 4.64852
0.24715 368.0500 2.388E+09 4.949E+09 3.110E+08 3.011E+09 0.13776 0.24075 0.26073 0.06944 0.00000 0.00000 0.12360 0.00000 0.12360 0.00000 0.50000 0.50000 4.61178
0.26341 364.9600 2.272E+09 4.808E+09 2.920E+08 2.883E+09 0.13583 0.23952 0.26090 0.07096 0.00000 0.00000 0.12269 0.00000 0.12269 0.00000 0.50000 0.50000 4.56446
0.29593 357.3700 2.050E+09 4.501E+09 2.610E+08 2.614E+09 0.13211 0.23616 0.26452 0.07323 0.00000 0.00000 0.12305 0.00000 0.12305 0.00000 0.50000 0.50000 4.46983
0.32846 347.5400 1.828E+09 4.243E+09 2.290E+08 2.358E+09 0.12843 0.23363 0.26692 0.07842 0.00000 0.00000 0.12360 0.00000 0.12360 0.00000 0.50000 0.50000 4.36879
0.36098 339.1000 1.589E+09 3.996E+09 2.010E+08 2.146E+09 0.12363 0.23296 0.26836 0.07832 0.00000 0.00000 0.12421 0.00000 0.12421 0.00000 0.50000 0.50000 4.26684
0.39350 330.5000 1.362E+09 3.751E+09 1.740E+08 1.945E+09 0.11868 0.23275 0.26959 0.07856 0.00000 0.00000 0.12284 0.00000 0.12284 0.00000 0.50000 0.50000 4.15161
0.42602 310.4000 1.102E+09 3.447E+09 1.440E+08 1.632E+09 0.11139 0.22858 0.27551 0.08786 0.00000 0.00000 0.12396 0.00000 0.12396 0.00000 0.50000 0.50000 4.03356
0.45854 302.3800 8.758E+08 3.139E+09 1.200E+08 1.432E+09 0.10343 0.22650 0.27706 0.08557 0.00000 0.00000 0.12279 0.00000 0.12279 0.00000 0.50000 0.50000 3.90909
0.49106 277.3400 6.812E+08 2.734E+09 8.120E+07 1.169E+09 0.09699 0.22246 0.26072 0.08995 0.00000 0.00000 0.12425 0.00000 0.12425 0.00000 0.50000 0.50000 3.78274
0.52358 266.6600 5.347E+08 2.555E+09 6.910E+07 1.047E+09 0.09030 0.22464 0.26250 0.08860 0.00000 0.00000 0.12292 0.00000 0.12292 0.00000 0.50000 0.50000 3.66100
0.55610 254.5100 4.089E+08 2.334E+09 5.750E+07 9.230E+08 0.08334 0.22561 0.26373 0.08536 0.00000 0.00000 0.12426 0.00000 0.12426 0.00000 0.50000 0.50000 3.54100
0.58862 232.3600 3.146E+08 1.828E+09 4.590E+07 7.608E+08 0.07983 0.22268 0.26865 0.08422 0.00000 0.00000 0.12569 0.00000 0.12569 0.00000 0.50000 0.50000 3.42100
0.62114 210.9400 2.387E+08 1.585E+09 3.600E+07 6.481E+08 0.07607 0.22493 0.26715 0.07915 0.00000 0.00000 0.12420 0.00000 0.12420 0.00000 0.50000 0.50000 3.30100
0.65366 188.9400 1.758E+08 1.323E+09 2.740E+07 5.397E+08 0.07218 0.22638 0.26503 0.07025 0.00000 0.00000 0.12575 0.00000 0.12575 0.00000 0.50000 0.50000 3.18100
0.68618 173.8700 1.260E+08 1.184E+09 2.090E+07 5.312E+08 0.06694 0.24642 0.24247 0.04358 0.00000 0.00000 0.12414 0.00000 0.12414 0.00000 0.50000 0.50000 3.06100
0.71870 162.6200 1.073E+08 1.020E+09 1.850E+07 4.600E+08 0.06651 0.24696 0.25513 0.03652 0.00000 0.00000 0.12581 0.00000 0.12581 0.00000 0.50000 0.50000 2.94100
0.75122 146.3200 9.087E+07 7.979E+08 1.630E+07 3.758E+08 0.06675 0.24513 0.27625 0.04505 0.00000 0.00000 0.12407 0.00000 0.12407 0.00000 0.50000 0.50000 2.82100
0.78374 136.4400 7.631E+07 7.097E+08 1.450E+07 3.289E+08 0.06620 0.24839 0.29088 0.04060 0.00000 0.00000 0.12588 0.00000 0.12588 0.00000 0.50000 0.50000 2.70100
0.81626 112.9600 6.105E+07 5.181E+08 9.070E+06 2.440E+08 0.06683 0.24572 0.27949 0.04518 0.00000 0.00000 0.12398 0.00000 0.12398 0.00000 0.50000 0.50000 2.58100
0.84878 104.0300 4.948E+07 4.549E+08 8.060E+06 2.115E+08 0.06607 0.25059 0.29677 0.03708 0.00000 0.00000 0.12596 0.00000 0.12596 0.00000 0.50000 0.50000 2.46101
0.88130 95.04400 3.935E+07 3.951E+08 7.080E+06 1.816E+08 0.06514 0.25583 0.31560 0.02786 0.00000 0.00000 0.12388 0.00000 0.12388 0.00000 0.50000 0.50000 2.34102
0.89756 87.41200 3.466E+07 3.538E+08 6.090E+06 1.603E+08 0.06550 0.25874 0.32146 0.02351 0.00000 0.00000 0.12342 0.00000 0.12342 0.00000 0.50000 0.50000 2.26873
0.91382 76.78100 3.041E+07 3.048E+08 5.750E+06 1.092E+08 0.06790 0.23439 0.39278 0.05827 0.00000 0.00000 0.12811 0.00000 0.12811 0.00000 0.50000 0.50000 2.18567
0.93008 72.42700 2.652E+07 2.814E+08 5.330E+06 1.001E+08 0.06820 0.24056 0.41066 0.05244 0.00000 0.00000 0.12366 0.00000 0.12366 0.00000 0.50000 0.50000 2.10261
0.93821 69.78600 2.384E+07 2.617E+08 4.940E+06 9.225E+07 0.06886 0.24603 0.43019 0.05050 0.00000 0.00000 0.12917 0.00000 0.12917 0.00000 0.50000 0.50000 2.01278
0.94634 62.49400 1.963E+07 1.588E+08 4.240E+06 6.322E+07 0.07018 0.22737 0.51247 0.07897 0.00000 0.00000 0.12693 0.00000 0.12693 0.00000 0.50000 0.50000 1.89076
0.95447 58.88600 1.600E+07 1.379E+08 3.660E+06 5.333E+07 0.06948 0.23028 0.55421 0.07889 0.00000 0.00000 0.13004 0.00000 0.13004 0.00000 0.50000 0.50000 1.76873
0.96260 55.27300 1.283E+07 1.188E+08 3.130E+06 4.453E+07 0.06880 0.23374 0.60239 0.07740 0.00000 0.00000 0.12753 0.00000 0.12753 0.00000 0.50000 0.50000 1.64670
0.97073 51.72400 1.008E+07 1.016E+08 2.640E+06 3.690E+07 0.06828 0.23815 0.65637 0.07490 0.00000 0.00000 0.12462 0.00000 0.12462 0.00000 0.50000 0.50000 1.52468
0.97886 48.25300 7.550E+06 8.506E+07 2.170E+06 2.992E+07 0.06681 0.24331 0.72156 0.07425 0.00000 0.00000 0.12173 0.00000 0.12173 0.00000 0.50000 0.50000 1.39655
0.98699 43.88400 4.600E+06 6.426E+07 1.580E+06 2.131E+07 0.06143 0.24597 0.82901 0.08110 0.00000 0.00000 0.12205 0.00000 0.12205 0.00000 0.50000 0.50000 1.22903
0.99512 12.06200 2.500E+05 6.609E+06 2.500E+05 4.850E+06 0.05426 0.26302 0.80031 0.07434 0.00000 0.00000 0.12247 0.00000 0.12247 0.00000 0.50000 0.50000 1.06151
1.00000 10.86700 1.700E+05 5.011E+06 1.900E+05 3.529E+06 0.04464 0.26025 0.90337 0.07110 0.00000 0.00000 0.12487 0.00000 0.12487 0.00000 0.50000 0.50000 0.96100
```

Listing A.4: NREL 5MW Tower Input File

```
0.01    RAYLEIGHDMP
1.0     STIFFTUNER
1.0     MASSTUNER
0.0     ADDMASS_0.0_0.0 - add a point mass at relative position 0.0 with 0.0kg mass
0.0     ADDMASS_1.0_0.0 - add a point mass at relative position 1.0 with 0.0kg mass

LENGTH  BMASSD     FLAP      EDGE      GJ        EA        RGX     RGY     RGZ     XCM     YCM     STRPI   XCE     YCE     XCS     YCS     KX      KY      CHORD
0.00000 5590.87000 6.153E+11 6.153E+11 4.727E+11 1.382E+11 0.35167 0.35167 0.49695 0.00000 0.00000 0.00000 0.00000 0.00000 0.00000 0.00000 0.50000 0.50000 6.00000
0.10000 5232.43000 5.355E+11 5.355E+11 4.113E+11 1.294E+11 0.35079 0.35079 0.49672 0.00000 0.00000 0.00000 0.00000 0.00000 0.00000 0.00000 0.50000 0.50000 5.78700
0.20000 4885.76000 4.641E+11 4.641E+11 3.563E+11 1.207E+11 0.35163 0.35163 0.49684 0.00000 0.00000 0.00000 0.00000 0.00000 0.00000 0.00000 0.50000 0.50000 5.57400
0.30000 4550.87000 3.990E+11 3.990E+11 3.070E+11 1.124E+11 0.35068 0.35068 0.49713 0.00000 0.00000 0.00000 0.00000 0.00000 0.00000 0.00000 0.50000 0.50000 5.36100
0.40000 4227.75000 3.423E+11 3.423E+11 2.634E+11 1.044E+11 0.35159 0.35159 0.49750 0.00000 0.00000 0.00000 0.00000 0.00000 0.00000 0.00000 0.50000 0.50000 5.14800
0.50000 3916.41000 2.919E+11 2.919E+11 2.238E+11 9.681E+10 0.35056 0.35056 0.49671 0.00000 0.00000 0.00000 0.00000 0.00000 0.00000 0.00000 0.50000 0.50000 4.93500
0.60000 3616.83000 2.457E+11 2.457E+11 1.891E+11 8.946E+10 0.35155 0.35155 0.49634 0.00000 0.00000 0.00000 0.00000 0.00000 0.00000 0.00000 0.50000 0.50000 4.72200
0.70000 3329.03000 2.064E+11 2.064E+11 1.592E+11 8.232E+10 0.35041 0.35041 0.49718 0.00000 0.00000 0.00000 0.00000 0.00000 0.00000 0.00000 0.50000 0.50000 4.50900
0.80000 3053.01000 1.718E+11 1.718E+11 1.325E+11 7.539E+10 0.35149 0.35149 0.49752 0.00000 0.00000 0.00000 0.00000 0.00000 0.00000 0.00000 0.50000 0.50000 4.29600
0.90000 2788.75000 1.418E+11 1.418E+11 1.091E+11 6.888E+10 0.35023 0.35023 0.49688 0.00000 0.00000 0.00000 0.00000 0.00000 0.00000 0.00000 0.50000 0.50000 4.08300
1.00000 2536.27000 1.159E+11 1.159E+11 8.888E+10 6.258E+10 0.35142 0.35142 0.49645 0.00000 0.00000 0.00000 0.00000 0.00000 0.00000 0.00000 0.50000 0.50000 3.87000
```

A.3. Structural Input Files for the SANDIA 34m turbine

Listing A.5: SANDIA 34m Main Input File

```
---------------------- QBLADE STRUCTURAL MODEL INPUT FILE -----------------
SANDIA 34m wind turbine
------------------------------- CHRONO PARAMETERS -------------------------
0.2                 GLBGEOEPS   - Global geometry epsilon for node placement
9.80665             GRAVITY     - gravity constant

------------------------------- MASS AND INERTIA --------------------------
0                   HUBMASS     - Hub Mass (kg)
0                   HUBINER     - Hub Inertia (kg*m^2)

------------------------------- DRIVETRAIN MODEL --------------------------
1                   GBRATIO     - gearbox ratio (N)
1                   GBOXEFF     - gearbox efficiency (0-1)
false               DRTRDOF     - model drivetrain dynamics (true / false)
0                   GENINER     - Generator side (HSS) Inertia (kg*m^2)
0                   DTTORSPR    - Drivetrain torsional stiffness (N*m/rad)
0                   DTTORDMP    - Drivetrain torsional damping (N*m*s/rad)

------------------------------- BRAKE MODEL -------------------------------
0                   BRKTORQUE   - maximum brake torque (s)
0                   BRKDEPLOY   - brake deploy time (s) (only used with DTU style controllers)
0                   BRKDELAY    - brake delay time (s) (only used with DTU style controllers)

------------------------------- BLADES ------------------------------------
2                   NUMBLD          - Number of blades
bladeSAND34.dat     BLDFILE_1       - Name of file containing properties for blade 1
bladeSAND34.dat     BLDFILE_2       - Name of file containing properties for blade 2
bladeSAND34.dat     BLDFILE_3       - Name of file containing properties for blade 2
21                  BLDDISC         - Number of structural nodes per blade
0                   ERRORPITCH_1    - pitch error blade1 (deg)
0                   ERRORPITCH_2    - pitch error blade2 (deg)
0                   ERRORPITCH_3    - pitch error blade2 (deg)

------------------------------- STRUTS ------------------------------------
*                   STRTFILE_1  - Name of file containing properties for strut1 (if blade has struts)
*                   STRTFILE_2  - Name of file containing properties for strut2 (if blade has struts)
*                   STRTDISC    - Number of structural nodes per strut

------------------------------- TOWER AND TORQUE TUBE ---------------------
5                   TWRHEIGHT   - Height of the (fixed - non rotating) tower [m]
towerSAND34.dat     TWRFILE     - Name of file containing properties for the tower
2                   TWRDISC     - Number of structural nodes for the tower
45                  TRQTBHEIGHT - Height (or length) of the torque tube (the rotating part of the tower) [m]
trqtubeeSAND34.dat  TRQTBFILE   - Name of file containing properties for the torque tube
10                  TRQTBDISC   - Number of structural nodes for the torque tube
5                   TRQTBCLEAR  - Clearance of the torque tube, must be <= TWRHEIGHT [m]
5                   HUBPOS      - height of the generator hub, connecting torque tube to tower  [m]
unused              TRQTBCONN   - Absolute height, starting after torquetube clearance, torque tube to tower bearing [m]
7                   RTRCLEAR    - Rotor clearance
0.975               BLDCONN     - Absolute height, after rotor clearance, of a blade torque tube connection in [m]
40.853              BLDCONN     - Absolute height, after rotor clearance, of a blade torque tube connection in [m]

------------------------------- BLADE CABLES (VAWT only) ------------------
cableSAND34.dat     CABFILE - file containing the definitions of cables

------------------------------- DATA OUTPUT TYPES -------------------------
true                FOR_OUT - store (local) forces at all chosen locations
true                ROT_OUT - store (local) body rotations at all chosen locations
true                MOM_OUT - store (local) moments at all chosen locations
true                DEF_OUT - store (local) deflections at all chosen locations
true                POS_OUT - store (global) positions at all chosen locations
true                VEL_OUT - store (global) velocities at all chosen locations
true                ACC_OUT - store (global) accelerations at all chosen locations
true                LVE_OUT - store (local) velocities at all chosen locations
true                LAC_OUT - store (local) accelerations at all chosen locations

------------------------------- DATA OUTPUT LOCATIONS ---------------------
any number, or zero, user defined positions can be chosen as output locations.
locations can be assigned at any of the following components:
blades, struts, tower, torquetube and guy cables.

See the following examples for the used nomenclature:

BLD_1_1.00          - exemplary position, blade 2 at  100% normalized radius
BLD_1_0.00          - exemplary position, blade 2 at  00% normalized radius
TWR_1.00            - exemplary position, tower at  100% normalized height
TWR_0.00            - exemplary position, tower at  00% normalized height
TRQ_1.00            - exemplary position, tower at  30% normalized height
TRQ_0.00            - exemplary position, tower at  00% normalized height
CAB_1_1.00          - exemplary position, cable 1 at  50% normalized length
CAB_1_0.00          - exemplary position, cable 1 at  50% normalized length
```

Listing A.6: SANDIA 34m Blade Input File

```
NORMHEIGHT  -   Indicates that the structural properties are assigned
                based on normalized height instead of normalized length
0.0024  RAYLEIGHDMP
1.0     STIFFTUNER
1.0     MASSTUNER
0.0     ADDMASS_0.00_0.00 - add a point mass at position 0.00 with 0.00kg mass
0.0     ADDMASS_1.00_0.00 - add a point mass at position 1.00 with 0.00kg mass

LENGTH  BMASSD  FLAP       EDGE       GJ         EA         RGX     RGY     RGZ     XCM     YCM     STRPI   XCE     YCE     XCS     YCS     KX      KY
0.0000  99.3000 1.5300E+07 2.7100E+08 1.5400E+07 2.5300E+09 0.0000  0.0000  0.0000  0.0000  0.0000  0.0000  0.0000  0.0000  0.0000  0.0000  0.0000  0.0000
0.0100  99.3000 1.5300E+07 2.7100E+08 1.5400E+07 2.5300E+09 0.0000  0.0000  0.0000  0.0000  0.0000  0.0000  0.0000  0.0000  0.0000  0.0000  0.0000  0.0000
0.1300  99.3000 1.5300E+07 2.7100E+08 1.5400E+07 2.5300E+09 0.0000  0.0000  0.0000  0.0000  0.0000  0.0000  0.0000  0.0000  0.0000  0.0000  0.0000  0.0000
0.1400  57.0000 4.8800E+06 1.1400E+08 5.1300E+06 1.4500E+09 0.0000  0.0000  0.0000  0.0000  0.0000  0.0000  0.0000  0.0000  0.0000  0.0000  0.0000  0.0000
0.1600  57.0000 4.8800E+06 1.1400E+08 5.1300E+06 1.4500E+09 0.0000  0.0000  0.0000  0.0000  0.0000  0.0000  0.0000  0.0000  0.0000  0.0000  0.0000  0.0000
0.1800  57.0000 4.8800E+06 1.1400E+08 5.1300E+06 1.4500E+09 0.0000  0.0000  0.0000  0.0000  0.0000  0.0000  0.0000  0.0000  0.0000  0.0000  0.0000  0.0000
0.1900  57.0000 4.8800E+06 1.1400E+08 5.1300E+06 1.4500E+09 0.0000  0.0000  0.0000  0.0000  0.0000  0.0000  0.0000  0.0000  0.0000  0.0000  0.0000  0.0000
0.2100  57.0000 4.8800E+06 1.1400E+08 5.1300E+06 1.4500E+09 0.0000  0.0000  0.0000  0.0000  0.0000  0.0000  0.0000  0.0000  0.0000  0.0000  0.0000  0.0000
0.2300  57.0000 4.8800E+06 1.1400E+08 5.1300E+06 1.4500E+09 0.0000  0.0000  0.0000  0.0000  0.0000  0.0000  0.0000  0.0000  0.0000  0.0000  0.0000  0.0000
0.2500  57.0000 4.8800E+06 1.1400E+08 5.1300E+06 1.4500E+09 0.0000  0.0000  0.0000  0.0000  0.0000  0.0000  0.0000  0.0000  0.0000  0.0000  0.0000  0.0000
0.2600  57.0000 4.8800E+06 1.1400E+08 5.1300E+06 1.4500E+09 0.0000  0.0000  0.0000  0.0000  0.0000  0.0000  0.0000  0.0000  0.0000  0.0000  0.0000  0.0000
0.2800  45.3000 2.9100E+06 6.7600E+07 3.1800E+06 1.1600E+09 0.0000  0.0000  0.0000  0.0000  0.0000  0.0000  0.0000  0.0000  0.0000  0.0000  0.0000  0.0000
0.3000  45.3000 2.9100E+06 6.7600E+07 3.1800E+06 1.1600E+09 0.0000  0.0000  0.0000  0.0000  0.0000  0.0000  0.0000  0.0000  0.0000  0.0000  0.0000  0.0000
0.3300  45.3000 2.9100E+06 6.7600E+07 3.1800E+06 1.1600E+09 0.0000  0.0000  0.0000  0.0000  0.0000  0.0000  0.0000  0.0000  0.0000  0.0000  0.0000  0.0000
0.3500  45.3000 2.9100E+06 6.7600E+07 3.1800E+06 1.1600E+09 0.0000  0.0000  0.0000  0.0000  0.0000  0.0000  0.0000  0.0000  0.0000  0.0000  0.0000  0.0000
0.3800  45.3000 2.9100E+06 6.7600E+07 3.1800E+06 1.1600E+09 0.0000  0.0000  0.0000  0.0000  0.0000  0.0000  0.0000  0.0000  0.0000  0.0000  0.0000  0.0000
0.4100  45.3000 2.9100E+06 6.7600E+07 3.1800E+06 1.1600E+09 0.0000  0.0000  0.0000  0.0000  0.0000  0.0000  0.0000  0.0000  0.0000  0.0000  0.0000  0.0000
0.4400  45.3000 2.9100E+06 6.7600E+07 3.1800E+06 1.1600E+09 0.0000  0.0000  0.0000  0.0000  0.0000  0.0000  0.0000  0.0000  0.0000  0.0000  0.0000  0.0000
0.4600  45.3000 2.9100E+06 6.7600E+07 3.1800E+06 1.1600E+09 0.0000  0.0000  0.0000  0.0000  0.0000  0.0000  0.0000  0.0000  0.0000  0.0000  0.0000  0.0000
0.4900  45.3000 2.9100E+06 6.7600E+07 3.1800E+06 1.1600E+09 0.0000  0.0000  0.0000  0.0000  0.0000  0.0000  0.0000  0.0000  0.0000  0.0000  0.0000  0.0000
0.5200  45.3000 2.9100E+06 6.7600E+07 3.1800E+06 1.1600E+09 0.0000  0.0000  0.0000  0.0000  0.0000  0.0000  0.0000  0.0000  0.0000  0.0000  0.0000  0.0000
0.5500  45.3000 2.9100E+06 6.7600E+07 3.1800E+06 1.1600E+09 0.0000  0.0000  0.0000  0.0000  0.0000  0.0000  0.0000  0.0000  0.0000  0.0000  0.0000  0.0000
0.5700  45.3000 2.9100E+06 6.7600E+07 3.1800E+06 1.1600E+09 0.0000  0.0000  0.0000  0.0000  0.0000  0.0000  0.0000  0.0000  0.0000  0.0000  0.0000  0.0000
0.6000  45.3000 2.9100E+06 6.7600E+07 3.1800E+06 1.1600E+09 0.0000  0.0000  0.0000  0.0000  0.0000  0.0000  0.0000  0.0000  0.0000  0.0000  0.0000  0.0000
0.6300  45.3000 2.9100E+06 6.7600E+07 3.1800E+06 1.1600E+09 0.0000  0.0000  0.0000  0.0000  0.0000  0.0000  0.0000  0.0000  0.0000  0.0000  0.0000  0.0000
0.6500  45.3000 2.9100E+06 6.7600E+07 3.1800E+06 1.1600E+09 0.0000  0.0000  0.0000  0.0000  0.0000  0.0000  0.0000  0.0000  0.0000  0.0000  0.0000  0.0000
0.6800  45.3000 2.9100E+06 6.7600E+07 3.1800E+06 1.1600E+09 0.0000  0.0000  0.0000  0.0000  0.0000  0.0000  0.0000  0.0000  0.0000  0.0000  0.0000  0.0000
0.7000  57.0000 4.8800E+06 1.1400E+08 5.1300E+06 1.4500E+09 0.0000  0.0000  0.0000  0.0000  0.0000  0.0000  0.0000  0.0000  0.0000  0.0000  0.0000  0.0000
0.7100  57.0000 4.8800E+06 1.1400E+08 5.1300E+06 1.4500E+09 0.0000  0.0000  0.0000  0.0000  0.0000  0.0000  0.0000  0.0000  0.0000  0.0000  0.0000  0.0000
0.7300  57.0000 4.8800E+06 1.1400E+08 5.1300E+06 1.4500E+09 0.0000  0.0000  0.0000  0.0000  0.0000  0.0000  0.0000  0.0000  0.0000  0.0000  0.0000  0.0000
0.7500  57.0000 4.8800E+06 1.1400E+08 5.1300E+06 1.4500E+09 0.0000  0.0000  0.0000  0.0000  0.0000  0.0000  0.0000  0.0000  0.0000  0.0000  0.0000  0.0000
0.7700  57.0000 4.8800E+06 1.1400E+08 5.1300E+06 1.4500E+09 0.0000  0.0000  0.0000  0.0000  0.0000  0.0000  0.0000  0.0000  0.0000  0.0000  0.0000  0.0000
0.7900  57.0000 4.8800E+06 1.1400E+08 5.1300E+06 1.4500E+09 0.0000  0.0000  0.0000  0.0000  0.0000  0.0000  0.0000  0.0000  0.0000  0.0000  0.0000  0.0000
0.8100  57.0000 4.8800E+06 1.1400E+08 5.1300E+06 1.4500E+09 0.0000  0.0000  0.0000  0.0000  0.0000  0.0000  0.0000  0.0000  0.0000  0.0000  0.0000  0.0000
0.8200  57.0000 4.8800E+06 1.1400E+08 5.1300E+06 1.4500E+09 0.0000  0.0000  0.0000  0.0000  0.0000  0.0000  0.0000  0.0000  0.0000  0.0000  0.0000  0.0000
0.8300  99.3000 1.5300E+07 2.7100E+08 1.5400E+07 2.5300E+09 0.0000  0.0000  0.0000  0.0000  0.0000  0.0000  0.0000  0.0000  0.0000  0.0000  0.0000  0.0000
0.9900  99.3000 1.5300E+07 2.7100E+08 1.5400E+07 2.5300E+09 0.0000  0.0000  0.0000  0.0000  0.0000  0.0000  0.0000  0.0000  0.0000  0.0000  0.0000  0.0000
1.0000  99.3000 1.5300E+07 2.7100E+08 1.5400E+07 2.5300E+09 0.0000  0.0000  0.0000  0.0000  0.0000  0.0000  0.0000  0.0000  0.0000  0.0000  0.0000  0.0000
```

Listing A.7: SANDIA 34m Tower and Torque Tube Input File

```
0.01    RAYLEIGHDMP
1.0     STIFFTUNER
1.0     MASSTUNER
0.0     ADDMASS_0.00_0.00 - add a point mass at relative position 0.00 with 0.00kg mass
0.0     ADDMASS_1.00_0.00 - add a point mass at relative position 1.00 with 0.00kg mass

LENGTH  BMASSD  FLAP       EDGE       GJ         EA         RGX     RGY     RGZ     XCM     YCM     STRPI   XCE     YCE     XCS     YCS     KX      KY      DIA
0.0000  353.430 9.1600E+09 9.1600E+09 6.8000E+09 8.2100E+09 0.0000  0.0000  0.0000  0.0000  0.0000  0.0000  0.0000  0.0000  0.0000  0.0000  0.0000  0.0000  1.0000
1.0000  353.430 9.1600E+09 9.1600E+09 6.8000E+09 8.2100E+09 0.0000  0.0000  0.0000  0.0000  0.0000  0.0000  0.0000  0.0000  0.0000  0.0000  0.0000  0.0000  1.0000
```

Listing A.8: SANDIA 34m Guy Cable Input File

```
Body1   Body2                Density   Area       Iyy        Emod       Pretension Damping Diam.  Drag   nNodes Name
...     ...                  [kg/m^3]  [m^2]      [m^4]      [N/m^2]    [N]        [-]     [m]    [-]    [-]    ...
TRQ_1.0 GRD_71.4_0_0         6000.00   6.331E-03  3.190E-06  1.166E+11  8.277E+05  0.10    0.09   0.99   8      GuyCable1
TRQ_1.0 GRD_-35.7_61.83_0    6000.00   6.331E-03  3.190E-06  1.166E+11  8.277E+05  0.10    0.09   0.99   8      GuyCable2
TRQ_1.0 GRD_-35.7_-61.83_0   6000.00   6.331E-03  3.190E-06  1.166E+11  8.277E+05  0.10    0.09   0.99   8      GuyCable3
```

A.4. Exemplary Simulation Input File

Listing A.9: Exemplary Simulation Input File

```
Exemplary Simulation Input File (.sim), including blade pitch and Active Flow Control Elements (AFC)

TIME    ROT     YAW     BLA 1   BLA 2   BLA 3   BLA1    BLA1    BLA1    BLA2
        SPEED   ANGLE   PITCH   PITCH   PITCH   AFC1    AFC2    AFC3    AFC1

0.00    12.00   0.00    0.00    0.00    0.00    0.00    0.00    0.00    0.00
1.00    12.00   0.00    0.00    0.00    0.00    0.00    0.00    0.00    0.00
9.00    12.00   0.00    0.00    0.00    0.00    0.00    0.00    0.00    0.00
56.00   12.00   0.00    0.00    0.00    0.00    0.00    0.00    0.00    0.00
100.00  12.00   0.00    0.00    0.00    0.00    0.00    0.00    0.00    0.00
```

A.5. Exemplary Prescribed Motion Input File

Listing A.10: Exemplary Simulation Input File

```
Exemplary Prescribed Motion Input File (.mot)

TIME    PLAT    PLAT    PLAT    PLAT    PLAT    PLAT
        ROLL    PITCH   YAW     SURGE   SWAY    HEAVE

0.00    0.00    0.00    0.00    0.00    0.00    0.00
1.00    0.00    0.00    0.00    0.00    0.00    0.00
9.00    0.00    0.00    0.00    0.00    0.00    0.00
56.00   0.00    0.00    0.00    0.00    0.00    0.00
100.00  0.00    0.00    0.00    0.00    0.00    0.00
```

A.6. Exemplary Hub Height Input File

Listing A.11: Exemplary Hub Height Input File

```
Sample hub-height wind file

Time    Wind    Wind    Vert.   Horiz.  Vert.   LinV    Gust
Speed   Dir     Speed   Shear   Shear   Shear   Speed

0.00    15.00   5.00    -1.00   0.02    0.14    0.00    0.00
0.10    16.55   4.76    -0.90   0.02    0.14    0.00    0.00
0.20    17.94   4.05    -0.80   0.02    0.14    0.00    0.00
0.30    19.05   2.94    -0.70   0.03    0.14    0.00    0.00
0.40    19.76   1.55    -0.60   0.03    0.14    0.00    0.00
0.50    20.00   0.00    -0.50   0.03    0.14    0.00    0.00
0.60    19.76   -1.55   -0.40   0.04    0.14    0.00    0.00
0.70    19.05   -2.94   -0.30   0.04    0.14    0.00    0.00
0.80    17.94   -4.05   -0.20   0.05    0.14    0.00    0.00
0.90    16.55   -4.76   -0.10   0.05    0.14    0.00    0.00
1.00    15.00   -5.00   0.00    0.05    0.14    0.00    0.00
1.10    13.46   -4.76   0.10    0.06    0.14    0.00    0.00
1.20    12.06   -4.05   0.20    0.07    0.14    0.00    0.00
1.30    10.96   -2.94   0.30    0.07    0.14    0.00    0.00
1.40    10.25   -1.55   0.40    0.08    0.14    0.00    0.00
1.50    10.00   0.00    0.50    0.09    0.14    0.00    0.00
1.60    10.25   1.55    0.60    0.10    0.14    0.00    0.00
1.70    10.96   2.94    0.70    0.11    0.14    0.00    0.00
1.80    12.06   4.05    0.80    0.12    0.14    0.00    0.00
1.90    13.46   4.76    0.90    0.13    0.14    0.00    0.00
2.00    15.00   5.00    1.00    0.15    0.14    0.00    0.00
```